Official journal of the CIOMP 2047-7538
www.nature.com/lsa

ARTICLE Open Access

Mn^{5+}-activated $Ca_6Ba(PO_4)_4O$ near-infrared phosphor and its application in luminescence thermometry

Miroslav D. Dramićanin[1,2]✉, Łukasz Marciniak[3], Sanja Kuzman[2], Wojciech Piotrowski[3], Zoran Ristić[2], Jovana Periša[2], Ivana Evans[4], Jelena Mitrić[5], Vesna Đorđević[2], Nebojša Romčević[5], Mikhail G. Brik[1,2,6,7,8] and Chong-Geng Ma[1]✉

Abstract

The near-infrared luminescence of $Ca_6Ba(PO_4)_4O:Mn^{5+}$ is demonstrated and explained. When excited into the broad and strong absorption band that spans the 500–1000 nm spectral range, this phosphor provides an ultranarrow (FWHM = 5 nm) emission centered at 1140 nm that originates from a spin-forbidden $^1E \rightarrow {}^3A_2$ transition with a 37.5% internal quantum efficiency and an excited-state lifetime of about 350 μs. We derived the crystal field and Racah parameters and calculated the appropriate Tanabe–Sugano diagram for this phosphor. We found that ^1E emission quenches due to the thermally-assisted cross-over with the $^3T_2$ state and that the relatively high Debye temperature of 783 K of $Ca_6Ba(PO_4)_4O$ facilitates efficient emission. Since $Ca_6Ba(PO_4)_4O$ also provides efficient yellow emission of the Eu^{2+} dopant, we calculated and explained its electronic band structure, the partial and total density of states, effective Mulliken charges of all ions, elastic constants, Debye temperature, and vibrational spectra. Finally, we demonstrated the application of phosphor in a luminescence intensity ratio thermometry and obtained a relative sensitivity of 1.92% K^{-1} and a temperature resolution of 0.2 K in the range of physiological temperatures.

Introduction

Mn^{5+} optical centers have the $[Ar]3d^2$ electron configuration and always encounter a strong crystal field when tetrahedrally coordinated in crystals. Their lower electronic states have the $^3A_2 < {}^1E < {}^1A_1 < {}^3T_2 < {}^3T_1$ progression in energy. The ground state ($^3A_2$) is orbitally non-degenerate and the first excited state ^1E has almost no nuclear displacement with respect to the $^3A_2$ state and can be split by the low-symmetry ligand field[1]. The ^1E energy of approximately 8000–9000 cm^{-1} is strongly affected by a nephelauxetic effect. At low temperatures, emission occurs solely from the spin-forbidden $^1E \rightarrow {}^3A_2$ electronic transition of a genuine electric dipole origin. At these temperatures, the emission from the spin-allowed $^3T_2 \rightarrow {}^3A_2$ transition is almost negligible since the low energy orbital of the $^3T_2$ state is localized more than 1000 cm^{-1} above the ^1E state, which results in its low population. Therefore, Mn^{5+} emissions appearing in the near infrared (NIR) spectral range at wavelengths longer than 1100 nm and have a narrow spectral band (FWHM < 10 nm) that can be split into two bands with an energy difference of up to 300 cm^{-1}. These emission bands are usually accompanied by vibronic sidebands and have decay times of a few tens to a few hundred microseconds.

The ultranarrow-band NIR luminescence of Mn^{5+} is especially favorable for NIR lasers[2–4] and the development of narrow-band NIR light sources for the selective identification of chemical analytes[5]. Recent research suggests that Mn^{5+} activated nanoparticles are excellent probes for deep-tissue luminescence imaging and luminescence

Correspondence: Miroslav D. Dramićanin (dramican@vinca.rs) or Chong-Geng Ma (cgma.ustc@gmail.com)
[1]School of Optoelectronic Engineering & CQUPT-BUL Innovation Institute, Chongqing University of Posts and Telecommunications, Chongqing 400065, PR China
[2]Centre of Excellence for Photoconversion, Vinca Institute of Nuclear Sciences-National Institute of the Republic of Serbia, University of Belgrade, P.O. Box 522, Belgrade 11001, Serbia
Full list of author information is available at the end of the article

thermometry in the second biological transparency window (1000–1350 nm) and that they show high photo- and chemical stabilities[6,7]. One of their features, especially favorable from the biomedical application perspective, is that they exhibit broad and strong absorption bands from the spin-allowed electronic transitions that span the 500–1000 nm range[8–13], which facilitates their excitation by the wavelength of the first optical biological window. They have a higher quantum efficiency (QE) than Ag_2S or Ag_2Se quantum dots, and do not contain toxic heavy metals like InAs or PbS quantum dots, nor suffer from photobleaching and photoblinking. In comparison to the lanthanide activated NIR bioimaging nanoprobes, Mn^{5+} nanoparticles are brighter due to higher values of the d-d absorption cross-section compared to the spin-forbidden f-f absorptions in the NIR-excited lanthanides. All these advantages of Mn^{5+} indicate that it is an ion with a very important and, so far, unexplored application potential worth large-scale intensive research.

Emissions from Mn^{5+} centers have been demonstrated in a considerably smaller number of host materials compared to Mn^{2+} and Mn^{4+} optical centers[14]. To facilitate Mn^{5+} emission, the material needs to provide both the tetrahedral environment for Mn^{5+} and a sufficiently large energy bandgap compared to the Mn^{5+} transitions' energies. More importantly, the host material must provide the stabilization of the Mn 5+ valence state, which imposes more constraints on the materials' structure and composition than the 2+ and 4+ valance states. For these reasons, the majority of Mn^{5+} emitting host materials contain electropositive ions such as alkaline earth metals and PO_4^{3-} and VO_4^{3-} groups (or SiO_4^{4-} group with a charge compensation). The typical examples of such materials are Mn^{5+} activated Li_3PO_4[15], $Sr_5(VO_4)_3F$[4,16], $Ba_5(PO_4)_3Cl$[17], $Sr_5(PO_4)_3Cl$[1,17,18], Ca_2PO_4Cl[1,17], Ca_2VO_4Cl[1,17], Sr_2VO_4Cl[1,17], Y_2SiO_5[19], and M_2SiO_4 (M = Ba, Sr, Ca)[20].

Recently, Kim et al.[21] have introduced the $Ca_6Ba(PO_4)_4O:Mn^{5+}$ as a new blue pigment that shows coloration due to intense Mn^{5+} absorption, but its luminescent properties have not been analyzed. Also recently, the efficient yellow emission from Eu^{2+} activated $Ca_6Ba(PO_4)_4O$ has been demonstrated[22–24], implying that $Ca_6Ba(PO_4)_4O$ is an interesting host material for luminescent ions. Considering $Ca_6Ba(PO_4)_4O$ structure and composition, one can observe seven electropositive ions (six Ca and one Ba) surrounding the rigidly connected PO_4 tetrahedra. Thus, one may assume that the Mn^{5+} emission, in this new host-activator combination, would be efficient and of high energy due to the nephelauxetic effect. For this reason, we prepared the $Ca_6Ba(PO_4)_4O:Mn^{5+}$ powder for this research and observed the intense NIR emission under the 650 nm excitation. The emission energy of 8772 cm^{-1} is among the highest energies detected for Mn^{5+} activated phosphors. Considering the potential use of $Ca_6Ba(PO_4)_4O$ for both yellow and NIR phosphors and the absence of data on its electronic and vibrational properties, we calculated and explained its electronic band structure, the partial and total density of states (DOS), effective Mulliken charges of all constituent ions, elastic constants, Debye temperature, and vibrational spectra of undoped and Mn^{5+} doped material. Then, we proceeded with the detailed characterization and analysis of $Ca_6Ba(PO_4)_4O:Mn^{5+}$ luminescence that includes the measurements of material absorption, excitation and emission spectra, emission decays, concentration quenching, quantum yield, the temperature dependence of emission band shift, bandwidth and decay, and the calculation of the crystal field parameters. This versatile characterization and analysis of $Ca_6Ba(PO_4)_4O:Mn^{5+}$ undoubtedly confirm the high potential of this material in NIR applications.

Experimental

The conventional solid-state reaction was employed for the preparation of $Ca_6BaP_{4-4x}Mn_{4x}O_{17}$ ($x = 0.005$, 0.0075, 0.0125, 0.01, 0.015, 0.02) powder samples. Stoichiometric amounts of $CaCO_3$ (Alfa Aesar, 98%), $BaCO_3$ (Alfa Aesar, 99.8%), $(NH_4)H_2PO_4$ (Alfa Aesar, 98%), and MnO (Aldrich, 99.99%) were thoroughly mixed in an agate mortar for 1 h with an appropriate amount of ethanol. Mixtures of the raw materials were placed in alumina crucibles and heated in an air atmosphere at 600 °C for 6 h, ground in an agate mortar, and further calcinated at 1280 °C for 10 h.

The crystal structure of powders was examined by powder X-ray diffraction (PXRD) using the Rigaku SmartLab instrument (Cu-K$\alpha_{1,2}$ radiation; $\lambda = 0.1540$ nm) at room temperature. Data were recorded over the 6°−130° 2θ range, with a 0.01° step size and 1 min/° counting time. All PXRD data were analyzed by the Rietveld method implemented in TOPAS Academic software[25,26]. Raman scattering measurements were performed using micro – Raman system TriVista 557 equipped with a triple monochromator and CCD detector (monochromator configuration 900/900/1800 points per millimeter) with 1.5 cm^{-1} resolution. For excitation, Ar laser line at 514.5 nm has an incident power of less than 60 mW to minimize the heating effect. Laser beam was focused on the samples by means of microscopic lenses with 100× magnification. Spectra were recorded in the range of 100–1200 cm^{-1}. Measurements of diffuse reflectance were performed on the Thermo Evolution 600 spectrometer equipped with an integrated sphere, using $BaSO_4$ as a reference over the 220–1350 nm wavelength range. The photoluminescence emission and emission decays were measured using the FLS1000 Fluorescence spectrometer (Edinburgh Instruments; 0.1 nm spectral resolution) supplied with R5509-72 photomultiplier tube from Hamamatsu in nitrogen-flow

cooled housing for near-infrared range detection. For measurements of the emission spectra and decays, the 668 nm laser diode excitation is used in the continuous and pulsed mode, respectively. The temperature of the sample was controlled using a THMS 600 heating-cooling stage from Linkam (0.1 K temperature stability and 0.1 K set point resolution). Emission decays at low temperatures were recorded at 1136 nm for all samples. The luminescence quantum efficiencies were measured using FLS980 Fluorescence Spectrometer from Edinburgh Instruments equipped with 450 W Xenon lamp, R5509-72 photomultiplier tube from Hamamatsu in nitrogen-flow cooled housing for near-infrared range detection, and calibrated integrating sphere for the direct absolute efficiency reading. The Al_2O_3 powder was used as a scattering reference. Thermometry was performed using a custom-made Peltier-based heating stage in the 20–100 °C range (0.02 °C precision). An Ocean Insight LSM-635A LED was used as the excitation source and is controlled by the Ocean Insight LDC-1 single channel driver and controller. The bifurcation optical Y cable was used for measuring PL emission spectra by Ocean Insight NIRQuest+ Spectrometers.

Results and discussion

The structure of $Ca_6Ba(PO_4)_4O$ and $Ca_6Ba(PO_4)_4O:Mn^{5+}$

The starting model used for Rietveld refinement and detailed structural analysis of the two key materials – the $Ca_6Ba(PO_4)_4O$ host and the sample containing 0.5% Mn – was the previously published crystal structure of $Ca_6Ba(PO_4)_4O$ determined from synchrotron powder diffraction data[22]. Refined parameters included the zero-point error, background polynomial terms, peak shape function terms, unit cell parameters, an isotropic atomic displacement parameter per atom type and atomic fractional coordinates, using bond valence sum restraints on the two P atoms. The key crystallographic parameters are summarized in Table 1. $Ca_6Ba(PO_4)_4O$ and $Ca_6Ba(PO_4)_4O$:0.5%Mn adopt monoclinic space group C2/m, with one Ba, two Ca, two P and seven O atoms in the asymmetric unit. Ba atoms are 12-coordinate, the two crystallographically unique Ca atoms are 7- and 8-coordinate, while both unique P atoms adopt tetrahedral coordination environments. Dopant Mn^{5+} ions replace P^{5+} on these two sites, which lie on a mirror plane (Wyckoff site 4 m in space group C2/m). In $Ca_6Ba(PO_4)_4O$, the average cation-oxygen bond lengths in the two tetrahedra are 1.534(13) and 1.529(15) Å, while bond angles range from 105.1(8) to 112.9(7)° and 105.3(7) to 112.8(9)°, with bond valence sums of 5.0(1) for both P atoms. In $Ca_6Ba(PO_4)_4O$:0.5%Mn, the coordination environments remain similar, as expected given a low doping level. Average bond lengths are 1.534(22) and 1.504(27) Å, while bond angles range from 103.4(16) to 112.8(12)° and from 105.5(13) to 112.5(11)°, with bond valence sums of 5.0(2) and 5.4(2) for P1 and P2 sites, (see Tables 2 and 3), respectively. The final Rietveld fits obtained are shown in Fig. 1a, b, while the unit cell and the P atom environments are given in Fig. 1c, d, respectively.

Electronic properties

A detailed calculation of the electronic properties of the $Ca_6Ba(PO_4)_4O$ was performed to verify if its electronic structure is suitable to facilitate the Mn^{5+} emission. The electronic configurations for all chemical elements in $Ca_6Ba(PO_4)_4O$ were as follows: O – $2s^22p^4$, P - $3s^23p^3$, Ca - $3s^23p^64s^2$, Ba - $5s^25p^66s^2$. The following parameters were used for the calculations: energy 10^{-5} eV per atom; maximal force 0.03 eVÅ^{-1}; maximal stress 0.05 GPa; maximal displacement 0.001 Å. K-points set was 2 × 2 × 2 for geometry optimization and 3 × 3 × 3 for the DOS calculations; the energy cut-off was 340 eV.

The structures obtained by geometry optimizations using the generalized gradient approximation (GGA) and the local density approximation (LDA) calculations are shown in Table 1 and are in excellent agreement, LDA especially, with the data obtained by Rietveld analysis of PXRD.

The band gaps in both GGA and LDA calculations, Fig. 2a, are direct, equal to 4.365 eV (GGA) and 4.475 eV (LDA) and have similar values to the reported bandgaps of 4.75 eV for the $Ca_4(PO_4)_2O$ and 5.0 eV for the $Ba_2Ca(PO_4)_2$[27,28]. Since the density-functional theory-based calculations (DFT) always tend to underestimate the true band gaps, the calculated values should be considered as lower band gap estimates.

The conduction band is due to the Ca 4s, 3d and Ba 6s states, Fig. 2b. The top of the valence band is remarkably flat, thus indicating extremely high effective masses of holes. The valence band consists of two sub-bands, which are separated by a narrow gap of about 0.5 eV. The upper one – from about −4.2 eV to 0 eV is made predominantly by the oxygen 2p states. The lower one (from −4.7 eV to about −7 eV) consists of the O 2p states and P 3p states, highly hybridized with each other. The P 3s states make another narrow band between −7.5 eV and −8.5 eV. The O 2s and P 3s states are spread between −22 eV and −17.5 eV, making several clearly seen maxima. The Ba 5s and 5p states are peaked at about −26 eV and −11 eV, respectively, whereas the Ca 3s and 3p states are localized deep in energy at about −38 eV and −20 eV, respectively.

The considered crystal has a high degree of covalency of chemical bonds, which can be assessed by calculating effective Mulliken charges. Since there are two crystallographically inequivalent P^{5+} ions, two Ca^{2+} ions and seven O^{2-} ions and since two types of calculations

Table 1 Summary of structural data for $Ca_6Ba(PO_4)_4O$ and $Ca_6Ba(PO_4)_4O:Mn^{5+}$ (space group C2/m)

	Exp. $Ca_6Ba(PO_4)_4O$			Exp. $Ca_6Ba(PO_4)_4O$:Mn		
a, Å	12.3006 (1)			12.2973 (2)		
b, Å	7.10472 (7)			7.10258 (1)		
c, Å	11.71540 (9)			11.7125 (1)		
β, °	134.4619 (4)			134.4552 (8)		
V, Å^3	730.73 (1)			730.22 (2)		
Fractional atomic coordinates						
	x	***y***	***z***	***x***	***y***	***z***
Ba	0	0	0	0	0	0
Ca1	0.7196 (6)	0	0.3117 (8)	0.719 (1)	0	0.311 (1)
Ca2	0.0505 (4)	0.7665 (5)	0.6929 (4)	0.0505 (8)	0.766 (1)	0.6930 (7)
O	0	0	0.5	0	0	0.5
O11	0.399 (1)	0	0.5822 (5)	0.39 4 (2)	0	0.5822 (8)
O12	0.281 (1)	−0.175 (1)	0.3367 (6)	0.281 (2)	−0.175 (2)	0.336 (1)
O13	0.120 (1)	0	0.366 (1)	0.120 (2)	0	0.365 (2)
O21	0.289 (1)	0	0.106 (2)	0.290 (3)	0	0.104 (3)
O22	0.242 (1)	0	−0.1373 (5)	0.241 (3)	0	−0.1368 (7)
O23	0.462 (1)	−0.179 (1)	0.114 (1)	0.461 (2)	−0.174 (2)	0.114 (1)
P1	0.2673 (6)	0	0.3999 (2)	0.266 (1)	0	0.3998 (2)
P2	0.3659 (8)	0	0.0469 (2)	0.365 (1)	0	0.0469 (3)
	Calculated					
	GGA			**LDA**		
a, Å	12.4130			12.0755		
b, Å	7.1493			6.9658		
c, Å	11.8311			11.4881		
β, °	134.3735			134.4363		
V, Å^3	750.489			689.983		
Fractional atomic coordinates						
	x	***y***	***z***	***x***	***y***	***z***
Ba	*x*	*y*	*z*	*x*	*y*	*z*
Ca1	0	0	0	0	0	0
Ca2	0.71621	0	0.30969	0.71770	0	0.31126
O	0.05261	0.76649	0.69427	0.05232	0.76734	0.69366
O11	0	0	0.5	0	0	0.5
O12	0.39056	0	0.58173	0.39300	0	0.58450
O13	0.28457	−0.17593	0.34032	0.28484	−0.17824	0.33934
O21	0.11338	0	0.34744	0.11195	0	0.34779
O22	0.29114	0	0.11117	0.29072	0	0.11278
O23	0.24386	0	−0.13571	0.24374	0	-0.13726
P1	0.46648	−0.17433	0.11348	0.46930	−0.17679	0.11594
P2	0.26593	0	0.39888	0.26621	0	0.39890

(GGA/LDA) were run, we give the ranges, in which these charges fall for all ions. They are −1.07-1.09 (in units of proton charge) for the oxygen ions, $+2.25 + 2.34$ for the phosphorus ions, $+1.25 + 1.31$ for the calcium ions, and $+1.39 + 1.47$ for the barium ions. The deviation from the formal charges is especially large for the P and O ions, whereas the Ca and Ba effective charges are closer to their formal ones. This is consistent with the P–O bonds being more covalent than the Ca–O and Ba–O ones.

With the calculated elastic constants, it is possible to estimate the Debye temperature using the

following equations:

$$\theta_D = \frac{h}{k}\left(\frac{3n}{4\pi}\frac{N_A\rho}{M}\right)^{1/3} v_m \quad (1)$$

$$v_m = \left[\frac{1}{3}\left(\frac{2}{v_t^3}+\frac{1}{v_l^3}\right)\right]^{-1/3} \quad (2)$$

$$v_l = \sqrt{\frac{3B+4G}{3\rho}},\ v_t = \sqrt{\frac{G}{\rho}} \quad (3)$$

where $h = 6.626 \times 10^{-34}$ J·s is the Planck's constant; $k_B = 1.381 \times 10^{-23}$ JK^{-1} is the Boltzmann constant; $N_A = 6.022 \times 10^{23}$ mol^{-1} is the Avogadro's number; ρ is the crystal's density; n is the number of atoms per one formula unit (twenty eight in the case of $Ca_6Ba(PO_4)_4O$), and M is the formula weight. The average, transverse and longitudinal sound velocities are denoted by v_m, v_t, v_l, correspondingly. The B (bulk modulus) and G (shear modulus) values are calculated as the average values of the corresponding Voigt and Reuss (denoted with the V and R subscripts, respectively) values from Table 4. With these equations and calculated elastic parameters, the Debye temperature for $Ca_6Ba(PO_4)_4O$ was estimated to be 496 K (GGA) and 551 K (LDA).

Table 2 P–O bond lengths (Å)

	Undoped $Ca_6Ba(PO_4)_4O$		Mn^{5+} doped $Ca_6Ba(PO_4)_4O$	
	P1	P2	P1	P2
	1.530 (5)	1.52 (3)	1.527 (8)	1.48 (6)
	1.523 (13)	1.542 (5)	1.53 (2)	1.537 (7)
	1.523 (13)	1.527 (12)	1.53 (2)	1.50 (2)
	1.56 (2)	1.527 (12)	1.55 (4)	1.50 (2)
Avg:	1.534 (13)	1.529 (15)	1.534 (22)	1.504 (27)

Vibrational spectra

For an undistorted tetrahedron (T_d symmetry), the four fundamental vibrational modes (all Raman active) are $a_1 + e + 2t_2$[1,29,30]. The $\nu_1(a_1)$ is the totally symmetric stretching mode, $\nu_2(e)$ is bending deformation, and $\nu_3(t_2)$ and $\nu_4(t_2)$ vibrations are the two stretching t_2 modes. With symmetry lowered from T_d to C_s, several bands appear for each vibrational mode. Raman scattering spectra of the $Ca_6Ba(PO_4)_4O$ and $Ca_6Ba(PO_4)_4O$:Mn^{5+} powders are shown in Fig. 3a, b, respectively. The following assignment is made for the $Ca_6Ba(PO_4)_4O$: ν_L (cm^{-1}) = 123, 153, 183, 215.4, 262.5, and 294.7 are the lattice modes; $\nu_1(a_1)$ (cm^{-1}) = 944 and 985.3; $\nu_2(e)$ = 434.5 (cm^{-1}); $\nu_3(t_2)$ (cm^{-1}) = 1040.1, and 1074.2; $\nu_4(t_2)$ (cm^{-1}) = 584.3 and 608.3. In Raman scattering spectra of the $Ca_6Ba(PO_4)_4O$:Mn^{5+} powder, Fig. 3b, additional vibrations from the MnO_4^{3-} ion are clearly visible: $\nu_1(a_1)$ (cm^{-1}) = 807; $\nu_2(e)$ (cm^{-1}) = 314.4; $\nu_3(t_2)$ (cm^{-1}) = 851.4; $\nu_4(t_2)$ (cm^{-1}) = 343.9, 356.2, and 368.5; ν_{1+} ν_L/ ν_{3+} ν_L (cm^{-1}) = 1128.5 and >1128.5. They agree with the data reported by Gonzalez-Vilchez and Griffith[29] for vibrational modes of the MnO_4^{3-} molecular ion.

Photoluminescence properties

Figure 4a, b displays the absorption, color (inset in Fig. 4a), and emission spectra of $Ca_6Ba(PO_4)_4O$:0.5%Mn^{5+} powder. The observed absorption and emission, the blue coloration of the Mn^{5+} doped powder, and the characteristic vibrational modes of MnO_4^{3-} in the Raman scattering spectrum of $Ca_6Ba(PO_4)_4O$:Mn^{5+} (Fig. 3b) all unambiguously demonstrate the presence of Mn^{5+} in the sample.

Table 3 O–P–O angles and their difference, δ, to regular tetrahedron angle of 109.5°

Undoped $Ca_6Ba(PO_4)_4O$				Mn^{5+} doped $Ca_6Ba(PO_4)_4O$			
P1	δ [°]	P2	δ [°]	Mn1	δ [°]	Mn2	δ [°]
109.8 (12)	0.3	112.8 (9)	3.3	110 (2)	0.5	111.9 (17)	2.4
107.9 (4)	−1.6	105.3 (7)	−4.2	108.8 (8)	−0.7	105.5 (13)	−4.0
107.9 (4)	−1.6	105.3 (7)	−4.2	108.8 (8)	−0.7	105.5 (13)	−4.0
105.1 (8)	−4.4	109.1 (11)	−0.4	103.4 (16)	−6.1	10 9 (2)	−0.5
112.9 (7)	3.4	111.9 (6)	2.4	112.8 (12)	3.3	112.5 (11)	3.0
112.9 (7)	3.4	111.9 (6)	2.4	112.8 (12)	3.3	112.5 (11)	3.0
Avg (δ)	*−0.08*		*−0.12*	Avg (δ)	*−0.07*		*−0.42*
Avg (abs(δ))	*2.4*		*2.8*	Avg (abs(δ))	*2.4*		*2.8*

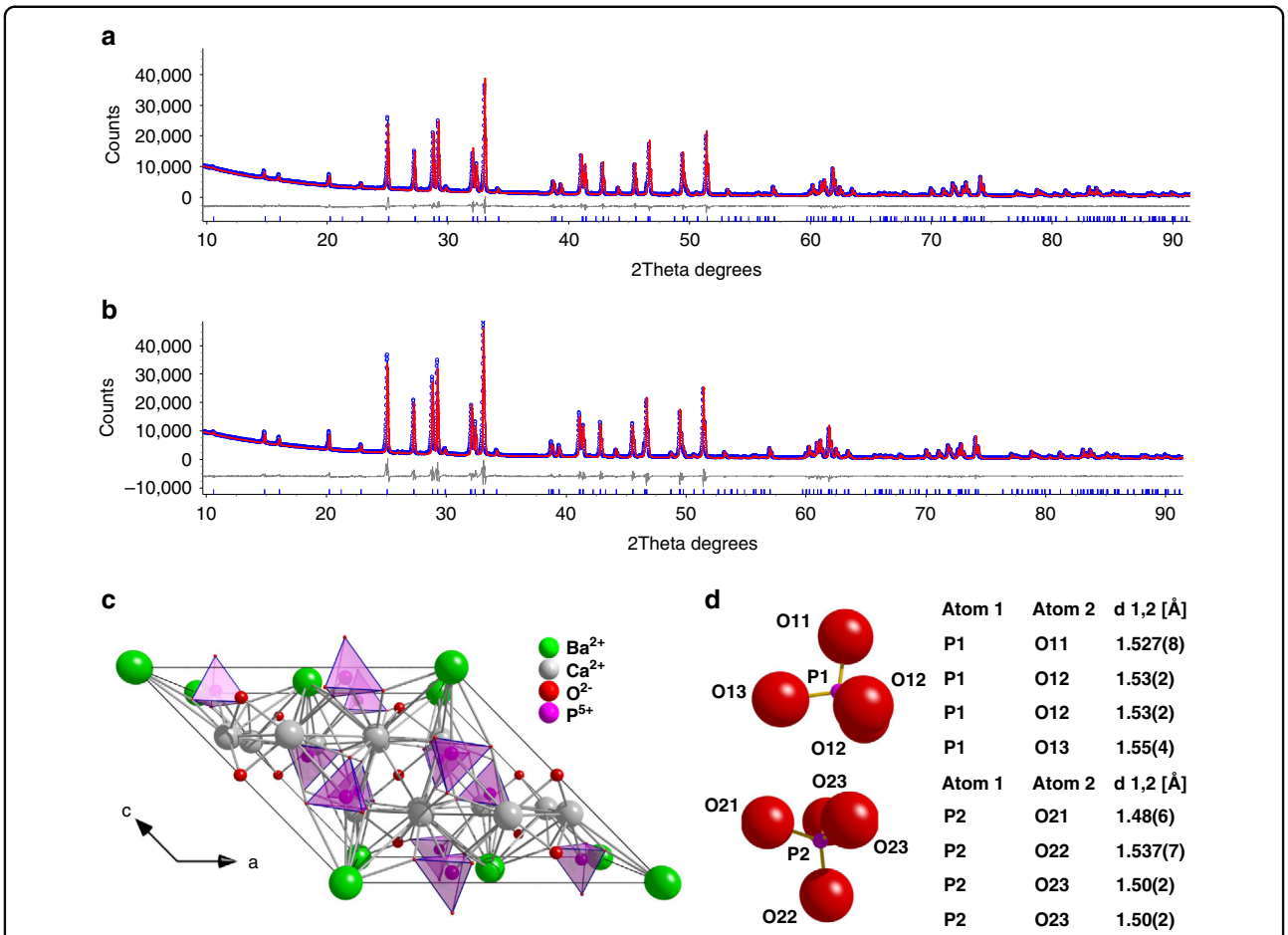

Fig. 1 The structure of $Ca_6Ba(PO_4)_4O:Mn^{5+}$. a Rietveld fits for $Ca_6Ba(PO_4)_4O$, $R_{wp} = 5.31\%$. **b** Rietveld fit for $Ca_6Ba(PO_4)_4O:Mn^{5+}$, $R_{wp} = 8.59\%$. In each case the blue curve represents the observed pattern, the red curve is the calculated pattern and the difference curves are shown in grey, while blue tick marks represent the positions of the Bragg peaks. **c** The crystal structure of $Ca_6Ba(PO_4)_4O$, with the unit cell viewed along the b-axis; **d** Geometries of two PO_4 tetrahedra with average P–O bond lengths in $Ca_6Ba(PO_4)_4O:Mn^{5+}$

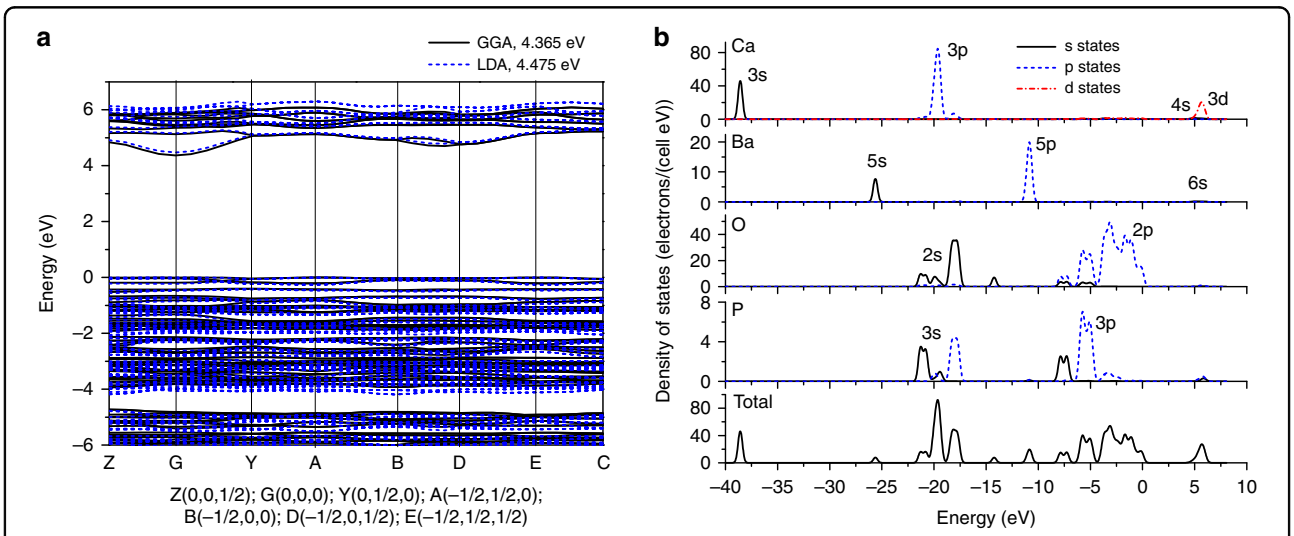

Fig. 2 Electronic properties of $Ca_6Ba(PO_4)_4O:Mn^{5+}$. a The electronic band structure of $Ca_6Ba(PO_4)_4O$. **b** Partial and total density of states of $Ca_6Ba(PO_4)_4O$

Table 4 Calculated elastic constants (in GPa) for $Ca_6Ba(PO_4)_4O$

	GGA	LDA
C_{11}	127.8	162.1
C_{22}	141.2	180.3
C_{33}	149.1	186.3
C_{44}	29.7	42.4
C_{55}	48.0	60.7
C_{66}	55.5	67.3
C_{12}	62.7	81.8
C_{13}	45.5	62.8
C_{15}	4.0	−2.0
C_{23}	38.9	56.4
C_{25}	−4.7	−11.7
C_{35}	−5.2	−7.7
C_{46}	3.5	−3.8
B_V	79.2	103.4
B_R	79.0	102.5
G_V	44.7	55.9
G_R	41.6	53.3

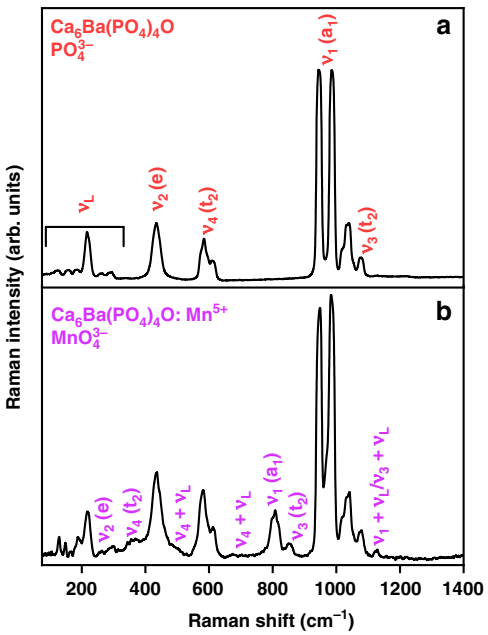

Fig. 3 Vibrational properties of $Ca_6Ba(PO_4)_4O:Mn^{5+}$. a Raman scattering spectra of $Ca_6Ba(PO_4)_4O$ powder. **b** Raman scattering spectra of $Ca_6Ba(PO_4)_4O:Mn^{5+}$ powder

Figure 4a depicts the Kubelka–Munk transformation of the $Ca_6Ba(PO_4)_4O:Mn^{5+}$ powder diffuse reflection measured between 220 and 1350 nm. The $O^{2-} \rightarrow Mn^{5+}$ charge-transfer band appears at around 301 nm (33,222 cm^{-1}) as expected for the tetraoxo-coordinated Mn^{5+} [31] and the peak at the lower wavelength (225 nm) is associated with the intrinsic host absorption. The strong absorption around 639 nm (15,649.5 cm^{-1}) is associated with the $^3A_2 \rightarrow {}^3T_1(^3F)$ electronic transition, which is electric dipole-allowed in an undistorted tetrahedral symmetry and is composed of three overlapping components due to the removal of the orbital degeneracy of the $^3T_1(^3F)$ state with the site symmetry lowering from T_d to C_s. The weak shoulder at about 943 nm (10,604.5 cm^{-1}) corresponds to the symmetry forbidden $^3A_2 \rightarrow {}^3T_2(^3F)$ transition (in T_d site symmetry) and becomes partially allowed with a symmetry lowering. The electric dipole-allowed $^3A_2 \rightarrow {}^3T_1(^3P)$ transition that corresponds to a two-electron jump is located at approximately 369 nm (27,100 cm^{-1}) and is barely visible due to the much more intense charge transfer band. The spin-forbidden transitions to the singlet states $^1A_1(^1G)$ at 740 nm (13,513.5 cm^{-1}) and $^1E(^1D)$ at 1140 nm (8772 cm^{-1}) are weak, sharp, and only weakly depend on the host materials properties. The transitions to $^1T_{1,2}$ singlet states are difficult to observe in the spectrum since they are very weak and superimposed on the main and stronger bands.

Emission spectra of $Ca_6Ba(PO_4)_4O:Mn^{5+}$ powder measured at −190 °C and 10 °C are shown in Fig. 4b with blue and red lines, respectively, and are typical for emissions from transitions of $3d^2$ electronic configuration in a tetrahedral environment as described by the Tanabe–Sugano diagram, Fig. 4c. The spectra show ultranarrow emission bands (FWHM = 3 nm (20 cm^{-1}) at −190 °C; FWHM = 5 nm (35 cm^{-1}) at 10 °C) from the $^1E \rightarrow {}^3A_2$ intraconfigurational transition (1140 nm), followed by vibrational sidebands with progressions of ≈320 cm^{-1} ($(\nu_2(e))$) and ≈800 cm^{-1} ($(\nu_1(a_1))$). This indicates the coupling of the ^1E excited state and the non-totally symmetric $\nu_2(e)$ mode of $MnO_4{}^{3-}$, i.e., a dynamic Jahn–Teller effect.

The very small splitting of ^1E emission band is due to only weakly distorted MnO_4 tetrahedra (see Table 3) and it is barely visible with our instrument resolution at the emission spectrum measured at low temperatures (−190 °C). The low-intensity broad emission band from the $^3T_2(^3F) \rightarrow {}^3A_2$ transition is centered at 1062 nm (9416 cm^{-1}) and can be resolved only spectral deconvolution, Fig. 4d.

Temperature dependence of the ^1E lifetime and emission peak spectral position are shown in Fig. 4e, f, respectively. The ^1E level emission decays show lifetime values of about 350 μs at room temperature and 560 μs at low temperatures. The temperature dependence of

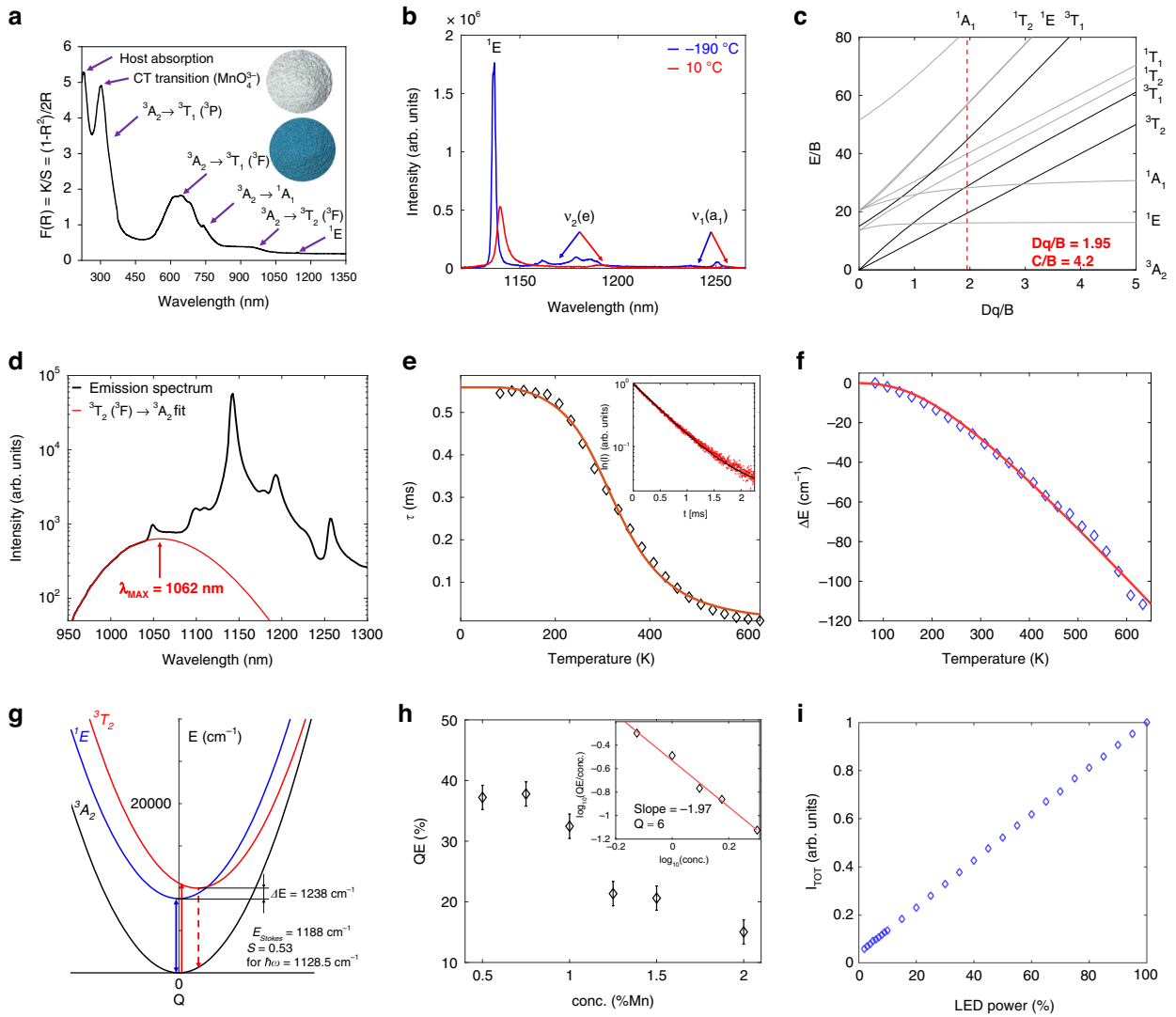

Fig. 4 Optical properties of the $Ca_6Ba(PO_4)_4O:Mn^{5+}$ powder. a The Kubelka–Munk transformation of the $Ca_6Ba(PO_4)_4O:Mn^{5+}$ diffuse reflectance The inset shows photographs of the $Ca_6Ba(PO_4)_4O$ (white) and $Ca_6Ba(PO_4)_4O:Mn^{5+}$ (blue) powders. **b** Emission spectra measured at −190 °C and 10 °C. **c** Tanabe–Sugano diagram for $3d^2$ electron configuration in tetrahedral coordination. **d** Emission spectrum of the $Ca_6Ba(PO_4)_4O:Mn^{5+}$ measured at room temperature (black line) and the fit to the Gaussian of the $^3T_2 \rightarrow {}^3A_2$ emission peak (red line) showing its maximum 1062 nm/9416 cm^{-1}. Spectra shown in logarithmic scale. **e** Temperature dependence of the excited state lifetime (symbols – experimental data, solid line – the fit to Eq. (4)). The inset shows emission decay measured at 208 K. **f** Temperature dependence of the ^1E emission peak spectral position (symbols – experimental data, solid line – the fit to Eq. (5)). **g** The estimate of configurational diagram based on the spectroscopic data with calculated Stokes shift (E_{Stokes}) and Huang–Rhys parameter (S). **h** Photoluminescence internal quantum efficiency (QE) of $Ca_6Ba(PO_4)_4O:Mn^{5+}$ powders for different concentrations of Mn. The inset shows linear dependence of the $\log_{10}$(QE/concentration) vs $\log_{10}$(concentration) for data equal and above critical concentration (0.75%) with a slope of −1.97 indicating that a multipolar dipole-dipole mechanism is responsible for the concentration quenching of emission. **i** The linear dependence of $Ca_6Ba(PO_4)_4O:Mn^{5+}$ emission intensity on excitation power

lifetime, Fig. 4e, shows that a low-temperature lifetime value is approximately the value of a radiative lifetime. Considering that the excited state is separated in energy from the ground state by 8772 cm^{-1}, almost eight quanta of the highest vibrational frequencies of the phosphor (≈1100 cm^{-1}) are needed to bridge the gap. Thus, a multiphonon non-radiative relaxation is not probable as the emission quenching mechanism. The ^1E emission deactivation through the crossing with a charge transfer band is also not probable due to very high energy difference. Therefore, we assume that the thermal quenching of the ^1E state population takes place by a thermally activated cross-over via $^3T_2$ state, see Fig. 4g, similarly to Mn^{4+} activated phosphors. The temperature dependence of the emission lifetime, shown in Fig. 4e, can be described by the

following equation[32–35]:

$$\tau(T) = \frac{\tau_{R0} \cdot \tanh(h\nu/2k_BT)}{1 + (\tau_{R0} \cdot \tanh(h\nu/2k_BT)/\tau_{NR}) \cdot \exp(-\Delta E/k_BT)} \quad (4)$$

where $\tau_{R0} = 560 \pm 19\,\mu s$ is the radiative lifetime at $T = 0\,K$, $k_B = 0.69503476\,cm^{-1}K^{-1}$ is the Boltzmann constant, $h\nu = 448 \pm 90\,cm^{-1}$ is the average energy of phonon coupled to the $^1E \rightarrow {}^3A_2$ transition, $1/\tau_{NR} = 1527 \pm 120\,ms^{-1}$ is the nonradiative decay rate, $\Delta E = 1631 \pm 200\,cm^{-1}$ is the activation energy of the process (the cross-over via the $^3T_2$ state), and T represents the temperature. The smaller the configuration coordinate parabola offset between the ground state ($^3A_2$) and the $^3T_2$ state, the larger the cross-over energy ΔE (activation energy of the process) needed to activate the non-radiative de-excitation process. Thus, the $^1E \rightarrow {}^3A_2$ emission of Mn^{5+} activated phosphors, which have large $^3T_2$ energies and smaller Stokes shifts, will start to quench at higher temperatures.

The shift of ^1E emission band with energy is shown in Fig. 4f. It can be described by the following equation:[36,37]

$$\delta E\left[cm^{-1}\right] = \alpha \cdot \left(\frac{T}{\theta_D}\right)^4 \cdot \int_0^{T/\theta_D} \frac{x^3}{e^x - 1} dx \quad (5)$$

where $\theta_D = 783 \pm 12\,K$ is the Debye temperature of the host material, $x = \hbar\omega_D/k_BT = \theta_D/T$, ω_D is Debye cut-off frequency, and $\alpha = -650 \pm 17\,cm^{-1}$ represents the electron-phonon coupling coefficient. The relatively high Debye temperature indicates a rigid structure which favors efficient emissions from optical centers[38].

The concentration dependence of an internal quantum efficiency (QE) is given in Fig. 4h. The largest value of 37.5 ± 2.0% is recorded for the 0.5% Mn^{5+} doped sample, after which the concentration quenching of emission occurs. This is a relatively high value for an NIR-emitting phosphor, and comparable to one obtained in $Ba_3(PO_4)_2$[7]. The $\log_{10}$(QE/concentration) vs $\log_{10}$(concentration) plot has a −1.97 slope, which is close to −2, which undoubtedly indicates that a multipolar electric dipole-dipole mechanism is responsible for the concentration quenching of emission. The linear dependence of $Ca_6Ba(PO_4)_4O:Mn^{5+}$ emission intensity on excitation power, Fig. 4i, is expected for the typical downshifting photoluminescence emission process.

The $3d^2$ electronic configuration of Mn^{5+} in a tetrahedral environment is described by the Tanabe–Sugano model for $3d^8$ electronic configuration in octahedral symmetry[39], see Fig. 4c. The crystal field and Racah parameters are calculated from the following equations using data from diffuse reflection and emission spectra[40,41]:

$$Dq = \frac{E(^3A_2 \rightarrow {}^3T_2)}{10} = \frac{10604.5}{10}\ cm^{-1} = 1060\ cm^{-1} \quad (6)$$

$$x = \frac{E(^3A_2 \rightarrow {}^3T_1) - E(^3A_2 \rightarrow {}^3T_2)}{Dq} = \frac{15649.5 - 10604.5}{1060.45} = 4.757 \quad (7)$$

$$B = \frac{x^2 - 10x}{15 \cdot (x - 8)} \cdot Dq = 544\ cm^{-1} \rightarrow \frac{10Dq}{B} = 19.5 \quad (8)$$

$$C = \frac{1}{2} \cdot \left(E(^3A_2 \rightarrow {}^1E) - 10Dq - 8.5B + \frac{1}{2}\sqrt{400Dq^2 + 40DqB + 49B^2}\right) = 2292\ cm^{-1} \quad (9)$$

$$C/B = 4.21 \quad (10)$$

By comparing the obtained Dq, B and C parameters with literature data, Table 5, one can observe that $Ca_6Ba(PO_4)_4O$ provides the smallest Dq and the largest B parameters amongst all phosphate hosts, and that Li_3VO_4 is the only host with a smaller Dq (considering available data).

By considering the obtained parameters and the configuration coordinate diagram, Fig. 4g, the relatively small value of Huang–Rhys parameter S = 0.53 is found for the assumed coupling to the ν_{1+} ν_L/ ν_{3+} ν_L vibrational mode with energy $\hbar\omega = 1128.5\ cm^{-1}$.

The Slater parameters are calculated from Racah parameters by the simple relations[42,43]:

$$F^{(2)} = 49F_2 = 7(7B + C) = 42271 cm^{-1} \quad (11)$$

$$F^{(4)} = 441F_4 = 441\frac{C}{35} = 28877\ cm^{-1} \quad (12)$$

Table 5 Comparison of the *Dq*, *B* and *C* parameters (all in cm^{-1}) for the tetrahedrally coordinated Mn^{5+} ions in different crystalline solids

Host material	*Dq*	*B*	*C*	Reference
Li_3PO_4	1208	475	2556	[49]
Ca_2PO_4Cl	1162	455	2657	[49]
Y_2SiO_5	1133	550	2255	[50]
$Sr_5(PO_4)_3Cl$	1100	500	2320	[3]
$YAlO_3$	1100	485	2256	[51]
$Sr_{10}(VO_4)_6F_2$	1088	518	2321	[52]
$Ca_6Ba(PO_4)_4O$	1060	544	2292	*This work*
Li_3VO_4	1049	646	2006	[53]

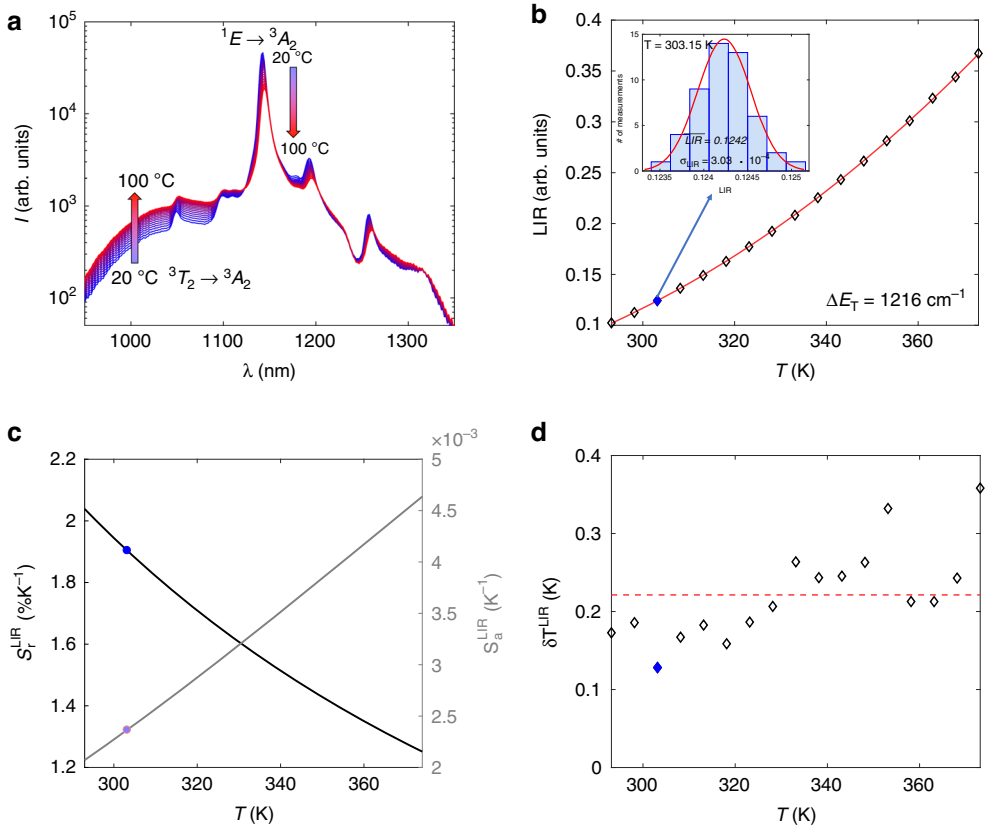

Fig. 5 Luminescence thermometry with $Ca_6Ba(PO_4)_4O:Mn^{5+}$ powder. a Photoluminescence emission spectra of $Ca_6Ba(PO_4)_4O:Mn^{5+}$ powder measured at different temperatures. **b** Luminescence intensity ratio (LIR) as a function of temperature (experimental data - diamond markers; fit to Eq. (13) - full line). The insert shows the LIR distribution histogram measured at 303.15 K (30 °C) – filled diamond marker. **c** Calculated absolute and relative sensitivities (marked values at 303.15 K (30 °C)). **d** Experimentally obtained values for temperature resolution – filled diamond marker represents the value at 303.15 K (30 °C)

Both values are considerably reduced from the free-ion values of $F^{(2)} = 91427\text{cm}^{-1}$ and $F^{(4)} = 56625\ \text{cm}^{-1}$[18].

As it follows from the Tanabe–Sugano diagram for the $3d^2$ configuration in the tetrahedral crystal field (Fig. 4c), the energy separation between the ground state $^3A_2$ and the first excited state ^1E (in the strong crystal field) is practically independent on the crystal field strength (both states are parallel to each other). At the same time, this energy interval is very close to the energy interval between the ^3F and ^1D states of the free ion, which is determined by the Racah parameters B and C, which vary from host to host because of the covalent effects. As a result, the nephelauxetic effect is dominating in this case.

Application in luminescence thermometry

We have tested the performance of Mn^{5+} activated $Ca_6Ba(PO_4)_4O$ (the sample containing 0. 5% Mn since it showed the best quantum efficiency) as a NIR luminescent thermometer operating in the second biological window and in the physiological temperature range. As can be seen from Fig. 5a, when temperature increases, the broad emission peak from the $^3T_2$ level in the 950 nm to 1030 nm range also increases in intensity, while the intensity of the narrow emission peak from the ^1E level around 1140 nm decreases with temperature. This occurs due to thermalization between ^1E and $^3T_2$ levels where the energy difference between these two levels (ΔE_T) is bridged by thermally exited electrons. Consequently, a simple Boltzmann-type relation for the luminescence intensity ratio (LIR) between the two abovementioned emission intensities applies[44,45]:

$$LIR(T) = \frac{I(^3T_2)}{I(^1E)} = B \cdot \exp\left(-\frac{\Delta E_T}{k_B T}\right) \quad (13)$$

where B is a temperature-invariant constant and T represents temperature. The fit of Eq. (13) (full line, Fig. 5b) to experimental LIR data (diamond markers, Fig. 5b) is almost perfect ($R^2 = 0.997$) and provides an energy difference ΔE_T of 1216 cm^{-1} that agrees with the energy difference obtained from spectroscopy (Fig. 4g).

To experimentally determine the uncertainty in the LIR (error budget), 50 emission spectra were acquired at each temperature. Then, the measurement distribution mean was used as the LIR value while a standard deviation (σ_{LIR}) was used as an uncertainty in LIR as shown in the insert of Fig. 5b on the LIR value distribution measured at 30 °C).

The absolute (S_a) and relative (S_r) sensitivities of the thermometer were then calculated from the following equations:

$$S_a\left[\mathrm{K}^{-1}\right] = \left|\frac{\partial LIR}{\partial T}\right|,\ S_r\left[\%\mathrm{K}^{-1}\right] = 100\% \cdot \left|\frac{\partial LIR}{\partial T}\frac{1}{LIR}\right| \tag{14}$$

and presented in Fig. 5c (blue dots represent values obtained at a temperature of 30 °C). The relative sensitivity value varies from 2.35%K^{-1} to 1.26%K^{-1} over the measurement range, being 1.92%K^{-1} at 30 °C. These are relatively high values[46], especially for luminescence thermometers operating in the second biological transparency window (>1000 nm). For example, Gschwend et al.[47] achieved a relative sensitivity of 0.43%K^{-1} for an LIR thermometer based on Mn^{5+}-activated $Ba_3(PO_4)_2$, while Shen et al.[48] achieved a relative sensitivity of 1.3%K^{-1} for an LIR thermometer based on Ag_2S quantum dots.

The temperature resolution (uncertainty in measured temperature, δT) is determined as a ratio between experimentally obtained LIR uncertainty (σ_{LIR}) and absolute sensitivity (S_a) for a given temperature, Fig. 5d:

$$\delta T = \frac{\sigma_{LIR}(T)}{S_a(T)} \tag{15}$$

and it has an average value of 0.21 K. Finally, repeatability of measurement (R_M) is quantified as[46]:

$$R_M = 1 - \frac{max\left|\overline{LIR} - LIR_i\right|}{\overline{LIR}} \tag{16}$$

where $\overline{LIR}$ is the average LIR measured at a certain temperature over all LIR_i acquired. Based on experimental data, an R_M value of 0.97 (97%) is obtained.

Conclusion

Because of its rigid structure, appropriate crystal sites for doping, and sufficiently large energy band gap to accommodate the energy levels of dopant ions, $Ca_6Ba(PO_4)_4O$ is an excellent host for Eu^{2+}, Sm^{2+} and Mn^{5+} luminescence centers. In this host, Mn^{5+} provides ultranarrow emission in the near-infrared spectral range at 1140 nm that can be easily excited over the broad spectral range that spans 500–1000 nm covering the entirety of the first biological transparency window and making this material an excellent near-infrared phosphor and non-toxic blue/turquoise pigment. The phosphor has an internal quantum efficiency of 37.5%, which is a high value considering the quantum efficiencies of inorganic NIR phosphors. The thermal quenching of the ^1E emission takes place by a thermally activated cross-over via the $^3T_2$ state with an activation energy of 1631 cm^{-1}. The optimal Mn^{5+} doping concentration is 0.5%. For higher doping concentrations, quantum efficiency decreases due to non-radiative deexcitation caused by a dipole-dipole electric interaction. Based on the available literature data, the $Ca_6Ba(PO_4)_4O:Mn^{5+}$ phosphor provides the smallest *Dq* and the largest *B* parameters amongst all phosphate hosts. This material is one of the best single-doped ratiometric luminescence thermometry sensors for use in a second biological transparency window due to the opposite temperature dependence of the ^1E and $^3T_2$ emission intensities. It provides a relative sensitivity of 1.92%K^{-1} and a temperature resolution of 0.2 K in the range of physiological temperatures, with a measurement repeatability of 97%. These findings, particularly the high value of quantum efficiency and strong absorption, tuneability of emission wavelength by changing the Mn^{5+} environment, long emission decay times that allow for time-gated measurements, and strong temperature susceptibility of emission, demonstrate the great potential of Mn^{5+}-activated phosphors for NIR applications. When reduced to nano dimension, $Ca_6Ba(PO_4)_4O:Mn^{5+}$ has great potential for bioimaging and biothermal imaging applications in the second biological transparency window. Future research will concentrate on the synthesis and applications of $Ca_6Ba(PO_4)_4O:Mn^{5+}$ nanoparticles.

Acknowledgements

The authors from Serbia acknowledge funding from the Ministry of Education, Science, and Technological Development of the Republic of Serbia. M.D.D. recognizes the support from the Chinese National Foreign Experts Program for "Belt and Road Initiative" Innovative Talent Exchange (Grant No. DL2021035001L). M.G.B. thanks the support from the Program for Foreign Experts (Grant No. W2017011) offered by Chongqing University of Posts and Telecommunications, Estonian Research Council grant PUT PRG111, European Regional Development Fund (TK141), NCN project 2018/31/B/ST4/00924 and 2021/40/Q/ST5/00336. C.-G.M. acknowledges the support of the National Natural Science Foundation of China (Grant No. 52161135110) and China-Poland Intergovernmental Science and Technology Cooperation Program (Grant No. 2020[15]/10).

Author details

[1]School of Optoelectronic Engineering & CQUPT-BUL Innovation Institute, Chongqing University of Posts and Telecommunications, Chongqing 400065, PR China. [2]Centre of Excellence for Photoconversion, Vinca Institute of Nuclear Sciences-National Institute of the Republic of Serbia, University of Belgrade, P.O. Box 522, Belgrade 11001, Serbia. [3]Institute of Low Temperature and Structure Research, Polish Academy of Sciences, Okólna 2, 50-422 Wroclaw, Poland. [4]Department of Chemistry, Durham University, Durham DH1 3LE, UK. [5]Institute of Physics, University of Belgrade, Pregrevica 118, 11080 Belgrade, Serbia. [6]Institute of Physics, University of Tartu, Tartu 50411, Estonia. [7]Department of Theoretical Physics, Jan Długosz University, Czestochowa PL 42200, Poland. [8]Academy of Romanian Scientists, Ilfov Str. No. 3, 050044 Bucharest, Romania

Author contributions

M.D.D.: Conceptualization, Methodology, Formal analysis, Writing- Original draft preparation; Writing- Revised draft preparation. Ł.M., Z.R., V.Đ.: Investigation, Formal analysis. Z.R., I.E., M.G.B.: Investigation, Formal analysis, Writing- Revised draft preparation. S.K., W.P., J.P., J.M., N.R., C.-G.M.: Investigation.

Data availability

The data that support the findings of this study are available from the corresponding author upon reasonable request.

Conflict of interest

The authors declare no competing interests.

Received: 30 April 2022 Revised: 8 August 2022 Accepted: 16 August 2022
Published online: 22 September 2022

References

1. Capobianco, J. A. et al. Near-infrared intraconfigurational luminescence spectroscopy of the Mn^{5+} ($3d^2$) ion in Ca_2PO_4Cl, $Sr_5(PO_4)_3Cl$, Ca_2VO_4Cl and Sr_2VO_4Cl. *J. Lumin.* **54**, 1–11, https://doi.org/10.1016/0022-2313(92)90043-9 (1992).
2. Merkle, L. D. et al. Laser action from Mn^{5+} in $Ba_3(VO_4)_2$. *Appl. Phys. Lett.* **61**, 2386–2388, https://doi.org/10.1063/1.108172 (1992).
3. Moncorgé, R., Manaa, H. & Boulon, G. Cr^{4+} and Mn^{5+} active centers for new solid state laser materials. *Optical Mater.* **4**, 139–151, https://doi.org/10.1016/0925-3467(94)90071-X (1994).
4. Merkle, L. D., Guyot, Y. & Chai, B. H. T. Spectroscopic and laser investigations of Mn^{5+}:$Sr_5(VO_4)_3F$. *J. Appl. Phys.* **77**, 474–480, https://doi.org/10.1063/1.359585 (1995).
5. Ma, L. J. et al. Systematic discovery about NIR spectral assignment from chemical structural property to natural chemical compounds. *Sci. Rep.* **9**, 9503, https://doi.org/10.1038/s41598-019-45945-y (2019).
6. Gschwend, P. M. et al. Bi_2O_3 boosts brightness, biocompatibility and stability of Mn-doped $Ba_3(VO_4)_2$ as NIR-II contrast agent. *J. Mater. Chem. B* **9**, 3038–3046, https://doi.org/10.1039/d0tb02792h (2021).
7. Cao, R. P. et al. Near-infrared emission $Ba_3(PO_4)_2$:Mn^{5+} phosphor and potential application in vivo fluorescence imaging. *Spectrochimica Acta Part A* **128**, 671–673, https://doi.org/10.1016/j.saa.2014.02.081 (2014).
8. Medina, E. A. et al. Intense turquoise colors of apatite-type compounds with Mn^{5+} in tetrahedral coordination. *Solid State Sci.* **52**, 97–105, https://doi.org/10.1016/j.solidstatesciences.2015.12.001 (2016).
9. Laha, S. et al. Stabilization of a tetrahedral ($Mn^{5+}O_4$) chromophore in ternary barium oxides as a strategy toward development of new turquoise/green-colored pigments. *Inorg. Chem.* **55**, 3508–3514, https://doi.org/10.1021/acs.inorgchem.5b02957 (2016).
10. Wang, Y. Q. et al. Synthesis and optical properties of intense blue colors oxides based on Mn^{5+} in tetrahedral sites in $Ba_7Al_{2-x}Mn_xO_{10+y}$. *Ceram. Int.* **47**, 686–691, https://doi.org/10.1016/j.ceramint.2020.08.177 (2021).
11. Cui, K. Y. et al. Synthesis and properties of novel inorganic green chromophore based on $Bi_{24}Al_{2-x}Mn_xO_{39}$. *Ceram. Int.* **47**, 8944–8948, https://doi.org/10.1016/j.ceramint.2020.12.016 (2021).
12. Zhou, Y. C. et al. Synthesis and properties of novel turquoise-green pigments based on $BaAl_{2-x}Mn_xO_{4+y}$. *Dyes Pigments* **155**, 212–217, https://doi.org/10.1016/j.dyepig.2018.03.042 (2018).
13. Dardenne, K., Vivien, D. & Huguenin, D. Color of Mn(V)-substituted apatites $A_{10}((B, Mn)O_4)_6F_2$, A = Ba, Sr, Ca; B = P, V. *J. Solid State Chem.* **146**, 464–472, https://doi.org/10.1006/jssc.1999.8394 (1999).
14. Zhou, Q. et al. Mn^{2+} and Mn^{4+} red phosphors: synthesis, luminescence and applications in WLEDs. A review. *J. Mater. Chem. C* **6**, 2652–2671, https://doi.org/10.1039/C8TC00251G (2018).
15. Hazenkamp, M. F. et al. Excited state absorption and laser potential of Mn^{5+}-doped Li_3PO_4. *Chem. Phys. Lett.* **265**, 264–270, https://doi.org/10.1016/S0009-2614(96)01434-0 (1997).
16. Kück, S., Schepler, K. L. & Chai, B. H. T. Evaluation of Mn^{5+}-doped $Sr_5(VO_4)_3F$ as a laser material based on excited-state absorption and stimulated-emission measurements. *J. Optical Soc. Am. B* **14**, 957–963, https://doi.org/10.1364/JOSAB.14.000957 (1997).
17. Herren, M. et al. Near-infrared luminescence of manganate(V)-doped phosphates and vanadates. *J. Luminescence* **53**, 452–456, https://doi.org/10.1016/0022-2313(92)90196-G (1992).
18. Capobianco, J. A. et al. Crystal-field analyis of Mn^{5+} ($3d^2$) in $Sr_5(PO_4)_3Cl$. *Optical Mater.* **1**, 209–216, https://doi.org/10.1016/0925-3467(92)90029-M (1992).
19. Hömmerich, U. et al. The optical center $M_nO_4^{3-}$ in Y_2SiO_5:Mn, X (X=Al, Ca). *Chem. Phys. Lett.* **213**, 163–167, https://doi.org/10.1016/0009-2614(93)85435-Q (1993).
20. Zhang, X. W. et al. Structural variation and near infrared luminescence in Mn^{5+}-doped M_2SiO_4 (M = Ba, Sr, Ca) phosphors by cation substitution. *J. Mater. Sci. Mater. Electron.* **29**, 6419–6427, https://doi.org/10.1007/s10854-018-8622-2 (2018).
21. Kim, S. W. et al. Discovery of novel inorganic Mn^{5+}-doped sky-blue pigments based on $Ca_6BaP_4O_{17}$: crystal structure, optical and color properties, and color durability. *Dyes Pigments* **139**, 344–348, https://doi.org/10.1016/j.dyepig.2016.12.038 (2017).
22. Komuro, N. et al. Synthesis, structure and optical properties of europium doped calcium barium phosphate – a novel phosphor for solid-state lighting. *J. Mater. Chem. C* **2**, 6084–6089, https://doi.org/10.1039/c4tc00732h (2014).
23. Ji, H. P. et al. Facile solution-precipitation assisted synthesis and luminescence property of greenish-yellow emitting $Ca_6Ba(PO_4)_4O$:Eu^{2+} phosphor. *Mater. Res. Bull.* **75**, 233–238, https://doi.org/10.1016/j.materresbull.2015.11.055 (2016).
24. Meng, Y. J. et al. Thermal stability of the luminescence of $Ca_6Ba(PO_4)_4O$:Eu^{2+} yellow phosphor for white light-emitting diodes. *Appl. Phys. A* **122**, 636, https://doi.org/10.1007/s00339-016-0141-5 (2016).
25. Rietveld, H. M. A profile refinement method for nuclear and magnetic structures. *J. Appl. Crystallogr.* **2**, 65–71, https://doi.org/10.1107/S0021889869006558 (1969).
26. Coelho, A. A. et al. The TOPAS symbolic computation system. *Powder Diffr.* **26**, S22–S25, https://doi.org/10.1154/1.3661087 (2011).
27. Deng, D. G. et al. $Ca_4(PO_4)_2O$:Eu^{2+} red-emitting phosphor for solid-state lighting: structure, luminescent properties and white light emitting diode application. *J. Mater. Chem. C* **1**, 3194–3199, https://doi.org/10.1039/C3TC30148F (2013).
28. Yu, H. et al. $Ba_2Ca(PO_4)_2$:Eu^{2+} emission-tunable phosphor for solid-state lighting: luminescent properties and application as white light emitting diodes. *J. Mater. Chem. C* **1**, 5577–5582, https://doi.org/10.1039/C3TC30998C (2013).
29. Gonzalez-Vilchez, F. & Griffith, W. P. Transition-metal tetra-oxo-complexes and their vibrational spectra. *J. Chem. Soc. Dalton Trans.* 1416–1421, https://doi.org/10.1039/DT9720001416 (1972).
30. Griffith, W. P. Raman studies on rock-forming minerals. Part II. Minerals containing MO_3, MO_4, and MO_6 groups. *J. Chem. Soc. A* 286-291, https://doi.org/10.1039/J19700000286 (1970).
31. Lachwa, H. & Reinen, D. Color and electronic structure of manganese(V) and manganese(VI) in tetrahedral oxo coordination. A spectroscopic investigation. *Inorg. Chem.* **28**, 1044–1053, https://doi.org/10.1021/ic00305a011 (1989).
32. Ristić, Z. et al. Near-infrared luminescent lifetime-based thermometry with Mn^{5+}-activated $Sr_3(PO_4)_2$ and $Ba_3(PO_4)_2$ phosphors. *ACS Appl. Electron. Mater.* **4**, 1057–1062, https://doi.org/10.1021/acsaelm.1c01207 (2022).
33. Senden, T., van Dijk-Moes, R. J. A. & Meijerink, A. Quenching of the red Mn^{4+} luminescence in Mn^{4+}-doped fluoride LED phosphors. *Light Sci. Appl.* **7**, 8, https://doi.org/10.1038/s41377-018-0013-1 (2018).
34. Dramićanin, M. D. et al. Li_2TiO_3:Mn^{4+} deep-red phosphor for the lifetime-based luminescence thermometry. *Chem. Select* **4**, 7067–7075, https://doi.org/10.1002/slct.201901590 (2019).
35. Srivastava, A. M. et al. Unusual luminescence of octahedrally coordinated divalent europium ion in $Cs_2M^{2+}P_2O_7$ (M^{2+}=Ca, Sr). *J. Luminescence* **129**, 919–925, https://doi.org/10.1016/j.jlumin.2009.03.018 (2009).
36. McCumber, D. E. & Sturge, M. D. Linewidth and temperature shift of the *R* lines in ruby. *J. Appl. Phys.* **34**, 1682–1684, https://doi.org/10.1063/1.1702657 (1963).
37. Yen, W. M., Scott, W. C. & Schawlow, A. L. Phonon-induced relaxation in excited optical states of trivalent praseodymium in LaF_3. *Phys. Rev. J. Archive* **136**, A271–A283, https://doi.org/10.1103/PhysRev.136.A271 (1964).
38. Pust, P. et al. Narrow-band red-emitting Sr[$LiAl_3N_4$]:Eu^{2+} as a next-generation LED-phosphor material. *Nat. Mater.* **13**, 891–896, https://doi.org/10.1038/nmat4012 (2014).
39. Tanabe, Y. & Sugano, S. On the absorption spectra of complex ions. I. *J. Phys. Soc. Jpn* **9**, 753–766, https://doi.org/10.1143/JPSJ.9.753 (1954).

40. Sugano, S., Tanabe, Y. & Kamimura, H. *Multiplets of transition-metal ions in crystals* (New York: Academic Press, 1970).
41. Brik, M. G. et al. Spin-forbidden transitions in the spectra of transition metal ions and nephelauxetic effect. *ECS J. Solid State Sci. Technol.* **5**, R3067–R3077, https://doi.org/10.1149/2.0091601jss (2016).
42. Schmidtke, H. H. The variation of slater-condon parameters F^k and racah parameters B and C with chemical bonding in transition group complexes. In: *Optical spectra and chemical bonding in inorganic compounds* (eds Mingos, D. M. P. & Schönherr, T.) 19–35 (Springer, Berlin, Heidelberg, 2004) https://doi.org/10.1007/b11303.
43. Racah, G. Theory of complex spectra. III. *Phys. Rev. J. Arch.* **63**, 367–382, https://doi.org/10.1103/PhysRev.63.367 (1943).
44. Dramićanin, M. Lanthanide and transition metal ion doped materials for luminescence temperature sensing. In: *Luminescence thermometry: methods, materials, and applications* (ed. Dramićanin, M.) (Elsevier, Amsterdam, 2018), https://doi.org/10.1016/B978-0-08-102029-6.00006-3.
45. Marciniak, L. et al. Luminescence thermometry with transition metal ions. A review. *Coordination Chem. Rev.* **469**, 214671, https://doi.org/10.1016/j.ccr.2022.214671 (2022).
46. Dramićanin, M. D. Trends in luminescence thermometry. *J. Appl. Phys.* **128**, 040902, https://doi.org/10.1063/5.0014825 (2020).
47. Gschwend, P. M. et al. Simultaneous nanothermometry and deep-tissue imaging. *Adv. Sci.* **7**, 2000370, https://doi.org/10.1002/advs.202000370 (2020).
48. Shen, Y. L. et al. Ag_2S nanoheaters with multiparameter sensing for reliable thermal feedback during in vivo tumor therapy. *Adv. Funct. Mater.* **30**, 2002730, https://doi.org/10.1002/adfm.202002730 (2020).
49. Brik, M. G. et al. Crystal field parameters and energy level structure of the MnO_4^{3-} tetroxo anion in Li_3PO_4, Ca_2PO_4Cl and $Sr_5(PO_4)_3Cl$ crystals. *J. Luminescence* **129**, 801–806, https://doi.org/10.1016/j.jlumin.2009.02.018 (2009).
50. Shen, Y. R., Riedener, T. & Bray, K. L. Effect of pressure on site-symmetry distortions of Mn^{5+} and Cr^{4+} in Y_2SiO_5. *Phys. Rev. B* **61**, 9277–9286, https://doi.org/10.1103/PhysRevB.61.9277 (2000).
51. Brik, M. G. et al. Spectroscopic and crystal field studies of $YAlO_3$ single crystals doped with Mn ions. *J. Phys. Condensed Matter* **21**, 025404, https://doi.org/10.1088/0953-8984/21/2/025404 (2009).
52. Scott, M. A. et al. Optical spectroscopy of $(MnO_4)^{3-}$ and $(VO_4)^{5-}$ in $Sr_{10}(VO_4)_6F_2$. *J. Phys. Condensed Matter* **9**, 9893–9908, https://doi.org/10.1088/0953-8984/9/45/017 (1997).
53. Andreici, E. L. Modeling of crystal field and spin-hamiltonian parameters for tetrahedral coordinated Mn^{5+} doped In Li_3VO_4. *AIP Conf. Proc.* **1472**, 101–107, https://doi.org/10.1063/1.4748075 (2012).

Materials Chemistry and Physics 333 (2025) 130341

Contents lists available at ScienceDirect

Materials Chemistry and Physics

journal homepage: www.elsevier.com/locate/matchemphys

High efficiency solar light photocatalytic degradation of mordant blue 9 by monoclinic $BiVO_4$ nanopowder

Stefan T. Jelić [a,*], Jovana Ćirković [b], Jelena Jovanović [a], Tatjana Novaković [c], Matejka Podlogar [d], Jelena Mitrić [e], Goran Branković [a], Zorica Branković [a]

[a] University of Belgrade, Institute for Multidisciplinary Research, Center of Excellence for Green Technologies, Kneza Višeslava 1, 11000, Belgrade, Serbia
[b] University of Belgrade, Institute for Multidisciplinary Research, Department of Materials Science, Kneza Višeslava 1, 11000, Belgrade, Serbia
[c] University of Belgrade, Institute of Chemistry, Technology and Metallurgy, Department of Catalysis and Chemical Engineering, Njegoševa 12, 11000, Belgrade, Serbia
[d] Jožef Stefan Institute, Jamova cesta 39, 1000, Ljubljana, Slovenia
[e] University of Belgrade, Institute of Physics, Laboratory for Electronic Materials, Pregrevica 118, 11000, Belgrade, Serbia

HIGHLIGHTS

- Mesoporous $BiVO_4$ was synthetized using simple sonochemical route.
- Visible-light degradation of mordant blue 9 dye is very effective at pH = 13.
- The $BiVO_4$ powder stays stable after fours consecutive cycles.

ARTICLE INFO

Keywords:
Solar light photocatalysis
Bismuth vanadate
Mordant blue 9

ABSTRACT

The research presented in this paper focuses on the influence of solution pH on the photocatalytic activity of single-phase monoclinic $BiVO_4$ nanopowder degrading highly toxic textile dye Mordant Blue 9 (MB9) under the simulated solar irradiation. $BiVO_4$ nanopowder was synthetized using a sonochemical route. The catalyst was confirmed to be single-phase and have relatively high surface area with mesoporous nanoparticles with 50 nm in diameter on average. Band gap was estimated to be 2.38 eV, proving high absorbance of the visible light. Photodegradation was observed in different pH values (pH = 1, 6, 8, 9, 11, 13) and the mechanism was proposed. Influence of catalyst concentration and its reusability at pH = 13 are also reported, showing no activity loss after four cycles.

1. Introduction

Dyes and their production are one of the greatest industrial polluters, accounting for pollution of drinking water, soil and air [1]. Many dyes, especially azo dyes, are used in textile, paper, leather, and cosmetic industries [2]. For efficient practical use, some dyes are required to be resistant to chemical and photolytic degradation, which makes the wastewater a great problem, as natural biodegradation for many of them is negligible. Some of the methods for water purification include microbial biotechnology [3], plant extract induced biodegradation [4], zeolite [5] and active carbon adsorption [6]. One of the most promising methods which has drawn great focus is photocatalysis, photodegradation in the presence of catalysts.

Titanium dioxide is the most frequently used photocatalyst but its relatively wide band gap (about 3 eV) makes it photoactive only under ultraviolet irradiation, thus the focus has moved to semiconductors with lower band gap for better utilization of the visible spectrum of sunlight [7,8].

Bismuth-based semiconductors, such as $BiFeO_3$, BiOCl, $BiWO_6$, BiOBr, $BiVO_4$ have been studied for their excellent visible-light photocatalytic properties, chemical and thermal stability and non-toxicity [9]. Among them, Bismuth vanadate ($BiVO_4$) is a good candidate as its band gap is at about 2.5 eV, making it a suitable photocatalyst in visible spectrum. There are three main crystalline phases in $BiVO_4$, which are scheelite monoclinic, scheelite tetragonal and zircon tetragonal structure [10]. The scheelite monoclinic phase of $BiVO_4$ has the best activity

* Corresponding author. Institute for Multidisciplinary Research, Kneza Višeslava 1, 11000 Belgrade, Serbia.
E-mail address: stefan@imsi.bg.ac.rs (S.T. Jelić).

https://doi.org/10.1016/j.matchemphys.2024.130341
Received 16 April 2024; Received in revised form 4 December 2024; Accepted 28 December 2024
Available online 30 December 2024

under visible light (Eg~2.4eV), much better than the other two types (Eg~3.1 eV) [11,12].

Recent studies regarding its synthesis and photocatalytic activity have been conducted, but more there's still room for further research [12,13].

Along with photocatalyst concentration, irradiation time, and intensity of light, pH value of the solution is an important factor that can significantly influence photocatalysis, and should be taken into account when describing activity of a catalyst.

In this work, single-phase monoclinic $BiVO_4$ nanopowder was synthesized using a modified ultrasound-assisted method previously proposed by Zhou et al., and their structural, optical and photocatalytic performance were investigated. Sonication is an effective way to erode solid surfaces and facilitate interparticle collisions, as well as to reduce agglomeration, leading to formation of greater surface area [14]. The main idea of the work was to investigate the adsorption process and photocatalytic degradation of naphthol azo dye Mordant Blue 9 (MB9) using monoclinic $BiVO_4$ powder at different pH values of aqueous solution under simulated sunlight irradiation.

2. Experimental

2.1. Synthesis of $BiVO_4$ powder

$BiVO_4$ powder was synthesized following the synthesis proposed by Zhou et al. [13]. 6 mmol of ammonium vanadate (NH_4VO_3, Merck, p.a.) and 6 mmol of bismuth(III) nitrate pentahydrate ($Bi(NO_3)_3 \times 5H_2O$, Merck, p.a.) were added to 100 mL of distilled water and stirred for an hour using magnetic stirrer. The mixture was exposed to ultrasound irradiation using Bandelin SONOPULS Ultrasonic Homogenizer HD 2070 at 85 % of the sound power for another hour. The precipitate was filtrated and washed using about 100 mL of distilled water and 50 mL of absolute ethanol, and then left to dry at 80 °C overnight.

2.2. Characterization

Phase composition and crystal structure of $BiVO_4$ powder were analyzed by an X-ray diffractometer (XRD; PANalytical X'Pert PRO, Almelo, The Netherlands) with CuKα1 radiation (l = 1.5405980 Å) and goniometer range of PW3050/60 operating at standard Bragg-Brentano configuration. Average crystallite size of the powder was determined using *Debye-Scherrer* equation [15]:

$$D = \frac{K\lambda}{\beta \cos\theta} \quad (2)$$

where D is the crystallite size (diameter for spherical particles), K is the shape factor (0.9 for spherical particles), λ is the wavelength of X-ray diffractometer radiation, θ is the Braggs angle in radians, and β is the full width at half maximum of the peak in radians.

Powder morphology and microstructure were examined by scanning electronic microscopy (SEM TESCAN Vega TS 5130 MM microscope), and by transmission electron microscopy (TEM, JEm-2100, JEOL microscope).

EDS analysis was conducted using scanning electronic microscopy (SEM JEOL JSM-6610LV microscope) with a detector for EDS (Xplore 30 by Oxford Instruments).

Raman measurements were performed using commercial NTegra Spectra system from NT-MDT. A linearly polarized semiconductor laser operating at a wavelength of 532 nm was used. All the spectra were obtained by setting the laser power to 2 mW within approximately 0.5 × 0.5 μm sized focus with exposure time of 600 s.

Band gap was determined using Shimadzu UV-2600 spectrophotometer equipped with an integrated sphere by recording UV–Vis diffuse reflectance spectrum in 200–800 nm range. The reflectance spectrum was measured relative to a reference sample of $BaSO_4$.

The Brunauer-Emmett-Teller (BET) theory was used to examine the adsorption ability of the powder. Powder specific surface area and pore size distribution of the sample were determined by nitrogen adsorption-desorption measurements using a Bel-Japan Minisorp II surface area & pore size analyzer.

2.3. Photocatalytic activity test

The photocatalytic performance of $BiVO_4$ samples at different values of pH was evaluated by degradation of MB9 under the simulated Sunlight irradiation (Osram Ultra-Vitalux 300W lamp). Dye information can be found in Table 1.

Experiments were performed at 20 °C by adding 0.1 g of $BiVO_4$ to 50 mL of aqueous solution of MB9 ($\rho_i = 10$ mg/L). Suspensions were stirred in the dark for 30 min to establish the adsorption-desorption equilibrium between photocatalyst and MB9. Then, the solution was exposed to the sunlight irradiation under constant stirring. At specific intervals of time, UV–Vis absorption measurements of certain amount of dye solution were carried out in the range of 200–600 nm. Decrease of absorption peak at around 520 nm with irradiation time, indicates decoloration of MB9 in the solution. This decrease is related to the photodegradation efficiency (η), defined as:

$$\eta = \left(1 - \frac{A_t}{A_0}\right) \times 100\% \quad (1)$$

where A_0 and A_t represent initial absorption and absorption after irradiation time t, respectively.

H_2SO_4 and NaOH were used to set the pH value of each solution. Concentration of the photocatalyst was also varied to observe how much it influences the kinetics of the degradation. At pH = 13, photocatalytic activity was tested using 0.1, 0.05, 0.025 and 0.0125 g of $BiVO_4$ in 50 mL of 10 mg/L aqueous solution of MB9.

To test reusability, photocatalyst was used in four consecutive cycles. The catalyst was centrifuged, washed using deionized water and left to dry while heated gently, prior to reuse for the next cycle. In each cycle, 0.1 g of $BiVO_4$, was added to 50 mL of MB9 solution (10 mg/L) at pH = 13, stirred for 30 min in the dark, and then radiated for 105 min.

3. Results and discussion

3.1. Characterization of the $BiVO_4$ photocatalyst

The phase composition of synthesized $BiVO_4$ powder was determined using X-ray diffraction, and corresponding diffraction pattern is presented in Fig. 1. All the diffraction peaks can be assigned to the (space group: I2/b) single phase scheelite monoclinic $BiVO_4$ structure, according to the JCPDS Card No:75–1866, with high crystallinity and sharp diffraction peaks at 18°, 29° and 31° of 2θ. Characteristics of scheelite monoclinic $BiVO_4$ are presence of the peak at 15° of 2θ and

Table 1
Physical characteristics and molecular structure of MB9.

Dye name	Mordant Blue 9
C.I. name	Mordant Blue 9
Class	Single Azo
C.I. number	14855
λ max	516 nm
Color	red light navy blue
Molecular formula	$C_{16}H_9ClN_2Na_2O_8S_2$
Molecular weight (g/mol)	502.82
Structural formula	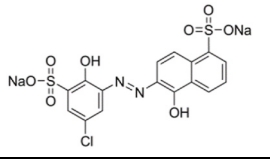

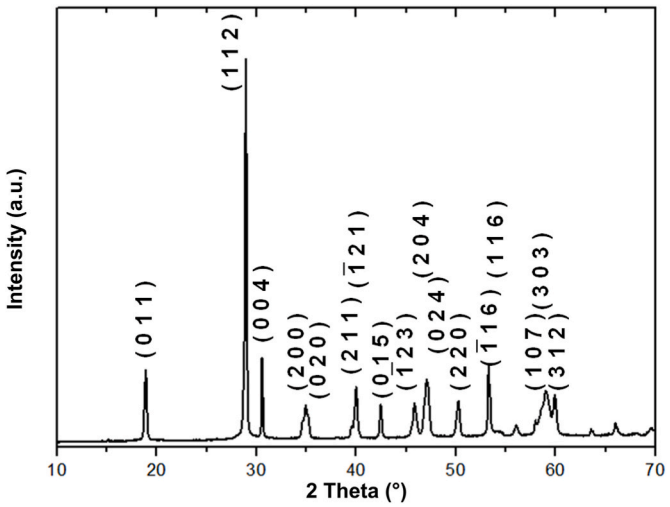

Fig. 1. XRD pattern of synthetized sample of $BiVO_4$.

well splitting of peaks at 18°, 35°, 46° and 51°of 2θ. XRD spectrum of the crystalline $BiVO_4$ synthesized by ultrasound method revealed that the that no peak at 15 of 2θ can be observed, and the peaks at 18°, 35°, 46° and 51° of 2θ are not well split, suggesting that our sample has not well-distorted scheelite monoclinic structure.

The average crystallite size calculated by Debye-Scherrer method was approximately 50 nm in diameter.

3.2. Microstructure of the $BiVO_4$ sample

The particle morphology was determined using scanning electron microscopy (SEM). Fig. 2 shows that the sample is mostly made of primary crystallites with a tendency to agglomerate forming larger irregular sub-micron spheres.

The morphology of monoclinic $BiVO_4$ was also investigated by TEM (Fig. 3). Fig. 3 shows that the surface of monoclinic $BiVO_4$ consisted of a

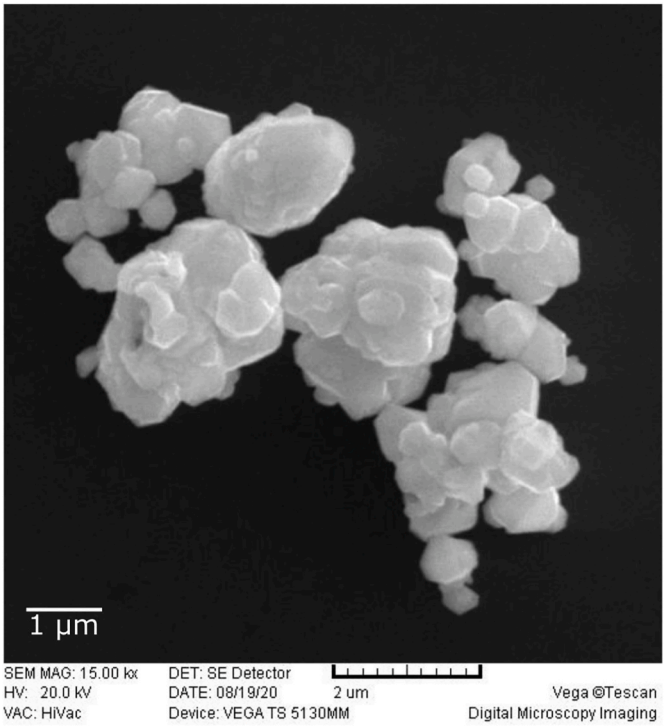

Fig. 2. SEM image of $BiVO_4$ sample.

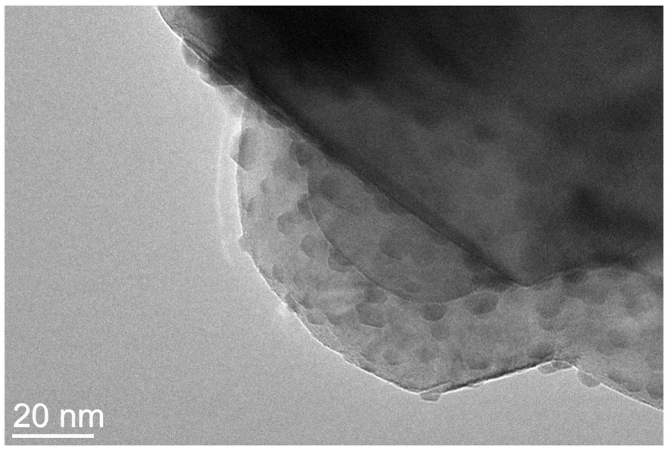

Fig. 3. TEM image of $BiVO_4$ sample.

lot of $BiVO_4$ nanoparticles with the average diameter of 5 nm. Similar morphology of $BiVO_4$ was obtained in the work of Yin et al. [16].

The elemental composition of the $BiVO_4$ sample was determined using Energy Dispersive Spectroscopy (EDS) analysis. The ratio of bismuth, vanadium and oxygen, as well as the mappings of the elements are presented in Fig. 4. The purity of the sample was confirmed by the absence of peaks for other elements.

3.3. Adsorption of $BiVO_4$

Adsorption of a material depends on its specific surface, which is an important parameter for photocatalysis process. BET method is a reliable way to determine the specific surface area of a material. To determine the specific surface area and pore size distribution, nitrogen adsorption-desorption isotherm was recorded. According to the IUPAC classification [17] the nitrogen adsorption−desorption isotherm is attributed to the type IVa, typical for mesoporous materials, and forms type H3 of hysteresis loop, as shown in Fig. 5. The pore size distribution was determined from the desorption branch of the isotherm, using the BJH (Barrett− Joyner−Halenda) method and is shown in Fig. 6. It can be observed that the $BiVO_4$ sample has bimodal pore size distribution in the mesoporous area with the first mode peak around 3 nm and the second

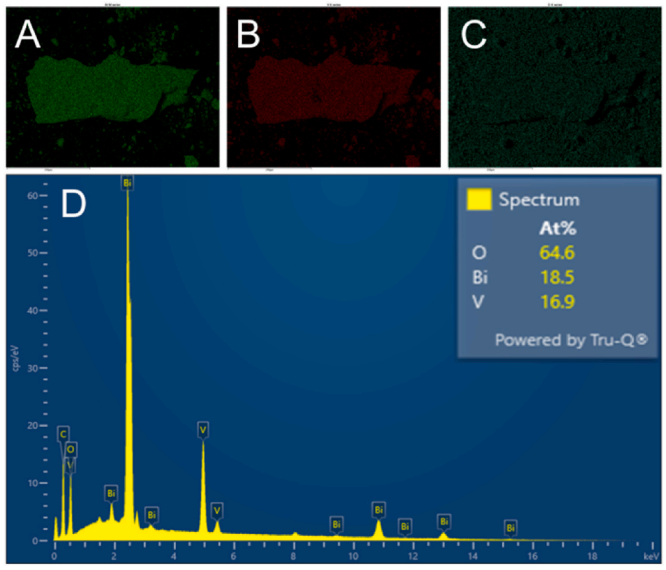

Fig. 4. Energy dispersive spectroscopy (EDS) analysis of $BiVO_4$ sample. The EDS mapping of the sample shows bismuth (A), vanadium (B), and oxygen (C). The EDS spectrum shows the component ratio in the $BiVO_4$ sample (D).

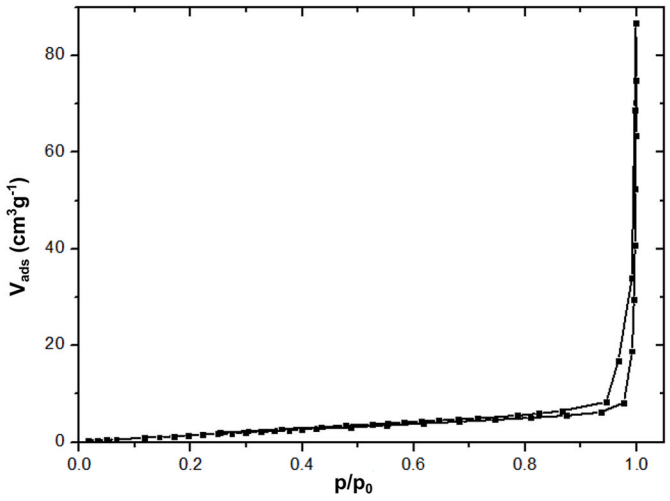

Fig. 5. Adsorption-desorption isotherm of N_2 adsorption test for $BiVO_4$ sample.

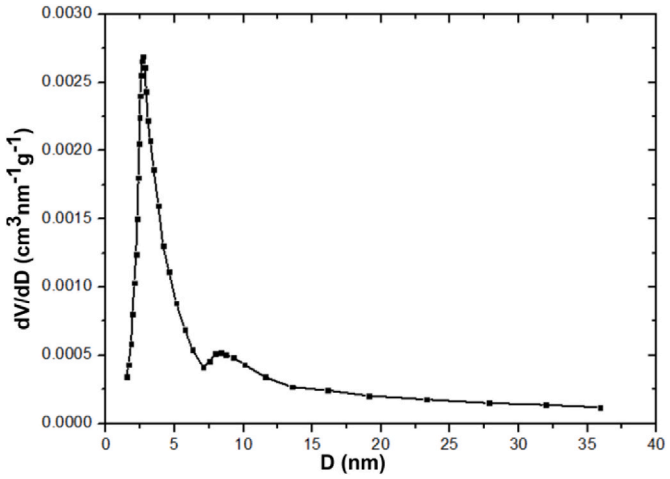

Fig. 6. Distribution of pore diameters of $BiVO_4$ sample.

one in the range of 7 nm. This type of hysteresis loop suggests slit-shaped pores in the sample [18]. The obtained adsorption-desorption isotherm aligns well with previous studies, all confirming H3 and H4 shapes that suggest slit-shaped pores [19–21]. While it's been observed that slip-shaped pores have lower adsorption rate than cylinder-shaped pores, the main parameter for adsorption rate are pore size and surface area [22].

Estimated BET surface area of $BiVO_4$ nanopowder was 9 m^2/g. The obtained surface area is higher than 4.16 m^2/g reported by Zhou et al. for $BiVO_4$ nanopowder prepared this way, and much higher than surface of $BiVO_4$ nanopowder obtained by solid-state reaction (SSR) – 0.26 m^2/g.

Before photocatalysis test, adsorption-desorption equilibrium of the photocatalyst and the MB9 dye was established in solution in the dark over 30 min, and it was shown for adsorption to be influenced by pH value of the solution. The amount of adsorbed MB9 dye at equilibrium per unit mass of $BiVO_4$ was determined using the following equation [23]:

$$q_e = \frac{(c_0 - c_e)V}{m}$$

Where q_e represents the adsorption capacity at equilibrium (mg/g), c_0 the starting concentration of MB9 (mg/L), c_e the equilibrium concentration of MB9 (mg/L), V the volume of the solution (L), and m the mass of $BiVO_4$ (g). The q_e values are provided in Table 2.

3.4. Raman spectral analysis

Relatively strong Raman bands at 125, 212, 334, 365 and 822 cm^{-1} (Fig. 7) confirm highly ordered crystal structure and single phase sample [24].

3.5. Band gap of the $BiVO_4$ sample

The electronic structure ie., value of the band gap, and positions of valence and conduction bands have a significant effect on its photocatalytic performance [25]. The electronic structure of monoclinic $BiVO_4$ has the hybridization of Bi 6s and O 2p orbitals of VB [26]. The transition of electrons from Bi 6s to V 3d corresponds to visible light, which is favorable for the photodegradation of organic pollutants under the visible light irradiation [27]. The optical band gap (E_g) was calculated by transforming absorbance spectrum of the sample using Tauc's plots [26,28].

Intersection of the tangent line on the Tauc plot and the x-axis as shown in Fig. 8 represents the value of Eg at 2.38 eV with direct transition, which aligns with values obtained by other researchers (2.3–2.5 eV) [29–31]. This band gap confirms that $BiVO_4$ is an effective visible-light photocatalyst in aqueous solutions, as required band gap falls between 2 eV and 3.2 eV [32].

3.6. Photocatalytic degradation of MB9

Photodegradation of organic pollutants by semiconductors usually occurred by the formation of reactive species such as hydroxyl radicals, superoxide radicals, nitrate radicals, photo excited electrons, and holes [30]. Due to photocatalytic effect both oxidative and reductive reactions may occur:

Oxidative:

$$h^+ + H_2O \rightarrow H^+ + \bullet OH \quad (5)$$

$$2\,h^+ + 2\,H_2O \rightarrow 2\,H^+ + H_2O_2 \quad (6)$$

$$H_2O_2 \rightarrow 2\,\bullet OH \quad (7)$$

Reductive:

$$e^- + O_2 \rightarrow \bullet O_2^- \quad (8)$$

$$\bullet O_2^- + H_2O + H^+ \rightarrow H_2O_2 + O_2 \quad (9)$$

$$H_2O_2 \rightarrow 2\,\bullet OH \quad (10)$$

Electrons and holes used in these reactions are gained from photo-induced excitation on the surface of the photocatalyst:

$$\text{photocatalyst} + h\nu \rightarrow \text{photocatalyst}\,(h+ + e-) \quad (11)$$

Besides the value of band gap, the potentials of valence band maxima (VBM) and conduction band minima (CBM) play significant roles in redox reaction in the solution and formation of reactive species. To determine VBM and CBM for $BiVO_4$, we calculated their potentials theoretically according to the electronegativity of the constituent atoms [33].

Fermi energy can be found using equation:

$$E_F = \chi - E_e \quad (12)$$

Table 2
Adsorption capacity at equilibrium at different pH values of solution.

pH	1	6	8	9	11	13
q_e (mg/g)	0.81	0.60	0.51	0.40	0.67	0.25

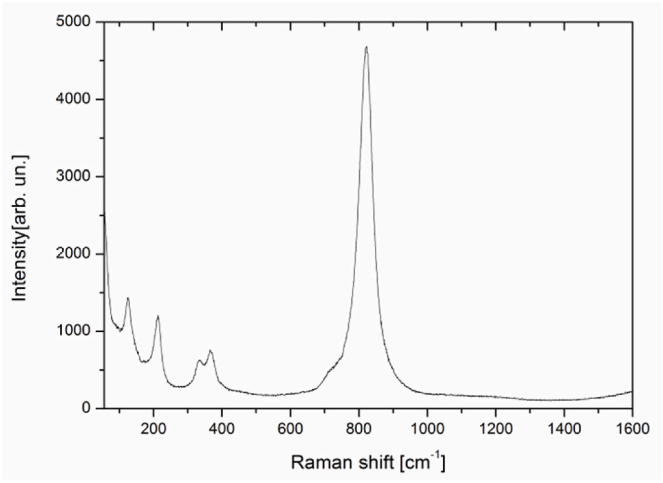

Fig. 7. Raman spectrum of $BiVO_4$ sample.

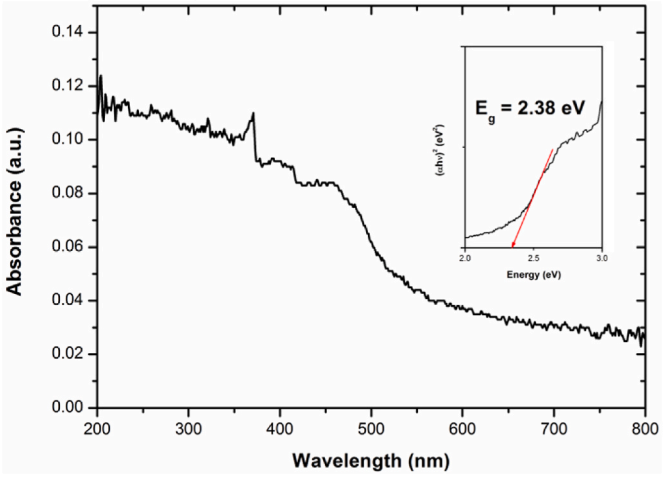

Fig. 8. UV–Vis absorbance spectrum of $BiVO_4$ sample. The inset shows corresponding $[\alpha h\nu]^2$ versus $h\nu$ plot.

where χ is the absolute electronegativity of the semiconductor, and E_e is the energy of a free electron in hydrogen scale (4.5 eV). The absolute electronegativity is the geometric mean value of the absolute electronegativity of all constituent atoms, whose absolute electronegativity is arithmetic mean of their first ionization energy and electron affinity. The absolute electronegativity of $BiVO_4$ is therefore:

$$\chi_{BiVO_4} = \sqrt[6]{\chi_{Bi}\chi_V\chi_O^4} = 6.03\ eV \tag{13}$$

and E_F is value is 1.53 eV. As Fermi energy value is usually exactly the average of VBM and CBM, their values are $\frac{E_g}{2}$ higher and lower than Fermi energy. The determined values of VBM and CBM are 2.77 eV and 0.29 eV, respectively (Fig. 9). For oxidative reaction to happen, VBM must be higher than the redox potential of the first step (2.38 eV vs. normal hydrogen electrode). On the other hand, for reductive reaction, CBM must be lower than redox potential of its first step (−0.16 eV vs. normal hydrogen electrode). Based on the estimated values of band energies it can be concluded that only conditions for oxidative path of photocatalysis are met, as VBM is higher than 2.38 eV. Absorption of a photon with energy greater than or equal to the band gap of material (2.48 eV) excites an electron from the valence band to its conduction band, i.e., creates an electron-hole pair, as shown in Fig. 9. The photogenerated holes may decompose MB9 molecules directly or can react

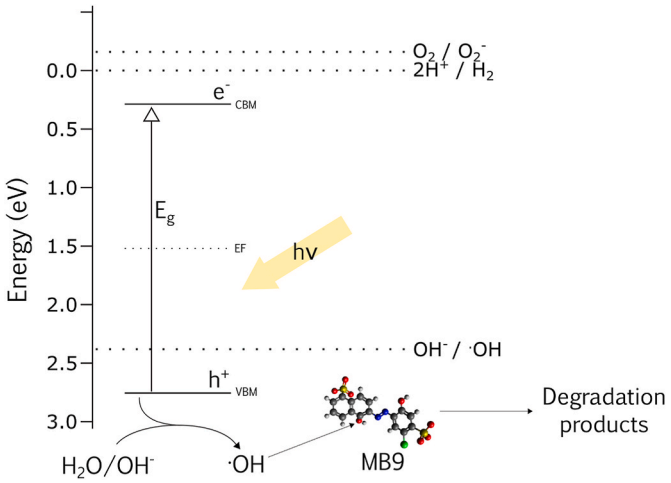

Fig. 9. Schematic view of the proposed mechanism for $BiVO_4$ photocatalytic degradation of MB9.

with adsorbed water molecules or surface hydroxyl groups to generate hydroxyl free radicals (·OH), which further decompose MB9 molecules.

3.7. Photocatalytic activity test

The pH value plays an important role in the reaction, as charge of the dye molecules and catalyst, as well as the presence of reactive species all depend on the pH value [34]. MB9 is an anionic dye with two hydroxyl groups that can be deprotonated (pKa_1 = 6.7, pKa_2 = 11.5) [35]. Accordingly, the molecule of the dye is not charged in aqueous solutions with pH values under 6.7, and it's negatively charged at higher pH values as one hydroxyl group is deprotonated at pH between 6.7 and another at pH over 11.5. $BiVO_4$ isoelectric point (IEP) ranges between pH 2.3 and 3.74 making it positively charged at pH values lower than the IEP, and negatively charged above [36–38]. The UV–Vis spectra of the dye without $BiVO_4$ at various pH values didn't show significant difference in different media, suggesting that the dye was stable in all environments, as presented in Fig. 10.

Alkaline solution is expected to be suitable for the photodegradation process as the expected oxidative path of photocatalysis requires hydroxide anions. Fig. 11 shows the rate of photodegradation in different pH values of the solution. In acidic solution (pH = 1), the rate of photocatalysis is the slowest and has the lowest rate while the adsorption is the highest. With rise of pH value of the solution, the photocatalysis

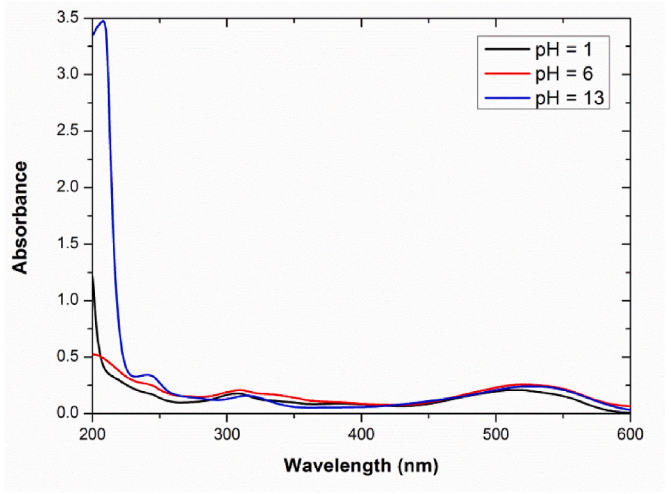

Fig. 10. The UV–Vis spectra of MB9 dye at various pH values.

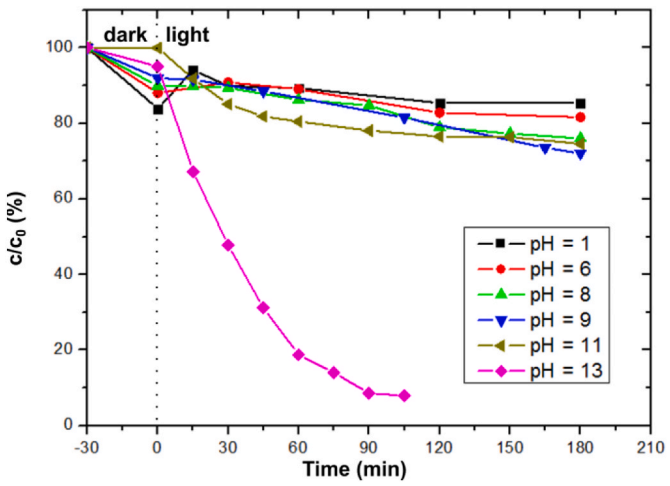

Fig. 11. Concentration changes of MB9 during the photocatalysis at different pH values.

efficiency and rate increase, as adsorption decreases. Relatively high adsorption at pH = 1 can be explained by the fact that MB9 is neutral at this pH value and its π electrons from aromatic rings can interact with positively charged $BiVO_4$ [39,40]. With the increase of pH value of aqueous dye solution, adsorption rate is much lower (around 10 % for pH values 6, 8 and 9) and negligible at pH = 11, which can be explained by electrostatic repulsion, as both the MB9 molecules and $BiVO_4$ are negatively charged. It can be noticed that the degradation was the most successful in alkaline environment, with photodegradation efficiency reaching 90 % in about 80 min at pH = 13, with efficiency in more acidic environment spanning between 10 % (pH = 1) and 20 % (pH = 11) in the same timeframe. Alkaline pH favors the formation of ·OH radicals through oxidation of OH^- ions in aqueous solution, increasing the effectiveness of photocatalytic process.

It has been noticed that upon irradiation at pH = 1 the dye concentration would increase at first, suggesting desorption, with concentration decreasing afterwards, due to degradation. This can be assumed to be the consequence of photoinduced desorption where light excites adsorbate prompting it to leave the surface of the adsorbent [41–43].

The UV–Vis spectrum of photodegradation of the dye at pH = 13 is presented in Fig. 12.

Influence of catalyst concentration was investigated by conducting the same photocatalytic activity test as described above, at pH = 13 for 0.05, 0.025 and 0.0125 g of $BiVO_4$. As shown in Fig. 13, the activity decreases with the concentration of catalyst, but still remains very effective.

3.8. Kinetics of the photocatalytic degradation

The kinetics of photocatalysis degradation of MB9 at different pH values and at pH = 13 for different concentrations of the catalyst were also investigated, and rate constants can be described as pseudo-first order reaction, using Langmuir-Hinshelwood model following equation:

$$ln\left(\frac{c}{c_0}\right) = -kt \quad (14)$$

Where, c_0 and c are concentration of MB9 at the beginning of the reaction and at time t, respectively, and k is the pseudo-first order reaction rate constant. The k value can be obtained by plotting $\ln(c/c_0)$ vs. t graph and finding the slope. Reaction rates for 0.1 g of $BiVO_4$ at different pH values can be found in Table 3, and for different concentrations of the photocatalyst at pH = 13 in Fig. 14.

3.9. Reusability of the photocatalyst

Evaluating reusability of a catalyst is very important for its practical application. As seen in Fig. 15, the degradation was almost absolute in every cycle after the first one, showing the catalyst to be very effective. Other studies of $BiVO_4$ as a photocatalyst used for photodegradation of rhodamine B [44] and methylene blue [45] have shown similar initial rate of photodegradation with slow decrease over following cycles, also indicating good reusability properties. Photodegradation rate of some similar photocatalysts like Bi_2O_3 were shows to have greater decrease over each consecutive cycle [46,47].

4. Conclusion

This paper presents the investigation of photocatalytic degradation of toxic azo dye MB9 using $BiVO_4$ nanopowder as a photocatalyst. The sonochemical route of the nanopowder $BiVO_4$ synthesis was suitable to obtain pure monoclinic mesoporous crystallites of the average crystallite size of 50 nm in diameter. BET analysis confirmed that obtained $BiVO_4$ nanopowder is mesoporous (with most pores of about 3 nm in diameter) making it a good candidate for a solar light photocatalyst. The calculated valence and conduction band energies (+2.77 eV and +0.29 eV, respectively) have indicated oxidative photodegradation pathway, with ·OH radicals generated in the process reacting with MB9. The

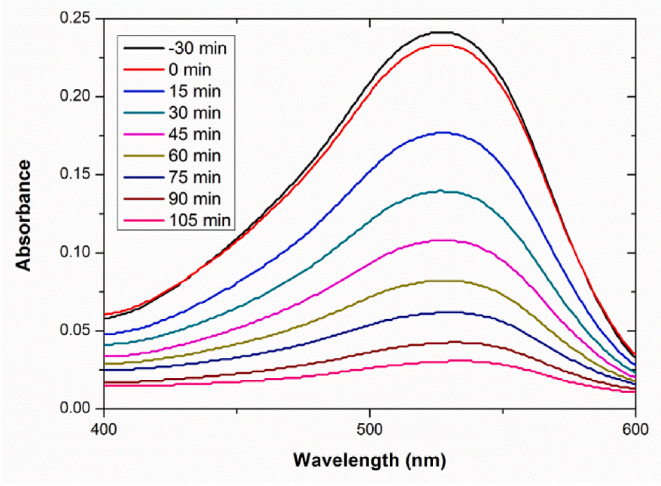

Fig. 12. The UV–Vis spectrum of MB9 dye during the photocatalyst degradation at pH = 13.

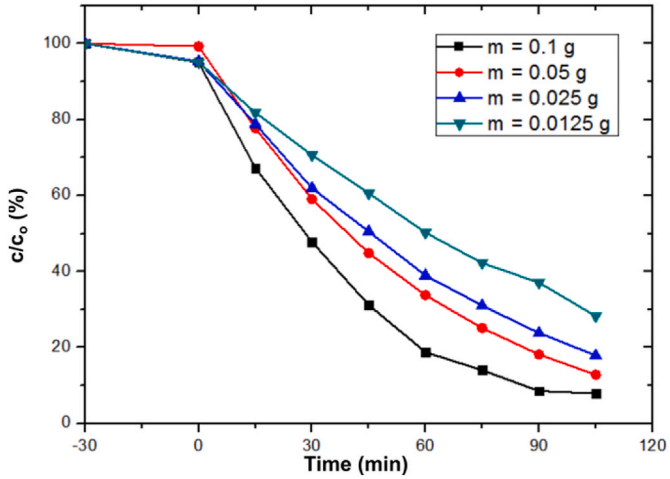

Fig. 13. Concentration change of MB9 during the photocatalysis for different concentrations of $BiVO_4$.

Table 3
Pseudo-first order reaction rate constant of photocatalytic degradation at different pH solutions.

pH	1	6	8	9	11	13
K	5.3×10^{-4}	7.6×10^{-4}	11.1×10^{-4}	15.0×10^{-4}	10.0×10^{-4}	0.0256

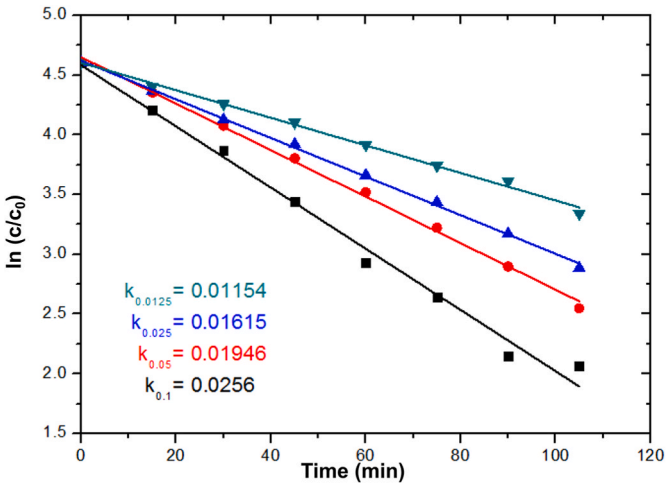

Fig. 14. Kinetics of photocatalytic degradation of MB9 using different concentrations of $BiVO_4$.

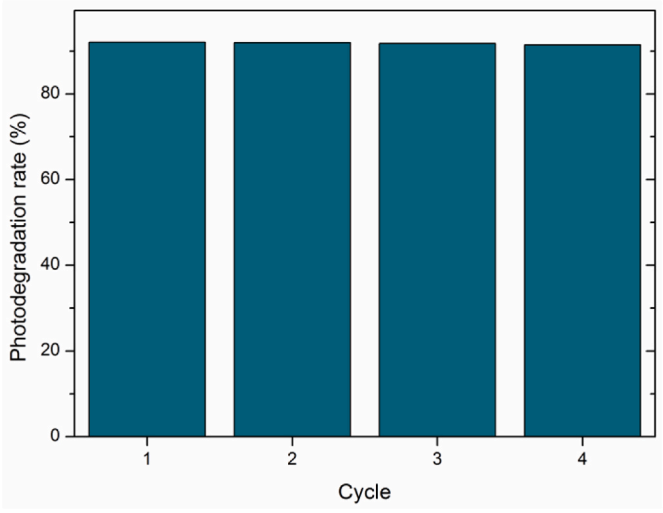

Fig. 15. The rate of photodegradation of MB9 in four consecutive cycles.

photocatalytic degradation is most effective in alkaline conditions (pH = 13), and has good reusability rate over four cycles, which is important for its potential practical use. Simple and economic synthesis of the $BiVO_4$, and effective decoloration of the MB9 solution in about 90 min proves the catalyst to have great potential for practical use.

CRediT authorship contribution statement

Stefan T. Jelić: Writing – original draft, Investigation, Data curation. **Jovana Ćirković:** Writing – review & editing, Supervision, Conceptualization. **Jelena Jovanović:** Investigation. **Tatjana Novaković:** Investigation. **Matejka Podlogar:** Investigation. **Jelena Mitrić:** Investigation. **Goran Branković:** Writing – review & editing. **Zorica Branković:** Writing – review & editing.

Declaration of competing interest

The authors declare that they have no known competing financial interests or personal relationships that could have appeared to influence the work reported in this paper.

Acknowledgements

The authors owe a special thanks to Dr. Aleksander Rečnik (Department of Nanostructured Materials, Jožef Stefan Institute, Ljubljana, Slovenia) for their valuable help with X-ray diffraction.

This work was financially supported by the Ministry of Education, Science and Technological Development of the Republic of Serbia through Contract No. 451-03-66/2024-03/200053.

Appendix A. Supplementary data

Supplementary data to this article can be found online at https://doi.org/10.1016/j.matchemphys.2024.130341.

Data availability

Data will be made available on request.

References

[1] B. Lellis, C.Z. Fávaro-Polonio, J.A. Pamphile, J.C. Polonio, Effects of textile dyes on health and the environment and bioremediation potential of living organisms, Biotechnol. Res. Innov. 3 (2019) 275–290, https://doi.org/10.1016/j.biori.2019.09.001.
[2] B. Said, R. Souad M', E.H. Ahmed, A review on classifications, recent synthesis and applications of textile dyes, Inorg. Chem. Commun. 3 (2020) 107891.
[3] M. Imran, D.E. Crowley, A. Khalid, S. Hussain, M.W. Mumtaz, M. Arshad, Microbial biotechnology for decolorization of textile wastewaters, Rev. Environ. Sci. Biotechnol. 14 (2015) 73–92, https://doi.org/10.1007/s11157-014-9344-4.
[4] D. Shahi, R. Sapkota, A comparative study on dye degradation by leaf and root extracts of parthenium hysterophorus L, Int. J. Appl. Sci. Biotechnol. 6 (2018) 327–331, https://doi.org/10.3126/ijasbt.v6i4.22110.
[5] Z. Ioannou, C. Karasavvidis, A. Dimirkou, V. Antoniadis, Adsorption of methylene blue and methyl red dyes from aqueous solutions onto modified zeolites, Water Sci. Technol. 67 (2013) 1129–1136, https://doi.org/10.2166/wst.2013.672.
[6] C. Djilani, R. Zaghdoudi, F. Djazi, B. Bouchekima, A. Lallam, A. Modarressi, M. Rogalski, Adsorption of dyes on activated carbon prepared from apricot stones and commercial activated carbon, J. Taiwan Inst. Chem. Eng. 53 (2015) 112–121, https://doi.org/10.1016/j.jtice.2015.02.025.
[7] T. Wu, G. Liu, J. Zhao, H. Hidaka, N. Serpone, Evidence for H2O2 generation during the TiO2-assisted photodegradation of dyes in aqueous dispersions under visible light illumination, J. Phys. Chem. B 103 (1999) 4862–4867, https://doi.org/10.1021/jp9846678.
[8] U.G. Akpan, B.H. Hameed, Parameters affecting the photocatalytic degradation of dyes using TiO2-based photocatalysts: a review, J. Hazard Mater. 170 (2009) 520–529, https://doi.org/10.1016/j.jhazmat.2009.05.039.
[9] J. Cirkovic, A. Radojkovic, D. Lukovic Golic, N. Tasic, M. Cizmic, G. Brankovic, Z. Brankovic, Visible-light photocatalytic degradation of Mordant Blue 9 by single-phase BiFeO3nanoparticles, J. Environ. Chem. Eng. 9 (2021), https://doi.org/10.1016/j.jece.2020.104587.
[10] S. Tokunaga, H. Kato, A. Kudo, Selective preparation of monoclinic and tetragonal BiVO4 with scheelite structure and their photocatalytic properties, Chem. Mater. 13 (2001) 4624–4628, https://doi.org/10.1021/cm0103390.
[11] S. Chaiwichian, B. Inceesungvorn, K. Pingmuang, K. Wetchakun, S. Phanichphant, N. Wetchakun, Synthesis and characterization of the novel BiVO 4/CeO 2 nanocomposites, Eng. J. 16 (2012) 153–160, https://doi.org/10.4186/ej.2012.16.3.153.
[12] L. Zhou, W. Wang, S. Liu, L. Zhang, H. Xu, W. Zhu, A sonochemical route to visible-light-driven high-activity BiVO4 photocatalyst, J. Mol. Catal. Chem. 252 (2006) 120–124, https://doi.org/10.1016/j.molcata.2006.01.052.
[13] S.H. Chen, Y.S. Jiang, H.Y. Lin, Easy synthesis of BiVO4 for photocatalytic overall water splitting, ACS Omega 5 (2020) 8927–8933, https://doi.org/10.1021/acsomega.0c00699.
[14] J.J. Hinman, K.S. Suslick, Nanostructured materials synthesis using ultrasound, Top. Curr. Chem. 375 (2017) 1–36, https://doi.org/10.1007/s41061-016-0100-9.
[15] A.L. Patterson, The scherrer formula for X-ray particle size determination, Phys. Rev. 56 (1939) 978–982, https://doi.org/10.1103/PhysRev.56.978.
[16] H. Yin, Y. Sun, D. Shi, X. Wang, L. Wang, Controlling crystallization and morphologies of monoclinic bismuth vanadate (BiVO4) dendrite with enhanced photocatalytic activities, Int. J. Phys. Sci. 6 (2011) 4287–4293.
[17] M. Thommes, K. Kaneko, A.V. Neimark, J.P. Olivier, F. Rodriguez-Reinoso, J. Rouquerol, K.S.W. Sing, Physisorption of gases, with special reference to the

evaluation of surface area and pore size distribution (IUPAC Technical Report), Pure Appl. Chem. 87 (2015) 1051–1069, https://doi.org/10.1515/pac-2014-1117.
[18] S. Yurdakal, C. Garlisi, L. Özcan, M. Bellardita, G. Palmisano, (Photo)catalyst characterization techniques, in: Heterog. Photocatal., Elsevier, 2019, pp. 87–152, https://doi.org/10.1016/B978-0-444-64015-4.00004-3.
[19] P. Dong, X. Xi, X. Zhang, G. Hou, R. Guan, Template-free synthesis of monoclinic BiVO4 with porous structure and its high photocatalytic activity, Materials 9 (2016) 1–11, https://doi.org/10.3390/ma9080685.
[20] M.M. Sajid, S.B. Khan, N.A. Shad, N. Amin, Z. Zhang, Visible light assisted photocatalytic degradation of crystal violet dye and electrochemical detection of ascorbic acid using a BiVO4/FeVO4 heterojunction composite, RSC Adv. 8 (2018) 23489–23498, https://doi.org/10.1039/c8ra03890b.
[21] Y. Chen, Y. Liu, X. Xie, C. Li, Y. Si, M. Zhang, Q. Yan, Synthesis flower-like BiVO 4/BiOI core/shell heterostructure photocatalyst for tetracycline degradation under visible-light irradiation, J. Mater. Sci. Mater. Electron. 30 (2019) 9311–9321, https://doi.org/10.1007/s10854-019-01261-9.
[22] B.D. Zdravkov, J.J. Čermák, M. Šefara, J. Janků, Pore classification in the characterization of porous materials: a perspective, Cent. Eur. J. Chem. 5 (2007) 385–395, https://doi.org/10.2478/s11532-007-0017-9.
[23] M. Gouamid, M.R. Ouahrani, M.B. Bensaci, Adsorption equilibrium, kinetics and thermodynamics of methylene blue from aqueous solutions using Date palm Leaves, Energy Proc. 36 (2013) 898–907, https://doi.org/10.1016/j.egypro.2013.07.103.
[24] X. He, C. Zhang, D. Tian, The structure, vibrational spectra, and thermal expansion study of AVO4 (A=Bi, Fe, Cr) and Co2V2O7, Materials 13 (2020) 1–9, https://doi.org/10.3390/ma13071628.
[25] S. Kunduz, G.S. Pozan Soylu, Highly active BiVO4 nanoparticles: the enhanced photocatalytic properties under natural sunlight for removal of phenol from wastewater, Sep. Purif, Technol. 141 (2015) 221–228, https://doi.org/10.1016/j.seppur.2014.11.036.
[26] J.K. Cooper, S. Gul, F.M. Toma, L. Chen, Y.S. Liu, J. Guo, J.W. Ager, J. Yano, I. D. Sharp, Indirect bandgap and optical properties of monoclinic bismuth vanadate, J. Phys. Chem. C 119 (2015) 2969–2974, https://doi.org/10.1021/jp512169w.
[27] L. Ren, L. Ma, L. Jin, J.B. Wang, M. Qiu, Y. Yu, Template-free synthesis of BiVO4 nanostructures: II. Relationship between various microstructures for monoclinic BiVO4 and their photocatalytic activity for the degradation of rhodamine B under visible light, Nanotechnology 20 (2009), https://doi.org/10.1088/0957-4484/20/40/405602.
[28] N. Tasić, J. Ćirković, V. Ribić, M. Žunić, A. Dapčević, G. Branković, Z. Branković, Effects of the silver nanodots on the photocatalytic activity of mixed-phase TiO2, J. Am. Ceram. Soc. 105 (2022) 336–347, https://doi.org/10.1111/jace.18059.
[29] G.S. Kamble, T.S. Natarajan, S.S. Patil, M. Thomas, R.K. Chougale, P.D. Sanadi, U. S. Siddharth, Y.C. Ling, BiVO4 as a sustainable and emerging photocatalyst: synthesis methodologies, engineering properties, and its volatile organic compounds degradation efficiency, Nanomaterials 13 (2023), https://doi.org/10.3390/nano13091528.
[30] G. Li, Y. Bai, W.F. Zhang, Difference in valence band top of BiVO 4 with different crystal structure, Mater. Chem. Phys. 136 (2012) 930–934, https://doi.org/10.1016/j.matchemphys.2012.08.023.
[31] Y. Hermans, A. Klein, K. Ellmer, R. van de Krol, T. Toupance, W. Jaegermann, Energy-band alignment of BiVO 4 from photoelectron spectroscopy of solid-state interfaces, J. Phys. Chem. C 122 (2018) 20861–20870, https://doi.org/10.1021/acs.jpcc.8b06241.
[32] I. Dincer, C. Zamfirescu, Hydrogen production by photonic energy, in: Sustain. Hydrog. Prod., Elsevier, 2016, pp. 309–391, https://doi.org/10.1016/B978-0-12-801563-6.00005-4.
[33] M.A. Basith, R. Ahsan, I. Zarin, M.A. Jalil, Enhanced photocatalytic dye degradation and hydrogen production ability of Bi25FeO40-rGO nanocomposite and mechanism insight, Sci. Rep. 8 (2018) 33–35, https://doi.org/10.1038/s41598-018-29402-w.
[34] W.Y. Wang, Y. Ku, Effect of solution pH on the adsorption and photocatalytic reaction behaviors of dyes using TiO2 and Nafion-coated TiO2, Colloids Surfaces A Physicochem. Eng. Asp. 302 (2007) 261–268, https://doi.org/10.1016/j.colsurfa.2007.02.037.
[35] Chemicalize - instant cheminformatics solutions. https://chemicalize.com, 2020.
[36] N.C. Castillo, L. Ding, A. Heel, T. Graule, C. Pulgarin, On the photocatalytic degradation of phenol and dichloroacetate by BiVO 4: the need of a sacrificial electron acceptor, J. Photochem. Photobiol. Chem. 216 (2010) 221–227, https://doi.org/10.1016/j.jphotochem.2010.08.021.
[37] S. Obregón, G. Colón, On the different photocatalytic performance of BiVO4 catalysts for Methylene Blue and Rhodamine B degradation, J. Mol. Catal. Chem. 376 (2013) 40–47, https://doi.org/10.1016/j.molcata.2013.04.012.
[38] K. Pingmuang, J. Chen, W. Kangwansupamonkon, G.G. Wallace, S. Phanichphant, A. Nattestad, Composite photocatalysts containing BiVO4 for degradation of cationic dyes, Sci. Rep. 7 (2017) 1–11, https://doi.org/10.1038/s41598-017-09514-5.
[39] S. Mecozzi, A.P. West, D.A. Dougherty, Cation−π interactions in simple aromatics: electrostatics provide a predictive tool, J. Am. Chem. Soc. 118 (1996) 2307–2308, https://doi.org/10.1021/ja9539608.
[40] N. Zacharias, D.A. Dougherty, Cation-π interactions in ligand recognition and catalysis, Trends Pharmacol. Sci. 23 (2002) 281–287, https://doi.org/10.1016/S0165-6147(02)02027-8.
[41] S. Borowski, T. Klüner, H.J. Freund, I. Klinkmann, K. Al-Shamery, M. Pykavy, V. Staemmler, Lateral velocity distributions in laser-induced desorption of CO from Cr2O3(0001): experiment and theory, Appl. Phys. Mater. Sci. Process 78 (2004) 223–230, https://doi.org/10.1007/s00339-003-2306-2.
[42] Y. Lu, M.T. Spitler, B.A. Parkinson, Regenerator dependent photoinduced desorption of a dicarboxylated cyanine dye from the surface of single-crystal rutile, Langmuir 23 (2007) 11637–11642, https://doi.org/10.1021/la701701e.
[43] H. Spieker, T. Klüner, Photoinduced desorption of CO from rutile TiO2: elucidation of a new desorption mechanism using first principles, Phys. Chem. Chem. Phys. 16 (2014) 18743–18748, https://doi.org/10.1039/c4cp02917h.
[44] E. da Cruz Severo, G.L. Dotto, A. Martínez-de la Cruz, E.L. Cuellar, E.L. Foletto, Enhanced photocatalytic activity of BiVO4 powders synthesized in presence of EDTA for the decolorization of rhodamine B from aqueous solution, Environ. Sci. Pollut. Res. 25 (2018) 34123–34130, https://doi.org/10.1007/s11356-018-3370-7.
[45] C. Mallikarjunaswamy, S. Pramila, G. Nagaraju, R. Ramu, V.L. Ranganatha, Green synthesis and evaluation of antiangiogenic, photocatalytic, and electrochemical activities of BiVO4 nanoparticles, J. Mater. Sci. Mater. Electron. 32 (2021) 14028–14046, https://doi.org/10.1007/s10854-021-05980-w.
[46] G. Kaur, S. Sharma, K. Kaur, P. Bansal, Synthesis, characterization, and visible-light-induced photocatalytic activity of powdered semiconductor oxides of bismuth and zinc toward degradation of Alizarin Red S, Water Environ. Res. 92 (2020) 1376–1387, https://doi.org/10.1002/wer.1333.
[47] V. Katoch, N. Sharma, M. Sharma, M. Baghoria, J.J. Panda, M. Singh, B. Prakash, Microflow synthesis and enhanced photocatalytic dye degradation performance of antibacterial Bi2O3 nanoparticles, Environ. Sci. Pollut. Res. 28 (2021) 19155–19165, https://doi.org/10.1007/s11356-020-11711-1.

Microchemical Journal 213 (2025) 113533

Contents lists available at ScienceDirect

Microchemical Journal

journal homepage: www.elsevier.com/locate/microc

Temperature-induced phase transitions in atorvastatin calcium trihydrate revealed by low-energy Raman analysis

J.J. Lazarević [a],*, S. Uskoković-Marković [b], J. Mitrić [a], N. Lazarević [a]

[a] Center for Solid State Physics and New Materials, Institute of Physics Belgrade, University of Belgrade, Pregrevica 118, Belgrade, 11080, Serbia
[b] Faculty of Pharmacy, University of Belgrade, Vojvode Stepe 450, Belgrade, 11221, Serbia

ARTICLE INFO

Keywords:
Raman spectroscopy
Low-energy region
Phase transitions
Atorvastatin calcium trihydrate

ABSTRACT

We present a comprehensive inelastic light scattering study of atorvastatin calcium trihydrate Form I across a broad temperature range (100 K to 460 K), with a focus on the low-energy spectral region, providing key insights into the crystal structure for the first time. The Raman spectra revealed significant temperature-dependent changes, particularly at 420 K, where external vibrations at approximately 34 cm^{-1}, 44 cm^{-1}, and 140 cm^{-1} disappeared, indicating a structural phase transition. Strong fluctuations near this temperature led to notable broadening in the linewidths of the 645 cm^{-1} and 1650 cm^{-1} modes. Additionally, a new mode around 75 cm^{-1} appeared at the phase transition, suggesting the presence of structural order in the anhydrous phase before reaching the isotropic melt.

1. Introduction

The majority of a potential drug candidates do not accomplish to become a drug product due to challenges related to stability, solubility, and interactions with other drugs. These issues often stem from the diverse physicochemical, mechanical, and biopharmaceutical properties exhibited by active pharmaceutical ingredients (APIs) and excipients in various solid-state forms, such as crystalline (including polymorphs, hydrates, solvates, salts, and cocrystals), and amorphous forms. These can influence the safety, quality, and efficacy of the drug. Many of the APIs form multiple hydrates. Crystal hydrates form when water molecules associate with solids and incorporate into a crystal lattice, leading to distinct physicochemical and mechanical properties compared to the anhydrous form. Dehydration commonly takes place during manufacturing, either by disrupting the original crystal lattice and forming a new one for the anhydrous form, or by preserving the existing structure. As bioavailability and ensuing biological activity depend on the exact solid state form, identifying the crystalline phase of the API in solid dosage forms is considered essential in the manufacturing process and regulatory affairs [1].

Statins are among the most commonly prescribed medications globally. They have a significant role in preventing and managing cardiovascular diseases in individuals with a high risk of cardiovascular events by lowering cholesterol levels, stabilizing plaques, reducing inflammation, improving endothelial function, and exerting antithrombotic effects [2–4]. In the Biopharmaceutical Classification System, statins fall under class II, indicating that they have poor solubility but can effectively permeate biological membranes. Their bioavailability varies significantly due to the effects of first-pass metabolism.

Atorvastatin calcium trihydrate (ACT), chemical name (βR, δR)-2-(4-fluorophenyl)–β, δ-dihydroxy-5-(1-methyl-ethyl)-3-phenyl-4-[(phenylamino)carbonyl]-1H-pyrrole-1-heptanoic acid, is a synthetic lipid-lowering agent that competitively inhibits hepatic hydroxymethylglutaryl coenzyme A (HMG-CoA) reductase. This enzyme catalyzes the conversion of HMG-CoA to mevalonate, a critical step in cholesterol synthesis. Originally marketed by Pfizer in Form I, it is considered as the best seller drug of all time, even after its patent loss in 2011. By increasing the number of low density lipoprotein (LDL) receptors on hepatic cell surfaces, atorvastatin enhances the uptake and breakdown of LDL, consequently reducing LDL production and the number of LDL particles. This mechanism leads to lowered plasma LDL-cholesterol, lipoprotein levels, and triglycerides. On the other hand, it increases serum levels of high density lipoprotein (HDL), so-called "good" cholesterol [5]. Similar to other statins, atorvastatin may exhibit direct antineoplastic effect by potentially stopping cell progression in the G1 phase of the cell cycle. Furthermore, atorvastatin may sensitize tumor cells to cytostatic drugs [6–8]. Additionally, a significant number of clinical trials showed a direct anti-inflammatory effects of statins that are not mediated by their antihyperlipidemic activity [9]. It has been shown that they reduce cardiovascluatory-related morbidity and mortality irrespective of the lipid profile and cardiac artery disease [10].

* Corresponding author.
E-mail address: jasmina.lazarevic@ipb.ac.rs (J.J. Lazarević).

https://doi.org/10.1016/j.microc.2025.113533
Received 19 October 2024; Received in revised form 5 March 2025; Accepted 31 March 2025
Available online 16 April 2025

Characterization of ACT crystal forms was performed by X-ray powder diffraction (XRPD) as described in the filed patents that regulate production, while quantification in solid dosage forms depended mostly on high-performance liquid chromatography, spectrophotometric methods, and electrophoresis [11]. Previous researches on atorvastatin were predominantly focused on thermal techniques, such as differential scanning calorimetry, thermogravimetric analysis, and nuclear magnetic resonance [11–16]. Lately, Raman spectroscopy has been applied to determine the APIs both in process samples and final products [17]. Moreover, Raman spectroscopy has the potential to be utilized as process analytical technology for monitoring manufacturing processes [18,19]. Furthermore, progress has been made in applying Raman spectroscopy for the quantitative analysis of ACT [17,20,21]. So far, the ACT solid-state characterization was extensively researched using thermoanalytical techniques and XRPD [11–16]. Raman spectroscopy stands out as a highly specific and selective technique, capable of identifying polymorphs and crystalline states with minimal to no sample preparation. Its short analysis time, ease of use, and versatility make it suitable for application at every stage of the manufacturing process. The Raman spectra of ACT have been previously reported by Christensen et al. [16], Skorda et al. [11], and Oprica et al. [22]; however, the temperature dependence of the low-energy spectral region has not yet been explored. In this study, we present Raman scattering measurements of ACT Form I over the temperature range of 100 K to 460 K, focusing on the low-energy spectra (20 cm^{-1} to 175 cm^{-1}) measured with high spectral resolution. These spectra, which predominantly reflect intermolecular vibrations and crystal structure, show a strong temperature-dependent evolution, directly revealing a structural transition.

2. Experiment

ACT crystallizes in at least 12 different forms [12], with crystalline Form I first identified in a U.S. patent Number 5969156 [23]. To avoid uncontrollable alterations in crystal structure and properties that may occur during sample preparation, all experiments in this study were conducted using powdered samples, as obtained. The ACT Form I reference standard used in this investigation had a purity of 99.27% (Alkaloid DOO, Belgrade, Serbia).

2.1. X – ray powder diffraction analysis of atorvastatin calcium trihydrate

Structural analysis to confirm Form I of powder ACT was performed with XRPD. The XRPD patterns were obtained using CuKα radiation (λ = 1.5418 Å) on a Rigaku Smartlab X-ray diffractometer. The measurements were performed in the 2θ range of 3°–50°, with a step size of 0.02° and a rate of 1.5°/min. The FullProf software package was used to refine the XRPD pattern of the prepared sample by using the whole-pattern decomposition procedure(Le Bail fitting) and calculate unit cell parameters [24].

2.2. μ-Raman spectroscopy

The Raman scattering measurements were performed using a TriVista 557 Raman spectrometer (S&I Spectroscopy and Imaging GmbH, Warstein, Germany), equipped with a Spec-10: 256E N_2 cooled CCD detector and coupled to the OLYMPUS BX51 optical microscope in a backscattering configuration. For this study, the spectrometer was set up in a triple subtractive mode. The system features three stages, each fitted with motorized turret and three gratings, allowing for quick switching between different regimes and grating configurations. The entrance slit and second intermediate slit were set to 100 μm, while the first intermediate slit was set to the value that ensures the full utilization of the CCD chip width. The Coherent Ar^+/Kr^+ laser was used as the excitation source, providing multiple high-quality lines at different wavelengths that could be easily switched to meet experimental needs. The laser lines were cleaned using a Semrock Narrowband Clean-up filters. An Olympus LMPlanFI 50×/0.50 microscope objective was used to focus the incident light onto the sample, with a laser spot diameter of approximately 4 μm. To prevent sample damage and avoid uncontrollable temperature-related effects, the laser power at the sample plane was maintained at low levels, approximately 1 mW. The acquisition time was set to 300 s.

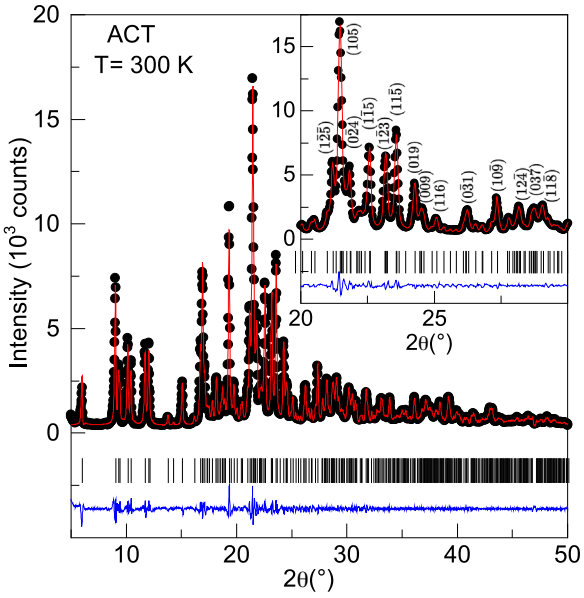

Fig. 1. XRPD pattern of refined ACT structure. Black represent experimental results, red solid lines are results from Le Bail fitting, black lines below XRPD pattern are peak positions, and blue line represents differences between experimental and fitted data.

For low-energy measurements, a 514.5 nm laser line and 1800/1800/2400 grooves/mm gratings were used. For measurements across a wider spectral range, a 647 nm laser line and 300/300/500 grooves/mm gratings were employed. These setups provided spectral resolutions of approximately 2 cm^{-1} and 13 cm^{-1}, respectively. They were optimized to balance laser line suppression, spectral resolution, and spectral range according to the specific experimental requirements.

Temperature-dependent Raman scattering measurements were conducted using a LINKAM THMS 600 heating/cooling stage, with the sample mounted on a custom copper plate. The heating/cooling rate was set to 5 K/min, followed by a 25 min thermalization period after each temperature change. The sample chamber was purged with argon, and continuous low-flow argon purging was maintained throughout the experiment. All the Raman scattering spectra are corrected by the corresponding Bose factor $n(T)$.

3. Results and discussion

As previously mentioned, ACT may exist in several phases. The crystal structure of ACT Form I has been previously solved and refined using synchrotron X-ray powder diffraction data [23], and further optimized using density functional theory techniques [12,14]. Temperature dependent XRPD measurements were reported in Refs. [15,16].

To verify the room temperature crystal structure of the obtained sample prior to the Raman scattering experiments, we performed XRPD analysis. The resulting XRPD pattern corresponding to the refined structure is shown in Fig. 1. The black dots in Fig. 1 represent experimental data, while the red solid line corresponds to the Le Bail fitting results. The black lines below the XRPD pattern indicate peak positions, and the blue line represents the difference between the experimental and fitted results. The XRPD pattern shows an excellent match with previously

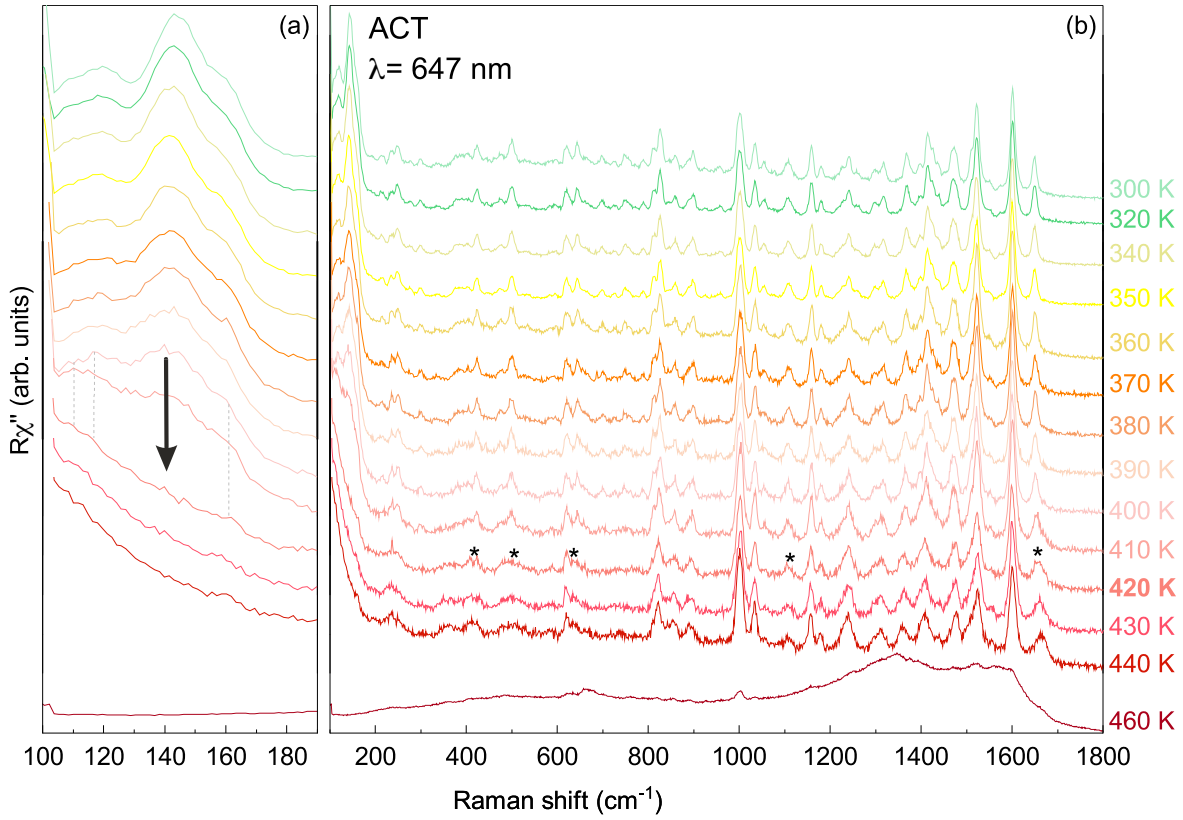

Fig. 2. Temperature dependent Raman spectra of ACT measured with 300/300/500 grooves/mm gratings combination and 647 nm laser line of (a) low and (b) wide energy spectral region. Black arrow indicates the disappearance of the 140 cm^{-1} peak, while dashed lines serve as guides to the eye. Asterisks mark the peaks that show pronounced discontinuities in their temperature evolution.

published data, with all observed peaks closely aligning with those reported in the literature [12,14,23], including synchrotron data [25], confirming that the analyzed sample corresponds to ACT Form I. The obtained results show total number of 1312 reflections. ACT crystallizes in $P1$ crystal group, with cell parameters a = 5.4497(2), b = 9.8976(4), c = 30.2558(2), α = 76.8631(2), β = 99.0525(8), γ = 4105.2850(3). This undoubtedly show that our ACT sample crystallizes in Form I.

To further highlight the key structural features, the top-right corner of Fig. 1 presents a zoomed-in section of the XRD pattern, displaying 2Θ values ranging from 20° to 30°, along with the corresponding Miller indices. This region is crucial for the identification of ACT Form I, and all indexed peaks match synchrotron measurements [23], providing further confirmation of the structure.

Additionally, Form I ACT appears to have smaller particle sizes, a more uniform particle size distribution, and greater stability than previously reported more amorphous products. Moreover, Form I ACT is purer and more stable than other amorphous forms [12]. These results conclusively confirm that our ACT sample crystallizes in Form I.

In molecular crystals, two types of vibrations can generally be distinguished: external vibrations, which occur between molecules, and internal vibrations, which occur within molecules [26]. External vibrations can be further classified based on the type of motion—either as translations, representing the translational movement of molecules, or librations, representing their rotational movement. They are, in particular, strongly linked to the structural properties of molecular compounds, offering valuable insights into structural phase transitions.

Intramolecular vibrations within a molecular crystal, compared to those in an isolated molecule, may show slight shifts in energy and/or changes in linewidth due to perturbations from the relatively weak intermolecular interactions. In the similar manner structural changes can also lead to variations in the energy and/or linewidth of these vibrations. Moreover, when the number of molecules in the primitive unit cell exceeds one, intramolecular vibrations may manifest as multiplets due to symmetry considerations and the typically weak nature of intermolecular interactions [26,27].

The vibrational structure of ACT can be determined by correlating the translational, rotational and vibrational motions of a single molecule to the corresponding site and crystal symmetries [26,27]. Given the very low symmetry of ACT Form I ($P1$), this straightforwardly results in only three librational modes and 474A symmetry internal vibrations that are expected to be observed in the Raman scattering experiment (Γ point distribution). While intramolecular vibrations dominate the Raman spectra of ACT, intermolecular vibrations are expected to be observed in the low-energy spectral region, below 175 cm^{-1}. Moreover, given the low symmetry of ACT ($P1$), no dependence of the Raman spectra on the polarization of the incident and scattered light is anticipated. As a result, a crossed polarization configuration was used in all light scattering experiments presented in this study, and this aspect will not be discussed further.

The ACT Raman spectra, measured in the temperature range from 300 K to 460 K using a 647 nm laser line and 300/300/500 grooves/mm gratings are shown in Fig. 2. It is noticeable that as the temperature increases, Raman modes soften and broaden, driven by thermal expansion and anharmonic effects [28,29]. In general, in the absence of phase transitions (and coupling to other elementary excitations) the temperature evolution of linewidth is fully driven by anharmonic coupling. On the other hand, the change in phonon frequency with temperature is not entirely due to anharmonic coupling, but also thermal expansion. Although thermal expansion itself occurs as a result of anharmonicity, it affects the quasi-harmonic frequencies through the harmonic force constant.

Closer inspection revealed discontinuities at 420 K in the temperature evolution of intensities and/or linewidths for the internal modes

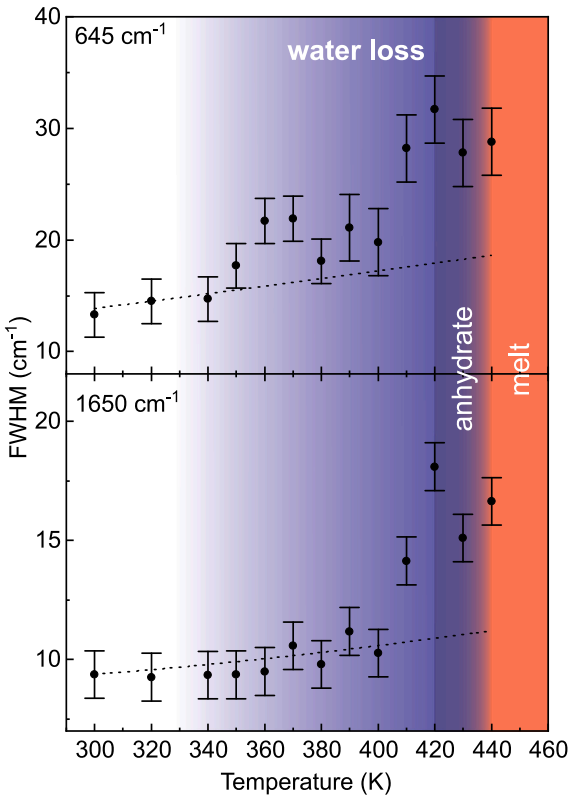

Fig. 3. Linewidth temperature dependence of peak structures at 645 cm^{-1} and 1650 cm^{-1} measured by 647 nm laser line. The values are error-weighted, and the dashed lines represent the anharmonic behavior described by $\Gamma = \Gamma_0\left(1+\frac{2\lambda_{ph-ph}}{exp(\frac{\hbar\omega_0}{2k_BT})-1}\right)$, where Γ_0 and ω_0 are the zero-temperature limits and λ_{ph-ph} is the phonon–phonon coupling constant [28].

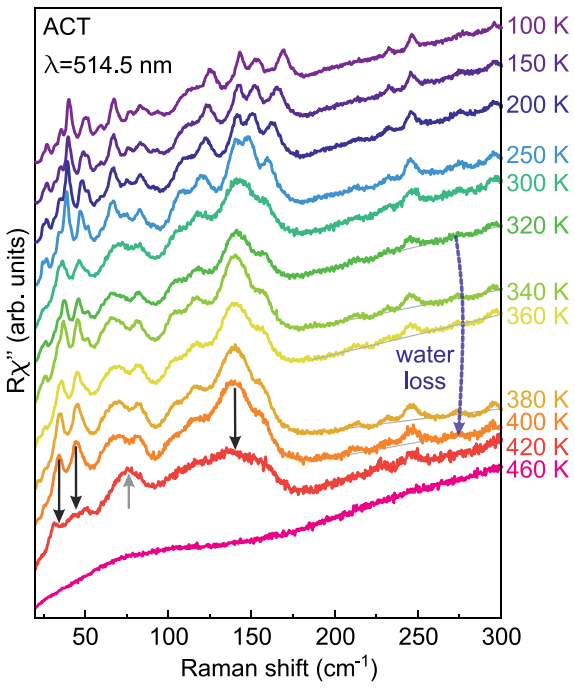

Fig. 4. Temperature dependent low-energy Raman spectra measured by 1800/1800/2400 grooves/mm gratings combination and 514.5 nm laser line ensuring high suppression of the elastically scattered light. Black arrows indicate the disappearing peaks, while the gray arrow marks the peak that appears at 420 K.

around 420 cm^{-1}, 505 cm^{-1}, 645 cm^{-1}, 1110 cm^{-1}, and 1650 cm^{-1} (marked by asterisks in Fig. 2). These modes were previously assigned [22] to in-plane OCO rocking + out-of-plane benzene deformation, C–C–C deformation, O–H out-of-plane deformation, CH wagging in the benzene ring + C–N–C stretching in the amide group + C–C–O stretching, and C=O stretching, respectively. Similar discontinuities may also be present for other modes, but due to the overlapping of a larger number of modes, finite spectral resolution, and/or low intensity, they are not easily discernible.

The temperature evolution of the linewidths for the peaks at 645 cm^{-1} and 1650 cm^{-1} is shown in Fig. 3. Above 340 K, the 645 cm^{-1} peak begins to deviate from the expected anharmonic behavior, as illustrated by the dashed lines. As evidenced by TGA and DSC results [15,16], this corresponds to the temperature range where the stepwise loss of H-bonded water molecules occurs (highlighted in the blue shaded area in Fig. 3). It should be noted that the exact temperatures of the dehydration process may vary between techniques due to differences in water vapor pressure around the sample. While no significant deviation is observed below 400 K for the 1650 cm^{-1} peak, both peaks exhibit strong, peak-like deviations in linewidth around 420 K. This is likely a result of strong fluctuations [29] indicating the structural phase transition at this temperature. In general, while selection rules based on symmetry determine whether a phonon mode can couple to structural fluctuations, the coupling strength is reflected in the phonon linewidth, which increases when phonons interact with dynamic structural fluctuations.

More notable changes are observed in the low-energy spectral region (see Fig. 3(a)). While the peak at 140 cm^{-1} completely disappears at 420 K, the peaks at 110 cm^{-1}, 117 cm^{-1}, and 160 cm^{-1}, although broadened, remain observable at higher temperatures. This suggests that the 140 cm^{-1} peak corresponds to external vibration (lattice libration) specific to ACT Form I, as previously discussed. In contrast, the peaks at 110 cm^{-1}, 117 cm^{-1}, and 160 cm^{-1} are internal in nature. To elucidate temperature induced changes in the crystal structure of ACT, we focus on the ultra-low energy region in wide temperature range.

The ultra-low energy Raman spectra (20–300 cm^{-1}) of ACT, measured over the temperature range of 100 K to 460 K using 1800/1800/2400 grooves/mm gratings with a 514.5 nm laser line, is presented in Fig. 4. The sample was first cooled from room temperature to 100 K and then gradually heated to 460 K. As expected, a large number of peaks become clearly discernible at 100 K due to anharmonic effects, as previously discussed. Upon heating, changes in the slope of the spectra are observed in the region associated with the stepwise loss of H-bonded water molecules in ACT [13,15,16]. This is not unexpected, as small changes in the electronic structure can cause variations in the spectral slope.

Closer inspection of the temperature evolution reveals the disappearance of peaks at approximately 34 cm^{-1} and 44 cm^{-1}, as indicated by the black arrows in Fig. 4, in addition to the previously observed peak at 140 cm^{-1} shown in Fig. 2. These three peaks correspond to external vibrations, consistent with earlier symmetry considerations. Their disappearance at 420 K indicates a structural phase transition and the breaking of crystal symmetry of Form I, as also suggested by the behavior of the previously analyzed internal vibrational modes. In light of the DSC and TGA results [15,16], this suggests that the Form I crystal structure is preserved until the transition to the anhydrous phase, consistent with second-harmonic generator and XRPD findings [15].

The most striking feature is the appearance of a new mode around 75 cm^{-1}, indicated by a gray arrow in Fig. 4. The emergence of this additional mode in the low-energy region at the phase transition temperature suggests an intermolecular origin for this vibration. This implies the presence of a certain, presumably one-dimensional, order

up to 460 K, beyond which the isotropic melt is reached. This interpretation is further supported by the $2\theta \sim 17°$ observation reported in Ref. [15], where X-ray diffraction reveals a broad, diffuse-like signal above the transformation temperature and just before the onset of the isotropic melt. While Raman spectroscopy can detect this type of order, the structural coherence might only extend across a few unit cells. Employing advanced nanoscale-sensitive characterization techniques, such as total X-ray scattering-based pair distribution function analysis, could enable a more comprehensive characterization of this behavior in future studies.

4. Conclusion

In this study, comprehensive temperature-dependent low-energy Raman analyses of ACT were conducted, revealing complex vibrational and structural changes induced by temperature. The previously reported stepwise loss of hydrogen-bonded water molecules was also detected in the low-energy Raman data. Moreover, the peak-like deviation from anharmonic behavior in the linewidths of the 645 cm^{-1} and 1650 cm^{-1} modes serves as a clear fingerprint of strong structural fluctuations at 420 K. At this temperature, three peaks, identified as external vibrations, characteristic of the Form I crystal structure, disappear, indicating the breaking of symmetry as the system enters the anhydrous phase. The appearance of a new vibrational mode around 75 cm^{-1} at the phase transition temperature indicates the presence of short-range order up to 460 K, beyond which the system transitions into an isotropic melt. This interpretation aligns with previous X-ray diffraction studies [Ref. [15]], where a broad, diffuse-like signal near $2\theta \sim 17°$ was observed above the transition temperature, just before the isotropic phase fully develops. While Raman spectroscopy can detect such structural order, the coherence may extend only over a few unit cells. Future studies employing nanoscale-sensitive techniques, such as total X-ray scattering-based pair distribution function analysis, could provide a more detailed characterization of these structural fluctuations and their role in phase transitions.

CRediT authorship contribution statement

J.J. Lazarević: Writing – review & editing, Writing – original draft, Methodology, Investigation, Formal analysis, Data curation, Conceptualization. **S. Uskoković-Marković:** Writing – review & editing, Supervision, Resources, Methodology. **J. Mitrić:** Writing – original draft, Investigation. **N. Lazarević:** Writing – review & editing, Visualization, Supervision, Resources, Methodology, Conceptualization.

Declaration of competing interest

The Authors have no competing interests to declare.

Acknowledgments

The authors acknowledge funding provided by the Institute of Physics Belgrade through the grant by the Ministry of Science, Technological Development and Innovation of the Republic of Serbia. The authors are grateful to Dr. Jelena Pešić and Dr. Emil Božin for fruitful discussions.

Data availability

Data will be made available on request.

References

[1] C.R. Gardner, C.T. Walsh, Ö. Almarsson, Drugs as materials: valuing physical form in drug discovery, Nat. Rev. Drug Discov. 3 (11) (2004) 926–934.
[2] S.P. Adams, M. Tsang, J.M. Wright, Lipid lowering efficacy of atorvastatin, Cochrane Database Syst. Rev. 12 (2012).
[3] B.F. Asztalos, K.V. Horvath, J.R. McNamara, P.S. Roheim, J.J. Rubinstein, E.J. Schaefer, Comparing the effects of five different statins on the hdl subpopulation profiles of coronary heart disease patients, Atherosclerosis 164 (2) (2002) 361–369.
[4] E.J. Schaefer, J.R. McNamara, T. Tayler, J.A. Daly, J.L. Gleason, L.J. Seman, A. Ferrari, J.J. Rubenstein, Comparisons of effects of statins (atorvastatin, fluvastatin, lovastatin, pravastatin, and simvastatin) on fasting and postprandial lipoproteins in patients with coronary heart disease versus control subjects, Am. J. Cardiol. 93 (1) (2004) 31–39.
[5] F.M. Sacks, M.A. Pfeffer, L.A. Moye, J.L. Rouleau, J.D. Rutherford, T.G. Cole, L. Brown, J.W. Warnica, J.M.O. Arnold, C.-C. Wun, et al., The effect of pravastatin on coronary events after myocardial infarction in patients with average cholesterol levels, N. Engl. J. Med. 335 (14) (1996) 1001–1009.
[6] A.K. Altwairgi, Statins are potential anticancerous agents, Oncol. Rep. 33 (3) (2015) 1019–1039.
[7] M. Jakobisiak, J. Golab, Potential antitumor effects of statins, Int. J. Oncol. 23 (4) (2003) 1055–1069.
[8] J. Longo, J.E. van Leeuwen, M. Elbaz, E. Branchard, L.Z. Penn, Statins as anticancer agents in the era of precision medicine, Clin. Cancer Res. 26 (22) (2020) 5791–5800.
[9] G. Weitz-Schmidt, Statins as anti-inflammatory agents, Trends Pharmacol. Sci. 23 (10) (2002) 482–487.
[10] I. Inoue, S.-I. Goto, K. Mizotani, T. Awata, T. Mastunaga, S.-I. Kawai, T. Nakajima, S. Hokari, T. Komoda, S. Katayama, Lipophilic hmg-coa reductase inhibitor has an anti-inflammatory effect: reduction of mrna levels for interleukin-1β, interleukin-6, cyclooxygenase-2, and p22phox by regulation of peroxisome proliferator-activated receptor α (pparα) in primary endothelial cells, Life Sci. 67 (8) (2000) 863–876.
[11] D. Skorda, C.G. Kontoyannis, Identification and quantitative determination of atorvastatin calcium polymorph in tablets using ft-raman spectroscopy, Talanta 74 (4) (2008) 1066–1070.
[12] R.L. Hodge, J.A. Kaduk, A.M. Gindhart, T.N. Blanton, Crystal structure of atorvastatin calcium trihydrate form i (lipitor®), (c33h34fn2o5) 2ca (h2o) 3, Powder Diffr. 35 (2) (2020) 136–143.
[13] K.A. Salazar-Barrantes, J.R. Vega-Baudrit, M. Navarro-Hoyos, A.M. Araya-Sibaja, Thermoanalytical techniques applied to the solid-state characterization of atorvastatin calcium trihydrate form I, Chem. Thermodyn. Therm. Anal. 14 (2024) 100130.
[14] G. Shete, V. Puri, L. Kumar, A.K. Bansal, Solid state characterization of commercial crystalline and amorphous atorvastatin calcium samples, AAPS PharmSciTech 11 (2) (2010) 598–609.
[15] C. Tizaoui, H. Galai, M. Barrio, S. Clevers, N. Couvrat, V. Dupray, G. Coquerel, J.-L. Tamarit, I.B. Rietveld, Does the trihydrate of atorvastatin calcium possess a melting point? Eur. J. Pharm. Sci. 148 (2020) 105334.
[16] N.P.A. Christensen, B. Van Eerdenbrugh, K. Kwok, L.S. Taylor, A.D. Bond, T. Rades, J. Rantanen, C. Cornett, Rapid insight into heating-induced phase transformations in the solid state of the calcium salt of atorvastatin using multivariate data analysis, Pharm. Res. 30 (2013) 826–835.
[17] Y.-I. Lim, J. Han, Y.-A. Woo, J. Kim, M.J. Kang, Rapid quantitation of atorvastatin in process pharmaceutical powder sample using raman spectroscopy and evaluation of parameters related to accuracy of analysis, Spectrochim. Acta Part A: Mol. Biomol. Spectrosc. 200 (2018) 26–32.
[18] T. De Beer, C. Bodson, B. Dejaegher, B. Walczak, P. Vercruysse, A. Burggraeve, A. Lemos, L. Delattre, Y. Vander Heyden, J.P. Remon, et al., Raman spectroscopy as a process analytical technology (pat) tool for the in-line monitoring and understanding of a powder blending process, J. Pharm. Biomed. Anal. 48 (3) (2008) 772–779.
[19] T. De Beer, A. Burggraeve, M. Fonteyne, L. Saerens, J. Remon, C. Vervaet, Near infrared and raman spectroscopy for the in-process monitoring of pharmaceutical production processes, Int. J. Pharm. 417 (1) (2011) 32–47, advanced characterization techniques..
[20] S. Mazurek, R. Szostak, Quantification of atorvastatin calcium in tablets by ft-raman spectroscopy, J. Pharm. Biomed. Anal. 49 (1) (2009) 168–172.
[21] T. Fukami, T. Koide, H. Hisada, M. Inoue, Y. Yamamoto, T. Suzuki, K. Tomono, Pharmaceutical evaluation of atorvastatin calcium tablets available on the internet: A preliminary investigation of substandard medicines in japan, J. Drug Deliv. Sci. Technol. 31 (2016) 35–40.
[22] M. Oprica, M. Iota, M. Daescu, S.N. Fejer, C. Negrila, M. Baibarac, Spectroscopic studies on photodegradation of atorvastatin calcium, Sci. Rep. 11 (1) (2021) 15338.
[23] C. Briggs, R. Jennings, R. Wade, K. Harasawa, S. Ichikawa, S. Minohara K. Nakagawa, U.S. Patent, Vol. 5, 1999, 959156.

[24] A. Le Bail, H. Duroy, J. Fourquet, Ab-initio structure determination of lisbwo6 by x-ray powder diffraction, Mater. Res. Bull. 23 (3) (1988) 447–452, http://dx.doi.org/10.1016/0025-5408(88)90019-0, URL https://www.sciencedirect.com/science/article/pii/0025540888900190.

[25] S.G. Antonio, F.R. Benini, F.F. Ferreira, P.C.P. Rosa, C. de Oliveira Paiva-Santos, Synchrotron x-ray powder diffraction data of atorvastatin, Powder Diffr. 23 (4) (2008) 350–355, http://dx.doi.org/10.1154/1.2996511.

[26] W.G. Fateley, Infrared and Raman selection rules for molecular and lattice vibrations: the correlation method, 1972.

[27] J. Lazarević, S. Uskoković-Marković, M. Jelikić-Stankov, M. Radonjić, D. Tanasković, N. Lazarević, Z. Popović, Intermolecular and low-frequency intramolecular raman scattering study of racemic ibuprofen, Spectrochim. Acta Part A: Mol. Biomol. Spectrosc. 126 (2014) 301–305.

[28] A. Baum, A. Milosavljević, N. Lazarević, M. Radonjić, B. Nikolić, M. Mitschek, Z.I. Maranloo, M. Šćepanović, M. Grujić-Brojčin, N. Stojilović, et al., Phonon anomalies in fes, Phys. Rev. B 97 (5) (2018) 054306.

[29] N. Lazarević, R. Hackl, Fluctuations and pairing in fe-based superconductors: Light scattering experiments, J. Phys.: Condens. Matter. 32 (41) (2020) 413001.

Physica B 713 (2025) 417392

Contents lists available at ScienceDirect

Physica B: Condensed Matter

journal homepage: www.elsevier.com/locate/physb

Plasmon-phonon interaction and surface optical mode in $Cd_{1-x}Fe_xTe_{1-y}Se_y$ single crystals

Jelena Mitric [a,*], Maja Romcevic [a], Witold D. Dobrowolski [b], Andrzej Mycielski [b], Nebojsa Romcevic [a]

[a] Institute of Physics Belgrade, University of Belgrade, Pregrevica 118, 11080, Belgrade, Serbia
[b] Institute of Physics, Polish Academy of Sciences, Aleja Lotnikow 32/46, PL-02668, Warsaw, Poland

ARTICLE INFO

Keywords:
Semiconductors
Electron-phonon interactions
Light absorption and reflection

ABSTRACT

The interaction between electrons and phonons represents a notable phenomenon in the realm of condensed matter physics, exerting a substantial influence on diverse electronic and optical characteristics of materials. Within this context, an exhaustive investigation of the Raman and Far – Infrared reflectivity spectra of $Cd_{1-x}Fe_xTe_{1-y}Se_y$ single crystals can yield valuable insights into the various impacts of Plasmon – phonon interactions on the fundamental physics of II – IV semiconductors. Spectral analysis was executed employing a suitable fitting procedure. In the analysis of Far – infrared spectra, a dielectric function incorporating the presence of Plasmon – LO phonon interaction was employed. Three principal lines in the spectra, contingent upon the composition, were discerned at approximately 140 cm^{-1}, 170 cm^{-1} and 200 cm^{-1}. 140 cm^{-1} feature corresponds to the longitudinal – transverse (LO – TO) splitting of the CdTe – like mode. The 170 cm^{-1} feature is associated with CdSe, while the 200 cm^{-1} feature is linked to the local Fe mode. These features were elucidated within the framework of the modified random – element – isodisplacement (MREI) mode. The calculated phonon frequencies demonstrated a high level of agreement with experimentally determined values. Additionally, in all samples, a surface layer characterized by a low concentration of free carriers (depleted region) was formed. Consequently, a surface optical mode (SOP) was registered at approximately 150 cm^{-1} in samples with a predominant CdTe component (y less that 15 %) and at around 190 cm^{-1} in samples with a majority CdSe content (y greater than 95 %).

1. Introduction

Compounds made from group II-VI elements mixed with transition metals are called dilute magnetic semiconductors (DMSs) because they have both magnetic and semiconducting properties. While many studies have focused on DMSs with manganese (Mn), researchers are now also exploring those with iron (Fe) and other transition metals [1].

Iron, like manganese, can replace some of the metal atoms in the crystal structure of these compounds. In this structure, each iron ion (Fe^{2+}) is surrounded by four neighboring anions (negatively charged atoms). Iron in this state has a specific electron arrangement ($3\,d^6$) that results in magnetic behavior. This creates two energy levels due to the crystal's cubic symmetry — a lower energy ground state called E_5 and a higher energy state called $5T_2$ [2].

However, iron doesn't dissolve well in cadmium telluride (CdTe), and the crystal form known as zinc blende only forms when the iron content is less than 6 %. $Cd_{1-x}Fe_xSe$ forms a different structure called wurtzite. When the amount of iron is low, mixed crystals like $Cd_{1-x}Fe_xTe_{1-y}Se_y$ can still form the zinc blende structure, which helps make their optical properties easier to understand.

Classical bulk solid-state physics can be broadly categorized into two primary domains, one predominantly addressing electronic properties and the other focusing on atomic dynamics. A sustained interest in optical phonons in semiconducting alloys has persisted for many years [3]. The vibrational spectra of semiconducting alloys serve to illustrate fundamental aspects of lattice vibrations and alloy physics [4].

The interaction between electrons and phonons is an important process in condensed matter physics, and it influences many physical phenomena [5,6]. The electron-phonon interaction significantly impacts various electronic and optical properties of materials, including electrical conductivity, thermal conductivity and superconductivity [7]. A comprehensive understanding of electron-phonon interaction is

* Corresponding author.
E-mail address: jmitric@ipb.ac.rs (J. Mitric).

https://doi.org/10.1016/j.physb.2025.417392
Received 11 March 2025; Received in revised form 23 April 2025; Accepted 14 May 2025
Available online 15 May 2025

imperative for predicting and optimizing material properties in technological applications. Substantial progress has been achieved in both theoretical and experimental investigations of this interaction in recent decades [8], yielding deeper insights into underlying mechanisms and effects on material properties. This knowledge has paved the way for developing new materials with tailored properties and optimized performance across diverse applications [9–11].

In our previous studies, we explored plasmon-phonon interactions in quaternary alloys, $Cd_{1-x}Mn_xTe_{1-y}Se_y$ [12] and $Hg_{1-x}Mn_xTe_{1-y}Se_y$ [13], as well as the interaction of surface phonons with plasmons in thin films of CdTe [14]. A model has been developed to determine the long-wavelength optical phonons in quaternary mixed crystals of the type $A_{1-x}B_xC_{1-y}D_y$, depending on their composition. However, as we'll see later, the phonon properties of $Cd_{1-x}Fe_xTe_{1-y}Se_y$ were described using a model for three-component alloys of the type $A_{1-x}B_xC$, and the properties of iron (Fe) were treated as if it were an impurity. In this paper, we extend our research to single crystals of $Cd_{1-x}Fe_xTe_{1-y}Se_y$ grown using the Bridgman technique. We employed X-ray Diffraction, Raman Spectroscopy, and Far-infrared Spectroscopy as experimental methods. Our goal was to thoroughly study phonon properties, including surface phonons, as well as some aspects of electron-phonon interactions.

2. Samples and experiment

Single crystals of $Cd_{1-x}Fe_xTe_{1-y}Se_y$ were grown using the Bridgman technique employing chemically pure constituents. The Fe concentration (x) was determined with a precision of ±0.005 through magnetic susceptibility measurements at room temperature. Additionally, a more precise determination of Fe content was carried out using an X-ray microprobe. Both methodologies yielded identical results within the margins of measurement error. The selenium content in the samples was deduced from these data. Samples with varying compositions were investigated (see Table 1). The results are confirmed using EDX analysis (see Supplementary).

The selenium quantity in this solid solution varies widely, while the added Fe concentration remains below 4 %. Therefore, it is justified to consider this material, in one part of the discussion, as a doped ternary solid solution, i.e. $CdTe_{1-y}Se_y$ + Fe.

Structural characteristics of $Cd_{1-x}Fe_xTe_{1-y}S$ samples were ascertained using a Philips PW 1050 diffractometer equipped with a PW 1703 generator, operating at 40 kV × 20 mA. Ni-filtered Co Kα radiation of 0.1778897 nm was employed at room temperature. A 15–85° scanning range was used over 2 h, with a scanning step of 0.05° and a scanning time of 10 s per step.

As illustrated in Fig. 1, three groups of spectra are observed. The first group comprises compositions with a low Se concentration. The diffractograms (Fig. 1a) confirm that the samples predominantly originate from CdTe, which exhibits a cubic structure with space group $F\overline{4}3m$. On the opposite side of the composition, for y greater than 0.95, as expected, CdSe is evident and absolutely dominant, possessing the same symmetry (Fig. 1c). For certain compositions samples consist both of CdTe and CdSe (Fig. 1b). Fe concentration was below 5 % in all samples, therefore it is not seen on presented diffractograms.

Far-infrared reflection spectra were acquired in the wavenumber range up to 350 cm^{-1} using an A BOMEM DA-8 FTIR spectrometer with a deuterated triglycine sulfate (DTGS) pyroelectric detector.

Micro-Raman spectra were collected in the backscattering configuration and analyzed using a Jobin Yvon T64000 spectrometer equipped with a nitrogen – cooled charge – coupled device (CCD) detector. The excitation source employed was the 514.5 nm (2.41 eV) line of an Ar – ion laser, and a microscope lens with a magnification of 100 × was used to focus the laser beam.

3. Results

3.1. Far – infrared spectroscopy

The far-infrared reflection spectra of $Cd_{1-x}Fe_xTe_{1-y}Se_y$ single crystal samples are presented in Fig. 2a–d, with experimental data depicted by circles. Notably, three prominent lines at approximately 140 cm^{-1}, 170 cm^{-1}, and 200 cm^{-1} are discernible in the spectra. As we will observe later, the feature near 140 cm^{-1} corresponds to the longitudinal – transverse (LO – TO) splitting of the CdTe – like mode. The feature near 170 cm^{-1} is associated with CdSe, while the peak at 200 cm^{-1} is attributed to Fe.

For ease of spectrum interpretation, Fig. 2b highlights a composition with $y = 0.03$ but varying two concentrations of added Fe. In the spectrum with lower Fe concentration, phonon features of CdTe at around 140 cm^{-1} and the structure at approximately 170 cm^{-1} from CdSe are clearly visible. For higher Fe concentration, in addition to the phonons observed at lower Fe concentration, a distinct phonon at around 190 cm^{-1} becomes evident. It is not challenging to conclude that this corresponds to a *Fe* impurity phonon. For higher selenium concentration exceeding 10 %, as shown in Fig. 2c, this effect is less pronounced but still noticeable and must be considered in the analysis. This holds true for all spectra in Fig. 2a. As expected, for Fe concentrations of 3 % and 4 % (samples CFTS1 and CFTS2, respectively), a clearly pronounced impurity phonon of Fe is observed. However, for a satisfactory fit, this phonon must also be taken into account for other compositions.

Fig. 2d depicts spectra from the CdSe side. For sample 13, i.e. 5 % CdTe, modes originating from CdTe are clearly observed along with the dominant structure attributed to CdSe. Due to the low concentration of Fe, its phonon is weakly noticeable. Conversely, for sample 14, the situation is reversed. 2 % Fe distinctly contributes to the structure at around 210 cm^{-1}, while CdTe modes are barely noticeable.

Subsequently, a more comprehensive examination of the Far – infrared spectra of $Cd_{1-x}Fe_xTe_{1-y}Se_y$ single crystal samples was conducted using a fitting procedure. The lines in Fig. 2 were derived employing a modified factored dielectric function model of coupled Plasmon – two different LO phonon modes [15] (Eq. (1)):

$$\varepsilon_f(\omega) = \varepsilon_\infty \frac{\prod_{j=1}^{3}\left(\omega^2 + i\gamma_{lj}\omega - \omega_{lj}^2\right)}{\omega\left(\omega + i\gamma_p\right)\prod_{m=1}^{2}\left(\omega^2 + i\gamma_{tm}\omega - \omega_{tm}^2\right)} \prod_{k=1}^{p} \frac{\omega^2 + i\gamma_{LOk}\omega - \omega_{LOk}^2}{\omega^2 + i\gamma_{TOk}\omega - \omega_{TOk}^2} \frac{\omega^2 + i\gamma_L\omega - \omega_L^2}{\omega^2 + i\gamma_0\omega - \omega_0^2} \quad (1)$$

The parameters ω_{lj} and γ_{lj} in the first numerator represent the eigenfrequencies and damping coefficients of the longitudinal Plasmon – phonon (LP + LO) waves, arising from the interaction of the initial modes. Correspondingly, the parameters in the first denominator characterize similar aspects of the transverse (TO) vibrations. The γ_p value signifies the damping coefficient of the LP mode in the limit of zero frequencies, while ε_∞ denotes the contribution of excitations at high frequencies relative to the spectrum interval of interest. ε_∞ is treated as an adjustable parameter to align calculated frequencies with

Table 1
Composition of prepared samples.

Sample	x [%]	y [%]
CFTS1	3	0
CFTS2	4	0.5
CFTS3	1	1
CFTS4	1	3
CFTS5	2	3
CFTS6	2	6
CFTS7	1	7
CFTS8	$8 \cdot 10^{-18}$cm^{-3}	10
CFTS9	$3.5 \cdot 10^{-19}$cm^{-3}	10
CFTS10	1	10
CFTS11	2	10
CFTS12	2	15
CFTS13	$6 \cdot 10^{-18}$cm^{-3}	95
CFTS14	2	99.8

experimental values, following standard practice [16–18]. The second term in Eq. (1) accounts for uncoupled crystal modes, where ω_{LOk} and ω_{TOk} are the longitudinal and transverse frequencies, respectively, and γ_{LOk} and γ_{TOk} are the corresponding damping coefficients. The third term represents the multi – phonon band, previously observed in CdTe – based alloys [19].

Dashed lines in Fig. 2 were generated for the case $p = 2$, considering the existence of two uncoupled modes. The oscillator indexed $p = 1$ in Eq. (1), representing the structure at about 200 cm^{-1}, is identified as one of the lattice vibration modes of $Cd_{1-x}Fe_xTe_{1-y}Se_y$ associated with Fe impurities. The oscillator indexed $p = 2$, accounting for the structure at about 100 cm^{-1}, is identified as a defect phonon [18], appearing as a very weak structure that can practically be omitted from the fit. A discrepancy between theoretical spectra and experimental data in the wavenumber range from 140 to 170 cm^{-1} was observed, prompting the utilization of the dielectric function (1) with $p = 3$. In $Cd_{1-x}Fe_xTe_{1-y}Se_y$ mixed crystals, as in some other semiconductors [18], a surface layer with a low concentration of free carriers (depleted region) may form. Consequently, surface phonons from this layer become visible. If the light penetration depth exceeds the surface layer thickness, both surface and bulk modes of the mixed crystal can be observed in reflection spectra. The oscillator indexed $p = 3$ in Eq. (1) describes the structure at about 150 cm^{-1}, primarily originating from CdTe for x less than *0.15*, while for compositions with x greater than *0.95*, this mode is around 185 cm^{-1}, associated with CdSe. The excellent agreement between experimental data and theoretical spectra (full line) supports this interpretation.

Based on this analysis, it is evident that the dielectric function (1) with $p = 3$ and Plasmon – two - phonon interaction fully describes the IR spectra. This approach directly yields TO frequencies and coupled Plasmon – LO modes. The frequencies of initial plasmons (ω_P) and LO phonons (ω_{LO}) are obtained as described in Ref. [4]:

$$\omega_P = \frac{\omega_{l1}\omega_{l2}\omega_{l3}}{\omega_{t1}\omega_{l2}} \tag{2}$$

$$\omega_{LO1,2} = \frac{1}{2}\left(\omega_{l1}^2 + \omega_{l2}^2 + \omega_{l3}^2 - \omega_P^2\right) \pm \pm\sqrt{\left(\frac{1}{4}\left(\omega_{l1}^2 + \omega_{l2}^2 + \omega_{l3}^2 - \omega_P^2\right)^2 - \omega_{l1}^2\omega_{l2}^2 - \omega_{l2}^2\omega_{l3}^2 - \omega_{l1}^2\omega_{l3}^2 + \omega_P^2(\omega_{t1}^2 + \omega_{t2}^2)\right)} \tag{3}$$

For illustration, in Fig. 3, an example of Plasmon – two different phonon interactions is provided for the composition $y = 0.03$. Experimental results are depicted by data points (o for ω_{l1}, ω_{l2}, and ω_{l3}, and * for ω_{TO1} and ω_{TO2}), obtained using the dielectric function (1). The positions of the uncoupled LO phonons (marked with ●) and plasma frequencies are determined based on Eqs. (2) and (3). Solid lines, representing coupled mode positions, are defined as solutions of the real part of Eq. (4) (Re{εs = 0}):

$$\varepsilon_S(\omega) = \varepsilon_\infty + \sum_{k=1}^{l} \frac{\varepsilon_\infty\left(\omega_{LOk}^2 - \omega_{TOk}^2\right)}{\omega_{TOk}^2 - \omega^2 - i\gamma_{TOk}\omega} - \frac{\varepsilon_\infty\omega_P^2}{\omega(\omega + i\gamma_P)} \tag{4}$$

Where ε_s is the dielectric function that accounts for the uncoupled phonons corresponding to the TO – modes, overlaid by a Drude part that considers the contribution from free carriers [20]. This procedure is carried out for each composition. From the figure, it is evident that the plasmon – two - phonon interaction is relatively weak, and the difference between the frequencies of coupled phonons and the initial LO phonon is only a few centimeters inverse. The results of this analysis are presented in Fig. 5, alongside the results of Raman measurements.

3.2. Raman Spectroscopy

The nonpolarized Raman spectra of $Cd_{1-x}Fe_xTe_{1-y}Se_y$ in the spectral range from 90 to 500 cm^{-1} at room temperature are depicted in Fig. 4. The experimental results are represented by a thin black line.

Firstly, concerning phonons at approximately 123 and 141 cm^{-1} observed in Fig. 4a–d, it is known from the literature [21] that these modes originate from individual Te atom or TeO_2, which is consistently formed on the sample surface. Additionally, TeO_2 is much thinner than the penetration depth of the laser light, thus not significantly impacting the accuracy of the Raman spectrum. In the literature [22,23], these phonons, along with the phonon at around 100 cm^{-1}, are associated with the spectra of pure Te without delving into the detailed nature of their formation. A more detailed analysis of the phonon formation

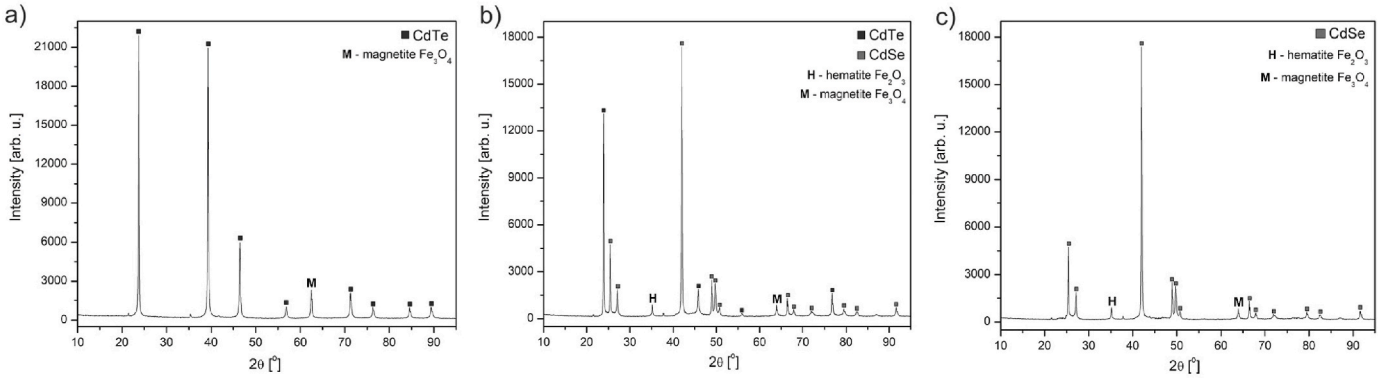

Fig. 1. XRD patterns for selected samples. Fig. 1a shows group of samples that have low Se concentration and dominant CdTe structure (CFTS1), Fig. 1b shows certain samples which consist both of CdTe and CdSe (CFTS5) and Fig. 1c represent samples on the opposite side of the composition, for y greater than 0.95 and dominant CdSe structure (CFTS8).

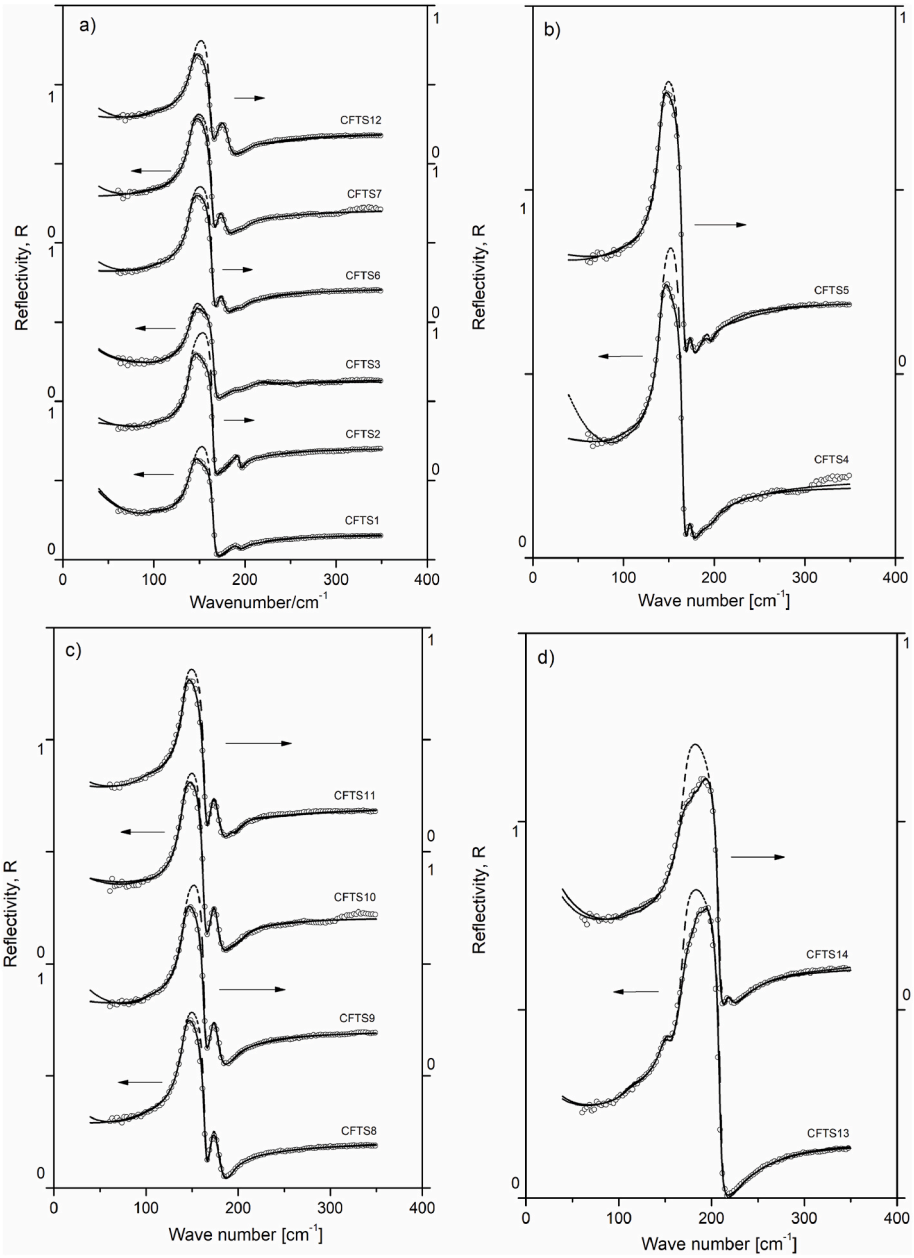

Fig. 2. Far – infrared reflection spectra of $Cd_{1-x}Fe_xTe_{1-y}Se_y$ samples. Fig. 2a and c represent all CFTS samples with lower and higher Se concentration, respectively. Fig. 2b highlights compositions with y = 0.03, but with varying concentrations of added Fe (CFTS 4 with lower and CFTS5 with higer Fe concentration). This holds true for Fig. 2d as well, where CFTS 13 has lower and CFTS14 higher Fe concentrations.

mechanism can be found in Ref. [24] and the references cited therein. In brief, these phonons are associated with the position of Te atoms and are not IR-active (depending on the symmetry of the local environment). Their position can vary by several cm^{-1} depending on the surrounding environment of the Te atoms and the degree of oxidation. As a result, they can only be partially removed by polishing the sample. However, this is not the primary focus of this paper. Moreover, similar to the IR measurements, on almost all samples with y less than 15 %, two multi – phonon bands are observed at around 270 and 330 cm^{-1}. For samples on the CdSe side, these multi-phonon ranges shift to approximately 350 and 405 cm^{-1}, respectively, with their positions following changes in the phonon positions from which they originate. For instance, the multi-phonon at 405 cm^{-1} corresponds to 2x ω_{LOCdSe}, as will be discussed later.

Full lines represent the results of deconvolution. Raman spectra are commonly analyzed using Lorentzian functions or a convolution of Lorentzian and Gaussian curves [25,26]. In our analysis, we consider all lines to be of the Lorentzian type. This indicates that all spectral lines are symmetric and that no Fano resonance was observed in the electron-phonon interaction [24], most likely due to the low concentration of free carriers.

Utilizing the results of IR measurements, a minimum of 11 lines are considered for deconvolution of Raman spectra. Besides two lines describing multi – phonon processes, three lines are included for TeO_2 phonons (at around 100, 123, and 141 cm^{-1}). The position of the TO phonon of CdTe is approximately 140 cm^{-1}, and it is obscured by one of these phonons, hence not considered separately. The deconvolution results, considering the LO phonon of CdTe, TO/LO pairs of CdSe, and the impurity phonon Fe, are shown on all spectra with dashed lines. As observed in Fig. 2, there is a clear discrepancy between the experimental and theoretical spectra at around 150 cm^{-1}. Therefore, the solid line is obtained when a surface phonon is added to the analysis, indicated by

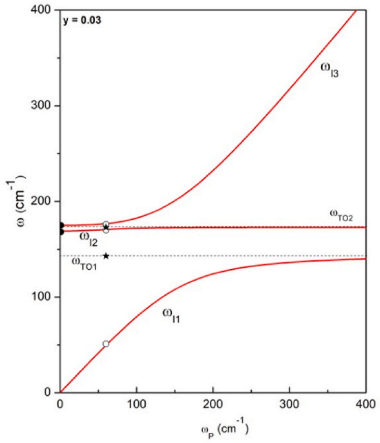

Fig. 3. Plasmon – two different phonon interaction for the composition y = 0.03. Experimental results are depicted by data points (o for ω_{l1}, ω_{l2}, and ω_{l3}, and * for ω_{TO1} and ω_{TO2}), obtained using the dielectric function (1). The positions of the uncoupled LO phonons (marked with ●) and plasma frequencies are determined based on Eqs. (2) and (3). Solid lines, representing coupled mode positions, are defined as solutions of the real part of Eq. (4) (Re{εs = 0}).

the dark red line. This way, the experimental spectrum is fully reproduced. The results of this analysis are presented in Fig. 5.

4. Discussion

4.1. Phonon properties

In principle, the analysis of phonon properties in our $Cd_{1-x}Fe_xTe_{1-y}Se_y$ samples can be approached in two ways. Firstly, we can treat this solid solution as a four-component system and use our model for the analysis of phonon properties of such alloys [27]. However, here we encounter the problem of the required parameters for the model. Namely, we have samples covering a wide range of y, i.e. added CdSe. On the other hand, we have compositions with a maximum of 4 % Fe. Additionally, unreliable data are available in the literature for the binary, cubic structures of FeTe and FeSe. This implies that we would have to assume many parameters, potentially compromising the validity of such an analysis.

An alternative approach takes into account the fact that the Fe concentration is low. In this case, the phonon properties of the ternary alloy $CdTe_{1-x}Se_x$ are analyzed first, and then the influence of Fe as an impurity is considered. This conclusion is also supported by the XRD analysis.

In general, we adopted the notation from Ref. [28], which classifies the phonon behavior in $AB_{1-x}C_x$-type alloys into three categories:

a) **Two-mode behavior**: each TO–LO mode pair of the end members (AB and AC) splits into separate impurity
b) **One-mode behavior**: each TO and LO mode of one end member (AB) shifts continuously to the corresponding TO and LO mode of the other end member (AC)
c) **Intermediate one-/two-mode behavior**: the LO-mode frequency shifts continuously from AB to AC, while the other modes behave according to the two-mode scenario.

Based on this framework, we chose the second approach. We had previously analyzed the phonon properties of $CdTe_{1-y}Se_y$ [26] and applied a modified Genzel model [28] in our analysis.

Therefore, we opted for the second approach. Briefly, to study the phonon mode behavior for the ternary compounds $CdTe_{1-y}Se_y$ [29], we used a model based on the Genzel model [28]. This model has provided good results in previous studies [30,31] for describing phonon behavior in ternary mixed crystals. In the $AB_{1-y}C_y$ type of mixed crystals, the crystal lattice comprises two sublattices, one filled by A atoms only and the other filled by B and C atoms randomly distributed. The local electric field (E_{loc}) was taken into account, and a connection between microscopic and macroscopic parameters was established using the Born-Huang procedure. The dependence of the force constant between first neighbors on concentration (y) was neglected, but second – neighbor force constants were involved. The solid lines in Fig. 5 were obtained using this model.

The experimental values for the TO and LO modes obtained from IR measurements are marked with open symbols, while the results from Raman measurements are represented by solid symbols. Parameters for the end compositions, i.e. CdTe and CdSe, were chosen to achieve the best match between experimental results and the applied model. These values are very close to the results from the literature [10,30,31]. The agreement between experimental and theoretical results is very good, considering the approximations on which these models are based. As expected, the results in Fig. 5 suggest that the phonons in $CdTe_{1-y}Se_y$ exhibit the two – mode behavior.

We labeled the structure at about $\omega_0 = 200\ cm^{-1}$ in Figs. 2 and 4 as a local Fe mode. It is known that if the semiconductor is doped with impurities that take the place of a heavier atom and are lighter than it (in our case, Fe takes the place of Cd in CdTe), then two new modes appear. These are the local mode, which appears above the optical band, and the gap mode, located between the acoustic and optical bands of the host material [32].

The impurity mode can appear due to the electron – phonon interaction [33]. Additionally, it occurs due to the difference in the masses of the original ion and the impurity that comes in its place, known as the isotope effect [34].

If only the (quasi) isotope effect is taken into account, the position of the local mode can be estimated in the simplest way, which is described in detail in Ref. [35]:

$$\frac{\omega_o}{\omega_{LO\ CdTe}} = \sqrt{\frac{m_{Cd}}{m_{Fe}}} \tag{5}$$

In this way, for CdTe, the value for $\omega_0 = 232.6\ cm^{-1}$ was determined. The experimentally obtained value for ω_0 for sample 1, i.e. CdTe without added Se, is $184\ cm^{-1}$. This means that the registered electron – phonon interaction has a significant contribution to the position of the local Fe phonon. Additionally, a change in the force constant in the vicinity of Fe could also influence the position of the local Fe phonon. The dashed line in Fig. 5 represents a guide for the eyes obtained by translating the LO phonon of CdSe. The trend observed for sample 1 is continued for the other samples, with the separation of the local mode calculated relative to the LO phonon of CdSe. This indicates that Fe has entered the lattice of $CdTe_{1-y}Se_y$.

Table 2 presents the results of multiphonon processes obtained by fitting the Raman spectra shown in Fig. 4. The main characteristics of these lines are their relatively low intensity and a full width at half maximum of approximately $40\ cm^{-1}$. Both factors affect the accuracy of determining the phonon positions. Nevertheless, it can be concluded that the phonons observed around $270\ cm^{-1}$ and $330\ cm^{-1}$, detected for all compositions with $y \leq 0.15$, correspond to $2 \times \omega_{TO}$, CdTe and $2 \times \omega_{LO}$, CdTe, respectively. On the other end of the composition range, i.e., for $y \geq 0.95$, the multiphonon at approximately $410\ cm^{-1}$ corresponds to $2 \times \omega_{LO}$, CdSe, while the multiphonon at $350\ cm^{-1}$ may represent either the sum of TO and LO phonons of CdSe or a double surface phonon. Due to the broadening of this phonon line, it is possible that both processes contribute.

4.2. Surface optical phonons

Surface optical (SO) phonons share conceptual similarities with bulk phonons, but their atomic amplitudes are confined to the near – surface

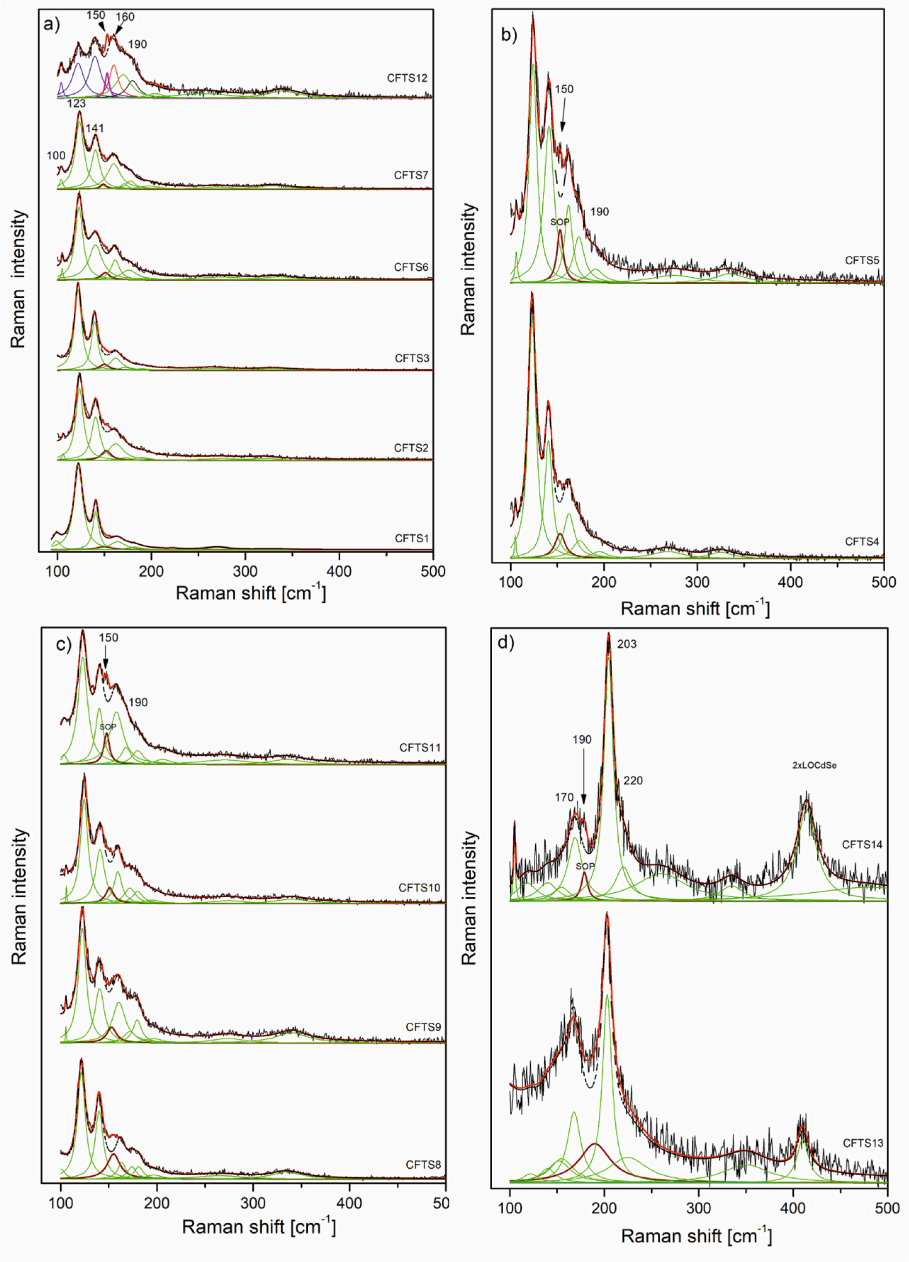

Fig. 4. a) The nonpolarized Raman spectra of $Cd_{1-x}Fe_xTe_{1-y}Se_y$ in the spectral range from 90 to 500 cm^{-1} at room temperature (representative samples) b) Raman spectra of composition with y = 0.03 but varying two concentrations of added Fe c) Raman spectra of $Cd_{1-x}Fe_xTe_{1-y}Se_y$ for higher Se concentration, exceeding 10 % d) Depicted Raman spectra from the CdSe side.

region of the material. The amplitudes of these phonons decay exponentially as one moves away from the sample surface. Two main types of SO phonon modes are generally recognized based on penetration depths: macroscopic and microscopic. Macroscopic SO modes include optical and acoustic SO phonon frequencies [36]. Acoustic SO modes in isotropic elastic media propagate along the surface or interface, with displacements in the sagittal plane defined by the normal to the surface and the direction of propagation [37]. These modes exhibit exponential decay into the bulk, with the penetration depth proportional to the wavelength in the long – wave limit. In contrast to an acoustic mode, the Fuchs-Kliewer phonon is associated with a macroscopic electric field [36]. The frequency of a Fuchs-Kliewer phonon can be determined by solving the Laplace equation for the electrostatic potential of an ionic crystal under appropriate electromagnetic boundary conditions. The frequency is then found to lie between the frequencies of the transverse optical (TO) and longitudinal optical (LO) bulk phonons.

The dispersion of surface optical modes at the interface between a semiconductor and a dielectric material can be calculated, taking into account the geometrical constraint and the dielectric properties of the surrounding medium. This is done by imposing the condition:

$$\varepsilon(\omega) + \varepsilon_m = 0 \tag{6}$$

Here, $\varepsilon(\omega)$ is the dielectric function of the semiconductor, and ε_m is the dielectric constant of the medium. The frequency of the surface optical (SO) phonon for an infinite semiconductor flat surface [35] is given by:

$$\varepsilon_{SOP} = \omega_{TO}\sqrt{\frac{\varepsilon_0 + \varepsilon_m}{\varepsilon_\infty + \varepsilon_m}} \tag{7}$$

where ε_0 and ε_∞ are the static and high – frequency dielectric constants,

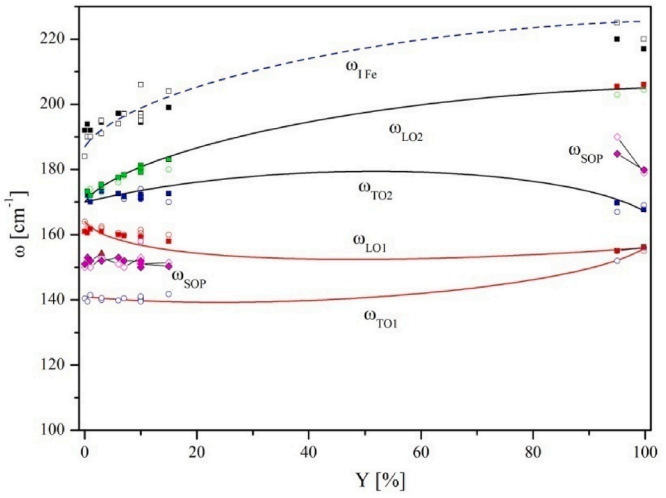

Fig. 5. Phonon mode behavior for the ternary compounds $CdTe_{1-y}Se_y$, based on the Genzel model. LO phonon of CdTe, TO/LO pairs of CdSe, and the impurity phonon Fe, are shown on all spectra with dashed lines. The solid line is obtained when a surface phonon is added to the analysis, indicated by the dark red line. The experimental values for the TO and LO modes obtained from IR measurements are marked with open symbols, while the results from Raman measurements are represented by solid symbols.

Table 2
Multiphonon processes obtained by fitting Raman spectra shown in Fig. 4.

Sample	$2x\omega_{TOCdTe}$	$2x\omega_{LOCdTe}$	$2x\omega_{TOCdSe}$	$2x\omega_{LOCdTe}$
CFTS1	270	330	–	–
CFTS2	275	320	–	–
CFTS3	265,5	350	–	–
CFTS4	268	325	–	–
CFTS5	275	335	–	–
CFTS6	275	335	–	–
CFTS7	270	330	–	–
CFTS8	265	335	–	–
CFTS9	274	340	–	–
CFTS10	275	340	–	–
CFTS11	270	335	–	–
CFTS12	255	340	–	–
CFTS13	–	–	350	410
CFTS14	–	–	335	414

respectively. ω_{TO} is the transverse optical (TO) mode frequency at zone center, and ε_m is the dielectric constant of the medium ($\varepsilon_m = 1$ in our case). The values for ω_{TO} and ε_∞ are obtained from our experiment, while the value for ε_0 is taken from the literature [38–41].

Thus, for the surface optical phonon (SOP) of CdTe, a value of 153 cm^{-1} is obtained, while on the CdSe side, it is 185 cm^{-1}. These values closely match the experimentally presented results in Fig. 5.

What sets this material apart from similar ones is the fact that the surface optical phonon is registered in a region where the concentration of free carriers is very low. An open question remains regarding whether the penetration depth of SOP is equal to the size of the region with low carrier concentration.

5. Conclusion

In this paper, our investigation into $Cd_{1-x}Fe_xTe_{1-y}Se_y$ single crystals through Far – infrared and Raman spectroscopy has provided valuable insights into the Plasmon – phonon interaction and surface optical modes. Far – infrared reflection spectra revealed distinct phonon features associated with CdTe, CdSe and Fe impurities. The fitting procedure, employing a modified factored dielectric function model, successfully described the spectra, highlighting the importance of a surface layer with low carrier concentration. The dielectric function with Plasmon – two - phonon interaction (p = 3) accurately captured the coupled modes, providing TO frequencies and coupled Plasmon – LO modes. The Raman spectra, spanning from 90 to 500 cm^{-1}, showcased TeO_2 – related phonons and multi – phonon bands, and the deconvolution process revealed a surface phonon at around 150 cm^{-1}. Our comprehensive analysis considered a two – mode behavior for phonons, aligning with the Genzel model, which proved effective in describing the experimental results. The local Fe mode, arising due to impurities, exhibited significant contributions from electron – phonon interaction and isotope effect. Additionally, the study of surface optical phonons elucidated frequencies of 153 cm^{-1} for CdTe and 185 cm^{-1} for CdSe, contributing a unique aspect to the material. The open question regarding the penetration depth of SOP in the region with low carrier concentration remains intriguing and warrants further exploration. Overall, our findings enhance the understanding of the intricate phonon properties in $Cd_{1-x}Fe_xTe_{1-y}Se_y$, setting the stage for future advancements in the exploration of similar semiconductor materials.

CRediT authorship contribution statement

Jelena Mitric: Writing – original draft, Software, Investigation, Conceptualization. **Maja Romcevic:** Supervision, Conceptualization. **Witold D. Dobrowolski:** Supervision, Resources. **Andrzej Mycielski:** Resources. **Nebojsa Romcevic:** Supervision, Conceptualization.

Funding

This research was supported by the Science Fund of the Republic of Serbia, Grant No. 7504386, Nano object in own matrix – Self composite – NOOM-SeC.

Declaration of competing interest

The authors declare that they have no known competing financial interests or personal relationships that could have appeared to influence the work reported in this paper.

Data availability

No data was used for the research described in the article.

References

[1] A. Mycielski, J. Appl. Phys. 63 (1988) 3279.
[2] A. Fazio, M.J. Caldas, A. Zunger, Phys. Rev. B 30 (1984) 3430.
[3] J.D. Dow, W.E. Packard, H.A. Blackstead, D.W. Jenkins, Chapter 5: phonons in semiconductor alloys, in: Dynamical Properties of Solids, Elsevier, 1995, pp. 349–424, https://doi.org/10.1016/S1874-5628(06)80007-0, vol. 7.
[4] Y.S. Chen, W. Shockley, G.L. Pearson, Phys. Rev. 151 (1966) 648.
[5] M. Rocca, T.S. Rahman, in: L. Vattuone (Ed.), Springer Handbook of Surface Science, Springer Nature Switzerland AG, 2020, https://doi.org/10.1007/978-3-030-46906-1.
[6] F. Giustino, Electron-phonon interactions from first principles, Rev. Mod. Phys. 89 (2017) 015003.
[7] B. Liao, B. Qiu, J. Zhou, S. Huberman, K. Esfarjani, G. Chen, Phys. Rev. Lett. 114 (2015) 115901, https://doi.org/10.1103/PhysRevLett.114.115901.
[8] M. Cardona, Electron–phonon interaction in tetrahedral semiconductors, Solid State Commun. 133 (2005) 3–18, https://doi.org/10.1016/j.ssc.2004.10.028.
[9] Y. Yamada, Y. Kanemitsu, Electron-phonon interactions in halide perovskites, NPG Asia Mater. 14 (2022) 48, https://doi.org/10.1038/s41427-022-00394-4.
[10] J. Zhou, et al., Nat. Commun. 11 (2020) 6040, https://doi.org/10.1038/s41467-020-19938-9.
[11] Y. Quan, S. Yue, B. Liao, Nanoscale microscale thermophys, Engineering 25 (2021) 73–90, https://doi.org/10.1080/15567265.2021.1902441.
[12] N. Romcevic, et al., J. Alloys Compd. 397 (2005) 52–57, https://doi.org/10.1016/j.jallcom.2005.01.041.
[13] M. Romčević, et al., Infrared Phys. Technol. 46 (2005) 379–387, https://doi.org/10.1016/j.infrared.2004.06.007.
[14] J. Mitric, et al., Physica E 104 (2018) 64–70, https://doi.org/10.1016/j.physe.2018.07.021.
[15] A.A. Kukharskii, Solid State Commun. 13 (1973) 1761.

[16] S. Perkowitz, R.H. Thorland, Phys. Rev. B 9 (1974) 545.
[17] P. Swiatek, A.M. Witowski, M. Grynberg, Phys. Status Solidi B 89 (1978) K1.
[18] M. Cardona, G. Gunterodt (Eds.), Light Scattering in Solids IV, vol. 54, Springer, Berlin, 1984, p. 63.
[19] M. Picquart, et al., Phys. Status Solidi B 99 (1980) 683.
[20] A.S. Pine, G. Dresselhaus, Phys. Rev. B 4 (22) (1971) 356, https://doi.org/10.1103/PhysRevB.4.356.
[21] V. Gopal, Infrared Phys. 18 (20) (1978) 121–125.
[22] J.H. Cape, et al., Surf. Sci. 62 (1979) 639–646, https://doi.org/10.1016/0039-6028(77)90106-6(21.
[23] M. Baleva, M. Momtchilova, Phys. Rev. B 50 (1994) 15056, https://doi.org/10.1103/PhysRevB.50.15056.
[24] J. Pandey, et al., Appl. Energy Mater 3 (2020) 2175–2182.
[25] J. Tang, A.C. Albrecht, in: H. Szmanski (Ed.), Raman Spectroscopy, Plenum Press, New York, 1970.
[26] M. Romcevic, N. Romcevic, J. Alloys Compd. 416 (2006) 64–71, https://doi.org/10.1016/j.jallcom.2005.09.002.
[27] B.H. Henry, in: J.R. During (Ed.), Raman Spectroscopy: Six Years on, vol. 10, Elsevier, Amsterdam, 1990.
[28] L. Genzel, et al., Phys. Status Solidi B 62 (1974) 83–92.
[29] M. Petrovic, et al., Infrared Phys. Technol. 67 (2014) 323–326, https://doi.org/10.1016/j.infrared.2014.08.010.
[30] N. Romcevic, et al., Phys. Status Solidi C 1 (2004) 977–980.
[31] S. Perkowitz, et al., Phys. Rev. B 9 (1974) 545–550.
[32] A.J. Sievers, in: K.D. Moller, W.B. Rothschild (Eds.), Far Infrared Spectroscopy, Wiley, New York, 1971, p. 525, https://doi.org/10.1016/0022-2860(73)85199-3.
[33] A.A. Gogolin, E.I. Rashba, Solid State Commun. 19 (1976) 1177–1179, https://doi.org/10.1016/0038-1098(76)90813-9.
[34] N. Romcevic, et al., J. Alloys Compd. 442 (2007) 324–327, https://doi.org/10.1016/j.jallcom.2006.09.164.
[35] J. Mitric, et al., J. Raman Spectrosc. 50 (2019) 802–808, https://doi.org/10.1002/jrs.5584.
[36] R. Fuchs, K.L. Kliewer, Phys. Rev. 140 (1965) A2076.
[37] R.F. Wallis, Surf. Sci. 299/300 (1994) 612.
[38] P. Sahoo, et al., in: A. Hashim (Ed.), Nanowires, IntechOpen, 2011, https://doi.org/10.5772/16779.
[39] T.G. Edossa, M.M. Woldemariam, Phys. Chem. Solid State 22 (2021) 16–23, https://doi.org/10.15330/pcss.22.1.16-23.
[40] S. Suresh, C. Arunseshan, Appl. Nanosci. 4 (2014) 179–184, https://doi.org/10.1007/s13204-012-0186-5.
[41] H. Abu-Farsakh, et al., ACS Omega 8 (2023) 14742–14751, https://doi.org/10.1021/acsomega.3c00757.

Physica E 134 (2021) 114923

Contents lists available at ScienceDirect

Physica E: Low-dimensional Systems and Nanostructures

journal homepage: www.elsevier.com/locate/physe

Surface optical phonon and multi – phonon transitions in YVO_4: Eu^{3+} nanopowders

J. Mitrić [a,*], N. Paunović [a], M. Mitrić [c], J. Ćirković [b], M. Gilić [a], M. Romčević [a], N. Romčević [a]

[a] Institute of Physics, University of Belgrade, Pregrevica 118, 11080, Belgrade, Serbia
[b] Institute for Multidisciplinary Research, University of Belgrade, Kneza Višeslava 1a, 11030, Belgrade, Serbia
[c] Institute Vinča, University of Belgrade, P.O. Box 522, 11001, Belgrade, Serbia

ARTICLE INFO

Keywords:
Surface optical phonon
Multi
Phonon
Yttrium orthovanadate
Europium
Infrared spectroscopy
uv
Vis spectroscopy

ABSTRACT

In this paper two methods of preparation of yttrium orthovanadate nanopowders were presented: Solid State Reaction (top – down approach) and Solution Combustion Synthesis (bottom – up approach). For starting structural characterization, X – Ray Powder Diffraction (XPRD) and Field Emission Scanning Electron Microscopy (FESEM) were used. We report the change in reflection spectra in europium doped YVO_4 nanopowders with comparison to its bulk analog. In UV–Vis reflection spectra we consider the change in values of band gap in these structures, after resizing it from bulk to nanomaterial. In Far – Infrared (FIR) reflection spectra, we registered the existence of Surface Optical Phonon (SOP) and different multi – phonon processes which alter the reflection spectra of bulk YVO_4. The influence of Eu ions is reflected through multi – phonon processes that occur and are connected with energy transfer from YVO_4 lattice to Eu ions. All IR spectra were modeled using classical oscillator model with Drude part added which takes into account the free carrier contribution. Since our samples are distinctively inhomogeneous materials, we use Effective Medium theory in Maxwell Garnett approximation to model its effective dieletric function.

1. Introduction

Semiconducting nanomaterials, especially nanophosphors have attracted great attention of researchers, due to their wide spectrum of applications in industry, technology as well as in fundamental science. When made in nanorange, phosphor materials exibit enhanced optical properties as against their bulk counterparts, due to quantum size effects and increased surface – to – volume ratio. Yttrium orthovanadate is a widely used red phosphor with many applications in just recent years – in solar cells [1], cancer treatment [2], biotechnology [3], optical imaging [4] etc.

For nanopowders, a valuable tool in the investigation of the structural and optical changes in a material made due to resizing the bulk crystal on nanoscale is the optical spectroscopy – in this case specifically far – infrared and UV – VIS spectroscopy. When excited by UV light, photoluminescence quantum yield of the europium emission in yttrium orthovanadate crystal, goes up to 70% [5]. In YVO_4:Eu^{3+} structure UV radiation excites the vanadate group, which has the ability of efficient excitation transfer to the europium ions (Fig. 1).

When irradiated with UV radiation, three major steps occur in the excitation and emission process in YVO_4:Eu^{3+} structure. First step is the absorption of UV light by $(VO_4)^{3-}$ groups. Then, thermal activated energy, which comes from the UV excitation source, migrates through the vanadate sub – lattice, inducing the transfer of excited energy to europium ions. In the end, strong red ($^5D_0$ – $^7F_2$) and orange ($^5D_0$ – $^7F_1$) emission due to de – excitation process of excited europium ions occur [6].

One of the important properties of semiconductors is their band gap. Studying the band gap of semiconductors is important for interpreting their structural and optical properties and it is of a great importance examining its expansion in order to understand their properties. Application of semiconductors is in large level determined by their band gap width. Bulk semiconductors are usually very limited in their application due to their small and indirect band gap. Bulk crystal is set up of a large number of atoms and molecules, with a number of adjacent energy levels, which form bulk electronic bands. With the reduction of particle size to a nano level, where every particle is made up out of a small number of atoms or molecules, the number of overlapping orbitals decreases, and the eventually width of the band gap of a nanomaterial gets narrower when compared to bulk crystal (this means that there will be

* Corresponding author.
E-mail address: jmitric@ipb.ac.rs (J. Mitrić).

https://doi.org/10.1016/j.physe.2021.114923
Received 7 May 2021; Received in revised form 3 August 2021; Accepted 4 August 2021
Available online 14 August 2021

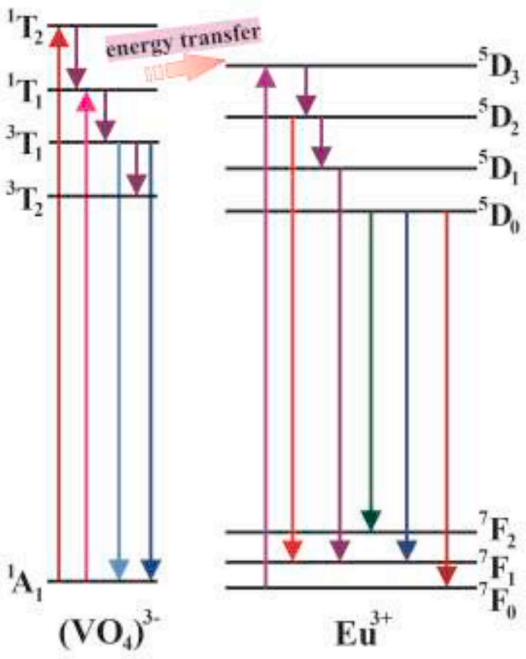

Fig. 1. Energy levels and energy transfer model of Eu^{3+} ion and $(VO_4)^{3-}$ tetrahedron in YVO4.

an increase of energy between valence and conduction band). This is the reason why nanomaterials have wider band gap compared to their bulk counterparts. The larger the band gap (i.e. forbidden region), the greater the restriction of the electron movement will be. This is well known as the *quantum size effect*. As a consequence of size reduction, there is a shift of absorption spectrum of nanomaterials towards the lower wavelengths, known as a *blue shift*.

In bulk crystals, bulk longitudinal (ω_{LO}) and transversal (ω_{TO}) optical phonon frequency occur. In crystals with relatively small dimensions, a new frequency appears – Surface Optical Phonon (SOP) frequency (ω_{SOP}) which is located between the ω_{LO} and ω_{TO} frequency. That means that due to effects of dimension, in addition to the modes of infinity lattice, surface modes will be manifested. And in the case of crystals with extremely low dimensions, only the surface mode perseveres.

Different types of interactions with electromagnetic radiation takes an important place in semiconductors. On one side, we have investigated electron – phonon interaction in ceramic nanopowders [7]; surface optical phonon – plasmon in thin films [8]. Besides that, we have studied damping influence on interaction appearance [9], plasmon – impurity local phonons [10], as well as plasmon – different phonons interactions [11].

A special attention should be given to the choice of method for nanopowder preparation, because nanostructured samples with good crystallization and homogenous particle size exhibit extraordinary properties different from their bulk analogs. At the same time, a very important thing for their application in industry and technology is finding a fast, cheap and reproducible technique for obtaining fine nanophosphors.

In this paper two types of methods were presented. One, the top – down approach, *Solid State Reaction Method* (SSR), (which implies extensive milling), which is a classical ceramic method and the other, bottom – up approach, *Solution Combustion Synthesis* (SCS). Top down approaches have advantages like large scale production and deposition over a large substrate; also, with these techniques, chemical purifications are not required. Disadvantages of top – down methods are varied particles shapes or geometry, different impurities (stresses, defects and imperfections); also, one must be very careful not to have broad size distribution of particles. Bottom – up approaches, on the other hand, offer ultra – fine nanoparticles, with controlled deposition and narrow size distribution. Unlike the previous techniques, bottom – up approaches do not offer large scale production so easily, and require chemical purification. Therefore, we have chosen one technique from both approaches so they can be compared. In this paper we offer two simple, fast, cheap and yet reproducible techniques for yttrium orthovanadate nanopowder preparation.

1.1. Bulk crystal of YVO_4

Yttrium orthovanadate crystal has a zircon – type of structure, and crystalizes in 141. Space group, $I4_1/amd$ shown in Fig. 2. In this structural type, Y ions occupy ***4a*** crystallographic (Wyckoff) site with coordinates $[[0, 3/4, 1/8]]$.

V ions occupy ***4b*** crystallographic site, and coordinates $[[0, 1/4, 3/8]]$; while O ions occupy ***16h*** crystallographic site, with coordinates $[[0, y, z]]$.

This structure belongs to 4/mmm Laue class, where fourfold axis is a unique symmetry operation and has an expressed anisotropy of physical properties. V ions are in tetrahedral surrounding of O ions, while the surrounding of Y ions is made of oxygen coordination sphere with eight O ions which form a highly distorted cube.

From a group – theory analysis [12] it is known for this type of symmetry with two chemical formulas in the primitive cell ($I4_1/amd$ – D_{4h}^{19}) to have following modes in the center of the Brillouin zone at the Γ point: $\Gamma(k = 0) = 2A_{1g} + 5E_g + 4B_{1g} + 1B_{2g} + 4A_{2u} + 5E_u + 1A_{2g} + 1A_{1u} + 1B_{1u} + 2B_{2u}$. E_u and A_{2u} modes show dipole moments oriented perpendicular and along the c directions, respectively; and four out of five E_u modes are infrared active.

Infrared reflection spectrum of bulk YVO_4 can be found in the literature [13]. In the measured reflectivity spectra, two sharp features at the lowest frequency can be found, and they correspond to the unscreened infrared – active optical phonon modes. This spectrum is characterized with four peaks of which three are easily seen, while the fourth is a shoulder of the second reflectivity band, and it is more evident at lower temperatures. Since bulk YVO_4 has no metallic contribution (i.e. free carrier contribution), the Lyddane – Sachs Teller (LST) relation (Lorenz oscillator model) can be an optimal model to analyze reflection spectra and to model an appropriate dieletric function of a material.

In this paper we report the change in reflection spectra of europium

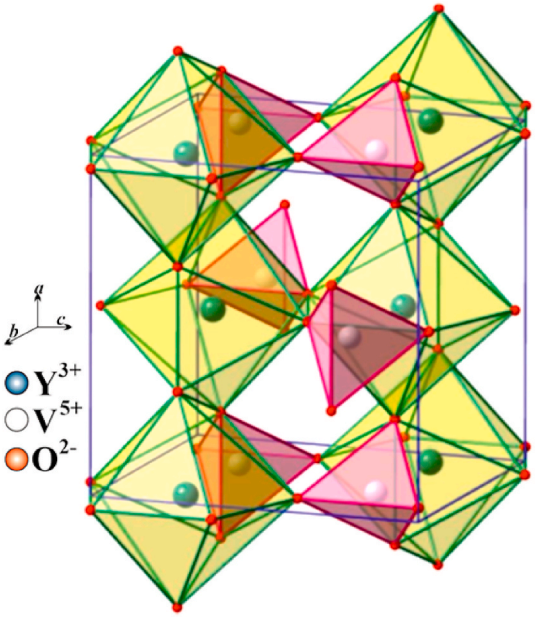

Fig. 2. Crystal structure of YVO4.

doped YVO_4 nanpowders with comparison to its bulk analog. In UV – VIS reflection spectra we consider the change in values of a band gap of europium doped YVO_4 when it is resized from bulk to nanomaterial. In IR reflection spectra we carry out phonon investigation in order to explain the change in optical properties of investigated nanopowders. We show the existence of surface optical phonon (SOP) and different phonon processes which alter the reflection spectra of bulk YVO_4. Full characterization of materials is made with X – Ray Powder Diffraction (XRPD) and Field Emission Scanning Electron Microscopy (FESEM).

2. Sample preparation and characterization methods

Nanopowders prepared by SCS were obtained using stoichiometric quantities of starting chemicals $Y(NO_3)_3{\cdot}6H_2O, NH_4VO_3, NH_4NO_3$ and $Y(NO_3)_3{\cdot}6H_2O$, purchased from ABCR with the purity of 99.99%. Urea was purchased from Sigma – Aldrich. Eu^{3+} concentration was 1%. 4.8 g of NH_4NO_3 and 3.003 g of urea, $(NH_2)_2CO$ which were used as an organic fuels were added to a dry mixture of 0.357 g $Eu(NO_3)_3{\cdot}\ 6H_2O$, 4,676 g of NH_4VO_3 and 15.32 g of $Y(NO_3)_3{\cdot}6H_2O$. Then, mixture was combusted with the flame burner at $\sim 500°C$. Then, the solid solution starts to act like cloud – shape mixture which then was annealed in air atmosphere at $1200°C$ for 2 h. The annealing of material offers full crystallinity. This sample was labeled as **YVS**.

Solid state reaction procedure was performed using stoichiometric quantities of starting chemicals, then powdered and baked on $900°C$ for 5 h. Starting chemicals, Y_2O_5, Y_2O_3 and Eu_2O_3 with purity of 99.99% were purchased from ABCR. Concentration of Eu ions was 1%. This sample was labeled as **YVC**. Both samples, YVS and YVC, were made in a series of 5 samples, and every measurement is an average of these 5 samples.

These two simple, but yet reproducible and efficient methods provide two morphologically different samples. In this way methods can be compared and analyzed.

Structural characteristics of yttrium orthovanadate nanopowders were obtained using Philips PW 1050 diffractometer equipped with a PW 1703 generator, 40 kV × 20 mA, using Ni filtered Co Kα radiation of 0.1778897 nm, at room temperature. 15–85° range was used during 2 h, with a scanning step of 0.05° and 10s scanning time per step.

Morphologies of prepared samples were examined by Field Emission Scanning Electron Microscopy using FEI Scios 2 with an acceleration voltage between cathode and anode 15 kV.

All UV–Vis reflectance spectra were recorded in the wavelength range of 200–1200 nm on the Shimadzu UV – 2600 spectrophotometer equipped with an integrated sphere. The reflectance spectra were measured relative to a reference sample of $BaSO_4$.

The infrared reflectivity measurements were performed at room temperature. BOMEM DA – 8 Fourier – transform infrared spectrometer was used. A Hyper beamsplitter and DTGS (deuterated triglycine sulfate) pyroelectric detector were used to cover the wave number region 80–650 cm^{-1}. Spectra were collected with 2 cm^{-1} resolution with 500 interferometer scans added for each spectrum.

2.1. X – ray powder diffraction

Results for YVC and YVS are shown in Fig. 3. The diffractograms confirm that both samples are monophased and that they crystallized in zircon – type of structure. All reflections are in good agreement with JCPDS card 17–0341. Also, all samples show no other reflections other than ones who originate from YVO_4 structure. Since Eu^{3+} concentration in these samples is 2%, one cannot be identified by XRD. Crystallite sizes are 53 nm and 58 nm for YVC and YVS, respectively. Crystallite sizes were determined using Debye Scherrer formula. This formula gives value of average crystallite size, and from our calculations the deviation is around 5 nm. To reduce this error, series of every sample were made (5 from each) to reduce the influence of chemical modification and other processing conditions). Even though Debye Scherrer is a rough method for determining crystallite size and one could use other methods for determining this value, like Williamson – Hall analysis which could in some way reduce this problem, this would suggest to rely on some other assumptions which could add up to an error. Crystallite size for sample YVC is smaller than one obtained in YVC. This was expected because of method of preparation. YVC was prepared using Solid State Reaction Method, which includes rather aggressive milling, and therefore results in smaller crystallite size than sample YVC, which was obtained with Solution Combustion Synthesis.

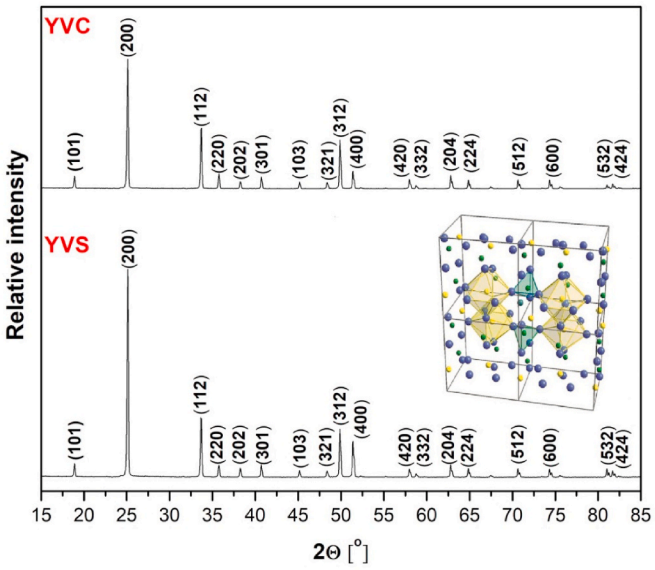

Fig. 3. XRD patterns of europium doped yttrium – orthovanadate nanopowder prepared by Solid State Reaction Method (YVC) and Solution Combustion Synthesis (YVS).

2.2. Field emission scanning electron microscopy

FESEM photographs are shown in Figs. 4 and 5, for YVS and YVC respectively; with 10 000 × and 35 000× magnification. Particle sizes are 2 m and 3 μm, for YVC and YVS, respectively. These values are much larger than the ones obtained with XRD. Reason for this is crystallite agglomeration. Regardless of agglomeration, trend in crystallite size between two methods of preparation remains the same as in crystallite sizes determined by XRD. One more thing must be noticed, and that is difference in crystallinity between samples. As can be seen from Figs. 4 and 5, sample YVC is more crystalline than YVS, which has more of a cloud – shape structure. This was marked with yellow rectangles in Figs. 4 and 5. On a larger scale, both samples consist of clearly defined and separated grains which can be seen on right hand side of Figs. 4 and 5.

3. Results and discussion

3.1. UV – VIS spectroscopy

In this section we investigated optical UV–Vis reflection spectra of europium – doped yttrium orthovanadate nanopowders. Special attention was given to obtaining band gap values. Band gap values were obtained using Tauc plot [14]. It is important to have information about band gap values, because band structure is responsible for the wide range of electrical characteristics. Tauc, Davis and Mott [15] have proposed an expression:

$$\alpha h\nu = A\left(h\nu - E_g\right)^{1/n} \quad (1)$$

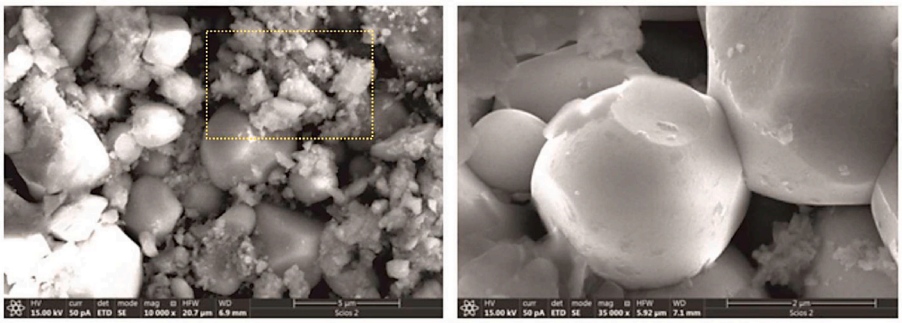

Fig. 4. FESEM photographs of europium doped yttrium – orthovanadate nanopowder prepared by Solid State Reaction Method (YVS).

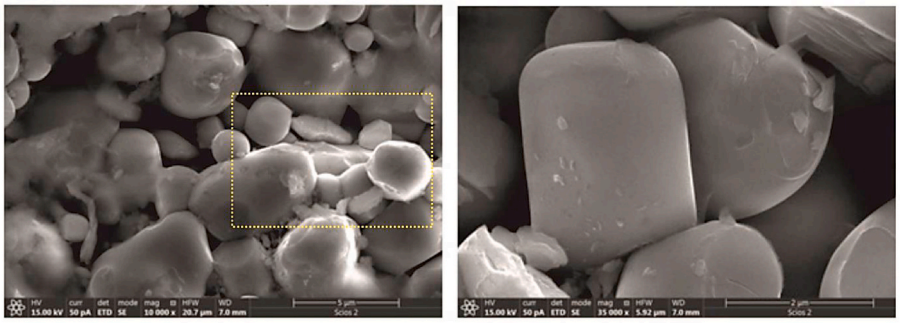

Fig. 5. (a) FESEM photographs of europium doped yttrium – orthovanadate nanopowder prepared by Solid State Reaction Method (YVC).

where α is the absorption coefficient (which is a property of a material; it defines the amount of light absorbed by it); h is the Planck's constant and $h\nu$ is the photon energy. A represents transition probability constant (which depends on the effective mass of the charge carriers in the material) and E_g is the band gap. Number n defines the nature of transition. If transition is direct, n equals 1/2 and 3/2, for the allowed and forbidden transitions, respectively. In the case of indirect transitions, n is 2 for allowed and 3 for forbidden transitions. In our case n is 3/2.

Then, the obtained diffuse reflectance spectra are converted to Kubelka – Munk function [16]:

$$\alpha = \frac{(1-R)^2}{2R} \tag{2}$$

where R is a reflectance value. Using Eqs. (1) and (2), we obtain $(\alpha h\nu)^{1/n}$ vs. $h\nu$ plot. By extrapolating the linear portion of mentioned dependence to the energy axes at the $(\alpha h\nu)^{1/n} = 0$ value, the band gap value is obtrained – the intercept of the plot with x – axe gives the value of band gap. The results obtained with UV – VIS spectroscopy, UV – VIS reflectance and diffuse reflectance Kubelka – Munk spectra for YVS and YVC are presented in Figs. 6 and 7 respectively.

From Table 1 values of calculated band gap for europium doped yttrium orthovanadate nanopowders prepared by two methods, as well as literature data for bulk YVO_4 were presented. With regard to section 2 where it was explained how band gap values increases with decreasing grain size, we got matching results. Namely, we got two values of band gap for samples made with two methods, YVC and YVS: 3, 55 eV and 3,17 eV, respectively. Since crystallite size of YVC (53 nm) is smaller than in YVS (58 nm), it is expected that the band gap value will be greater for YVC, due to quantum size effect described earlier. Both E_g values for nanophosphors are greater that the E_g value for bulk crystal YVO_4, which is expected. With this we conclude that Solid State Reaction Method provides samples with higher band gap values that samples prepared by Solution Combustion Synthesis.

When under the UV–Vis radiation, three major steps occur in YVO_4: Eu^{3+}: 1. absorbance of radiation by $(VO_4)^{3-}$ groups; 2. transfer of the excited energy to Eu^{3+} ions which migrated through vanadate sublattice; and 3. red emission induced by de – excitation process of excited Eu^{3+} ions. This was represented in Fig. 1.

Peak at around 272 nm originates from absorption of $(VO_4)^{3-}$ groups [17]. According to the literature, this peak is an attribution to charge transfer from oxygen ligands to the central vanadium atom in $(VO_4)^{3-}$ group. In that way, UV–Vis spectra from Figs. 6a and 7a prove there is an energy transfer between $(VO_4)^{3-}$ and Eu^{3+} ions. Peak at 343 nm originates from $(VO_4)^{3-}$ in the lattice [18]. Peak at 272 in YVS is clearly seen. On the other hand, in YVC sample, splitting of 272 mode is obvious. The mode split because reflectance values cannot go below zero values; and increase in intensity of reflectance compared to YVS is caused by multi – phonon processes which seem to be more dominant in YVC rather than in YVS.

In one of our previous papers [19] it is shown how Eu ions exchange with of Y ions, and without any significant disturbance of symmetry take place in YVO_4 structure. Clearly, Eu ions have more influence in YVC sample, which has more crystallinity and smaller crystallite size, and are more efficiently distributed throughout the YVC sample. More evidence on multi – phonon processes which are present in YVC will be shown more clearly using Infrared Spectroscopy.

Results like this also confirm that these materials are suitable for many optical devices. Following our previous research [20] these phosphors represent an excellent hosts for optical excitation and emission of europium. Also, since the samples were made using two different techniques on different temperatures (500 and 900 °C), a certain evidence of thermal stability on emission quantum yield and lifetime was shown which is in good agreement with the literature [21].

3.2. Infrared spectroscopy

Subject of this paper are distinctively inhomogeneous materials. They are built out of embedded components in a matrix, and every one of them has its own macroscopic properties. A macroscopic property can

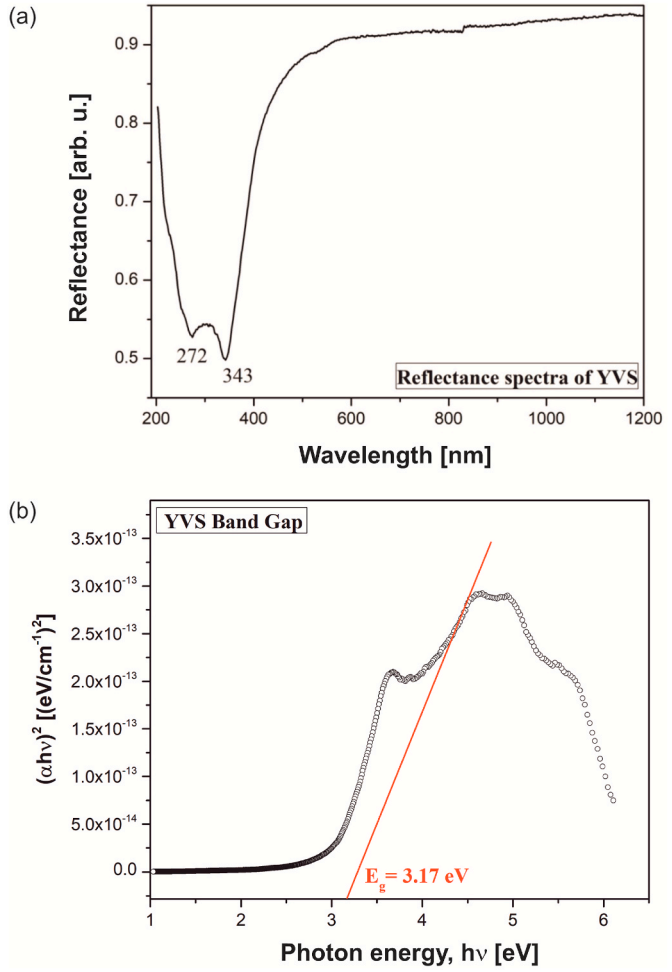

Fig. 6. (a) UV – VIS reflectance spectra of europium doped yttrium – orthovanadate nanopowder prepared by Solid State Reaction (YVC). (b) Kubelka – Munk plot for europium – doped yttrium – orthovanadate nanopowder prepared by Solid State Reaction (YVS).

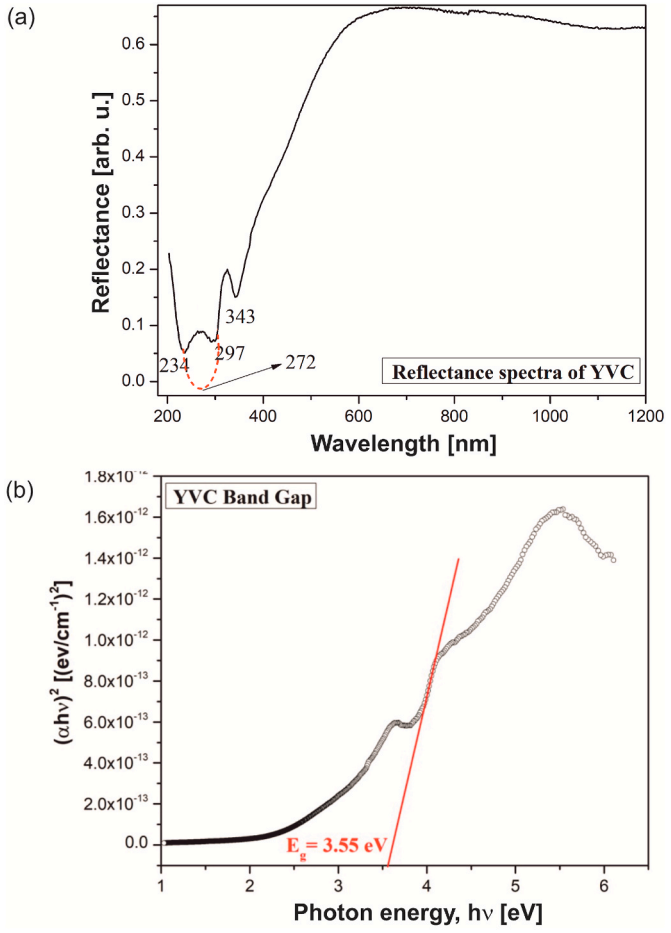

Fig. 7. (a) UV – VIS reflectance spectra of europium doped yttrium – orthovanadate nanopowder prepared by Solution Combustion Synthesis (YVC). (b) Kubelka – Munk plot for europium – doped yttrium – orthovanadate nanopowder prepared by Solution Combustion Synthesis.

be attributed to every component of this material, as well as to a matrix. For example, this can be a dielectric permittivity. A medium where dielectric permittivity of every component and its surrounding (matrix) can be substituted with one value of dielectric permittivity, *an effective dielectric permittivity*, is called an effective medium, and theory which describes this is known as Effective Medium Theory. In other words, within this model, a heterogeneous system can be seen, from a bigger scale, as a homogeneous system, with its own properties which are often called effective properties, with one important fact: on a scale comparable with the dimensions of the system constituents, the system cannot be regarded as a homogeneous medium. Theory of effective medium has several approximations [22], of which two are most common: Maxwell Garnet and Brugemann approximation. The first one implies that constitutive parts of one medium are very well separated out of matrix they've been embedded in, and that there is no electrostatic interactions between them. On the other hand, Brugemann approximation describes systems where constitutive parts cannot be separated out of their surroundings.

When visible light, λ, interacts with a material described above, where its nanoparticles have characteristic size d, and dielectric function ε_2, which are randomly distributed in a matrix with a dielectric constant ε_1, in the limit $\lambda \gg d$, the heterogeneous composite can be treated as a homogenous, and this system can be described with Effective Medium Theory. Since the samples we investigate are well defined, spherical and separated nano grains (as seen in Figs. 4 and 5), we use Maxwell Garnet

Table 1
Band gap values for YVC, YVS and literature data for bulk YVO_4 bulk crystal.

YVC	YVS	YVO_4 bulk (literature) [22]
3.56 eV	3.16 eV	2.85 eV

model for the present case. Following postulates of this approximation, for the effective permittivity of so called homogeneous medium we get [23]:

$$\varepsilon_{eff} = \varepsilon_1 + 3f_1\frac{\varepsilon_1(\varepsilon_2 - \varepsilon_1)}{\varepsilon_2 + 2\varepsilon_1} \tag{3}$$

where ε_2 is a dielectric permittivity of nanoparticles located randomly in a homogeneous environment with dielectric permittivity ε_1, which is, in our case, air; and occupy a volume fraction f (so called filling factor).

For modeling dielectric permittivity of above described nanoparticles, we have used a classical oscillator model with Drude part added (second addition in Eq. (3)) which takes into account the free carrier contribution [24].:

$$\varepsilon_2(\omega) = \varepsilon_\infty\left(\prod_{k=1}^{n}\frac{\omega_{LO}^2 - \omega^2 + i\gamma_{LO}\omega}{\omega_{TO}^2 - \omega^2 + i\gamma_{TO}\omega} - \frac{\omega_P^2}{\omega(\omega - i\tau^{-1})}\right) \tag{4}$$

where ε_∞ is a bound charge contribution (assumed to be constant), transverse and longitudinal frequencies are noted with ω_{TO} and ω_{LO}, γ_{TO} and γ_{LO} are their damping coefficients, ω_P is plasma frequency and free

carrier relaxation time is marked by τ.

Calculated spectra were obtained by a fitting procedure using a previously described model which is represented with solid lines in Figs. 8 and 9. Using the least – square fitting procedure of the experimental (R_{exp}) and theoretical (R_{th}) reflectivity, at q arbitrarily taken points, the parameter adjustment was carried out, automatically.

$$\delta = \sqrt{\frac{1}{q}\sum_{j=1}^{q}\left(R_{exp} - R_{th}\right)^2} \tag{5}$$

Minimalization of δ was carried out until it met the conditions of commonly accepted experimental error of less than 3%.

Theoretical model in Figs. 8c and 9, show excellent match with the experimental results, for YVS and YVC samples, respectively. In Table 2, best fitting parameters are presented. In Eq. (4), transversal optical frequency, ω_{TO}, was precieved as the characteristic frequency for a given material. As regards to spectra from Fig. 8a and 8b, they show the procedure, step by step, in order to get the best fit presented in Fig. 8c. Model used in Fig. 8a did not take into account the existence of SOP. Actually, this model suits the bulk structure of YVO_4 the best, when there's no SOP [25]. After we took this into account, we notice that, when bulk YVO_4 was resized to nanoscale, wide mode on the highest frequencies in bulk spectrum of YVO_4 [13] split into two modes. Since this was modeled with dielectric function which takes into account the existence of SOP, we conclude that the reason for splitting this wide

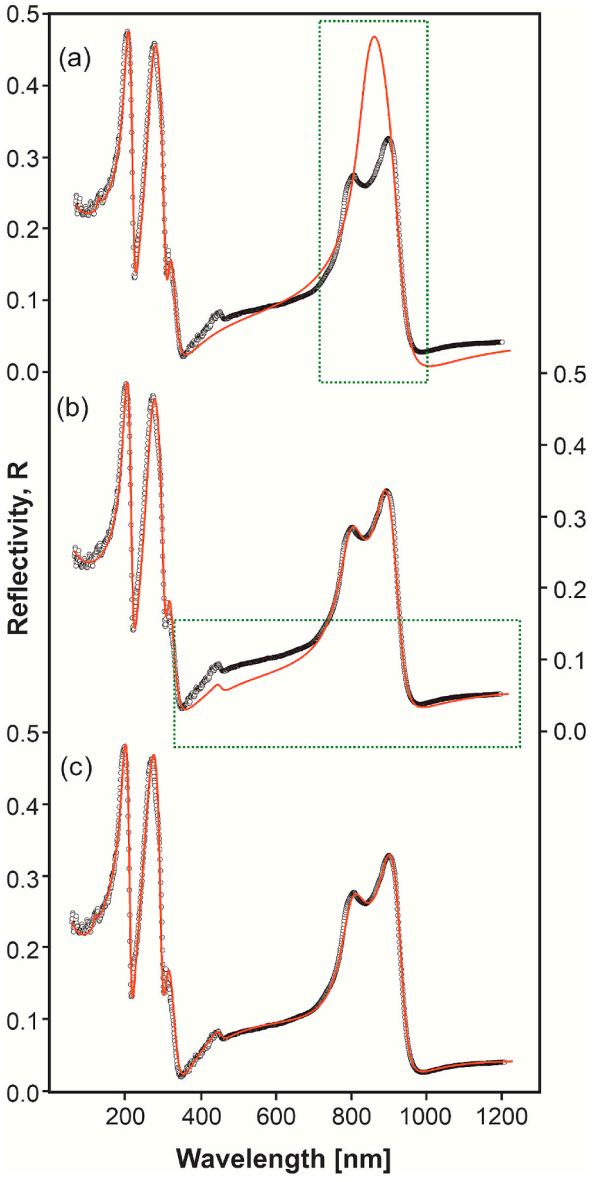

Fig. 8. Infrared reflection spectra of YVO_4 nanopowders prepared by Solution Combustion Synthesis (sample YVS). Experimental spectra are presented by open circles, while solid red lines are calculated spectra obtained by a fitting procedure based on the model given by Eqs. (3) and (4). Spectrum (a) shows fitting procedure without taking into account SOP phonons, (b) spectrum without taking into account multiphonon processes and (c) IR reflection spectrum of YVS when SOP phonons and multiphonon process were considered.

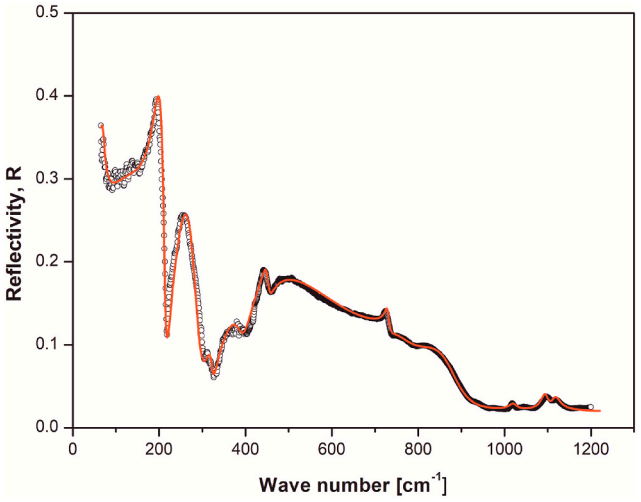

Fig. 9. Infrared reflection spectra of YVO4 nanopowders prepared by Solid State Reaction (sample YVC). Experimental spectra are presented by open circles, while solid red lines are calculated spectra obtained by a fitting procedure based on the model given by Eqs. (3) and (4).

Table 2
Best fitted parameters of IR reflection spectra for YV, YVC and YVC; bulk literature data and their assignments.

	YVC [cm^{-1}]	YVS [cm^{-1}]	Bulk YVO4 (Literature data) [cm^{-1}] [13]	Assignment
ε_∞	1.8	2.25	4.0	
F	0.79	0.93	1	
Γ_P	85	200		
ω_P	100	89		Plasmon frequency which plays role of ω_-
ω_{TO3}	212	198	195	E_u mode, IR active
ω_{LO3}	214	219	220	
ω_{TO4}	234	259	263	E_u mod, IR active
ω_{LO4}	292	300	309	
ω_{TO5}	321	311	309	E_u mod, IR active
ω_{LO5}	323	337	311	
ω_{TO6}	397	–		Multiphonon processes
ω_{LO6}	393	–		
ω_{TO7}	400	470		
ω_{LO7}	645	650		
ω_{TO8}	450.5	452		
ω_{LO8}	452	454		
ω_{TO9}	730.2	–		
ω_{LO9}	731	–		
ω_{TO10}	759	794	780	SOP formation. E_u mod, IR active
ω_{LOSOP}	863	890		SOP phonon
ω_{LO10}	887	935	930	
ω_{TO11}	1020	–		Multiphonon processes
ω_{LO11}	1021	–		
ω_{TO12}	1093.5	–		
ω_{LO12}	1096	–		
ω_{TO13}	1116	–		
ω_{LO13}	1117.5	–		

mode is occurrence of SOP mode in these structures. After including SOP modes into reflection spectra of nanostructures, we still have slight differences between experimental and theoretical results (Fig. 8b) at frequency between two sharp modes at lowest, and one wide mode at highest frequencies.

Reasons for this slight difference presented in Fig. 8b are different multi – phonon processes, with frequencies obtained in Table 2. After we took this into account, we got excellent match of theoretical and experimental results, shown in Fig. 8c.

From this we conclude that influence in reflection IR spectra in majority comes from SOP mode and not from multi – phonons. Still, when we compare two spectra from 8c and 9, we do see differences, which originate from different contributors to reflection IR spectra. In sample made with Solution Combustion Synthesis (YVS), the contribution of SOP is greater than in samples made with Solid State Reaction (YVC). Yet, in sample YVC, influence of multi – phonon contributors is greater than in YVS which is also shown in UV–Vis measurements. We see that from Table 2, for the wavenumbers greater than 1020 cm^{-1}, where we modeled multi – phonon modes for YVC and not for YVS, because of the greater influence of SOP in this sample which completely covered possible multi – phonon processes in YVS. From all of this, we can say that, when we compare to nanopowders prepared with two different methods, one can say that for YVS, influence of SOP mode dominates, and for sample YVC, multi – phonon modes dominate over SOP modes.

Now, let us discuss the results obtained in Table 2. In Eq. (3) we have defined the parameter called filling factor. It is a parameter which describes the volume fraction occupied by the nanoparticle (or nanoparticle aggregates) in the surrounding medium. In Table 2, filling factors of prepared nanopowders, YVC and YVS, together with value for bulk crystal YVO_4 are presented. Intensity and shape change of SOP modes presented in Figs. 8 and 9 (described with Eq. (4)) are notably affected by variation of filling factor, f.

In our case, position of SOP modes maxima directly follows the change in filling factor. Position of SOP modes frequencies are obtained from Eq. (6) [26], and the results are presented in Fig. 10.

$$\omega_{SOP} = \max\left(I_m\left(-\frac{1}{\varepsilon_{eff}}\right)\right) \tag{6}$$

In bulk crystal YVO_4 [13], at room temperature, four modes in infrared reflection spectra have been detected at 195, 263, 311 and 780 cm^{-1}. These modes are separated into internal (motions of the tetrahedral VO_4) and external (translations and rotations of the VO_4 tetrahedron). All of these modes, as expected, are shifted after resizing bulk to nanomaterial to 212, 234, 323 and 759 cm^{-1} for YVC, and to 198, 259, 337 and 794 cm^{-1} for YVS, respectively. Appearance of new phonons is due to break – down of the selection rules, as a consequence of resizing of the bulk crystal to nanostructure. Some modes occur due to appearance of surface optical phonon mode and some due to multi – phonon processes (one is, as we said, more dominant in YVS and other in YVC) in addition to modes which occur owing to Eu ion and its interaction with YVO_4 lattice. All of the modes are represented and assigned in Table 2.

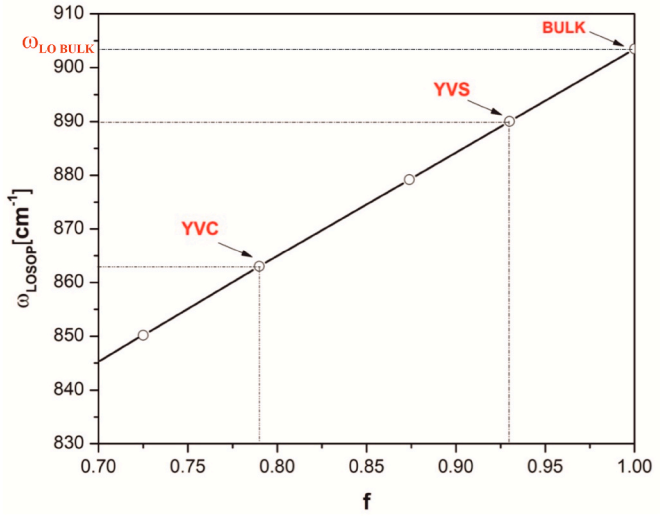

Fig. 10. Surface Optical Phonon mode position vs. filling factor.

Based on these results, it is clear that filling factor of prepared nanopowders depends on method of preparation, but yet it has a linear dependence of occurred surface optical phonon frequency. Also, SOP mode has the role of the LO phonon which we have also showed in our earlier works in different nanostructures [8].

Vibrational spectroscopy of nanostructures for discovering surface optical phonons represents an extremely active and exciting field with many possibilities for scientific and technological development. This arising new phenomena offer not only new perspective for material characterization, but also a fundamental understanding of processes at nanoscale. Better understanding of phonon properties of phosphors shown in this paper leads to wide application of these nanostructured materials for nanophosphor coatings [27], biomedical application [28], luminescence efficiency [29] etc. Also, discovery of surface phonons in these materials offer great use in heteronanostructures [30] to enhance the photoluminescence properties.

On the other side, multiphonon processes have been investigated for the first time in this nanostructured orthovanadate. Understanding multiphonon processes and charge transfers within a phosphor structure leads to its better application in self – assembled quantum dots [31] and different luminescent materials [32].

4. Conclusion

In this paper we showed two methods of preparation of yttrium orthovanadate nanopowders, Solution Combustion Synthesis and Solid State Reaction Method. Samples prepared by Solution Combustion Synthesis offer slightly bigger crystallite size, and therefore smaller width of band gap compared to samples prepared by Solid State Reaction Method, which provides samples with band gap up to 3.56 eV which was obtained using UV–Vis spectroscopy. Splitting of 272 nm mode from UV–Vis spectra for sample made by Solid State Reaction Method gives an indication of more dominant multi – phonon modes in this sample rather than in one made by Solid Combustion Synthesis. This was caused by doping and transfer of excited energy which migrates through vanadate sublattice to Eu ions; and after causes red emission induced by de – excitation process of excited Eu ions. For modeling Infrared Reflection spectra of both samples, Effective Medium Theory in Maxwell Garnett approximation was used and classical oscillator model, with Drude part added which takes into account concentration of free carriers. We showed that in both samples characteristic frequency of Surface Optical Phonon occurs as a consequence of resizing bulk crystal to nano scale. Also, that SOP has greater influence in sample prepared by Solution Combustion Synthesis, while in sample prepared by Solid State Reaction Method multi – phonon modes are more dominant and cover SOP modes. This was a confirmation of previous UV–Vis results. Since change in intensity and shape of SOP modes depends on variation of filling factor, we have considered the values of filling factor and its dependence on SOP mode position and came to a conclusion that SOP frequency has a linear dependence on filling factor, where SOP mode plays a role of LO phonon. All results obtained, show not only occurrence of nanoscale phenomena – surface optical phonon and multiphonon processes in YVO_4:Eu^{3+} nanostructures, but its potential use in wide fields of science and technology.

Declaration of competing interest

The authors declare that they have no known competing financial interests or personal relationships that could have appeared to influence the work reported in this paper.

Acknowledgments

The authors acknowledge funding provided by the Institute of Physics Belgrade through the grant by the Ministry of Education, Science, and Technological Development of the Republic of Serbia.

References

[1] T. Voitenko, S.A. Nedilko, K. Savva, M. Androuulidaki, S.G. Nedilko, E. Stratakis, O. Chukova, A. Papadopoulos, Deposition of luminiscent vanadate nanoparticles on silicon solar cells, in: IEE 40th International Conferece on Electronics and Nanotechnology (ELNANO), Kyiv, Ukraine 251 – 254, 2020.
[2] D. Hu, D. Li, X. Liu, Z. Zhou, J. Tang, Y. Shen, Vanadium – based nanomaterials for cancer diagnosis and treatment, Biomed. Mater. (2020) in press.
[3] D. Dosev, M. Nichkova, I.M. Kennedy, Inorganic lanthanide nanophosphors in biotechnology, J. Nanosci. Nanotechnol. 8 (3) (2008) 1052–1067 (16).
[4] L.P. Singh, N.V. Jadhav, S. Sharma, B.N. Pandey, S.K. Srivastava, R. S. Ningthoujam, Hybrid nanomaterials YVO_4:Eu/Fe_3O_4 for optical imaging and hyperthermia in cancer cells, J. Mater. Chem. C 3 (2015) 1965–1975.
[5] W.L. Wanmaker, A. Bril, J.W. Vrugt, J. Broos, Luminiscent properties of Eu – activated phosphors of the type AIIIBnOn, Philips Res. Rep. 21 (1966) 270.
[6] J. Su, X. Mi, J. Sun, L. Yang, C. Hui, L. Lu, Z. Bai, X. Zhang, Tunable luminescence and energy transfer properties in YVO4:Bi^{3+}, Eu^{3+} phosphors, J. Mater. Sci. 52 (2) (2017) 1–11.
[7] J. Mitrić, J. Križan, J. Trajić, G. Križan, M. Romčević, N. Paunović, B. Vasić, N. Romčević, Structural properties of Eu3+ doped Gd2Zr2O7 nanopowders: far – infrared spectroscopy, Opt. Mater. 75 (2018) 662–665.
[8] J. Mitrić, N. Paunović, M. Mitrić, B. Vasić, U. Ralević, J. Trajić, M. Romčević, W. D. Dobrowolski, I.S. Yahia, N. Romčević, Surface optical phonon – plasmon interaction in nanodimensional CdTe thin films, Physica: Low Dimens. Syst. Nanostruct. 104 (2018) 64–70.
[9] N. Romčević, M. Romčević, W.D. Dobrowolski, L. Kilanski, M. Petrović, J. Trajić, B. Hadžić, Z. Lazarević, M. Gilić, J.L. Ristić – Đurović, N. Paunović, A. Reszka, B. J. Kowalski, I.V. Fedorchenko, S.F. Marenkin, Far – infrared spectrscopy of $Zn_{1-x}Mn_xGeAs_2$ single crystals: plasma damping influence on plasmon – phonon interaction, J. Alloys Compd. 649 (2015) 375–379.
[10] N. Romčević, J. Trajić, T.A. Kuznetsova, M. Romčević, B. Hadžić, D.R. Khokhlov, Far – infrared study of impurity local modes in Ni – doped PbTe, J. Alloys Compd. 442 (2007) 324–327.
[11] J. Trajić, M. Romčević, M. Romčević, V.N. Nikiforov, Mater. Res. Bull. 42 (2007), 2201–2192.
[12] C. Pecharroman, M. Ocana, P. Tartaj, C.J. Serna, Optical constants of tetragonal and cubic zirconias in the infrared, Mater. Res. Bull. 29 (1994) 417.
[13] C.Z. Bi, J.Y. Ma, J. Yan, X. Fang, D.Z. Yao, B.R. Zhao, X.G. Qiu, Far – infrared optical properties of YVO_4 single crystal, Eur. Phys. J. B 51 (2006) 167–171.
[14] P. Makula, M. Pacia, W. Macyk, How to corretly determine the band gap energy of modified semiconductor photocatalysts based on UV – Vis spectra, J. Phys. Chem. Lett. 9 (23) (2018) 6814–6817.
[15] X. Li, H. Zhu, J. Wei, K. Wang, E. Xu, Zh Li, D. Wu, Determination of band gaps of self – assembled carbon nanotube films using Tauc/Davis – Mott model, Appl. Phys. A 97 (2009) 341–344.
[16] P. Kubelka, F. Munk, Ein Beitrag zur Optik der Farbanstriche, Zeits F. Teck. Physik. 12 (1931) 593–601.
[17] H. Wang, O. Odawara, H. Wada, Facile and chemically puyre preparation of YVO4: Eu3+ colloid with novel nanostructures via laser ablation in water, Sci. Rep. 6 (2016) 20507.
[18] J. Su, X. Mi, J. Sun, L. Yang, C. Hui, L. Lu, Z. Bai, X. Zhang, Tunable luminescence and energy transfer properties in YVO4:Bi^{3+}, Eu^{3+} phosphors, J. Mater. Sci. 2 (52) (2017).
[19] J. Mitrić, U. Ralević, M. Mitrić, J. Ćirković, G. Križan, M. Romčević, M. Gilić, N. Romčević, Isotope – like effect in YVO4:Eu3+ nanopowders: Raman spectroscopy, J. Raman Spectrosc. 50 (2019) 802–808.
[20] D. Šević, M.S. Rabasović, J. Križan, S. Savić – Šević, M. Mitrić, M. Gilić, B. Hadžić, N. Romčević, Characterization and luminiscence kinetics of Eu^{3+} doped YVO_4 nanopowders, Mater. Res. Bull. 88 (2017) 121–126.
[21] A. Huignard, V. Buissette, A.-C. Franville, T. Gacoin, J.-P. Boilot, Emission processes in YVO4:Eu nanoparticles, J. Phys. Chem. B 107 (2003) 6754–6759.
[22] J. Trajić, M.S. Rabasović, S. Savić – Šević, D. Šević, B. Babić, M. Romčević, J. L. Ristić – Đurović, N. Paunović, J. Križan, N. Romčević, Far – infared spectra of dysprosium doped yttrium aluminum garnet nanopowder, Infrared Phys. Technol. 77 (2016) 226–229.
[23] J.C.M. Garnett, Colours in meta glasses and in metallic films, Philos. Trans. Royal Soc. A 203 (1904) 385–420.
[24] I.J. Uhanov, Opt. Svojstva Poluprovodnikov, Nauka, Moskva, 1977.
[25] C.Z. Bi, J.Y. Ma, J. Yan, X. Fang, D.Z. Yao, B.R. Zhao, X.G. Qiu, Far – infrared optical properties of YVO_4 single crystal, Eur. Phys. J. B 51 (2006) 167–171.
[26] B. Hadžić, N. Romčević, M. Romčević, I. Kuryliszyn – Kudelska, W. Dobrowolski, J. Trajić, D.V. Timotijević, U. Narkiewicz, D. Sibera, Surface optical phonons in ZnO(Co) nanoparticles: Raman study, J. Alloys Compd. 540 (2012) 49–56.
[27] R. Kubrin, Nanophosphor coatings: technology and applications, opportunities and challenges, KONA Powder and Particle Journal 31 (22 – 52) (2014).
[28] T. Thu Huong, H. Thi Phuong, L. Thi Vinh, H. Thi Khuyen, T. Kim Anh, L. Quoc Minh, Functionalized YVO_4:Eu^{3+} nanophosphors with desirable properties for biomedical applications, J. Sci – Adv. Mater Dev. 1 (3) (2016) 295–300.
[29] T. Minakova, S. Mjakin, V. Bakhmetyev, M. Sychov, I. Zyatikov, I. Ekimova, V. Kozik, Y.-W. Chen, I. Kurzina, High efficient $YVPO_4$ luminescent materials activated by europium, Crystals 9 (2019) 658.
[30] H. Zhu, H. Hu, Z. Wang, D. Zuo, Synthesis of YVO4:Eu3+/YBO3 heteronanostructures with enhanced photoluminescence properties, Nanoscale Res. Lett. 4 (2009) 1009–1014.
[31] L. Magnusdottir, A. Uskov, S. Bischoff, J. Mork, Multiphonon capture processes in self-assembled quantum dots, in: Technical Digest. Summaries of Papers Presented at the Quantum Electronics and Laser Science Conference. Postconference Technical Digest (IEEE Cat. No.01CH37172), 2001, pp. 206–207.
[32] R. Liu, L. Liu, Y. Liang, Energy transfer and color – tunable luminescence properties of YVO4:Re (Re = Eu3+, Sm3+, Dy3+, Tm3+) phosphors via molten salt synthesis, Opt. Mater. Express 8 (6) (2018) 1686.

chemosensors

MDPI

Article

Characterization of Flexible Copper Selenide Films on Polyamide Substrate Obtained by SILAR Method—Towards Application in Electronic Devices

Gediminas Jakubauskas [1], Martina Gilic [2,3], Edita Paluckiene [1], Jelena Mitric [2], Jovana Cirkovic [4], Uros Ralevic [2], Egle Usoviene [1], Egidijus Griskonis [1] and Neringa Petrasauskiene [1,*]

[1] Department of Physical and Inorganic Chemistry, Kaunas University of Technology, Radvilenu 19, 50254 Kaunas, Lithuania
[2] Institute of Physics Belgrade, University of Belgrade, Pregrevica 118, 11080 Belgrade, Serbia
[3] Institut of Experimental Physics, Freie Universität Berlin, Arnimallee 14, 14195 Berlin, Germany
[4] Institute for Multidisciplinary Research, University of Belgrade, Kneza Viseslava 1, 11000 Belgrade, Serbia
* Correspondence: neringa.petrasauskiene@ktu.lt

Abstract: Thin copper selenide films were synthesized on polyamide sheets using the successive ionic layer adsorption and reaction (SILAR) method at three different temperatures. It was found that elevating the temperature of the solution led to the creation of copper selenide films with different features. X-ray diffraction characterization revealed that all films crystallized into a cubic $Cu_{2-x}Se$, but with different crystallinity parameters. With elevating the temperature, grain size increased (6.61–14.33 and 15.81 for 40, 60 and 80 °C, respectively), while dislocation density and the strain decreased. Surface topology was investigated with Scanning Electron Microscopy and Atomic Force Microscopy, which revealed that the grains combined into agglomerates of up to 100 nm (80 °C) to 1 µm (40 °C). The value of the direct band gap of the copper selenide thin films, obtained with UV/VIS spectroscopy, varied in the range of 2.28–1.98 eV. The formation of $Cu_{2-x}Se$ was confirmed by Raman analysis; the most prominent Raman peak is located at 260 cm^{-1}, which is attributed to binary copper selenides. The thin $Cu_{2-x}Se$ films deposited on polyamide showed *p*-type conductivity, and the electrical resistivity varied in the range of 20–50 Ω. Our results suggest that elevated temperatures prevent large agglomeration, leading to higher resistance behavior.

Keywords: copper selenide; polyamide; SILAR method

Citation: Jakubauskas, G.; Gilic, M.; Paluckiene, E.; Mitric, J.; Cirkovic, J.; Ralevic, U.; Usoviene, E.; Griskonis, E.; Petrasauskiene, N. Characterization of Flexible Copper Selenide Films on Polyamide Substrate Obtained by SILAR Method—Towards Application in Electronic Devices. *Chemosensors* **2022**, *10*, 313. https://doi.org/10.3390/chemosensors10080313

Academic Editor: Vardan Galstyan

Received: 22 June 2022
Accepted: 1 August 2022
Published: 5 August 2022

1. Introduction

Copper selenide can be formed in various stoichiometric compositions, such as CuSe, Cu_2Se, $CuSe_2$, Cu_3Se_2, Cu_7Se_4, Cu_5Se_4, Cu_3Se_4, and non-stoichiometric compositions $Cu_{2-x}Se$ [1–3]. The stoichiometric composition of copper selenide strongly influenced its crystalline structure and electronic behavior—it alters its electronic, chemical, and thermal properties [4,5]. Copper-deficient $Cu_{2-x}Se$ is an intrinsic *p*-type semiconductor with direct bandgap energies in the range of 2.0 to 2.4 eV, the work function of 4.17 eV, and high photo-electrochemical conversion efficiency (~14.6%) [3,5–8]. These features of $Cu_{2-x}Se$ can be used as Shottky diodes [9], self-repairable electrodes [10], and photovoltaic devices [8]. Furthermore, the $Cu_{2-x}Se$ columnar superstructures are used as low-cost and highly efficient counter electrodes in quantum dot sensitized solar cells [11,12].

Several decades ago, due to concerns about homeland security, medical and environmental monitoring as well as food safety, a large interest was shown in the development of gas sensors for detecting volatile and toxic gases. $Cu_{2-x}Se$ exhibits good sensitivity and short response and recovery times to Hg^{2+} [13], and organic gases such as ethanol and acetone [14].

Many works have been reported on the formation of $Cu_{2-x}Se$ on substrates, such as glass [1,6,15], and fluorine-doped tin oxide [8,11,12,16].

Flexible electronics is a growing field that is promising to develop various new commercial products such as displays, solar cells, flexible photovoltaics, and biomedical sensors due to their lightweight and low cost [17–21]. Flexible polymer substrates possess unique features such as low cost, low thickness, low mass, and excellent mechanical deformability. They can remain in the environmental, chemical, and thermal environments required for the construction of electronic circuits while maintaining their mechanical flexibility [22,23]. Recently, ferroelectric semiconductors have been increasingly studied [24,25].

When $Cu_{2-x}Se$ is deposited on a flexible transparent polymer substrate (polyvinylchloride, polyvinyl alcohol), the possibility of using thin flexible polymer substrates appears in the fabrication of flexible optoelectronic devices [26]. $Cu_{2-x}Se$ films on polyester sheets can be used as a transparent electrode for inorganic and organic hybrid light emitters, as a possible replacement for indium tin oxide or fluorine-doped tin oxide [7].

This work reports the preparation and characterization of electrically conductive copper selenide onto polyamide 6 (PA) sheets. Polyamide 6 was chosen as a cheap, chemically stable, and flexible substrate. Flexibility is the ability of the material to be bent without mechanical failures such as fracture and plastic deformation. One of the few mechanical parameters that describe the deformation of a material is Young's modulus, which characterizes the resistance of a material to elastic deformation. Young's moduli of polyamide 6 are lower than those of other polymers. For example, polyimide and polyethylene terephthalate have a Young's modulus of 4 GPa and 3 GPa, respectively, while the Young's modulus of polyamide 6 is 2.4 GPa [17,27,28]. As a semihydrophilic flexible polymer, PA is capable of adsorbing molecules or ions of various electrolytes from nonaqueous and aqueous solutions [29,30]. Unlike glass and fluorine-doped tin oxide substrates, on which copper selenide builds a thin film, polymer allows the material to partially diffuse in it, so the final product is a conductive composite (PA with copper selenide nanocrystals embedded in it).

$Cu_{2-x}Se$ films can be prepared by chemical bath deposition [1,7,31], combined electrochemical followed by chemical bath deposition [8], sonochemical synthesis [32], ion beam sputtering deposition [33], electrochemical [12], successive ionic layer adsorption and reaction [15,34], and other methods.

Here, copper selenide nanocrystals were formed on the surface as well as inside the polyamide using the simple and versatile successive ionic layer adsorption and reaction (SILAR) method. The method used differs from other chemical methods, as it does not require specialized equipment or conditions; it is quite inexpensive and simple, convenient for large area deposition, and it can be used at room temperature [34]. As a low-temperature process, it also avoids oxidation [35]. The SILAR method consists of two stages: first, copper ions are adsorbed on the polyamide surface from a precursor solution containing copper ions; second, copper selenide thin films are formed by treating the layer formed in the first stage with a solution containing selenium ions. To the best of our knowledge, the copper selenide/PA composite by employing the SILAR method has never been obtained before. We suggest that slightly elevated solution temperatures could facilitate crystalline formation in the polymer matrix and therefore improve the optical and electric properties of the as-obtained composites. Combined with the natural abundance of material and the low cost of composite production, the copper selenide/PA composite could be a possibility for printable electronics on flexible substrates or in sensors in the future.

Structural characterization of the composites was performed with the help of X-ray diffraction, Scanning electron microscopy combined with Energy-dispersive X-ray spectroscopy, and Raman Spectroscopy, while the optical properties were characterized with UV/VIS spectroscopy. The surface morphology of the films was investigated with Atomic Force Microscopy. The conductivity of the composites was checked with a multimeter.

2. Materials and Methods

2.1. Materials and Film Preparation

The reactive solutions were made with just pure analytical reagents and purified water. All reagents were obtained from Sigma-Aldrich and used as received. Only freshly prepared solutions were used for experiments and were not de-aerated during the experiments.

Thin copper selenide films were deposited on a PA sheet (PA 6, Tecamid 6, density 1.13 g/cm^{-3}, thickness 500 µm, surface resistance ~1 $k\Omega/m^2$), which was obtained from Ensinger GmbH (Germany). Before the experiments, the PA films were boiled in distilled water for 2 h to remove the remaining unpolymerized monomer residues. Then, they were dried with filter paper and incubated over anhydrous $CaCl_2$ for 24 h.

The copper sulfate solution ($CuSO_4$) was used as the cationic solution and the freshly prepared sodium selenosulfate solution (Na_2SeSO_3) was used as the anionic solution for the deposition of a thin film of copper selenide on PA using the SILAR method.

To prepare the Na_2SeSO_3 solution, selenium powder (99% purity) and anhydrous sodium sulfite were dissolved in distilled water for 8 h at 80 °C with constant stirring. It was kept for 24 h in a sealed container, to allow undissolved selenium to settle. A clear solution was obtained after it was filtered [34].

In one SILAR cycle, the substrate was immersed separately in solutions of anionic and cationic precursors. The substrate was washed with an ion exchange solution (distilled water) to avoid a homogeneous deposition between each immersion.

Thin copper selenide films on polyamide substrate were grown by repeating these cycles 30 times at different temperatures (40 °C, 60 °C, and 80 °C). The proposed reaction mechanism of the obtained film could be found in [34].

2.2. Characterization of Copper Selenide Films

X-ray diffraction (XRD) measurements were performed using a Philips PW 1050 diffractometer equipped with a PW 1730 generator, 40 kV × 20 mA, using Ni filtered Co Kα radiation of 0.1778897 nm at room temperature. Measurements were carried out in the 2 h range of 10 to 70° with a scanning step of 0.05° and a scan time of 10 s per step. The experimental values of d (lattice spacing) for copper selenide are determined using the Bragg relation [36]. The average grain size (D) was calculated based on the full width at the half-maximum intensity (FWHM) of the main reflections by applying Scherrer's formula [37,38]. Furthermore, to have more information on the number of defects in the films, the dislocation density (δ) [34] and the strain (ε) values were calculated [39].

Scanning electron microscopy (SEM) was performed using a Raith GMBH e-Line instrument equipped with a field emission gun operating at 10 kV accelerating voltage, magnification: 20,000 k. A secondary electron signal was used for imaging. Energy-dispersive X-ray spectroscopy (EDX) imaging was performed using QUANTAX EDS with an X-Flash Detector 3001 and ESPRIT software.

The UV/VIS absorbance and diffusion reflectance spectra were recorded in the wavelength range of 200–800 nm on a Shimadzu UV-2600 spectrophotometer equipped with an integrated sphere. The diffuse reflectance and absorbance spectra were measured relative to a reference sample of $BaSO_4$. The optical band gap from the diffuse reflectance measurements was calculated using the Tauc plot [40,41]. The acquired diffuse reflectance spectra are converted to Kubelka–Munk function [42]. The optical band gap was estimated by extrapolating the linear portion of a plot of $(\alpha h\nu)^2$ versus $h\nu$ to $\alpha = 0$. Using this function, a plot of $(\alpha h\nu)^2$ against $h\nu$ is obtained.

Raman measurements were performed using TriVista 557 micro-Raman system in backscattering configuration, equipped with a nitrogen-cooled CCD detector. The 514.5 nm line of Ar^+/Kr^+ ion laser was used as the excitation source. The measurements were performed with low laser power to prevent a local overheating of the sample.

The surface morphology of copper selenide samples was investigated by atomic force microscopy (AFM). AFM imaging was performed using the NTEGRA Prima system from NT MDT. AFM measurements were performed at room temperature and under ambient

conditions. The AFM topography and phase images were acquired simultaneously using NSG01 probes with a typical resonant frequency of 150 kHz and a 10 nm curvature radius of the tip apex.

The constant current resistivity of the copper selenide films was measured using a multimeter MS8205F (Mastech, Shenzhen, China) with special electrodes. The electrodes were produced from two nickel-plated copper plates with a 1 cm spacing and the dielectric material between them.

3. Results

3.1. XRD Characterization of Copper Selenide Thin Films

The crystal structures and orientations of the thin copper selenide films on the PA substrate were investigated by X-ray diffraction patterns and are shown in Figure 1. The XRD results revealed that all films have a polycrystalline structure.

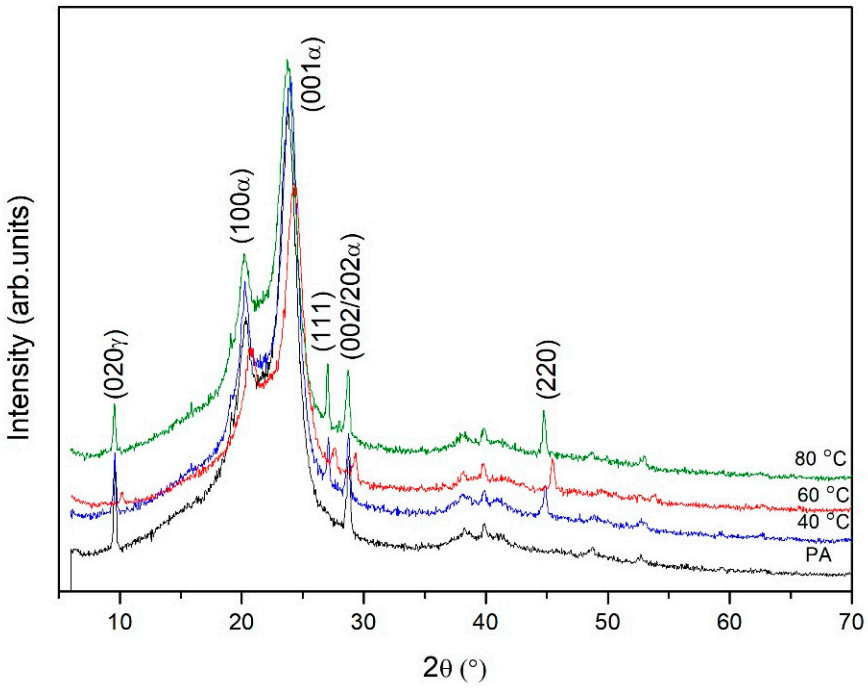

Figure 1. XRD patterns of the initial PA and copper selenide thin films.

Semicrystalline peaks of polyamide were observed between 9° and 30° (in 2θ). These peaks, according to JCPDS 12-923, appear at 20.3° and 23.8° with the corresponding d-spacing of 4.36 and 3.74, respectively. They are attributed to the (100α) and (001α) crystal planes, respectively, showing the presence of a dominant crystalline α-phase [28,43,44]. Two reflections were also observed at around 2θ = 9.6° (020γ) and 28.8° (002/202α). XRD analysis showed that the temperature of the solutions of anionic and cationic precursors used in the experiment influenced the composition of the obtained thin films. The X-ray peaks on diffractograms are more intense when the solutions' temperature is higher. The peaks at 28° and 45° are absent in the spectrum of pure PA and they correspond to planes (111) and (220) of a cubic phase of $Cu_{2-x}Se$ Berzelianite (JCPDS 6-680). It is common $Cu_{2-x}Se$ phase [12,15]. The experimental values of the Miller indices *d*, *2θ* and (*hkl*) of PA and copper selenide thin films are given in Table 1.

Table 1. Values of the Miller indices *d*, 2*θ* and (*hkl*) of PA and copper selenide thin films.

Miller Indices (hkl)		Temperature							
		PA		40 °C		60 °C		80 °C	
		(2θ)	*d* (Å)	(2θ)	*d* (Å)	(2θ)	*d* (Å)	(2θ)	*d* (Å)
PA	(020γ)	9.6	9.21	9.65	9.16	10.2	8.67	9.6	9.21
	(100α)	20.35	4.36	20.3	4.37	20.95	4.24	20.25	4.38
	(001α)	23.8	3.74	24	3.70	24.3	3.66	23.75	3.74
$Cu_{2-x}Se$	(111)	–	–	27.15	3.28	27.7	3.22	27.1	3.28
PA	(002/202α)	28.75	3.10	28.8	3.10	29.4	3.04	28.75	3.10
$Cu_{2-x}Se$	(220)	–	–	44.95	2.02	45.5	1.99	44.8	2.02

Changes in the intensities and full width at half maximum (FWHM) values of these peaks were observed with the use of different temperatures of solutions. The intensities of the diffraction peak increased slightly with changing temperature of the solution temperature from 40 to 80 °C. The structural parameters for the (220) peak such as FWHM (β), grain size (D), dislocation density (δ), and strain (ε) for all films were evaluated by XRD patterns and presented in Table 2. As shown, grain size increases, while dislocation density and strain decrease with the change in the deposition temperature.

Table 2. Grain size (D), dislocation density (δ), strain (ε) and full width at half maximum (FWHM, β) values of copper selenide thin films.

Temperature	2*θ* (°)	β (°)	*D* (nm)	$\delta \cdot 10^{-3}$ (nm^{-2})	$\varepsilon \cdot 10^{-3}$ (nm^{-2})
40 °C	44.95	1.30	6.61	22.89	13.72
60 °C	45.5	0.60	14.33	4.86	6.25
80 °C	44.8	0.54	15.81	4.00	5.76

These changes can be attributed to the improvement in film crystallization and to the inductive lattice matching, which has a strong impact on structural parameters. The higher values of D, and the smaller β, δ and ε values indicate better crystallization of thin films. Regarding the values of D, β, and δ, the best results were obtained for the film made at 80 °C, suggesting that a higher temperature facilitates the crystallization of the film.

3.2. Scanning Electron Microscopy and Energy Dispersive X-ray Analysis

Scanning electron microscopy was used to evaluate the changes in surface morphology of the copper selenide layer on the PA substrate, with the changes in synthesis parameters. The SEM micrographs of the samples are presented on the left-hand side of Figure 2, with a magnification of 20,000 k. The images clearly show that the polymer is well-covered with copper selenide thin films.

Copper selenide grains grow in irregular shapes and sizes. By changing temperature, it could be seen that when the temperature increases, the copper selenide film becomes denser, coated with tightly packed spherical grains that, in turn, were combined into agglomerates of 100 nm to 1 µm. Micrographs show a compact structure composed of single types of small, densely packed microcrystals. The thin copper selenide films on surface of PA are well dispersed, relatively uniform, and consist of randomly oriented particles. Such morphological forms can produce a very rough surface with high porosity, which leads to increased catalytic activity.

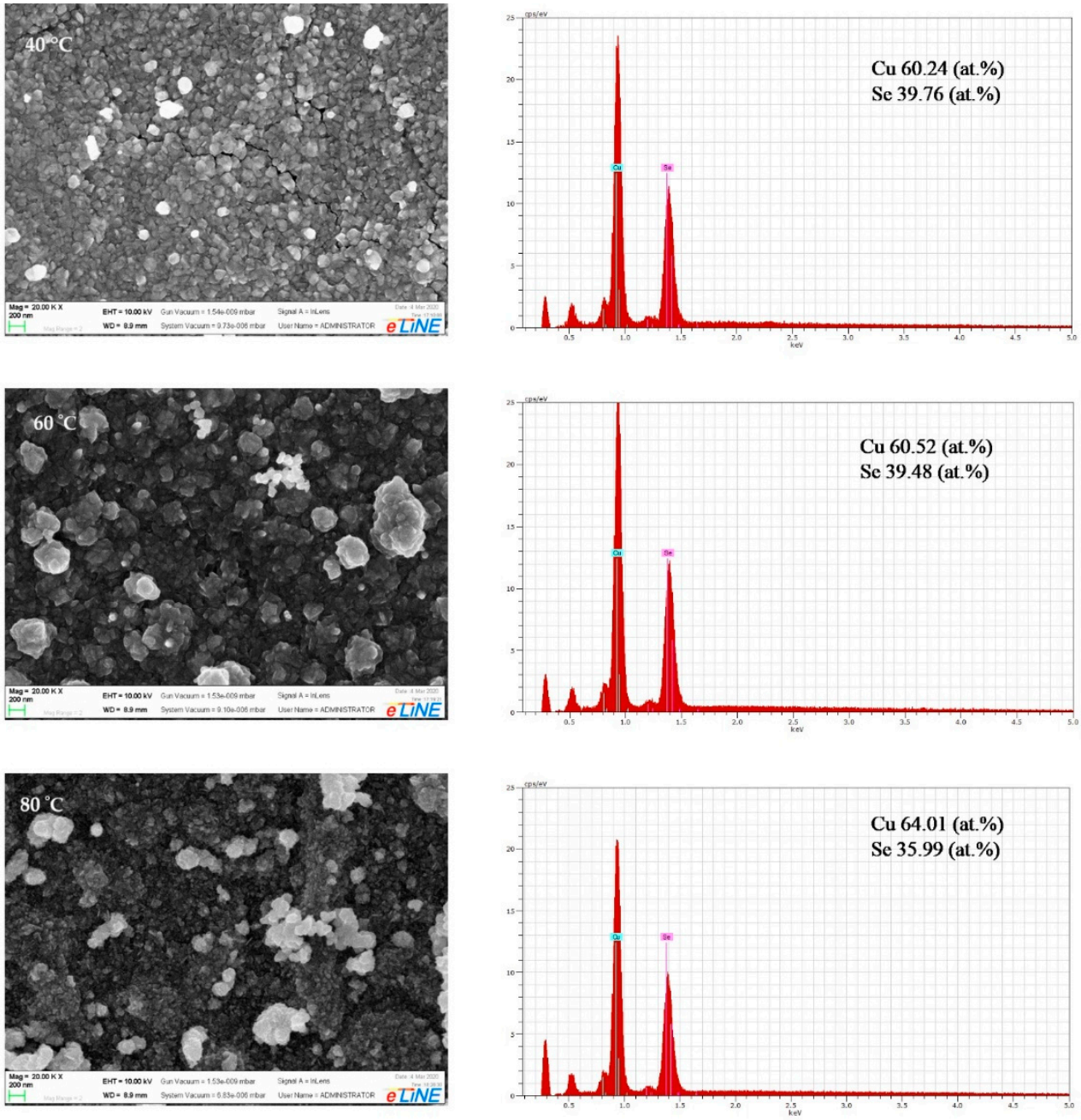

Figure 2. SEM micrographs and EDX spectra of copper selenide/PA thin films.

The elemental analysis of the copper selenide thin films was performed using an EDX micro-analytic unit attached with scanning electron microscopy and shown on the right-hand side of Figure 2. The presence of emission lines in the investigated energy range indicates that copper selenide films were successfully deposited on the polyamide substrates and the expected elements (selenium and copper) were detected. The element analysis revealed the presence of Cu and Se with the average atomic percentages shown on the right side of Figure 2. All films show a higher atomic presence of Cu than Se, which confirms the presence of $Cu_{2-x}Se$. The Cu/Se ratio measured by EDX analysis was 1.52–1.78, which is in good agreement with the XRD results.

3.3. Measurements of Electrical Resistivity

The resistance of thin films of copper selenide formed on PA plotted in Figure 3 is measured from the close contact up to the 1 cm distance of electrodes, and it includes the contact resistance of the electrode contacts. On the contrary, the pure PA substrate shows no electrical conductivity—the material is a pure insulator.

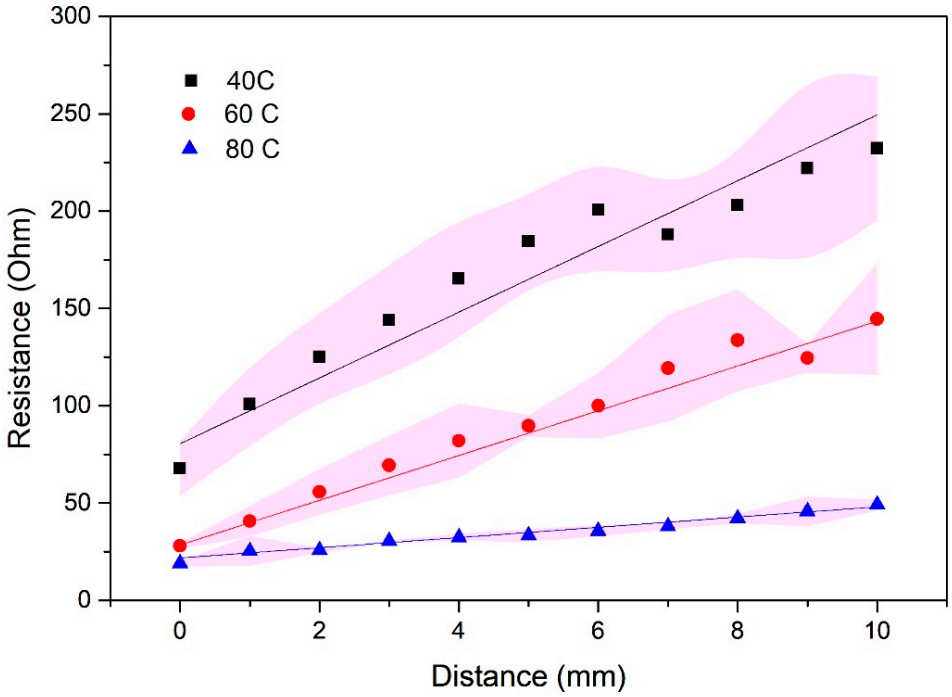

Figure 3. Resistance vs. distance graph for copper selenide films on PA. The results are the averaged values of 4 measurements, and error bars are indicated as the pink area.

At a distance of 1 cm between the electrodes, the resistances of films obtained at 40 °C, 60 °C and 80 °C are 270 Ω, 124 Ω and 49 Ω, while the values for the close contact between the electrodes were obtained to be 50 Ω, 26 Ω and 20 Ω, respectfully. The corresponding slopes are 16, 11, and 2.6, which implies that the electrical properties of the film improve with elevating the temperature. Compared to XRD results, the sample obtained at 80 °C has the best crystallinity, which is directly connected with higher conductivity (i.e., lower resistivity). As it can be seen in the graph, the error bar values are minimal for the sample obtained at 80 °C, and they increase with decreasing the temperature.

3.4. Optical Analysis of Copper Selenide Thin Films

The absorbance and diffuse reflectance spectra of thin films of copper selenide on PA in the wavelength range of 200–800 nm are presented in Figure 4. An increase in the absorbance of the copper selenide films is observed with the increased temperature of solutions, as well as the opposite effect of the reflectance.

The determination of band gaps in semiconductors is significant for obtaining basic solid-state physics.

In this study, we used the Tauc plot for the determination of the optical band gap from diffuse reflectance measurements [40–42]. The experimental values of energy gaps for copper selenide thin films are determined to be 2.28 eV for the sample obtained at 80 °C, 2.14 eV for the sample at 60 °C, and 1.98 eV for the sample obtained at 40 °C (Figure 5). This is in good agreement with the values of the reported data [3,5,6].

The obtained band gap values are also consistent with AFM data, according to the rule—the smaller particle size, the bigger the band gap.

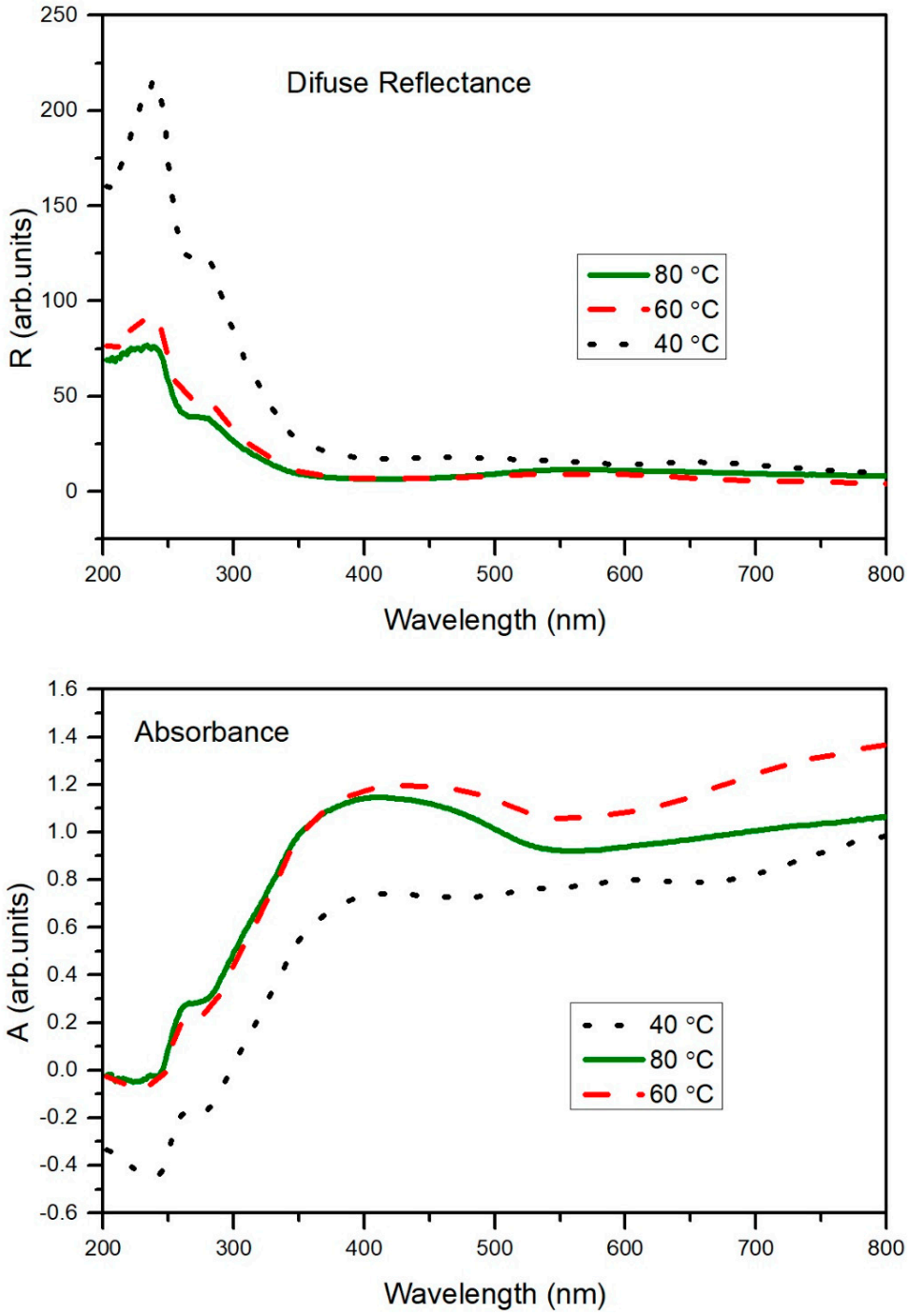

Figure 4. Diffuse reflectance and absorbance spectra of copper selenide/PA thin films.

3.5. Raman Analysis of Copper Selenide Thin Films

Raman spectroscopy is a useful spectroscopic technique for detecting the vibration energy levels of compounds and for further confirming the crystal structure.

Consequently, further clarity on the crystalline phase of the copper selenide thin films was explored by Raman analysis. As shown in Figure 6, the typical Raman spectra of three copper selenide film samples (deposited at different temperatures) exhibit similar peak positions.

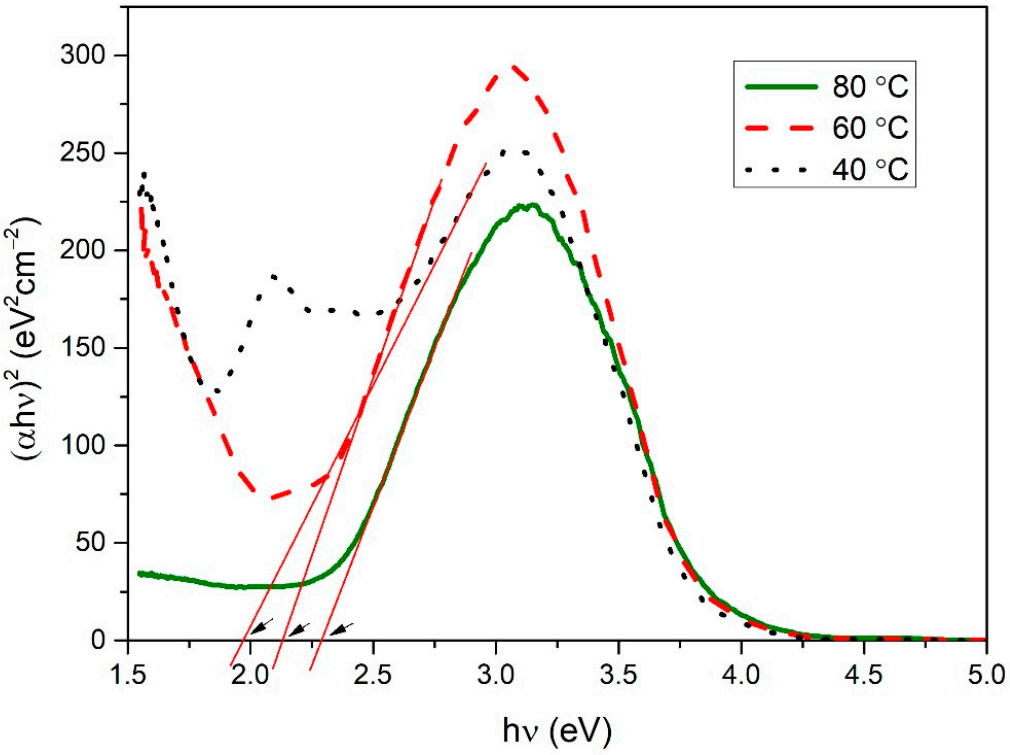

Figure 5. Plots of $(\alpha h\nu)^2$ versus hν for copper selenide/PA thin films.

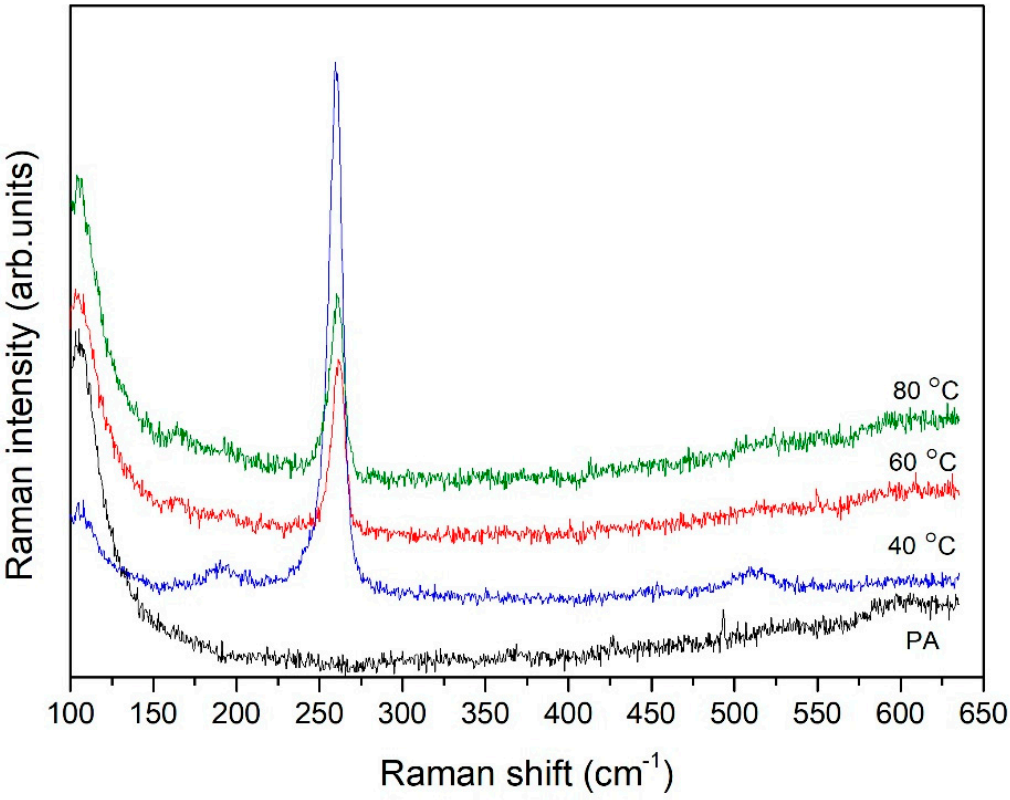

Figure 6. Raman spectra of the copper selenide/PA thin films.

The only strong peak, observed at 260 cm^{-1}, can be assigned to the Se–Se stretching vibration in $Cu_{2-x}Se$ and is consistent with the previous reports [11,45], while the peak at 187 cm^{-1} corresponds to the Cu-Se vibration [46]. The peak at 520 cm^{-1} is the first overtone

of the intensive peak at 260 cm^{-1}. Raman analysis confirms the composition of the copper selenide/PA films. There are no modes of elemental selenium or copper. The background at the beginning of the spectra comes from PA.

3.6. AFM Analysis of Copper Selenide Thin Films

Atomic force microscopy is a very suitable method for visualizing the surface morphology and quantitative analysis of surface roughness. 2D and 3D images, as well as histograms of 5 × 5 µm areas of copper selenide/PA films, are presented in Figure 7. The height and surface morphology of the copper selenide thin films formed on PA depend on the temperature of the solutions of anionic and cationic precursors used in the experiment: the microstructure of the thin film changes according to the deposition temperature. The surface image shows that the surface of the film is rough with particles gathered into agglomerates. The typical parameters of the quantitative analysis of AFM images are presented in Table 3. With an increase in the precursor solution temperature, the surface roughness decreases and the film becomes more compact and dense. Average roughness is ~194 nm at a precursor solution temperature of 40 °C and decreases to ~16 nm and ~13 nm in case of the temperature of 60 °C and 80 °C. As can be seen, a thin film of copper selenide deposited at 80 °C temperature solution has greater uniformity and homogeneity than other films.

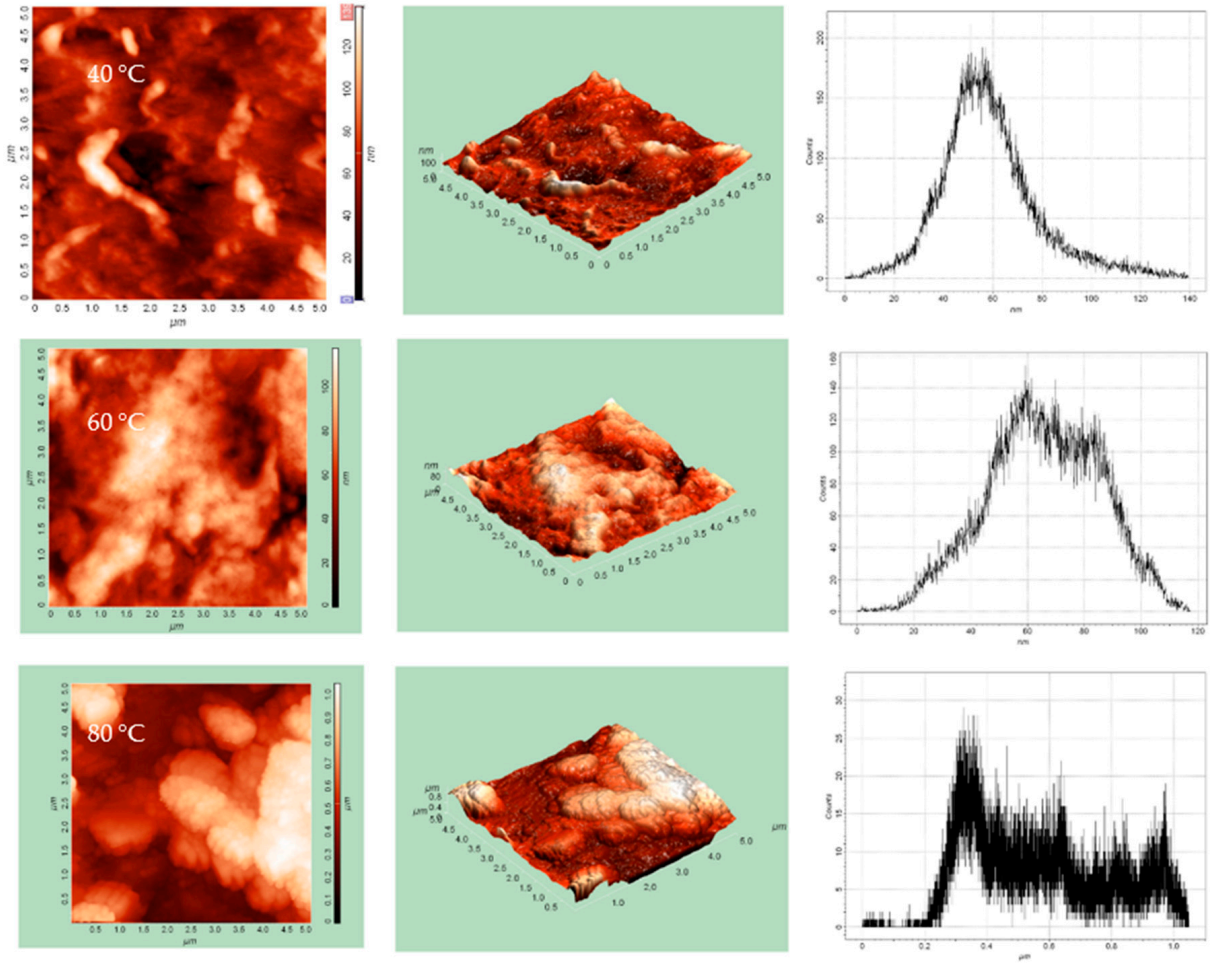

Figure 7. 2D and 3D AFM images and histograms of copper selenide/PA films.

Table 3. Surface roughness parameters of copper selenide thin films.

Parameters	Temperature		
	40 °C	**60 °C**	**80 °C**
Maximum height of peaks, h_{max}, nm	1048.41	117.32	123.16
Average height, h_{mean}, nm	565.57	65.64	49.99
Average Roughness, R_a, nm	194.62	16.24	13.32
RMS Roughness, R_q, nm	227.76	19.90	17.21
Surface skewness, R_{sk}	0.42	−0.13	0.58

4. Conclusions

$Cu_{2-x}Se$ thin films can be deposited on a flexible polyamide substrate by using the SILAR method, while by adjusting the temperature of precursor solutions we can affect and tune the optical, structural, and electrical properties of as obtained films. XRD analysis revealed that $Cu_{2-x}Se$ exists in the cubic crystal structure. The band gap energy of $Cu_{2-x}Se$ films was found to be in the order of 1.98–2.28 eV. Raman analysis confirmed the formation of the $Cu_{2-x}Se$ phase (260 cm^{-1}) without any elemental selenium or copper phase. A thin film of copper selenide deposited at 80 °C temperature solution has greater uniformity and homogeneity than other films, the largest grain size, but with the smallest agglomerates, the largest band gap value, and the best conductivity.

Author Contributions: Conceptualization, N.P. and G.J.; methodology, N.P., G.J. and E.P.; validation, M.G., N.P. and G.J.; formal analysis, N.P., G.J. and E.P.; investigation, G.J., J.M., J.C. and U.R.; data curation, M.G., J.C., U.R. and E.G.; writing—original draft preparation, G.J. and N.P.; writing—review and editing, N.P., M.G. and E.P.; visualization, G.J. and E.U.; supervision, N.P. and M.G. All authors have read and agreed to the published version of the manuscript.

Funding: This research received no external funding.

Institutional Review Board Statement: Not applicable.

Informed Consent Statement: Not applicable.

Data Availability Statement: Not applicable.

Conflicts of Interest: The authors declare no conflict of interest.

References

1. García, V.M.; Nair, P.K.; Nair, M.T.S. Copper Selenide Thin Films by Chemical Bath Deposition. *J. Cryst. Growth* **1999**, *203*, 113–124. [CrossRef]
2. Tyagi, K.; Gahtori, B.; Bathula, S.; Jayasimhadri, M.; Singh, N.K.; Sharma, S.; Haranath, D.; Srivastava, A.K.; Dhar, A. Enhanced Thermoelectric Performance of Spark Plasma Sintered Copper-Deficient Nanostructured Copper Selenide. *J. Phys. Chem. Solids* **2015**, *81*, 100–105. [CrossRef]
3. Thirumavalavan, S.; Mani, K.; Sagadevan, S. Investigation of the Structural, Optical and Electrical Properties of Copper Selenide Thin Films. *Mater. Res.* **2015**, *18*, 1000–1007. [CrossRef]
4. Zhao, L.; Wang, X.; Yun, F.F.; Wang, J.; Cheng, Z.; Dou, S.; Wang, J.; Snyder, G.J. The Effects of Te^{2-} and I^{-} Substitutions on the Electronic Structures, Thermoelectric Performance, and Hardness in Melt-Quenched Highly Dense $Cu_{2-x}Se$. *Wiley Online Libr.* **2015**, *1*, 1400015. [CrossRef]
5. Hussain, R.A.; Hussain, I. Copper Selenide Thin Films from Growth to Applications. *Solid State Sci.* **2020**, *100*, 106101. [CrossRef]
6. Hankare, P.P.; Khomane, A.S.; Chate, P.A.; Rathod, K.C.; Garadkar, K.M. Preparation of Copper Selenide Thin Films by Simple Chemical Route at Low Temperature and Their Characterization. *J. Alloy. Compd.* **2009**, *469*, 478–482. [CrossRef]
7. Silva, S.F.C.; Zanatta, B.S.; Rabelo, A.C.; Bottecchia, O.L.; Tozoni, J.R.; Oliveira, O.N.; Marletta, A. Flexible and Transparent Electrodes of $Cu_{2-X}Se$ with Charge Transport via Direct Tunneling Effect. *Adv. Electron. Mater.* **2021**, *7*, 2001189. [CrossRef]
8. Zyoud, A.; Murtada, K.; Kwon, H.; Choi, H.J.; Kim, T.W.; Helal, M.H.S.; Faroun, M.; Bsharat, H.; Park, D.H.; Hilal, H.S. Copper Selenide Film Electrodes Prepared by Combined Electrochemical/Chemical Bath Depositions with High Photo-Electrochemical Conversion Efficiency and Stability. *Solid State Sci.* **2018**, *75*, 53–62. [CrossRef]
9. Kalenga, M.P.; Govindraju, S.; Airo, M.; Moloto, M.J.; Sikhwivhilu, L.M.; Moloto, N. Fabrication of a Schottky Device Using CuSe Nanoparticles: Colloidal versus Microwave Digestive Synthesis. *J. Nanosci. Nanotechnol.* **2015**, *15*, 4480–4486. [CrossRef]
10. Singh, S.C.; Li, H.; Yao, C.; Zhan, Z.; Yu, W.; Yu, Z.; Guo, C. Structural and Compositional Control in Copper Selenide Nanocrystals for Light-Induced Self-Repairable Electrodes. *Nano Energy* **2018**, *51*, 774–785. [CrossRef]

11. Xu, J.; Yang, Q.; Kang, W.; Huang, X.; Wu, C.; Wang, L.; Luo, L.; Zhang, W.; Lee, C.S. Water Evaporation Induced Conversion of CuSe Nanoflakes to $Cu_{2-X}Se$ Hierarchical Columnar Superstructures for High-Performance Solar Cell Applications. *Part. Part. Syst. Charact.* **2015**, *32*, 840–847. [CrossRef]
12. Zhou, R.; Huang, Y.; Zhou, J.; Niu, H.; Wan, L.; Li, Y.; Xu, J.; Xu, J. Copper Selenide (Cu_3Se_2 and $Cu_{2-x}Se$) Thin Films: Electrochemical Deposition and Electrocatalytic Application in Quantum Dot-Sensitized Solar Cells. *Dalton Trans.* **2018**, *47*, 16587. [CrossRef] [PubMed]
13. Zhang, H.; Xia, Y. Ratiometry, Wavelength, and Intensity: Triple Signal Readout for Colorimetric Sensing of Mercury Ions by Plasmonic $Cu_{2-x}Se$ Nanoparticles. *ACS Sens.* **2016**, *1*, 384–391. [CrossRef]
14. Wang, Z.; Peng, F.; Wu, Y.; Yang, L.; Zhang, F.; Huang, J. Template Synthesis of $Cu_{2-x}Se$ Nanoboxes and Their Gas Sensing Properties. *Cryst. Eng. Comm.* **2012**, *14*, 3528–3533. [CrossRef]
15. Astam, A.; Akaltun, Y.; Yildirim, M. Conversion of SILAR Deposited Cu_3Se_2 Thin Films to $Cu_{2-X}Se$ by Annealing. *Mater. Lett.* **2016**, *166*, 9–11. [CrossRef]
16. Bhuse, V.M.; Hankare, P.P.; Garadkar, K.M.; Khomane, A.S. A Simple, Convenient, Low Temperature Route to Grow Polycrystalline Copper Selenide Thin Films. *Mater. Chem. Phys.* **2003**, *80*, 82–88. [CrossRef]
17. Li, X.; Li, P.; Wu, Z.; Luo, D.; Yu, H.-Y.; Lu, Z.-H. Review and Perspective of Materials for Flexible Solar Cells. *Mater. Rep. Energy* **2021**, *1*, 100001. [CrossRef]
18. Yoon, H.; Kang, S.M.; Lee, J.K.; Choi, M. Hysteresis-Free Low-Temperature-Processed Planar Perovskite Solar Cells with 19.1% Efficiency. *Energy Environ. Sci.* **2016**, *9*, 2262–2266. [CrossRef]
19. Aernouts, T.; Vanlaeke, P.; Geens, W.; Poortmans, J.; Heremans, P.; Borghs, S.; Mertens, R.; Andriessen, R.; Leenders, L. Printable Anodes for Flexible Organic Solar Cell Modules. *Thin Solid Film.* **2004**, *451–452*, 22–25. [CrossRef]
20. Fonrodona, M.; Escarré, J.; Villar, F.; Soler, D.; Asensi, J.M.; Bertomeu, J.; Andreu, J. PEN as Substrate for New Solar Cell Technologies. *Sol. Energy Mater. Sol. Cells* **2005**, *89*, 37–47. [CrossRef]
21. Chen, H.; Gu, Z.G.; Zhang, J. Chiral-Induced Ultrathin Covalent Organic Frameworks Nanosheets with Tunable Circularly Polarized Luminescence. *J. Am. Chem. Soc.* **2022**, *144*, 7245–7252. [CrossRef] [PubMed]
22. Hassan, M.; Abbas, G.; Li, N.; Afzal, A.; Haider, Z.; Ahmed, S.; Xu, X.; Pan, C.; Peng, Z. Significance of Flexible Substrates for Wearable and Implantable Devices: Recent Advances and Perspectives. *Adv. Mater. Technol.* **2022**, *7*, 2100773. [CrossRef]
23. Wang, K.; Cheng, S.; Hu, Q.; Yu, F.; Cheng, Y.; Huang, K.; Yuan, H.; Jiang, J.; Li, W.; Li, J.; et al. Vertical Graphene-Coated Cu Wire for Enhanced Tolerance to High Current Density in Power Transmission. *Nano Res.* **2021**, *14*, 1–7. [CrossRef]
24. Chen, Y.; Gao, C.; Yang, T.; Li, W.; Xu, H.; Sun, Z.; Chen, Y.; Gao, C.; Yang, T.; Li, W.; et al. Research Advances of Ferroelectric Semiconductors of 2D Hybrid Perovskites toward Photoelectronic Applications. *Chin. J. Struct. Chem.* **2022**, *41*, 2204001–2204011. [CrossRef]
25. Chang, H.B.; Liu, J.B.; Dong, Z.; Wang, D.D.; Xin, Y.; Jiang, Z.L.; Tang, S.S. Enhancement of Photocatalytic Degradation of Polyvinyl Chloride Plastic with Fe_2O_3 Modified $AgNbO_3$ Photocatalyst under Visible-Light Irradiation. *Jiegou Huaxue* **2021**, *40*, 1595–1603. [CrossRef]
26. Vikulov, S.; di Stasio, F.; Ceseracciu, L.; Saldanha, P.L.; Scarpellini, A.; Dang, Z.; Krahne, R.; Manna, L.; Lesnyak, V. Fully Solution-Processed Conductive Films Based on Colloidal Copper Selenide Nanosheets for Flexible Electronics. *Adv. Funct. Mater.* **2016**, *26*, 3670–3677. [CrossRef]
27. Qu, C.; Hu, J.; Liu, X.; Li, Z.; Ding, Y. Morphology and Mechanical Properties of Polyimide Films: The Effects of UV Irradiation on Microscale Surface. *Materials* **2017**, *10*, 1329. [CrossRef]
28. Parodi, E.; Peters, G.W.M.; Govaert, L.E. Structure-Properties Relations for Polyamide 6, Part 1: Influence of the Thermal History during Compression Moulding on Deformation and Failure Kinetics. *Polymers* **2018**, *10*, 710. [CrossRef]
29. Janickis, V.; Petrašauskiene, N.; Žalenkiene, S.; Morkvenaite-Vilkoňciene, I.; Ramanavǐcius, A. Morphology of CdSe-Based Coatings Formed on Polyamide Substrate. *J. Nanosci. Nanotechnol.* **2018**, *18*, 604–613. [CrossRef]
30. Ivanauskas, R.; Milasiene, D. Fabrication of Polyamide-Ag2Se Composite Films with Controllable Properties by an Adsorption–Diffusion Method. *J. Phys. Chem. Solids* **2020**, *145*, 109533. [CrossRef]
31. Lakshmi, M.; Bindu, K.; Bini, S.; Vijayakumar, K.P.; Sudha Kartha, C.; Abe, T.; Kashiwaba, Y. Chemical Bath Deposition of Different Phases of Copper Selenide Thin Films by Controlling Bath Parameters. *Thin Solid Film.* **2000**, *370*, 89–95. [CrossRef]
32. Xu, S.; Wang, H.; Zhu, J.J.; Chen, H.Y. Sonochemical Synthesis of Copper Selenides Nanocrystals with Different Phases. *J. Cryst. Growth* **2002**, *234*, 263–266. [CrossRef]
33. Li, Y.D.; Fan, P.; Zheng, Z.H.; Luo, J.T.; Liang, G.X.; Guo, S.Z. The Influence of Heat Treatments on the Thermoelectric Properties of Copper Selenide Thin Films Prepared by Ion Beam Sputtering Deposition. *J. Alloy. Compd.* **2016**, *658*, 880–884. [CrossRef]
34. Güzeldir, B.; Sağlam, M. Using Different Chemical Methods for Deposition of Copper Selenide Thin Films and Comparison of Their Characterization. *Spectrochim. Acta Part A Mol. Biomol. Spectrosc.* **2015**, *150*, 111–119. [CrossRef]
35. Pathan, H.M.; Lokhande, C.D. Deposition of Metal Chalcogenide Thin Films by Successive Ionic Layer Adsorption and Reaction (SILAR) Method. *Bull. Mater. Sci.* **2004**, *27*, 85–111. [CrossRef]
36. Bragg, W.H.; Bragg Apr, W.L.; H Bragg, B.W.; Professor of Physics, C. The Reflection of X-Rays by Crystals. *Proc. R. Soc. London. Ser. A Contain. Pap. A Math. Phys. Character* **1913**, *88*, 428–438. [CrossRef]
37. Patterson, A.L. The Scherrer Formula for X-Ray Particle Size Determination. *Phys. Rev.* **1939**, *56*, 978. [CrossRef]

38. Nath, D.; Singh, F.; Das, R. X-Ray Diffraction Analysis by Williamson-Hall, Halder-Wagner and Size-Strain Plot Methods of CdSe Nanoparticles—A Comparative Study. *Mater. Chem. Phys.* **2020**, *239*, 122021. [CrossRef]
39. Ashraf, M.; Akhtar, S.M.J.; Khan, A.F.; Ali, Z.; Qayyum, A. Effect of Annealing on Structural and Optoelectronic Properties of Nanostructured ZnSe Thin Films. *J. Alloy. Compd.* **2011**, *509*, 2414–2419. [CrossRef]
40. Tauc, J.; Grigorovici, R.; Vancu, A. Optical Properties and Electronic Structure of Amorphous Germanium. *Phys. Status Solidi (B)* **1966**, *15*, 627–637. [CrossRef]
41. Makuła, P.; Pacia, M.; Macyk, W. How To Correctly Determine the Band Gap Energy of Modified Semiconductor Photocatalysts Based on UV-Vis Spectra. *J. Phys. Chem. Lett.* **2018**, *9*, 6814–6817. [CrossRef] [PubMed]
42. Petrović, M.; Gilić, M.; Ćirković, J.; Romčević, M.; Romčević, N.; Trajić, J.; Yahia, I. Optical Properties of CuSe Thin Films—Band Gap Determination. *Sci. Sinter.* **2017**, *49*, 167–174. [CrossRef]
43. Banerjee, S.S.; Janke, A.; Gohs, U.; Heinrich, G. Electron-Induced Reactive Processing of Polyamide 6/Polypropylene Blends: Morphology and Properties. *Eur. Polym. J.* **2018**, *98*, 295–301. [CrossRef]
44. Zhao, X.Y.; Zhang, B.Z. The Effects of Annealing (Solid and Melt) on the Time Evolution of the Polymorphic Structure of Polyamide 6. *J. Appl. Polym. Sci.* **2010**, *115*, 1688–1694. [CrossRef]
45. Minceva-Sukarova, B.; Najdoski, M.; Grozdanov, I.; Chunnilall, C.J. Raman Spectra of Thin Solid Films of Some Metal Sulfides. *J. Mol. Struct.* **1997**, *410–411*, 267–270. [CrossRef]
46. Malavekar, D.B.; Bulakhe, R.N.; Kale, S.B.; Patil, U.M.; In, I.; Lokhande, C.D. Synthesis of Layered Copper Selenide on Reduced Graphene Oxide Sheets via SILAR Method for Flexible Asymmetric Solid-State Supercapacitor. *J. Alloy. Compd.* **2021**, *869*, 159198. [CrossRef]

materials

MDPI

Article

Exploring the Biological and Chemical Properties of Emerging 3D-Printed Dental Resin Composites Compared to Conventional Light-Cured Materials

Nikola Živković [1], Stefan Vulović [2,*], Miloš Lazarević [3], Anja Baraba [4], Aleksandar Jakovljević [5,6], Mina Perić [7], Jelena Mitrić [8] and Aleksandra Milić Lemić [2]

1 Department of Restorative Odontology and Endodontics, School of Dental Medicine, University of Belgrade, Rankeova 4, 11000 Belgrade, Serbia; nikola.zivkovic@stomf.bg.ac.rs
2 Department of Prosthodontics, School of Dental Medicine, University of Belgrade, Rankeova 4, 11000 Belgrade, Serbia; aleksandra.milic@stomf.bg.ac.rs
3 School of Dental Medicine, University of Belgrade, Dr Subotića Starijeg 8, 11000 Belgrade, Serbia; milos.lazarevic@stomf.bg.ac.rs
4 University of Zagreb, School of Dental Medicine, Department of Endodontics and Restorative Dentistry, Gundulićeva 5, 10000 Zagreb, Croatia; baraba@sfzg.unizg.hr
5 Department of Pathophysiology, School of Dental Medicine, University of Belgrade, Dr Subotića Starijeg 1, 11000 Belgrade, Serbia; a.jakovljevic@stomf.bg.ac.rs
6 Research Laboratories, Implant-Research Center, School of Dental Medicine, University of Belgrade, Nebojšina 35, 11000 Belgrade, Serbia
7 Institute of Molecular Genetics and Genetic Engineering, University of Belgrade, Vojvode Stepe 444a, 11000 Belgrade, Serbia; mina.peric@imgge.bg.ac.rs
8 Institute of Physics, University of Belgrade, Pregrevica 118, 11000 Belgrade, Serbia; jmitric@ipb.ac.rs
* Correspondence: stefan.vulovic@stomf.bg.ac.rs

Abstract

Advances in additive manufacturing have accelerated the development of 3D-printed dental resin composites. These materials contain a higher proportion of organic matrix and less filler than light-cured representatives, which may affect their behavior in the oral environment. This study aimed to evaluate the biological and chemical properties of 3D-printed dental resin composites before and after artificial aging, and to compare them with the light-cured representative. Specimens from a light-cured composite (Omnichroma—OMCR) and two 3D-printed composites (GT Temp PRINT—GTPR; SprintRay CROWN—SPRY) were subjected to aging treatments: unaged (T0) or thermocycled for 5000 (T1) and 10,000 cycles (T2). Biological evaluation was performed using MTT assay and Live/Dead cell fluorescence microscopy using human gingival fibroblasts, whereas Raman spectroscopy analysed materials' structural changes. Materials exhibited good biocompatibility (>70% cell viability), with OMCR displaying greater variability. OMCR was more susceptible to chemical degradation under thermal stresses than both 3D-printed materials. Tested 3D-printed composites can provide comparable or even superior biological and chemical properties compared to light-cured representative, likely due to optimized resin formulations and post-curing protocols that improve polymer network organization and reduce residual monomer release. These findings support the potential of tested 3D-printed composites for manufacturing dental restorations.

Keywords: 3D-printed dental resin composites; biocompatibility; chemical stability; thermocycling

Academic Editor: Bongju Kim

Received: 24 October 2025
Revised: 5 November 2025
Accepted: 10 November 2025
Published: 14 November 2025

Citation: Živković, N.; Vulović, S.; Lazarević, M.; Baraba, A.; Jakovljević, A.; Perić, M.; Mitrić, J.; Milić Lemić, A. Exploring the Biological and Chemical Properties of Emerging 3D-Printed Dental Resin Composites Compared to Conventional Light-Cured Materials. *Materials* **2025**, *18*, 5170. https://doi.org/10.3390/ma18225170

1. Introduction

The emergence of three-dimensional (3D)-printed resins in restorative dentistry has significantly transformed clinical workflows, allowing for faster, more streamlined procedures and the fabrication of highly esthetic and functionally reliable indirect restorations. These materials, specifically developed for additive manufacturing, provide notable advantages in terms of customization, precision, and production efficiency. However, their unique composition, characterized by a higher proportion of resin matrix and lower filler content, raises certain concerns regarding biocompatibility, particularly related to the potential release of residual monomers. Maintaining the biocompatibility of dental materials is essential for preserving tissue integrity, supporting fibroblast activity, and ensuring patient safety [1]. Residual monomers released from composite restorations may diffuse through dentinal tubules toward the pulp or leach into the oral cavity [2]. When present in the oral environment, these compounds may enter systemic circulation through saliva or blood and exert systemic cytotoxicicity [3,4]. In addition, exposure to intraoral conditions, including fluctuations in pH, temperature, and moisture, induces physicochemical alterations in the resin, which may further affect its biological performance and compromise the long-term stability of restorations [5].

Although manufacturers rarely disclose detailed information about the resin matrix composition, filler morphology, or photoinitiator system, 3D-printed dental resin composites typically contain methacrylate-based monomers such as urethane dimethacrylate (UDMA), tetraethylene glycol dimethacrylate (TEGDMA), and 2-hydroxyethyl methacrylate (HEMA) [6]. These monomers have been shown to induce cytotoxic effects on human gingival cells [7,8], highlighting the importance of assessing the biological safety of these materials. The extent of monomer elution depends not only on the material's chemical formulation but also on printing parameters, post-curing procedures, and the type of additive manufacturing technology employed [9]. Currently, stereolithography (SLA) and digital light processing (DLP) are the two dominant 3D printing techniques in dentistry [10]. SLA cures the resin point-by-point using a focused ultraviolet (UV) laser, whereas DLP polymerizes entire layers simultaneously using a digital projector [11] and has become the preferred 3D printing method for dental applications owing to its enhanced fabrication efficiency. Regardless of the printing method, achieving a high degree of polymerization is crucial to minimize the release of leachable components, including residual monomers and photoinitiators [12], which are primarily responsible for the cytotoxicity of resin materials. However, polymerization never reaches complete conversion, since some methacrylate double bonds (C=C) remain unreacted [13]. The final chemical integrity of polymerized resins is influenced by the filler-to-matrix ratio, resin formulation, and curing efficiency [5]. Studies have shown that nano-filled composites and materials with lower filler content exhibit altered polymerization kinetics and reduced structural stability [14]. This is particularly relevant for 3D-printed materials, which typically feature a lower filler load. Therefore, evaluating the chemical structure and molecular stability of such materials is fundamental for validating their clinical performance.

Although several in vitro studies have demonstrated acceptable mechanical performance of 3D-printed dental resin composites [15–18], data concerning their biocompatibility and chemical stability remain scarce, especially after exposure to simulated aging conditions. Therefore, the present study aimed to evaluate the biological and chemical properties of 3D-printed dental resin composites intended for temporary and permanent fixed dental prostheses (FDPs) before and after artificial aging, and to compare them with the light-cured representative. The null hypotheses were that: 1. There would be no significant differences in cell viability among tested materials before and after aging. 2. There would

be no significant differences in chemical integrity among the tested materials before and after aging.

2. Materials and Methods

2.1. Specimen Preparation

A total of 126 disc-shaped specimens (5 mm in diameter, 2 mm in thickness) were prepared from three dental resin composite materials (Table 1), with 42 per each material (n = 42) (Figure 1). The total specimen size was calculated using G*Power 3.1.9.7 software (Heinrich Heine University, Düsseldorf, Germany) according to the F test and "ANOVA: fixed effects, main effects, and interactions" considering large effect size 0.4, α 0.05, power 0.95, numerator df 4, and 9 groups (3 materials × 3 aging treatments).

Table 1. Materials used in the study.

Name	Fabrication	Code	Matrix	Filler	Filler Load	Manufacturer
Omnichroma	Light-cured dental resin composite	OMCR	UDMA, TEGDMA	Spherical SiO_2-ZrO_2 fillers	79 wt. %	Tokuyama, Tokyo, Japan
GC Temp PRINT	3D-printed dental resin composite for temporary FDPs	GTPR	UDMA (MMA free)	Silica nanoparticles	~20 wt. %	GC Europe, Leuven, Belgium
SprintRay CROWN	3D-printed dental resin composite for permanent FDPs	SPRY	UDMA, TEGDMA, other dimethacrylates	Ceramic nanoparticles	>50 wt. %	SprintRay, Los Angeles, CA, USA

3D—three-dimensional; UDMA—urethane dimethacrylate; TEGDMA—tetraethylene glycol dimethacrylate; MMA—methyl methacrylate; FDP—fixed dental prostheses.

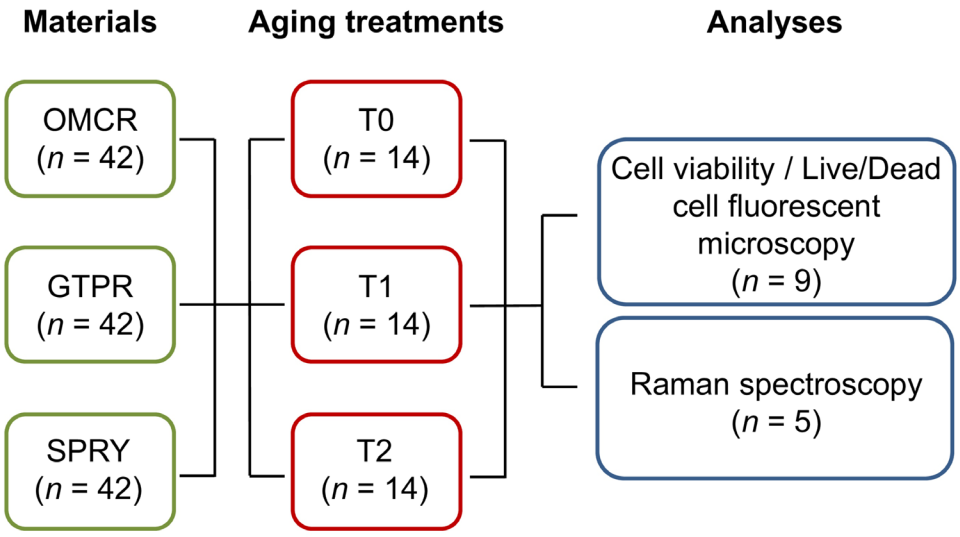

Figure 1. Number of specimens used in the study. OMCR—Omnichroma; GTPR—GC Temp PRINT; SPRY—SprintRay CROWN; T0—unaged; T1—aged for 5000 thermal cycles; T2—aged for 10,000 thermal cycles.

Specimens of tested light-cured composite (Omnichroma, Tokuyama, Tokyo, Japan) (OMCR) were fabricated following a standardized conventional procedure. The material was inserted into a silicone mold (5 mm × 2 mm), covered with a Mylar strip (SS White, Philadelphia, PA, USA) and a microscope glass slide, then gently pressed to obtain a smooth surface and eliminate voids. Polymerization was carried out through the Mylar strip and

glass for 20 s using a curing unit (Bluephase Style, Ivoclar Vivadent, Schaan, Liechtenstein) with an intensity of 1000 mW/cm^2.

Specimens of 3D-printed composite for temporary (GC Temp PRINT, GC Europe, Leuven, Belgium) (GTPR) and permanent FDPs (SprintRay CROWN, SprintRay, Los Angeles, CA, USA) (SPRY) were designed to match required dimensions using software (Exocad 3.0, Darmstadt, Germany), exported as standard tessellation language (STL), and processed in another software (AccuWare V3.2.0.60, Shining 3D, Hangzhou, China). Printing was performed on a DLP printer (AccuFab-L4D, Shining 3D) under the following parameters: 90° build orientation, 50 µm layer thickness, and 405 nm wavelength. To prevent cross-contamination, a dedicated resin tray was used for each material. All 3D-printed specimens exhibited a solid internal structure that remained unchanged during the entire experimental procedure. After printing, the specimens were cleaned in 90% isopropyl alcohol using a cleaning system (FH-WA-01, Formlabs, Somerville, MA, USA) for 20 min, air-dried, and post-cured in a UV unit (FabCure 2, Shining 3D) for 30 min, following the manufacturers' recommendations. Support structures were removed after curing.

All specimens were subsequently polished with silicon carbide abrasive papers (grits 600–1200, Buehler, Lake Bluff, IL, USA) under continuous water cooling for 20 s per side to ensure a uniform surface before further analyses. Final dimensions were confirmed using a digital caliper (Lukas Tools, Vogel, Kevelaer, Germany).

Before aging, all specimens were stored in distilled water at 37 °C for 24 h to stabilize the cross-linked polymer matrix and to remove residual unreacted monomers that could influence subsequent testing, in compliance with International Organization for Standardization (ISO) 7405:2025 [19] and previous research [20].

2.2. Aging Protocol

The specimens were randomly assigned to three independent aging treatments (n = 14) (Figure 1). In the first treatment, the specimens were unaged (T0). The specimens of the other two subgroups were subjected to thermocycling using a dedicated device (Thermo Cycler THE 1200, SD Mechatronik, Feldkirchen-Westerham, Germany). The procedure was adapted from the previously described protocol [21] and involved alternating immersion in cold (5 °C) and hot (55 °C) water baths, with a dwell time of 60 s in each bath and a transfer interval of 10 s between them, through 5000 (T1) and 10,000 cycles (T2) cycles. To minimize microbial growth, the specimens were rinsed with distilled water and placed in freshly prepared solutions every three days during the aging period.

2.3. Cell Viability

2.3.1. Cell Culture

Evaluation of biological properties was carried out using primary human gingival fibroblast (HGF) cultures derived from three healthy donors (aged 18–22 years) who underwent surgical extraction of impacted mandibular third molars. The study was conducted in accordance with the Declaration of Helsinki, and approved by the Institutional Ethics Committee. Informed consent was obtained from all participants involved in the study.

HGFs were isolated using the explant technique [22]. Gingival tissue samples (approximately 3 mm^2) obtained during surgery were immediately transferred to the cell culture laboratory in sterile containers. Samples were washed twice with phosphate-buffered saline (PBS) containing 1% antibiotic–antimycotic solution, finely sectioned with a sterile scalpel, and placed in T25 culture flasks. Cells were cultured in complete growth medium consisting of high-glucose Dulbecco's Modified Eagle Medium (DMEM) (Gibco, Thermo Fisher Scientific, Waltham, MA, USA), supplemented with 10% heat-inactivated fetal bovine serum and 1% antibiotic–antimycotic solution. Cultures were incubated at 37 °C in a hu-

midified atmosphere containing 5% CO_2. The culture medium was renewed every 48–72 h, and cells were subcultured at approximately 80% confluence using 0.05% TrypLE (Gibco, Thermo Fisher Scientific) for 7 min at 37 °C. Cells from passages 3 and 4 were employed in all assays to ensure experimental reproducibility and minimize inter-donor variability. To confirm cell identity and purity, characterization of the isolated HGFs was performed using flow cytometry [23].

2.3.2. Preparation of the Eluates

Within each group, nine specimens were designated for cell viability testing (n = 9) (Figure 1). Prior to testing, specimens were cleaned in an ultrasonic bath (US20, JSP, Chiyoda-ku, Tokyo, Japan) using 98% isopropanol for 2 min, followed by air drying under sterile conditions. Conditioned media were prepared in accordance with ISO 10993-12:2021 [24]. The surface area-to-volume ratio was standardized at 2.2 cm^2 per 0.73 mL of complete growth medium. Specimens were incubated in complete growth medium at 37 °C in a humidified atmosphere containing 5% CO_2 for 24 h to allow the leaching of potential cytotoxic components. The resulting eluates were collected and used for subsequent cell viability assays.

2.3.3. MTT Assay

HGFs were seeded in 96-well plates at a density of 10,000 cells/well in 100 µL of complete growth medium and incubated for 24 h at 37 °C in a humidified atmosphere containing 5% CO_2 to allow the formation of a semi-confluent monolayer. After reaching semi-confluency, the growth medium was replaced with the previously prepared composite eluates, and the cells were incubated for 24 h, 48 h, and 72 h, in accordance with ISO 10993-5:2021 [25] and previous research [26]. Before assessing cell viability, cell culture supernatants were collected at each time point and stored at −80 °C for subsequent analyses.

A 3-(4,5-dimethylthiazol-2-yl)-2,5-diphenyltetrazolium bromide (MTT) (Sigma-Aldrich, St. Louis, MO, USA) at a concentration of 5 mg/mL in DMEM (Gibco, Thermo Fisher Scientific) was used for determination of cell viability. MTT solution was added to each well and incubated for 4 h at 37 °C. The resulting formazan crystals were solubilized by adding 100 µL of dimethyl sulfoxide (Sigma-Aldrich), and absorbance was measured at 570 nm using a microplate reader (RT-2100C, Rayto, Guangming, Shenzhen, China). All experiments were performed in technical triplicate and independently repeated three times.

Cell viability (%) was calculated relative to the control (cells cultured in complete growth medium only, set as 100%) using the following formula:

$$Cell\ viability\ (\%) = \frac{\left(OD_{sample} - OD_{blank}\right)}{\left(OD_{PC} - OD_{blank}\right)} \times 100$$

where OD represents the optical density, OD_{sample} corresponds to the absorbance of the test sample, OD_{blank} indicates the background absorbance, and OD_{PC} refers to the absorbance of the control.

The cytotoxic response to the tested resins was classified according to ISO 10993-12:2021 [24] as follows: non-cytotoxic (>90% survival), slightly cytotoxic (60–90% survival), moderately cytotoxic (30–60% survival), and severely cytotoxic (<30% survival).

2.4. Live/Dead Cell Fluorescent Microscopy

HGFs were seeded in 24-well plates at a density of 1×10^4 cells/well and cultured in complete growth medium under standard conditions (37 °C, 5% CO_2). After 24 h of initial incubation, the medium was replaced with the previously prepared materials specimens' eluates, followed by additional 24 h incubation. Cell viability was evaluated

using the Live/Dead cell imaging kit (488/570) (Cat. No. R37601, Invitrogen, Thermo Fisher Scientific), according to the manufacturer's instructions. Briefly, the culture medium was removed, cells were rinsed with PBS, and then incubated in 2× staining solution for 15 min at room temperature. Fluorescence imaging was performed using a microscope (Axiovert 5, Zeiss, Oberkochen, Germany) equipped with an LD A-Plan 20×/0.35 objective lens and Fluorescein Isothiocyanate (FITC)/Tetramethylrhodamine Isothiocyanate (TRITC) filter sets to visualize live (green fluorescence) and dead (red fluorescence) cells. Cells cultivated in complete growth medium served as the positive control, whilst cells exposed to 96% ethanol for 5 min were designated as the negative control.

2.5. Raman Spectroscopy

To evaluate the initial chemical integrity of the tested materials and to monitor possible structural changes following artificial aging, Raman spectroscopy was performed on the surfaces of five specimens per each group (n = 5) (Figure 1). Measurements were carried out using a commercial NTegra Spectra system (NT-MDT, Moscow, Russia) equipped with a confocal optical microscope. A diode-pumped solid-state laser operating at 532 nm served as the excitation source. The laser power at the sample surface was set to 2 mW and focused within an area of approximately 0.5 × 0.5 μm^2. Spectra were collected with an exposure time of 360 s per measurement, covering a spectral range of 400–1800 cm^{-1} with a spectral resolution of 2–4 cm^{-1}. Prior to each measurement, the spectrometer was calibrated using the first-order silicon band at 520.7 cm^{-1}. All spectra were recorded in an unpolarized configuration to minimize orientation-dependent spectral variations.

2.6. Statistical Analysis

Cell viability data were analysed using statistical software (SPSS 22.0, Chicago, IL, USA). The normality of data distribution was confirmed using the Kolmogorov-Smirnov test. Comparisons among materials within the same aging treatment, as well as comparisons among independent aging treatments within the same material, were performed using one-way analysis of variance (ANOVA), followed by Tukey's post hoc test. Data were presented as mean ± standard deviation (SD). All p values of <0.05 were considered statistically significant.

3. Results

3.1. Cell Viability

The results of the cell viability assay are presented in Figures 2 and 3.

Regarding the comparison among materials within the same aging treatment (Figure 2), at T0, all tested materials exhibited cell viability above the biocompatibility threshold of 70%. OMCR showed the lowest viability among the tested materials, significantly lower than the control after 24 h ($p < 0.05$). GTPR and SPRY demonstrated slightly higher viability, but without statistically significant differences compared to OMCR ($p > 0.05$). Similar trends were observed after 48 h, with no significant differences among the materials ($p > 0.05$), although all values remained significantly lower than those of the control ($p < 0.05$). After 72 h, OMCR again showed the lowest viability and was the only material with significantly lower viability compared to the control ($p < 0.05$).

At T1, after 24 h, OMCR and GTPR exhibited significantly lower viability than the control ($p < 0.05$), while SPRY showed no significant difference ($p > 0.05$). After 48 h, viability increased in all materials, with no significant differences compared to the control ($p > 0.05$). This trend continued after 72 h, where all materials showed further increases in viability, exceeding control values, though differences remained non-significant ($p > 0.05$).

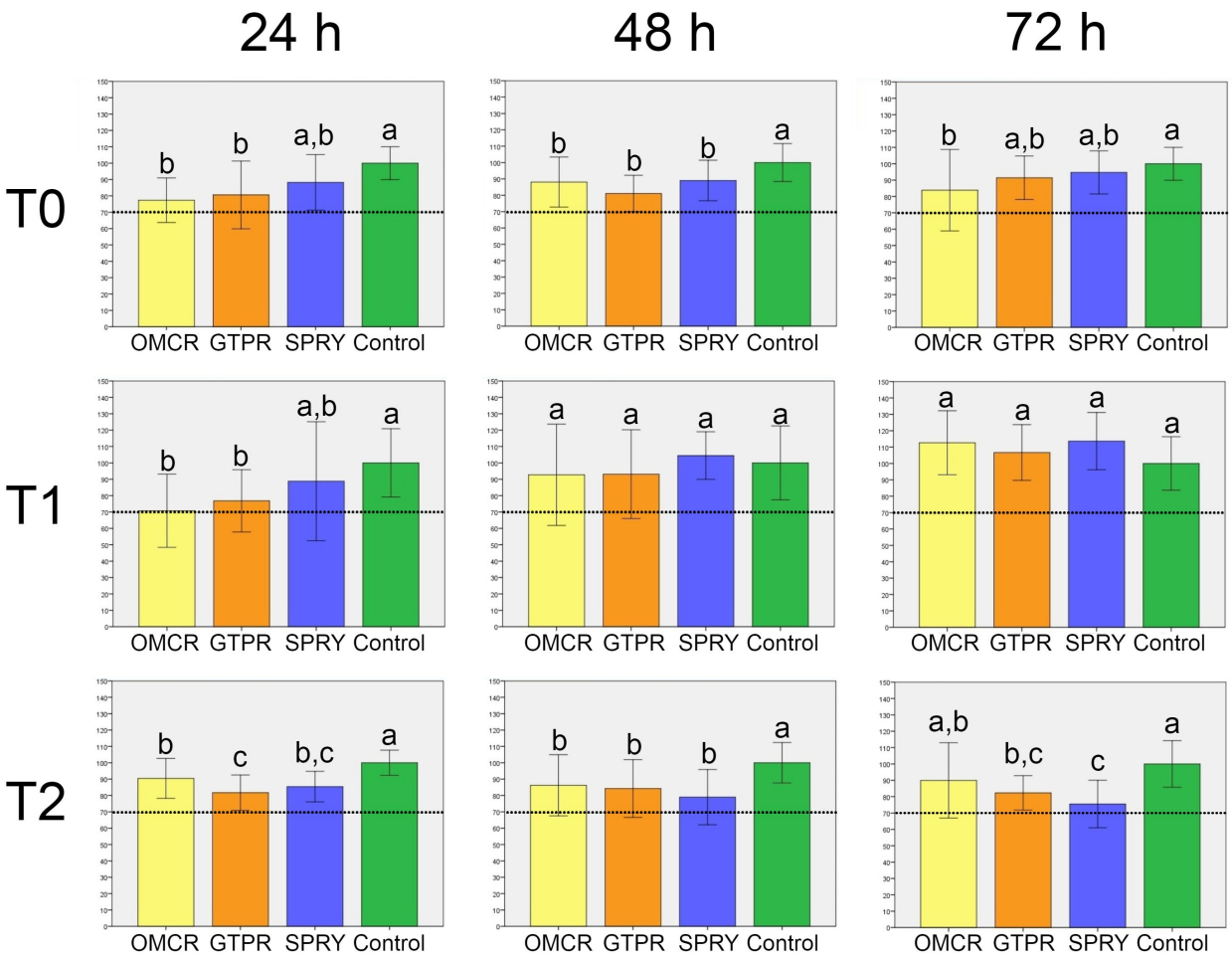

Figure 2. Cell viability (%) (mean ± standard deviation (SD)) of the tested materials (comparison among materials within the same aging treatment). OMCR—Omnichroma; GTPR—GC Temp PRINT; SPRY—SprintRay CROWN; T0—unaged; T1—aged for 5000 thermal cycles; T2—aged for 10,000 thermal cycles; Dotted lines—70% cell viability; Bars that do not share the same letter differ significantly from each other ($p < 0.05$; Tukey's post hoc test).

At T2, across all time points (24 h, 48 h, and 72 h), cell viability in all materials was significantly lower than in the control ($p < 0.05$), except between OMCR and control after 72 h ($p > 0.05$). Statistically significant differences were observed between OMCR and GTPR after 24 h, and between OMCR and SPRY after 72 h ($p < 0.05$).

Regarding the comparison among independent aging treatments within the same material (Figure 3), OMCR exhibited significantly lower cell viability at T0 and T1 compared to T2 after 24 h ($p < 0.05$), and at T0 and T2 compared to T1 after 72 h ($p < 0.05$). No other comparisons within OMCR showed statistically significant differences ($p > 0.05$).

For GTPR, significant differences were observed only after 72 h, where cell viability at T1 was significantly higher than T0 and T2 ($p < 0.05$). All other comparisons were not statistically significant ($p > 0.05$).

In the SPRY, cell viability was significantly higher at T1 compared to both T0 and T2 after 48 h and 72 h ($p < 0.05$).

3.2. Live/Dead Cell Fluorescent Microscopy

Representative micrographs of fluorescent live/dead staining of HGFs incubated for 24 h with eluates from unaged tested materials' specimens are presented in Figure 4. Micrographs of all tested materials showed extensive green fluorescence, indicating a high proportion of viable cells. The staining pattern closely resembled that of the positive

control, which predominantly exhibited green-fluorescent viable cells, in contrast to the negative control micrograph showing uniform red fluorescence, characteristic of non-viable cell populations.

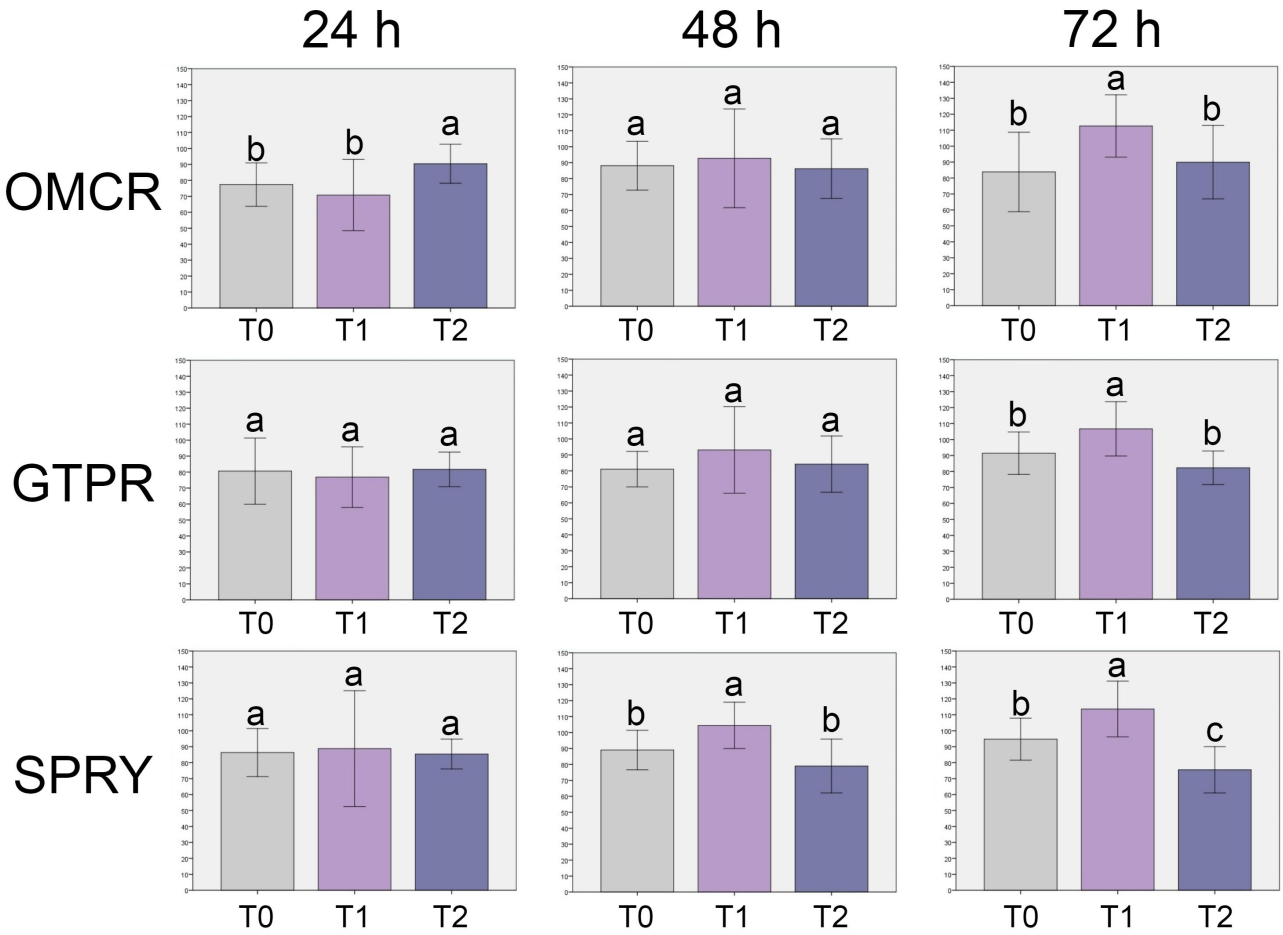

Figure 3. Cell viability (%) (mean ± standard deviation (SD)) of the tested materials (comparison among aging treatments within the same material). OMCR—Omnichroma; GTPR—GC Temp PRINT; SPRY—SprintRay CROWN; T0—unaged; T1—aged for 5000 thermal cycles; T2—aged for 10,000 thermal cycles; Dotted lines—70% cell viability; Bars that do not share the same letter differ significantly from each other ($p < 0.05$; Tukey's post hoc test).

3.3. Raman Spectroscopy

Raman spectra of the tested materials' specimens are presented in Figure 5.

Raman spectra revealed distinct differences in the response of the investigated composites to thermal aging. Representative OMCR spectra demonstrated a progressive reduction in band intensity, particularly in the C–H stretching region (2880–3068 cm^{-1}), accompanied by broadening of the carbonyl peak around ~1716 cm^{-1}, suggesting high sensitivity to thermal aging. All major band assignments of OMCR samples are presented in Table 2.

Representative GTPR spectra initially exhibited increased intensity of characteristic bands after 5000 cycles, notably the C–H stretching doublet at 2929 and 2954 cm^{-1}, as well as the aromatic and carbonyl peaks near ~1003 and ~1711 cm^{-1}. Following 10,000 cycles, a partial reduction in intensity was observed in the carbonyl region, suggesting minor structural changes. All major band assignments of OMCR samples are presented in Table 3.

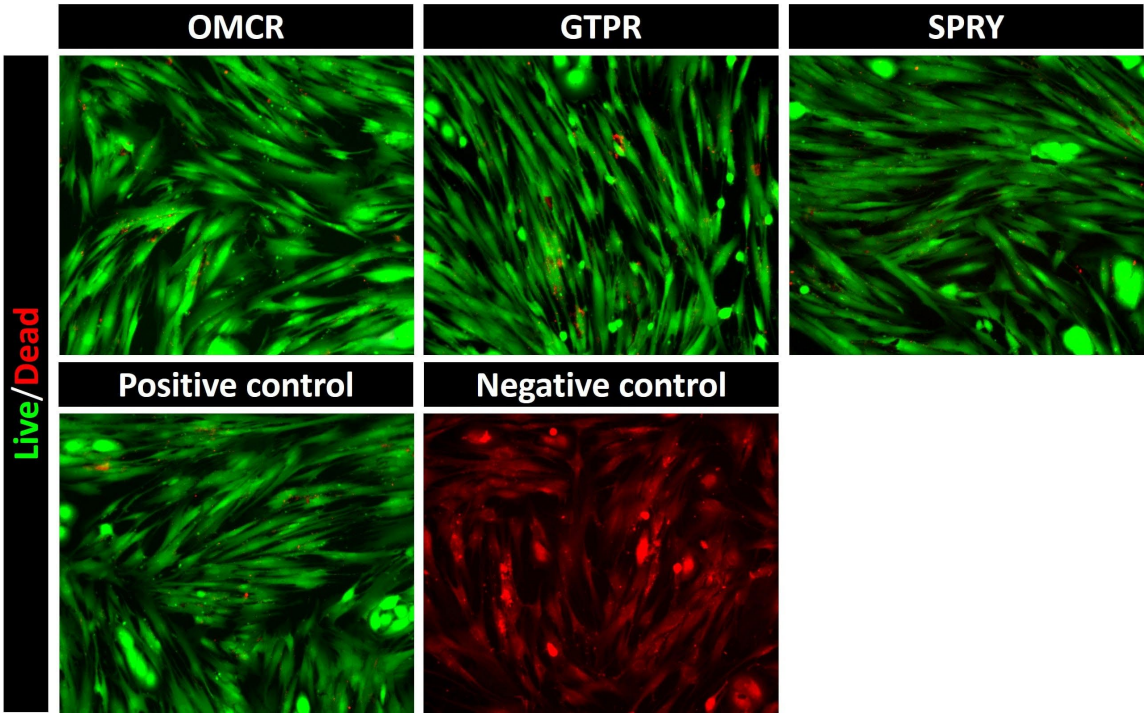

Figure 4. Live/Dead cell fluorescent microscopy analysis of human gingival fibroblasts (HGF) treated with tested materials' specimen eluates. Representative micrographs were recorded at ×20 magnification. OMCR—Omnichroma; GTPR—GC Temp PRINT; SPRY—SprintRay CROWN.

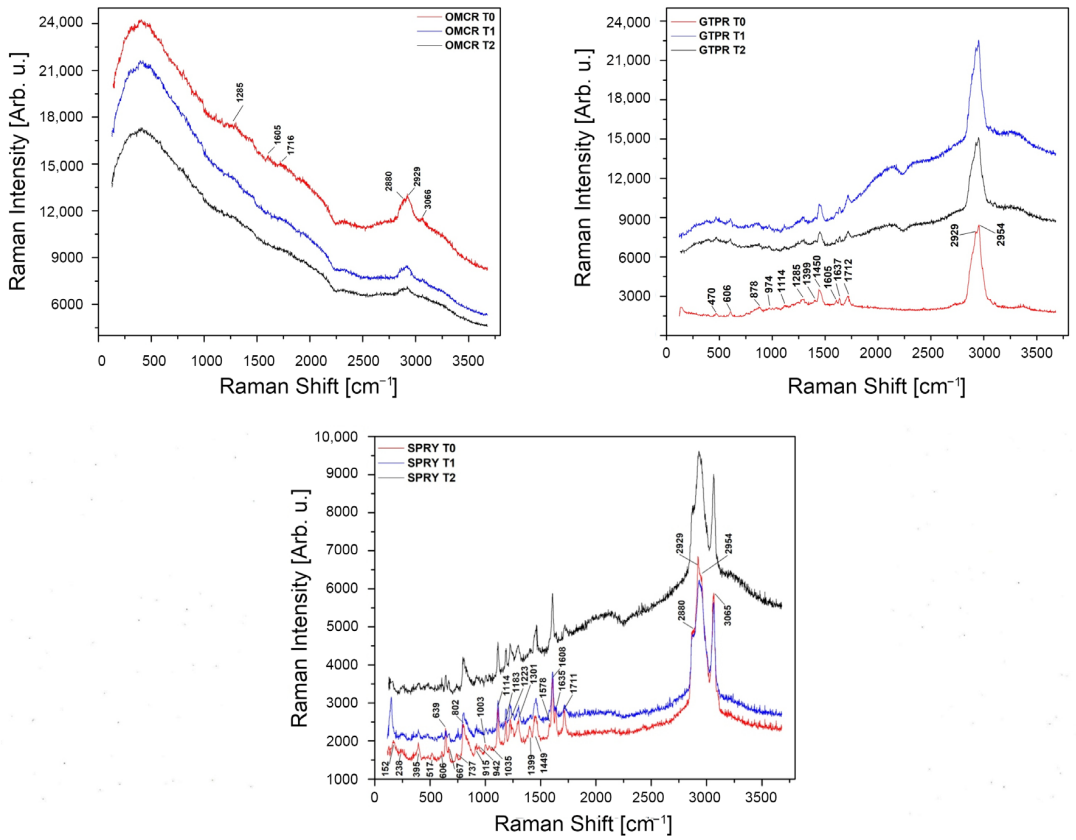

Figure 5. Raman spectra of the tested materials' specimens. OMCR—Omnichroma; GTPR—GC Temp PRINT. SPRY—SprintRay CROWN. Each spectrum is consisting of three curves: red—T0 (unaged specimens), blue—T1 (specimens aged for 5000 thermal cycles), and black—T2 (specimens aged for 10,000 thermal cycles).

Table 2. Raman bands assignations of Omnichroma (OMCR) specimens.

Raman Active Band [cm^{-1}]	Assignment	Reference
1285	Asymmetric C–C–O stretching	[27]
1605	C=C stretching	[28]
1716	C=O stretching	[29]
2880	Symmetric CH_2/CH_3 stretching	[13,30]
2929	Asymmetric CH_2/CH_3 stretching	[28]
3066	=C–H stretching	[29]

Table 3. Raman bands assignations of GC Temp PRINT (GTPR) specimens.

Raman Active Band [cm^{-1}]	Assignment	Reference
~470	Si–O–Si bending	[31]
606	Si–O/ring deformation	[13]
878	C–O–C stretching	[29]
974	C–O–C stretching	[29]
1114	C–O stretching of ester linkages	[28]
1285	Asymmetric C–C–O stretching	[32]
1399	CH_2 scissoring/CH_3 deformation	[13]
1450	CH_2 scissoring/CH_3 deformation	[13]
1605	C=C stretching	[28]
1637	C=C stretching	[28]
1712	C=O stretching	[30]
2929	CH_2/CH_3 asymmetric stretching	[30]
2954	CH_2/CH_3 asymmetric stretching	[30]

Figure 5 also depicts representative spectra of SPRY specimens before and after thermocycling, with key band assignments summarized in Table 4. The control spectrum displayed well-defined and intense bands across all major modes. Even after thermocycling, the C–H stretching and carbonyl bands remained sharp and prominent, with only minor intensity variations. Distinct aromatic (~1003 cm^{-1}) and carbonyl (~1711 cm^{-1}) peaks were consistently observed, indicating that SPRY maintained its chemical structure with negligible changes following aging.

Table 4. Raman bands assignations of SprintRay CROWN (SPRY) specimens.

Raman Active Band [cm^{-1}]	Assignment	Reference
238	Zr–O stretching	[31]
395	Mixed metal–oxygen	[31]
517	Si–O	[13]
606	Si–O	[13]
639	Si–O	[13]
667	Si–O	[13]
737	Si–O	[13]
802	C–O–C vibration	[29]
915	C–O–C vibration	[29]
942	C–O–C vibration	[29]
1003	Aromatic ring breathing	[30]
1035	C–O stretching	[28]
1114	C–O stretching	[28]
1183	Asymmetric C–C–O stretching	[32]
1223	Asymmetric C–C–O stretching	[32]
1301	Asymmetric C–C–O stretching	[32]
1399	CH_2/CH_3 deformation	[30]
1449	CH_2/CH_3 deformation	[30]
1578	C=C stretching	[28]

Table 4. *Cont.*

Raman Active Band [cm^{-1}]	Assignment	Reference
1608	C=C stretching	[28]
1635	C=C stretching	[28]
1711	C=O stretching	[13]
2880	CH_2/CH_3 asymmetric stretching	[30]
3065	=C–H stretching	[29]

4. Discussion

This study investigated the biological and chemical properties of light-cured and 3D-printed dental resin composites before and after artificial aging. Biological evaluation integrated cell viability of HGFs obtained through MTT assay and Live/Dead cell fluorescence microscopy to qualitatively validate the biocompatibility findings for eluates derived from unaged specimens. Chemical integrity, molecular and structural changes in the tested materials were analysed using Raman spectroscopy. This technique provided detailed insights into molecular vibrations, polymer chain organization, and bond stability within the resin matrix, making it a valuable tool for detecting structural rearrangements, degradation, and post-curing reactions [33]. The combination of biological and chemical assessment methods enabled a more comprehensive understanding of material performance after simulated aging. HGFs were selected as the cell model due to their high metabolic activity, anatomical proximity to restorative margins, prolonged exposure to dental materials, and key role in extracellular matrix remodeling and soft tissue repair. These features make HGFs among the first cells to interact with substances released from restorative materials, establishing them as a relevant and widely accepted in vitro model for assessing the biological response to dental resin composites [34]. In addition to HGFs, other cell types have been utilized in similar investigations, including human gingival keratinocytes [35], dental pulp stem cells [36], human leukocytes [37], as well as various fibroblast lineages [38,39]. The experimental timeline in this study was designed to assess the acute cellular response, with cell viability monitored daily for up to 72 h. Analyses were performed before (T0) and after thermocycling (T1 and T2). Thermocycling was employed as an in vitro aging procedure to simulate thermal fluctuations in the oral environment, ranging from 5 °C to 55 °C, thus reproducing clinical exposure to hot and cold stimuli [40]. The process was achieved through 5000 cycles to simulate six months (T1), and 10,000 cycles to simulate one year of clinical service (T2), according to previous studies [41,42]. Although thermocycling was conducted to more closely approximate intraoral conditions, some authors have argued that the applied temperature range may be excessively broad and not entirely representative of real clinical circumstances [21]. Conversely, accelerated aging protocols involving intensified environmental stressors are often used to estimate material longevity, as they provide insights into degradation kinetics under controlled conditions and allow extrapolation of the time required for the material to reach its failure point [40]. Additionally, thermally induced fatigue within polymer networks can cause several detrimental effects, including water sorption, polymer swelling, matrix breakdown, leaching of residual monomers, and molecular rearrangements. These phenomena may substantially impair biological behavior and chemical stability of the dental resin composites [43,44].

With regard to the cell viability, at T0, all tested materials demonstrated lower cell viability compared with the control, however, the values remained above the critical 70% threshold, indicating slightly cytotoxic behavior and, therefore, acceptable biocompatibility. Light-cured OMCR exhibited the lowest viability values at T0 after each 24 h, suggesting potential early-stage cytotoxic effects. Nevertheless, this was followed by recovery in later aging stages, particularly at T1, after 48 h and 72 h, reflecting the dynamic nature of

material-cell interactions. These findings are consistent with previous research [45], where it was also observed an initial decline in cell viability for OMCR, followed by subsequent stabilization. This behavior may be associated with incomplete monomer-to-polymer conversion and ongoing in situ polymerization, resulting in a higher initial release of residual monomers. Among the 3D-printed composites, at T0, GTPR exhibited lower cell viability compared to SPRY, likely due to the synergistic effect of filler reinforcement and optimized post-curing parameters. However, both materials showed progressive improvement at T1, indicating increased biological stability. This pattern may be attributed to the early release of unreacted monomers, followed by continued post-curing polymerization and reduced leaching during storage, which collectively diminished cytotoxic effects. Similar results were reported in recent study [46], in which this phenomenon was linked to decreased monomer mobility within the polymer network over time, thereby limiting further release of residual compounds. At T1, the tested materials' biological response stabilized, particularly after 48 h and 72 h. It seems that after 5000 cycles, the polymer matrix acted as a protective barrier, mitigating structural fatigue and minimizing the release of unreacted monomers. Interestingly, OMCR, that previously demonstrated significantly lower cell viability compared to control at T0 after each period, showed notable improvement following aging, even surpassing control value after 72 h. This observation is consistent with the findings of the previous research [44], which reported a progressive increase in the degree of conversion (DC) during the first 4000 thermal cycles of a commercial dental composite. The observed fluctuations in cell viability in OMCR, reflected by higher standard deviations at specific time points, may result from inherent biological variability or subtle differences in experimental conditions. Such variability highlights the necessity of incorporating multiple observation intervals and complementary analytical methods when evaluating the biological performance of dental materials. Following 10,000 thermal cycles (T2), all tested materials showed lower cell viability compared to control after each 24 h, 48 h, and 72 h periods; however, values remained above the established biocompatibility threshold. The reason for decreased cell viability at T2 might be the fact that repeated thermal expansion and contraction likely induced internal stresses and fatigue within the polymer matrix, leading to microstructural defects [47] that contributed to the delayed release of residual monomers from dental composites [48]. Among the 3D-printed composites, at T2, after 48 h and 72 h, GTPR exhibited slightly higher cell viability than SPRY for the first time, although the difference was not significant.

Live/Dead cell fluorescent micrographs confirmed good cell viability among all materials, with predominantly green-fluorescent viable cells observed in cultures exposed to eluates from all tested materials. The cell morphology and density were comparable to those of the positive control, indicating that the released substances did not induce cytotoxic effects or morphological alterations in HGFs. In contrast, the negative control displayed exclusively red-fluorescent, non-viable cells, thereby confirming the reliability and sensitivity of the assay. These results collectively demonstrate that tested materials exhibit favorable short-term biocompatibility profiles.

Considering all aforementioned, the first null hypothesis that no significant differences would be found in cell viability among tested materials before and after aging was rejected.

With regard to the evaluation of tested materials' chemical integrity using Raman spectroscopy analysis, OMCR exhibited the greatest susceptibility to thermal stress, characterized by a gradual decrease in C–H stretching intensity and broadening of the carbonyl band that represent spectroscopic features commonly associated with polymer chain scission, oxidation, and weakened filler–matrix coupling [49–51]. These structural modifications indicate that OMCR may be more prone to degradation when subjected to clinically relevant temperature variations. In contrast, GTPR initially responded to 5000 thermocycles

with an increase in C–H vibrational intensity, suggesting thermally activated secondary curing of residual double bonds. This phenomenon aligns with the transient improvement in cell viability observed at earlier intervals. The persistence of distinct C–H and C–O peaks indicates the formation of a denser and more cross-linked polymer network with restricted chain mobility [52]. However, prolonged exposure to thermal cycling (10,000 cycles) led to broadening of the carbonyl region and partial reduction of C=C bands, signifying the onset of hydrolytic degradation processes [53,54]. SPRY demonstrated higher structural stability, maintaining intense and sharp vibrational bands corresponding to aromatic and carbonyl groups, which remained largely unchanged after thermocycling. These results underscore the superior molecular integrity under simulated intraoral conditions of SPRY [55,56].

Considering all aforementioned, the second null hypothesis that no significant differences in chemical integrity among the tested materials before and after aging was also rejected.

The obtained findings suggest that properly processed 3D-printed composites can achieve comparable and even superior biological and chemical properties than conventional light-cured materials. Although the complete composition of the 3D-printed dental resin composites is mostly not disclosed, these materials usually contain common organic components such as UDMA and TEGDMA, whereas they differ mainly in filler type, content, and distribution. These variations, together with differences in polymerization mode, likely account for the distinct biological and chemical behavior of 3D-printed dental resin composites observed in the literature. In accordance with this statement, in the present study, despite the higher organic matrix fraction and lower filler content compared to light-cured representative, tested 3D-printed composites did not exhibit substantial degradation or monomer release. This stability may be attributed to a more homogeneous filler dispersion, which reduced the effective volume of the resin matrix and limited the proportion of unpolymerized monomers [57,58], as also seen in previous studies [59,60]. Furthermore, strict compliance with optimized post-curing protocols has been shown to markedly increase the degree of monomer conversion, enhance chemical stability, and minimize cytotoxic responses in gingival fibroblasts, ensuring cytotoxicity remains well below clinically relevant thresholds [46,61].

This study has several limitations that should be acknowledged. First, only one light-cured composite and two 3D-printed composites were evaluated. Therefore, the findings cannot be generalized to all restorative materials produced using these technologies but instead reflect the behavior of the selected products under the specific experimental conditions applied. Future investigations should include a wider spectrum of materials to better capture the variability associated with resin chemistry, filler composition, and manufacturing protocols. Likewise, the experiments were conducted under in vitro conditions using HGFs as a single-cell model. Although HGFs are relevant and widely accepted for assessing soft tissue responses, the absence of other biological factors, such as saliva, enzymes, oral microbiota, and immune components, limits direct extrapolation of the findings to the complex in vivo environment. Furthermore, the biological assessment was restricted to viability-based assays (MTT and Live/Dead staining), without inclusion of complementary endpoints such as oxidative stress generation, inflammatory cytokine release, or apoptotic signaling. Incorporating such analyses in future studies would provide a more comprehensive understanding of the cellular responses elicited by different materials. Moreover, the artificial aging simulation was limited to thermocycling at 5000 and 10,000 cycles, corresponding approximately to six months and one year of clinical function, respectively. While this approach is suitable for materials primarily designed for temporary restorations, extended aging protocols are required to evaluate the long-term durability of definitive restorative materials. Mechanical properties, including flexural

strength, surface hardness, and wear resistance, were not examined, although these parameters are critical for predicting clinical performance under hydrothermal stress. Finally, chemical characterization relied exclusively on Raman spectroscopy. While Raman analysis provided valuable molecular-level insights into polymer network changes and degradation mechanisms, it cannot identify the degree of monomer conversion and leaching of unreacted components that may affect materials' behavior. Therefore, additional analytical techniques, such as Fourier-transform infrared spectroscopy (FTIR), scanning electron microscopy with energy-dispersive X-ray spectroscopy (SEM/EDS), or X-ray photoelectron spectroscopy (XPS), would offer a more detailed characterization of surface morphology, elemental composition, and chemical bonding. Likewise, introducing the quantitative measurements of residual or released monomers in eluates may provide further insight into material stability and potential cytotoxic effects. Nevertheless, the findings of this study might be useful for clinical practice. The demonstrated favorable biocompatibility and chemical stability of 3D-printed dental resin composites indicate that these materials can be safely employed for provisional restorations and potentially for definitive restorations when processed under optimized post-curing protocols. Moreover, clinicians are advised to strictly adhere to manufacturer-recommended post-curing procedures to maximize polymer network conversion and minimize residual monomer release, thereby enhancing long-term performance and ensuring patient safety. However, future clinical studies are essential to confirm these findings.

5. Conclusions

Within the limitations of this study, the following conclusions can be drawn:

1. All tested materials demonstrated cell viability levels consistently above the established biocompatibility threshold. Tested light-cured composite showed the greatest variability in its biocompatibility profile, whereas the 3D printed composites exhibited a more stable biological response across all evaluation stages.
2. The light-cured composite displayed greater susceptibility to chemical degradation under thermal stress compared to both tested 3D-printed composites.
3. When properly processed, 3D-printed composites can offer comparable or even superior biocompatibility and chemical integrity compared to the light-cured composite. This is likely due to optimized resin formulations and post-curing protocols that promote improved polymer network organization and reduce residual monomer release, supporting their potential for clinical application in provisional and, possibly, definitive restorative procedures.

Author Contributions: Conceptualization, N.Ž., A.J. and A.M.L.; Methodology, A.M.L.; Software, N.Ž. and M.L.; Validation, S.V. and A.J.; Formal analysis, M.L., A.B., M.P. and J.M.; Investigation, N.Ž., S.V., M.L., A.B., M.P. and J.M.; Resources, A.J. and A.M.L.; Data curation, N.Ž., S.V., A.B. and J.M.; Writing—original draft preparation, N.Ž., M.L., A.B., M.P. and J.M.; Writing—review and editing, S.V., A.J. and A.M.L.; Visualization, N.Ž.; Supervision, A.J. and A.M.L.; Project administration, A.M.L.; Funding acquisition, M.P. and A.M.L. All authors have read and agreed to the published version of the manuscript.

Funding: This research was funded by Ministry of Science, Technological Development and Innovation of the Republic of Serbia, grant numbers 451-03-136/2025-03/200042 and 451-03-137/2025-03/200129.

Institutional Review Board Statement: The study was conducted in accordance with the Declaration of Helsinki, and approved by the Institutional Ethics Committee of School of Dental Medicine, University of Belgrade (No 36/12 from 16 April 2024).

Informed Consent Statement: Informed consent was obtained from all participants involved in the study.

Data Availability Statement: The original contributions presented in this study are included in the article. Further inquiries can be directed to the corresponding author.

Acknowledgments: The authors would like to thank the dental laboratory "Dental M Press" and Maja Šćepanović for technical support in producing materials specimens.

Conflicts of Interest: The authors declare no conflicts of interest.

Abbreviations

The following abbreviations are used in this manuscript:

3D	Three-dimensional
DC	Degree of conversion
DLP	Digital light processing
DMEM	Dulbecco's Modified Eagle Medium
FDP	Fixed dental prostheses
FITC	Fluorescein Isothiocyanate
FTIR	Fourier-transform infrared spectroscopy
GTPR	GC Temp PRINT
HEMA	2-hydroxyethyl methacrylate
HGF	Human gingival fibroblast
ISO	International Organization for Standardization
MMA	Methyl methacrylate
MTT	3-(4,5-dimethylthiazol-2-yl)-2,5-diphenyltetrazolium bromide
OD	Optical density
OMCR	Omnichroma
PBS	Phosphate-buffered saline
SEM/EDS	Scanning electron microscopy with energy-dispersive X-ray spectroscopy
SLA	Stereolithography
SPRY	SprintRay CROWN
TEGDMA	Tetraethylene glycol dimethacrylate
TRITC	Tetramethylrhodamine Isothiocyanate
UDMA	Urethane dimethacrylate
UV	Ultraviolet
XPS	X-ray photoelectron spectroscopy

References

1. Alshamrani, A.; Alhotan, A.; Kelly, E.; Ellakwa, A. Mechanical and Biocompatibility Properties of 3D-Printed Dental Resin Reinforced with Glass Silica and Zirconia Nanoparticles: In Vitro Study. *Polymers* **2023**, *15*, 2523. [CrossRef]
2. Polydorou, O.; König, A.; Hellwig, E.; Kümmerer, K. Long-Term Release of Monomers from Modern Dental-Composite Materials. *Eur. J. Oral Sci.* **2009**, *117*, 68–75. [CrossRef]
3. Reichl, F.X.; Durner, J.; Hickel, R.; Kunzelmann, K.H.; Jewett, A.; Wang, M.Y. Distribution and Excretion of TEGDMA in Guinea Pigs and Mice. *J. Dent. Res.* **2001**, *80*, 1412–1415. [CrossRef]
4. Geurtsen, W. Biocompatibility of Resin-Modified Filling Materials. *Crit. Rev. Oral Biol. Med.* **2000**, *11*, 333–355. [CrossRef] [PubMed]
5. Wiertelak-Makała, K.; Szymczak-Pajor, I.; Bociong, K.; Śliwińska, A. Considerations about Cytotoxicity of Resin-Based Composite Dental Materials: A Systematic Review. *Int. J. Mol. Sci.* **2024**, *25*, 152. [CrossRef] [PubMed]
6. Bagheri, A.; Jin, J. Photopolymerization in 3D Printing. *ACS Appl. Polym. Mater.* **2019**, *1*, 593–611. [CrossRef]
7. Lottner, S.; Shehata, M.; Hickel, R.; Reichl, F.X.; Durner, J. Effects of Antioxidants on DNA Double-Strand Breaks in Human Gingival Fibroblasts Exposed to Methacrylate-Based Monomers. *Dent. Mater.* **2013**, *29*, 991–998. [CrossRef]

8. Schulz, S.D.; König, A.; Steinberg, T.; Tomakidi, P.; Hellwig, E.; Polydorou, O. Human Gingival Keratinocyte Response to Substances Eluted from Silorane Composite Material Reveal Impact on Cell Behavior Reflected by RNA Levels and Induction of Apoptosis. *Dent. Mater.* **2012**, *28*, e135–e142. [CrossRef]
9. Wedekind, L.; Güth, J.F.; Schweiger, J.; Kollmuss, M.; Reichl, F.X.; Edelhoff, D.; Högg, C. Elution Behavior of a 3D-Printed, Milled and Conventional Resin-Based Occlusal Splint Material. *Dent. Mater.* **2021**, *37*, 701–710. [CrossRef] [PubMed]
10. Jain, S.; Sayed, M.E.; Shetty, M.; Alqahtani, S.M.; Al Wadei, M.H.D.; Gupta, S.G.; Othman, A.A.A.; Alshehri, A.H.; Alqarni, H.; Mobarki, A.H.; et al. Physical and Mechanical Properties of 3D-Printed Provisional Crowns and Fixed Dental Prosthesis Resins Compared to CAD/CAM Milled and Conventional Provisional Resins: A Systematic Review and Meta-Analysis. *Polymers* **2022**, *14*, 2691. [CrossRef]
11. Dawood, A.; Marti, B.M.; Sauret-Jackson, V.; Darwood, A. 3D Printing in Dentistry. *Br. Dent. J.* **2015**, *219*, 521–529. [CrossRef]
12. Susila, A.V.; Balasubramanian, V. Correlation of Elution and Sensitivity of Cell Lines to Dental Composites. *Dent. Mater.* **2016**, *32*, e63–e72. [CrossRef] [PubMed]
13. Yoon, T.H.; Lee, Y.K.; Lim, S.; Kim, C.W. Degree of polymerization of resin composites by different light sources. *J. Oral Rehabil.* **2002**, *29*, 1165–1173. [CrossRef] [PubMed]
14. Zhang, X.; Zhang, Q.; Meng, X.; Ye, Y.; Feng, D.; Xue, J.; Wang, H.; Huang, H.; Wang, M.; Wang, J. Rheological and Mechanical Properties of Resin-Based Materials Applied in Dental Restorations. *Polymers* **2021**, *13*, 2975. [CrossRef]
15. Reymus, M.; Fabritius, R.; Kessler, A.; Hickel, R.; Edelhoff, D.; Stawarczyk, B. Fracture Load of 3D-Printed Fixed Dental Prostheses Compared with Milled and Conventionally Fabricated Ones: The Impact of Resin Material, Build Direction, Post-Curing, and Artificial Aging—An In Vitro Study. *Clin. Oral Investig.* **2019**, *24*, 701–710. [CrossRef] [PubMed]
16. Kessler, A.; Reymus, M.; Hickel, R.; Kunzelmann, K.H. Three-Body Wear of 3D-Printed Temporary Materials. *Dent. Mater.* **2019**, *35*, 1805–1812. [CrossRef]
17. Scotti, C.K.; Velo, M.M.; Rizzante, F.A.; de Lima Nascimento, T.R.; Mondelli, R.F.; Bombonatti, J.F. Physical and Surface Properties of a 3D-Printed Composite Resin for a Digital Workflow. *J. Prosthet. Dent.* **2020**, *124*, 614.e1–614.e8. [CrossRef]
18. Mudhaffer, S.; Althagafi, R.; Haider, J.; Satterthwaite, J.; Silikas, N. Effects of Printing Orientation and Artificial Ageing on Martens Hardness and Indentation Modulus of 3D Printed Restorative Resin Materials. *Dent. Mater.* **2024**, *40*, 1003–1014. [CrossRef]
19. *ISO 7405:2025*; Dentistry—Evaluation of Biocompatibility of Medical Devices Used in Dentistry. International Organization for Standardization (ISO): Geneva, Switzerland, 2025.
20. Blumer, L.; Schmidli, F.; Weiger, R.; Fischer, J. A Systematic Approach to Standardize Artificial Aging of Resin Composite Cements. *Dent. Mater.* **2015**, *31*, 855–863. [CrossRef]
21. Morresi, A.L.; D'Amario, M.; Capogreco, M.; Gatto, R.; Marzo, G.; D'Arcangelo, C.; Monaco, A. Thermal Cycling for Restorative Materials: Does a Standardized Protocol Exist in Laboratory Testing? A Literature Review. *J. Mech. Behav. Biomed. Mater.* **2014**, *29*, 295–308. [CrossRef]
22. Guerrero-Gironés, J.; López-García, S.; Pecci-Lloret, M.R.; Pecci-Lloret, M.P.; Rodríguez-Lozano, F.J.; García-Bernal, D. In Vitro Biocompatibility Testing of 3D Printing and Conventional Resins for Occlusal Devices. *J. Dent.* **2022**, *123*, 104163. [CrossRef]
23. Vuković, M.; Lazarević, M.; Mitić, D.; Karisik, M.J.; Ilić, B.; Andrić, M.; Jevtić, B.; Roganović, J.; Milasin, J. Acetylsalicylic Acid (ASA) Regulation of Osteo/Odontogenic Differentiation and Proliferation of Human Dental Pulp Stem Cells (DPSCs) In Vitro. *Arch. Oral Biol.* **2022**, *144*, 105564. [CrossRef]
24. *ISO 10993-12:2021*; Biological Evaluation of Medical Devices—Part 12: Sample Preparation and Reference Materials. International Organization for Standardization (ISO): Geneva, Switzerland, 2021.
25. *ISO 10993-5:2021*; Biological Evaluation of Medical Devices—Part 5: Tests for in vitro cytotoxicity. International Organization for Standardization (ISO): Geneva, Switzerland, 2021.
26. Bayarsaikhan, E.; Lim, J.H.; Shin, S.H.; Park, K.H.; Park, Y.B.; Lee, J.H.; Kim, J.E. Effects of Postcuring Temperature on the Mechanical Properties and Biocompatibility of Three-Dimensional Printed Dental Resin Material. *Polymers* **2021**, *13*, 1180. [CrossRef] [PubMed]
27. Carey, P.R. *Biochemical Applications of Raman and Resonance Raman Spectroscopies*; Academic Press: New York, NY, USA, 1982; pp. xi, 262.
28. Moszner, N.; Salz, U. New developments of polymeric dental composites. *Prog. Polym. Sci.* **2001**, *26*, 535–576. [CrossRef]
29. Pereira, S.G.; Nunes, T.G.; Kalachandra, S.; Lemos, M.F.; Watson, T.F.; Martin, N. Effect of water sorption on the mechanical properties of resin composites. *J. Mater. Sci. Mater. Med.* **2005**, *16*, 297–303.
30. Ferraro, J.R.; Nakamoto, K. *Introductory Raman Spectroscopy*, 2nd ed.; Elsevier: New York, NY, USA, 2003.
31. Braga, L.S.; Ballester, E.R. Raman spectroscopy of dental resin composites: Filler and polymer contributions. *Biomaterials* **2002**, *23*, 2131–2137.
32. Asmussen, M.S. Polymerization kinetics and spectral characterization of Bis-GMA/TEGDMA composites. *Dent. Mater.* **1989**, *5*, 330–336.

33. Soares, L.E.; Rocha, R.; Martin, A.A.; Pinheiro, A.L.; Zampieri, M. Monomer Conversion of Composite Dental Resins Photoactivated by a Halogen Lamp and a LED: A FT-Raman Spectroscopy Study. *Quim. Nova* **2005**, *28*, 229–232. [CrossRef]
34. Fadl, A.; Leask, A. Hiding in Plain Sight: Human Gingival Fibroblasts as an Essential, Yet Overlooked, Tool in Regenerative Medicine. *Cells* **2023**, *12*, 2021. [CrossRef]
35. Frasheri, I.; Aumer, K.; Keßler, A.; Miosge, N.; Folwaczny, M. Effects of Resin Materials Dedicated for Additive Manufacturing of Temporary Dental Restorations on Human Gingival Keratinocytes. *J. Esthet. Restor. Dent.* **2022**, *34*, 1105–1112. [CrossRef]
36. Kamalak, H.; Kamalak, A.; Taghizadehghalehjoughi, A. Cytotoxic Effects of New-Generation Bulk-Fill Composites on Human Dental Pulp Stem Cells. *Cell. Mol. Biol.* **2018**, *64*, 62–71. [CrossRef]
37. Wellner, P.; Mayer, W.; Hickel, R.; Reichl, F.X.; Durner, J. Cytokine Release from Human Leukocytes Exposed to Silorane- and Methacrylate-Based Dental Materials. *Dent. Mater.* **2012**, *28*, 743–748. [CrossRef]
38. Borelli, B.; Zarone, F.; Rivieccio, V.; Riccitiello, F.; Simeone, M.; Sorrentino, R.; Rengo, S.; Spagnuolo, G.; Procino, A. Polyacrylic Resins Regulate Transcriptional Control of Interleukin-6, gp80, and gp130 Genes in Human Gingival Fibroblasts. *J. Oral Sci.* **2017**, *59*, 87–91. [CrossRef]
39. Wuersching, S.N.; Hickel, R.; Edelhoff, D.; Kollmuss, M. Initial Biocompatibility of Novel Resins for 3D Printed Fixed Dental Prostheses. *Dent. Mater.* **2022**, *38*, 1587–1597. [CrossRef] [PubMed]
40. Szczesio-Wlodarczyk, A.; Sokolowski, J.; Kleczewska, J.; Bociong, K. Ageing of dental composites based on methacrylate resins—A critical review of the causes and methods of assessment. *Polymers* **2020**, *12*, 882. [CrossRef] [PubMed]
41. Souza, R.O.A.; Özcan, M.; Michida, S.M.A.; de Melo, R.M.; Pavanelli, C.A.; Bottino, M.A.; Soares, L.E.S.; Martin, A.A. Conversion Degree of Indirect Resin Composites and Effect of Thermocycling on Their Physical Properties. *J. Prosthodont.* **2010**, *19*, 218–225. [CrossRef] [PubMed]
42. Pieniak, D.; Przystupa, K.; Walczak, A.; Niewczas, A.M.; Krzyżak, A.; Bartnik, G.; Gil, L.; Łonkwic, P. Hydro-Thermal Fatigue of Polymer Matrix Composite Biomaterials. *Materials* **2019**, *12*, 3650. [CrossRef]
43. Pieniak, D.; Walczak, A.; Walczak, M.; Przystupa, K.; Niewczas, A.M. Hardness and Wear Resistance of Dental Biomedical Nanomaterials in a Humid Environment with Non-Stationary Temperatures. *Materials* **2020**, *13*, 1255. [CrossRef]
44. Ghavami-Lahiji, M.; Firouzmanesh, M.; Bagheri, H.; Jafarzadeh Kashi, T.S.; Razazpour, F.; Behroozibakhsh, M. The Effect of Thermocycling on the Degree of Conversion and Mechanical Properties of a Microhybrid Dental Resin Composite. *Restor. Dent. Endod.* **2018**, *43*, e26. [CrossRef]
45. Beltrami, R.; Colombo, M.; Rizzo, K.; Di Cristofaro, A.; Poggio, C.; Pietrocola, G. Cytotoxicity of Different Composite Resins on Human Gingival Fibroblast Cell Lines. *Biomimetics* **2021**, *6*, 26. [CrossRef]
46. Kirby, S.; Pesun, I.; Nowakowski, A.; França, R. Effect of Different Post-Curing Methods on the Degree of Conversion of 3D-Printed Resin for Models in Dentistry. *Polymers* **2024**, *16*, 549. [CrossRef]
47. Boussès, Y.; Brulat-Bouchard, N.; Bouchard, P.O.; Tillier, Y. A Numerical, Theoretical and Experimental Study of the Effect of Thermocycling on the Matrix–Filler Interface of Dental Restorative Materials. *Dent. Mater.* **2021**, *37*, 772–782. [CrossRef]
48. Tokay, U.; Koyuturk, A.E.; Aksoy, A.; Ozmen, B. Do the Monomers Release from the Composite Resins after Artificial Aging? *Microsc. Res. Tech.* **2015**, *78*, 255–259. [CrossRef]
49. Sideridou, S.A.; Tserki, V.; Papanastasiou, G. IR and Raman Studies of Photopolymerization and Degradation in Dimethacrylate Networks. *Dent. Mater.* **2003**, *19*, 598–605.
50. Yoshida, K.; Greener, E.H. Resin–Filler Interactions and Raman Spectral Features in Dental Composites. *J. Biomed. Mater. Res.* **2001**, *57*, 96–102.
51. Yap, H.S.; Choo, C.W. Effect of Thermocycling on the Chemical Stability of Resin Composites Monitored by Raman Spectroscopy. *Dent. Mater.* **2004**, *20*, 527–533.
52. Cramer, S.R.; Stansbury, J.W.; Bowman, C.N. Monitoring Polymerization and Degradation in Dental Resins Using Raman Spectroscopy. *Dent. Mater.* **2006**, *22*, 858–867.
53. Gale, M.S.; Darvell, B.W. Thermal Cycling Procedures for Laboratory Testing of Dental Restorations. *J. Dent.* **1999**, *27*, 89–99. [CrossRef] [PubMed]
54. Ferracane, J.L. Hygroscopic and Hydrolytic Effects in Dental Polymer Networks. *Dent. Mater.* **2006**, *22*, 211–222. [CrossRef]
55. Schneider, L.F.J.; Cavalcante, L.M.; Silikas, N. Shrinkage Stresses Generated during Resin-Composite Applications: A Review. *J. Dent. Biomech.* **2010**, *1*, 131630. [CrossRef] [PubMed]
56. Rusu, L.C.; Ardelean, L.C.; Negrutiu, M.L.; Sinescu, C.; Podoleanu, A.G. Raman Spectroscopy Applications in Dental Medicine. *Rom. J. Morphol. Embryol.* **2015**, *56*, 747–752.
57. Gad, M.M.; Fouda, S.M.; Al-Harbi, F.A.; Näpänkangas, R.; Raustia, A. PMMA Denture Base Material Enhancement: A Review of Fiber, Filler, and Nanofiller Addition. *Int. J. Nanomed.* **2017**, *12*, 3801–3812. [CrossRef]
58. Han, Z.; Zhu, B.; Chen, R.; Huang, Z.; Zhu, C.; Zhang, X. Effect of Silver-Supported Materials on the Mechanical and Antibacterial Properties of Reinforced Acrylic Resin Composites. *Mater. Des.* **2015**, *65*, 1245–1252. [CrossRef]

59. Lee, J.-H.; Jo, J.-K.; Kim, D.-A.; Patel, K.D.; Kim, H.-W.; Lee, H.-H. Nano-Graphene Oxide Incorporated into PMMA Resin to Prevent Microbial Adhesion. *Dent. Mater.* **2018**, *34*, e63–e72. [CrossRef] [PubMed]
60. Hamid, S.K.; Alghamdi, L.A.; Alshahrani, F.A.; Khan, S.Q.; Matin, A.; Gad, M.M. In Vitro Assessment of Artificial Aging on the Antifungal Activity of PMMA Denture Base Material Modified with ZrO_2; Nanoparticles. *Int. J. Dent.* **2021**, *2021*, 5560443. [CrossRef] [PubMed]
61. Hassanpour, M.; Narongdej, P.; Alterman, N.; Moghtadernejad, S.; Barjasteh, E. Effects of Post-Processing Parameters on 3D-Printed Dental Appliances: A Review. *Polymers* **2024**, *16*, 2795. [CrossRef]

Hindawi
Journal of Spectroscopy
Volume 2023, Article ID 5490018, 8 pages
https://doi.org/10.1155/2023/5490018

Research Article

Effect of Laser Heating on Partial Decomposition of $Bi_{12}SiO_{20}$ (BSO) Single Crystal: Raman Study

Nebojsa Romcevic,[1] **Branka Hadzic**,[1] **Marija Prekajski Đorđević**,[2] **Peda Mihailovic**,[3] **Milica Curcic**,[1] **Jelena Trajic**,[1] **Jelena Mitric**,[1] **and Maja Romcevic**[1]

[1]*Institute of Physics Belgrade, University of Belgrade, Belgrade 11080, Serbia*
[2]*Vinca Institute of Nuclear Sciences, University of Belgrade, Belgrade 11000, Serbia*
[3]*School of Electrical Engineering, University of Belgrade, Belgrade 11000, Serbia*

Correspondence should be addressed to Nebojsa Romcevic; romcevi@ipb.ac.rs

Received 2 March 2023; Revised 17 April 2023; Accepted 28 April 2023; Published 4 May 2023

Academic Editor: Emiliano Bonera

The effect of laser (532 nm line of Verdi G) heating during the Raman measurements, on partial decomposition of $Bi_{12}SiO_{20}$ single crystal, was addressed in this study. The degree of decomposition directly depends on the power density and duration of the laser treatment, which are registered by the phonon Raman spectra. After laser treatment, AFM measurements register additional small spherical islands on the surface. Analysis performed on irradiated and unirradiated samples showed significant changes in transmission spectra, X-ray diffraction (XRD) pattern, Verdet constant, magneto-optical property, and absorption coefficient. The material obtained after laser irradiation can be described as specific nanocomposite consisting of bismuth oxide and silicon oxide-based nano-objects (dimensions below 15 nm in diameter), which are arranged in a matrix of $Bi_{12}SiO_{20}$.

1. Introduction

Sillenite crystals belong to the $Bi_{12}MO_{20}$ group (where M = Si, Ge, and Ti) compounds, that have a body-centered cubic crystalline structure with the space group $I23$ [1]. Crystal $Bi_{12}SiO_{20}$ has parameters $a = 1.01067$ nm, $Z = 2$ (two identical motives in the unit cell). The density functional theory calculations presented bandgap energy of Bi_1SiO_{20} as 3.43 eV [2]. Experimentally determined values are lower [3]. These optically active crystals can exhibit many strong effects such as magneto-optical, photo-induced, and electro-optical effects. Also, they possess numerous interesting properties, such as high values of piezo-electric, dielectric and elasto-optic constants, as well as high dark electric resistance [1]. These crystals, usually as bulk crystals, have widespread applications as active elements in many devices, such us optical limiting, holography, spatial light modulation, optical phase conjugation, optical memories fiber optic sensors, and Pockels cells [4–6].

Lasers have great applications in material processing [7] and their role is only getting more expanded. The surface of a single crystal can be lasering treated [8] whereby a thin surface layer of the material is transformed when it interacts with the laser beam. This process is strictly controlled with the laser beam wavelength and power, its duty cycle, and repetition rate. The final result of how material is modified depends on a sample, since all materials have unique properties that dictate how they will interact with the laser radiation [9, 10].

Raman spectroscopy is an established technique to measure local material properties [11]. As such, it is very suitable for research related to the surface of the sample. However, since it uses a laser for excitation, structural changes may occur on the surface of the sample caused by local heating. In some cases, these modifications can lead to the decomposition of the sample, which results in a changed Raman signal [12, 13]. Changes in the spectrum can be in the position and half-width of phonon lines on the spectrum of

the starting material, as well as lead to the appearance of new lines caused by permanent modifications in the sample [14, 15].

In our previous paper [16], we registered the decomposition of $Bi_{12}SiO_{20}$ (BSO) single crystal due to femtosecond laser irradiation. By far-infrared spectroscopy and AFM measurements, the existence of bismuth oxide nano-objects on the surface of the sample was registered. XRD could not register these changes. Also, it was not possible to establish control parameters between the formed nano-objects and the conditions of the experiment because the sample was treated in advance. Also, for the same reason, it was not possible to determine the exact phase composition of nano-objects.

The aim of this work is to continue the investigation of the influence of locally induced heating, with an increase in the power density of the semiconductor laser during Raman measurements, on the $Bi_{12}SiO_{20}$ single crystal. In this way, direct results related to the current state of $Bi_{12}SiO_{20}$ decomposition will be provided, as well as parameters that can control that process. Complementary techniques such as X-ray diffraction (XRD), atomic force microscopy (AFM), UV-Vis transmission, and magneto-optical measurements will be used in the characterization of the obtained materials.

2. Materials and Methods

The Czochralski technique was applied to grow $Bi_{12}SiO_{20}$ single crystal, which is described in more detail in Ref. [16]. In short, MSR 2 crystal puller controlled by a Eurotherm was used. A platinum crucible was used to contain the melt, which was placed in an alumina vessel on zircon–oxide wool. Crystal growth was occurred in an air. Bi_2O_3 and SiO_2 were used for the synthesis of crystals. Starting materials were mixed in 6 : 1 stoichiometric ratio. Optimal pull rate was chosen in the range 5-6 mm/h. Equations of the melt hydrodynamics were used to calculate the critical crystal diameter, $d_c = 10$ mm, and critical rotation, $\omega_c = 20$ rpm. The crucible was not rotating during crystal growth. The crystal boule was cooled at ~50°C/h down to a room temperature, after the crystal growth. Crystals grew in [111] direction, without core being observed. Finally, crystals were cut and polished.

Polished crystal samples were treated using Verdi G optical pumped semiconductor laser with a 532 nm wavelength with different irradiation times during Raman experiment.

Atomic Force Microscopy (AFM) was used to determine topography of the samples with NTEGRA prima from NT-MDT.

The X-ray diffraction (XRD) data was measured using an X-ray diffractometer (XRD) Rigaku Ultima IV, Japan. The PDXL2 v2.0.3.0 software, with reference to the diffraction patterns available in the International Center for Diffraction Data (ICDD) [17], was used for phase identification and data analysis.

The UV-Vis transmission spectra were collected in the 200–900 nm range using a Perkin-Elmer Lambda 4B UV-Vis spectrophotometer.

Raman spectra of prepared samples were obtained using backscattering configuration of Jobin Yvon T64000 spectrometer equipped with nitrogen cooled CCD detector. The spectra were recorded in the spectral range 80–650 cm^{-1} at room temperature using a 532 nm Verdi G optical pumped semiconductor laser line.

Parameters such as Faraday rotation, bulk absorption, and optical activity were measured at 632.8 nm using a He-Ne laser. This was obtained by an orthogonal polarization detection polarimetric method [18].

3. Results

3.1. Raman Spectroscopy. Raman spectra of $Bi_{12}SiO_{20}$ (BSO) single crystal, nanocrystalline powders, and thin films have been measured and analyzed in the past [19–22]. Identification of the observed peaks was performed on the basic of the factor group analysis for the SiO_4 tetrahedra, OBi_3, and Bi_3O_4 structural fragments. The Raman spectrum of the our $Bi_{12}SiO_{20}$ single crystal is shown in Figure 1(a). The spectrum was recorded with a laser power density of 0.1 mW/μm^2 and the measurement time of 5 s, which did not cause structural changes in the sample. The spectrum of $Bi_{12}SiO_{20}$ exhibits intense modes at about 87, 97, 104, 128, 144, 167, 176, 204, 269, 322, and 536 cm^{-1}. As expected, our spectrum from Figure 1(a) is identical to the literature data [19–22].

Raman spectra of a $Bi_{12}SiO_{20}$ single crystal recorded consecutively at different laser powers (0.5–2 mW/μm^2) and the recording time of each measurement of 30 s, at the same place on the sample are shown in Figure 1(b). The intensity of the peaks registered in Figure 1(a) increases with increasing laser power. In addition, starting with the laser power of 0.7 mW/μm^2 additional structures were seen on the spectra at about 122, 235, 456, and 487 cm^{-1}. They are significantly weaker than already registered phonons, but their intensity also increases with increasing laser power. The result was checked with the same laser power, but with a measurement times of 1 s and 60 s. Raman spectra of $Bi_{12}SiO_{20}$ single crystal recorded at laser power density of 1.5 mW/μm^2 and different recording times at different locations on the sample are shown in Figure 1(c). A very short 1 s measurement excites a spectrum similar to that in Figure 1(a). An increase in recording time leads to the same effect registered in Figure 1(b). To explain the registered effect, it was necessary to do additional experiments.

3.2. AFM. Figure 2 shows the results of AFM measurements of the $Bi_{12}SiO_{20}$ single crystal and the same sample after the Raman measurements (shown in Figure 1(c)). In Figure 2(a), we can clearly see that the surface of the untreated sample is quite smooth with no visible cracks, and only traces of mechanical polishing can be seen. Figures 2(b) and 2(c) show the surface of the sample after laser treatment of 1.5 mW/μm^2, according to the procedure described in Section 3.1, with two different time lengths of each measurement (30 s and 60 s), respectively. Nano-objects, small white dots in the images, with a diameter of about 11 nm (Figure 2(b)) and 15 nm (Figure 2(c)) were observed on both

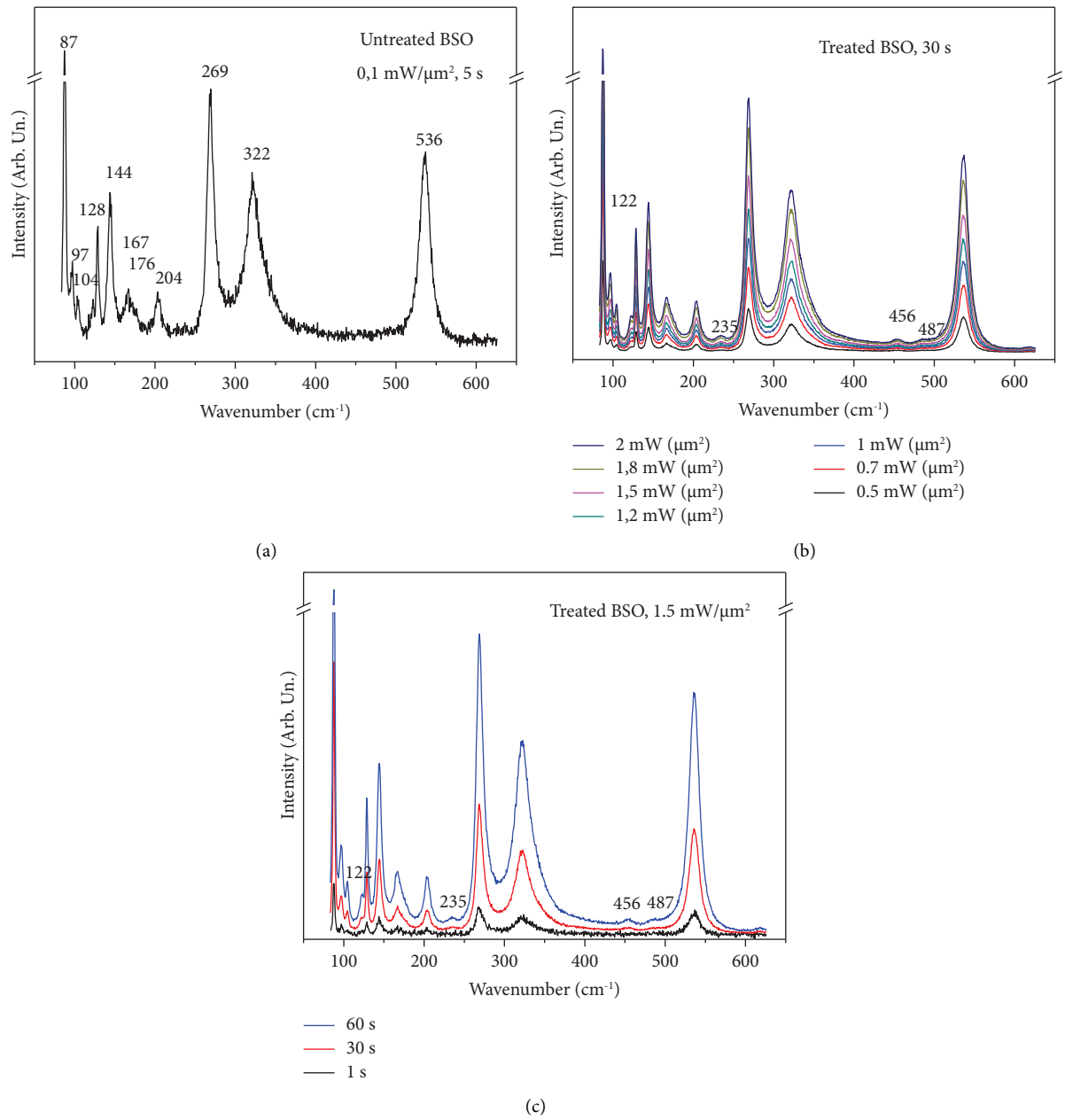

FIGURE 1: (a) Raman spectrum of the $Bi_{12}SiO_{20}$ single crystal. (b) Raman spectra of $Bi_{12}SiO_{20}$ single crystal recorded consecutively at different laser powers at the same location on the sample. (c) Raman spectra of $Bi_{12}SiO_{20}$ single crystal recorded with laser power of 1.5 mW/μm^2 and different recording times at different locations on the sample.

images. In Figure 2(c) we see that the density of nano-objects is significantly higher than that registered in Figure 2(b).

3.3. XRD Measurements. The XRD patterns of prepared BSO single crystal and BSO laser treated (1.5 mW/μm^2, 60 s) are presented in Figure 3. From the XRD pattern of untreated BSO single crystal (the bottom spectrum) it is clearly seen that all peaks correspond to $Bi_{12}SiO_{20}$. Results show that only selenite ($Bi_{12}SiO_{20}$) phase is present, which corresponds to the JCPDF Card No. 37-0485. When compared to laser treated BSO single crystal (upper spectrum), except silenite peaks are observed. These peaks correspond to: Bi_4O_7 (JCPDF Card No. 01-074-2352), Bi_2O_3 (00-057-0400, 00-051-1161, and 01-079-6679), and SiO_2 (01-071-5334) phases. All additional phases are marked with different symbols in Figure 3.

XRD results clearly and unequivocally show the influence of locally induced heating with laser power on $Bi_{12}SiO_{20}$ single crystal as the separation of new phases in the form of different Bi_4O_7, Bi_2O_3, and SiO_2. These results explain the appearance of additional structures seen on the Raman spectra whose intensity increases with increasing

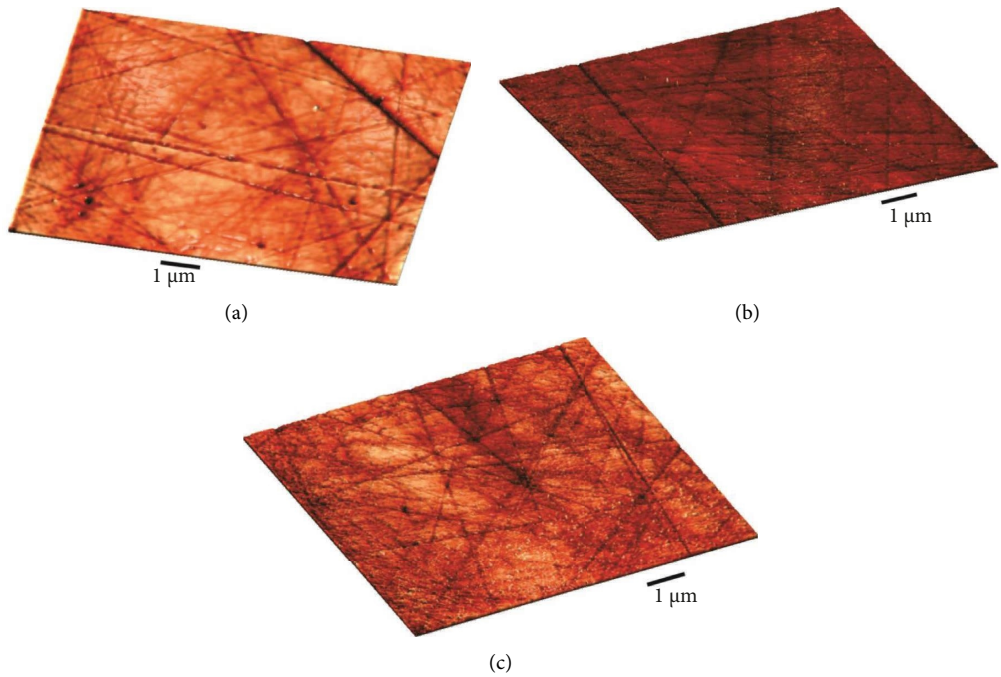

FIGURE 2: AFM results of: untreated $Bi_{12}SiO_{20}$ single crystal (a); laser treated $Bi_{12}SiO_{20}$ sample $P = 1.5\,mW/\mu m^2$: 30 s (b); and 60 s (c).

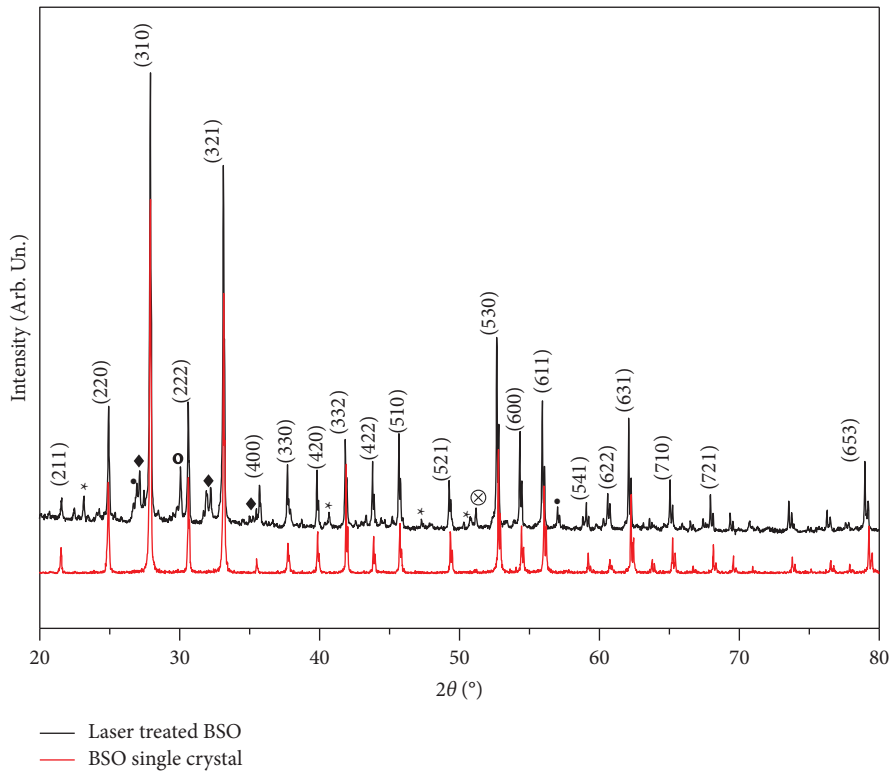

FIGURE 3: X-ray diffraction results of untreated and laser treated BSO single crystal, peaks of $Bi_{12}SiO_{20}$ phase marked with hkl, $*Bi_4O_7$ (JCPDF Card No. 01-074-2352), ◆SiO_2 (01-071-5334), ○Bi_2O_3 (00-057-0400), ●Bi_2O_3 (00-051-1161), and ⊗Bi_2O_3 (01-079-6679).

laser power and measurement time. The appearances of secondary phases also explain the phenomenon of additional small white dots (nano-objects) in the AFM images of laser-treated samples.

3.4. UV-Vis Spectroscopy. In Figure 4(a) the results of transmission measurements of BSO samples in the UV-VIS region are presented. It is noticeable that for the laser-treated sample in the area of wavelength above 550 nm, the

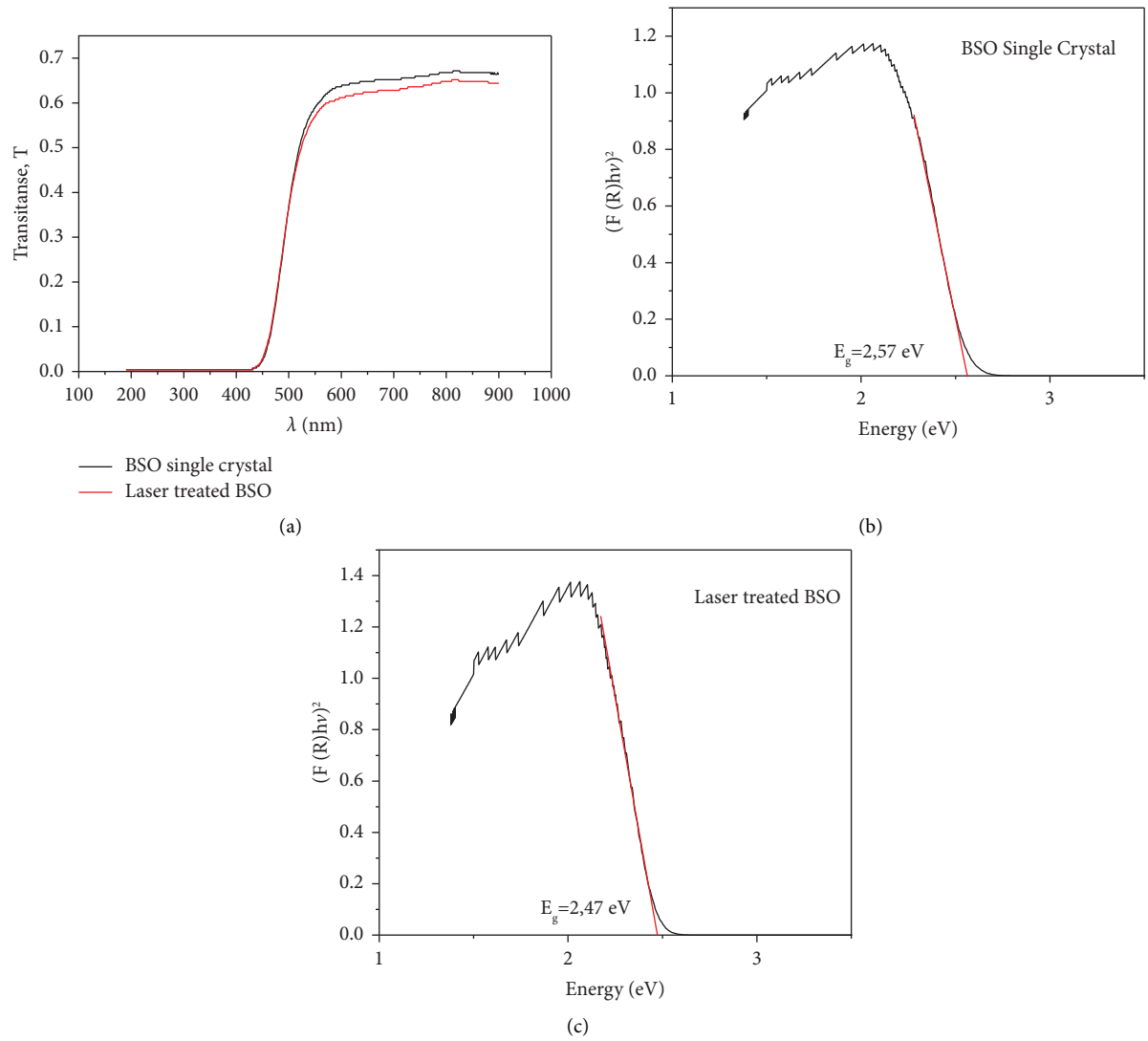

FIGURE 4: (a) UV-Vis transmittance spectra of $Bi_{12}SiO_{20}$ single crystal treated by laser power. Kubelka–Munk analysis for laser untreated (b) and treated (c) sample.

transmittance was reduced by about 5%. To determine the value of the energy gap eg, we using the well-known Kubelka–Munk theory (see for example, [3] and the literature cited there). The results of the analysis are shown in Figures 4(b) and 4(c).

For the untreated BSO single crystal, an energy gap value of 2.57 eV was obtained. This energy is lower than accepted band gap energy of BSO [3]. This smaller energy was associated with defect centers, as analyzed in [23–25]. A value of 2.47 eV was obtained for the laser-treated sample. Such a simple model cannot provide a complete picture of the modifications made in the sample, but it can indicate a macroscopic change, i.e. a parameter that is in some way its consequence.

3.5. Optical Activity, Faraday Rotation, and Bulk Absorption. Optical activity and Faraday rotation were measured by the free space setup described in [26]. It was noted that significant light scattering in the sample causes cross-talk of the two channels for the orthogonal polarizations detection. Therefore, birefringent crystal was replaced with a Wollaston prism decoupling the channels but also spoiling evenness of channels losses and forcing the use of two photodiodes. Two channels gain that include optoelectronic conversion efficiencies were equalized by transimpedance resistors.

Background light influence was eliminated using an optical chopper and lock-in amplifier. Laser's polarization instability was converted to light irradiation fluctuations by polarizing prism mounted after the laser. Δ/Σ normalization method used is insensitive to light irradiation fluctuations but introduces another problem. It was also noted that treated BSO induces more depolarization of light compared to untreated one. This is partially the consequence of nano-objects at the surface of the treated BSO. Contribution of depolarized light is canceled in the subtraction but not in the sum leading to reduced result for Optical activity and Faraday rotation. It is possible to compensate this effect but only for particular crystal orientation. Instead of that we

averaged the results for tree different crystal orientations. Results are presented in Table 1 having in mind scattering while measuring the absorption coefficient lens was used after crystal to focus the light on photodiode. Verdet constant was divided by absorption coefficient to obtain the magneto-optical quality of sample.

Table 1: Optical properties of $Bi_{12}SiO_{20}$ single crystal.

	Untreated BSO	Treated BSO
Optical rotatory power (rad/mm)	0.37	0.36
Verdet constant (rad/Tm)	61	58
Absorption coefficient (cm^{-1})	1.03	1.05
Magneto optical quality (rad/T)	0.59	0.55

4. Discussion

As far as we know, [18] preparation technique which was used ensured maximum quality samples in the limits corresponding to the starting components purity. In the case of $Bi_{12}GeO_{20}$ [27], the positive effect of laser radiation on optical characteristics was registered only in materials obtained from starting materials of lower quality. With quality single crystals, it was not possible to improve the optical parameters in this way. This is also the case with $Bi_{12}SiO_{20}$, which we treated with a laser, i.e. we have a change of several percentages at maximum laser power.

We can interpret the additional structures from Figures 1(b) and 1(c) as follows. Figure 2 clearly shows nano-objects with dimensions of about 15 nm with very narrow dimensional distributions. It is easy to connect these nano-objects with the new phases from Figure 3, registered for the treated sample. These new phases show their characteristics on Raman spectra as well. First, four polymorphic phases of bismuth–oxide are known: the one stable at the room temperature, orthorhombic α-Bi_2O_3, and three high-–temperature ones: β-, δ-, and γ-Bi_2O_3 [28–30]. Since new structures are visible even at relatively low laser powers, as well as on XRD at room temperature, we can conclude that only the orthorhombic α-Bi_2O_3 phase is present. In this way, we easily connect the additional structures in the Raman spectra at around 122 cm^{-1} and 456 cm^{-1} with this phase [31]. XRD also registered the Bi_4O_7 phase. This phase has a phonon at 118 cm^{-1} [32], so the presence of the influence of this phase on the phonon registered at 122 cm^{-1} in our experiment is not excluded. The situation is much clearer for the phonon at 486 cm^{-1}. This phonon is associated with Bi-O stretching vibrations in distorted linked BiO_6 units in the previously registered Bi_4O_7 phase [33, 34].

On the other hand, the diversity of SiO_2-based phases is even greater [35]. However, we think that in our case, SiO_2 clusters have T_d symmetry and corresponding Raman modes at 235 cm^{-1}. Also, experimentally at 463.6 cm^{-1} and theoretically at 461 cm^{-1}, there is a SiO_2 phonon of the same symmetry. Therefore, the origin of the phonon at 456 cm^{-1} cannot be accurately determined, i.e. due to the weak intensity of the experimental result, it is difficult to separate the influence of this phonon from that of α-Bi_2O_3. This result is in agreement with Ref. [19, 20].

In this way, it is clearly shown that laser heating during the Raman experiment produces nano-objects consisting of bismuth oxide and silicon oxide arranged in a matrix of $Bi_{12}SiO_{20}$ single crystal. This structure by its composition can be classified as a nanocomposite because the dispersed phase is in the nanometric size, with the specificity that the nano-object is formed from the same material, or its parts, such as a matrix.

Our results presented in this paper can be interpreted in at least two ways. First, it can be said that the made modification did not lead to the improvement of the characteristics of the observed material. That is true in principle. But this is practically expected, because the starting material, BSO single crystal, was obtained from ultrapure components, which led to the exceptional optical quality of the sample, as it was the case with the $Bi_{12}GeO_{20}$ crystal [18, 27].

However, the modification made led to a partial, but almost controlled, decomposition of the base material. A stable structure was created, which gives the prospect of using nano-objects in robust electronics. Namely, due to their extremely small sizes, nanomaterials (one, two, or three dimensions of less than 100 nm) cannot be used in large scale, particularly as long-bearing materials in engineering applications. For this it has long been a desire to develop bulk composites incorporating these nanomaterials (for example, nanocomposites) to harness their extraordinary properties in bulk applicable materials. Initial ideas and principles are given in [36]. The most important fact is that the characteristics of the nanomaterials are fundamentally different in comparison with the bulk materials [37]. In our opinion, this way of obtaining specific nanocomposites deserves attention.

In addition, in this paper, it is once again shown, this time directly, that during Raman measurement of complex structures and materials, the used laser power should be taken into account. It is very useful to measure Raman spectra with high laser powers. The spectrum is more intense, and the lines are more pronounced. The same applies to the duration of the measurement. However, in those cases, partial decomposition of the observed material or structure may occur, which results in the existence of lines on the spectrum do not belong to the original material, but they are the result of local and partial decomposition. Such results lead to wrong conclusions.

5. Conclusion

High-quality single crystal $Bi_{12}SiO_{20}$, with parameters E_g of 2.57 eV, Verdet constant of 61 rad/Tm, and magneto-optical quality of 0.59 rad/T growth by the Czochralski technique. We used 532 nm line of Verdi G optical pumped semiconductor laser, during the Raman experiment, to modify the surface on a $Bi_{12}SiO_{20}$ single crystal. By measuring phonon spectra with Raman spectroscopy, starting from the laser power density of 0.7 $mW/\mu m^2$, and irradiation time greater than 1 s, we have registered new structures at about 122, 235, 456, and 478 cm^{-1}. AFM measurements confirm that the $Bi_{12}SiO_{20}$ crystal has decomposed on the surface, and newly formed bismuth oxide and silicon oxide-based

nano-objects in the $Bi_{12}SiO_{20}$ matrix was found. This decomposition of $Bi_{12}SiO_{20}$ single crystal led to small changes in the electrical and magneto-optical characteristics of the base material. This structure by its composition can be classified as a nanocomposite because the dispersed phase is in the nanometric size, with the specificity that the nano-objects are formed from the same material or its parts, such as a matrix.

Data Availability

Data are available upon reasonable request.

Conflicts of Interest

The authors declare that they have no conflicts of interest.

Acknowledgments

This research was supported by the Science Fund of the Republic of Serbia, Grant no. 7504386, Nano object in own matrix–Self composite–NOOM-SeC.

References

[1] A. F. Lima, S. A. S. Farias, and M. V. Lalic, "Structural, electronic, optical, and magneto-optical properties of $Bi_{12}MO_{20}$ (M = Ti, Ge, Si) sillenite crystals from first principles calculations," *Journal of Applied Physics*, vol. 110, no. 8, Article ID 083705, 2011.

[2] D. Hou, X. Hu, Y. Wen et al., "Electrospun sillenite $Bi_{12}MO_{20}$ (M = Ti, Ge, Si) nanofibers: general synthesis, band structure, and photocatalytic activity," *PCCP: Physical Chemistry Chemical Physics*, vol. 15, no. 47, Article ID 20698, 2013.

[3] M. Isik, S. Delice, N. M. Gasanly, N. H. Darvishov, and V. E. Bagiev, "Temperature-dependent band gap characteristics of $Bi_{12}SiO_{20}$ single crystals," *Journal of Applied Physics*, vol. 126, no. 24, Article ID 245703, 2019.

[4] V. M. Skorikov, Y. F. Kargin, A. V. Egorysheva, V. V. Volkov, and M. Gospodinov, "Growth of sillenite-structure single crystals," *Inorganic Materials*, vol. 41, no. S1, pp. S24–S46, 2005.

[5] R. A. Ganeev, A. I. Ryasnyansky, B. Palpant, and S. Debrus, "Third-order nonlinearities of $Bi_{12}GeO_{20}$ crystal measured by nanosecond radiation," *Journal of Applied Physics*, vol. 97, no. 10, Article ID 104303, 2005.

[6] M. Itoh, T. Katagiri, H. Mitani, M. Fujita, and Y. Usuki, "Comparative study of excitonic structures and luminescence properties of $Bi_4Ge_3O_{12}$ and $Bi_{12}GeO_{20}$," *Physica Status Solidi (B)*, vol. 245, no. 12, pp. 2733–2736, 2008.

[7] P. Schaaf, Ed., *Springer Series in Materials Science*, Springer Verlag, Berlin, Germany, 2010.

[8] M. A Montealegre, G. Castro, P. Rey, J. L. Arias, P. Vazquez, and M. Gonzalez, "Surface treatments by laser technology," *Contemporary Materials*, vol. 1, no. 1, pp. 19–30, 2010.

[9] A. K. Roy, Ed., *Hybrid Atomic-Scale Interface Design for Materials Functionality*, Elsevier, Amsterdam, Netherlands, 2021.

[10] M. V. Shugaev, C. Wu, O. Armbruster et al., "Fundamentals of ultrafast laser–material interaction," *MRS Bulletin*, vol. 41, no. 12, pp. 960–968, 2016.

[11] By M. Cardona, Ed., *Light Scattering of Solids 1*, Springer, Berlin, Germany, 1975.

[12] B. Hadzic, N. Romcevic, D. Sibera et al., "Laser power influence on Raman spectra of ZnO(Co) nanoparticles," *Journal of Physics and Chemistry of Solids*, vol. 91, pp. 80–85, 2016.

[13] B. Hadzic, B. Vasic, B. Matovic et al., "Influence of laser-induced heating on MnO nanoparticles," *Journal of Raman Spectroscopy*, vol. 49, no. 5, pp. 817–821, 2018.

[14] S. Xie, M. P. Rosynek, and H. Lunsford, "Effect of laser heating on the local temperature and composition in Raman spectroscopy: a study of $Ba(NO_3)_2$ and BaO_2 decomposition," *Applied Spectroscopy*, vol. 53, no. 10, pp. 1183–1187, 1999.

[15] S. Kouteva-Arguirova, T. Z. Arguirov, D. Wolfframm, and J. Reif, "Influence of local heating on micro-Raman spectroscopy of silicon," *Journal of Applied Physics*, vol. 94, no. 8, p. 4946, 2003.

[16] N. Romcevic, M. Lekic, A. Kovacevic, N. Paunovic, B. Vasic, and M. Romcevic, "Structural properties of femtosecond laser irradiation induced bismuth oxide-based nano-objects in Bi12SiO20 (BSO) single crystal," *Physica E: Low-Dimensional Systems and Nanostructures*, vol. 148, Article ID 115653, 2023.

[17] *Powder Diffraction File, PDF-2 Database, Announcement of New Database Release*, International Centre for Diffraction Data (ICDD), 2012.

[18] Z. Z. Lazarevic, P. Mihailovic, S. Kostic et al., "Determination of magneto-optical quality and refractive index of bismuth germanium oxide single crystals grown by Czochralski technique," *Optical Materials*, vol. 34, no. 11, pp. 1849–1859, 2012.

[19] S. Venugopalan and A. K. Ramdas, "Raman spectra of bismuth germanium oxide and bismuth silicon oxide," *Physical Review B: Condensed Matter*, vol. 5, no. 10, pp. 4065–4079, 1972.

[20] B. Mihailova, M. Gospodinov, and L. Konstantinov, "Raman spectroscopy study of sillenites. I. Comparison between $Bi_{12}(Si,Mn)O_{20}$ single crystals," *Journal of Physics and Chemistry of Solids*, vol. 60, no. 11, pp. 1821–1827, 1999.

[21] I. F. Vasconcelos, M. A. Pimenta, and A. S. B. Sombra, "Optical properties of $Bi_{12}SiO_{20}$ (BSO) and $Bi_{12}TiO_{20}$ (BTO) obtained by mechanical alloying," *Journal of Materials Science*, vol. 36, no. 3, pp. 587–592, 2001.

[22] J. C. Alonso, R. Diamant, E. Haro-Poniatowski et al., "Raman characterization of $Bi_{12}SiO_{20}$ thin films obtained by pulsed laser deposition," *Applied Surface Science*, vol. 109-110, pp. 359–361, 1997.

[23] M. Isik, N. Sarigul, and N. M. Gasanly, "Thermoluminescence characteristics of $Bi_{12}SiO_{20}$ single crystals," *Journal of Luminescence*, vol. 224, Article ID 117280, 2020.

[24] R. Oberschmid, "Absorption centers of $Bi_{12}GeO_{20}$ and $Bi_{12}SiO_{20}$ crystals," *Physica Status Solidi (A)*, vol. 89, no. 1, pp. 263–270, 1985.

[25] M. Isik, S. Delice, H. Nasser, N. M. Gasanly, N. H. Darvishov, and V. E. Bagiev, "Optical characteristics of Bi12SiO20 single crystals by spectroscopic ellipsometry," *Materials Science in Semiconductor Processing*, vol. 120, Article ID 105286, 2020.

[26] P. Mihailovic, S. Petricevic, and J. Radunovic, "Improvements in difference-over-sum normalization method for Faraday effect magnetic field waveforms measurement," *Journal of Instrumentation*, vol. 1, no. 12, Article ID P12002, 2006.

[27] A. KovaŁeviĿ, J. L. RistiĿ-DjuroviĿ, M. LekiĿ et al., "Influence of femtosecond pulsed laser irradiation on bismuth germanium oxide single crystal properties," *Materials Research Bulletin*, vol. 83, pp. 284–289, 2016.

[28] B. Isecke and J. Osterwald, "Gleichgewichtsuntersuchungen am sws," *Zeitschrift für Physikalische Chemie*, vol. 115, no. 1, pp. 17–24, 1979.

[29] F. D. Hardcastle and I. E. Wachs, "The molecular structure of bismuth oxide by Raman spectroscopy," *Journal of Solid State Chemistry*, vol. 97, no. 2, pp. 319–331, 1992.
[30] E. Oniyama and P. G. Wahlbeck, "Phase equilibria in the Bismuth–Oxygen system," *Journal of Physical Chemistry B*, vol. 102, no. 22, pp. 4418–4425, 1998.
[31] K. Trentelman, "A note on the characterization of bismuth black by Raman microspectroscopy," *Journal of Raman Spectroscopy*, vol. 40, no. 5, pp. 585–589, 2009.
[32] O. Depablos-Rivera, A. Martinez, and S. E. Rodil, "Interpretation of the Raman spectra of bismuth oxide thin films presenting different crystallographic phases," *Journal of Alloys and Compounds*, vol. 853, Article ID 157245, 2021.
[33] H. Guan and Y. Feng, "Facile synthesis and purplish blue luminescence of the binary mixed valence compound Bi_4O_7 microcrystals," *Materials Letters*, vol. 143, pp. 269–272, 2015.
[34] V. Dimitrov, Y. Dimitriev, and A. Montenero, "IR spectra and structure of V_2O_5, GeO_2, Bi_2O_3 glasses," *Journal of Non-crystalline Solids*, vol. 180, no. 1, pp. 51–57, 1994.
[35] C. De La Rocha and D. J. Conley, "Mystical crystals of silica," *Silica Stories*, Springer, Berlin, Germany, 2017.
[36] Y. Dzenis, "Structural nanocomposites," *Science*, vol. 319, no. 5862, pp. 419-420, 2008.
[37] T. E. Twardowski, *Introduction to Nanocomposites Material Properties, Processing, Characterization*, Destech Publications, Lancaster, Pa, USA, 2007.

UP-CONVERSION BEHAVIOUR OF Er^{3+}/Yb^{3+} ACTIVATED Gd_2O_3 PHOSPHOR FOR MAGNETIC RESONANCE APPLICATION[**]

Praveen Kumar Yadaw [1], J. Mitrić [2], N. Romčević [2], Vikas Dubey[3*], N. Kumar Swamy [1], M. C. Rao [4*], Ravindranadh Koutavarapu [5*]

[1] School of Engineering & Technology, ISBM University, Gariyaband, India
[2] Institute of Physics Belgrade, Belgrade, Serbia
[3] Department of Physics, North-Eastern Hill University (NEHU), Shillong, Meghalaya, India; e-mail: jsvikasdubey@gmail.com
[4] Department of Physics, Andhra Loyola College, Vijayawada, India; e-mail: raomc72@gmail.com
[5] Department of Robotics Engineering, College of Mechanical and IT Engineering, Yeungnam University, Republic of Korea; e-mail: ravindra_physicist@ynu.ac.kr

We present new aspects of erbium or ytterbium doped pure gadolinium oxide ($Gd_2O_3:Er^{3+}/Yb^{3+}$) as a suitable candidate for drug delivery and magnetic resonance (MR) applications. The samples were prepared using the conventional sol–gel synthesis technique. The structural studies revealed that the prepared sample was monophased and crystallizes in a cubic structure. FTIR measurements confirmed the creation of $Gd_2O_3:Er^{3+}/Yb^{3+}$ phosphor. SEM micrographs clearly indicated that the particles crystallized in uniform shape, exhibiting nano-rod formation, with the particle size ranging from 55 to 5 nm. TEM images revealed that Er^{3+} and Yb^{3+} co-doped Gd_2O_3 nanoparticles were the collection of the nano-rods 2–4 nm thick and 18–20 nm long. Also, photoluminescence analysis of the phosphor samples for variable concentrations of doping ions was presented. When doped with Er^{3+}/Yb^{3+}, nano-rod Gd_2O_3 emits intense green emission and some red emission peaks, under a 980-nm near-infrared laser. Our study shows that as-prepared samples may be useful for optical imaging systems and that nano-rod formation may be used as a major host carrier for drug delivery.

Keywords: *rare earth activated phosphors, X-ray diffraction, Fourier transform infrared, scanning electron microscope, photoluminescence, magnetic resonance.*

АП-КОНВЕРСИЯ АКТИВИРОВАННОГО ИОНАМИ Er^{3+}/Yb^{3+} ЛЮМИНОФОРА Gd_2O_3 ДЛЯ МАГНИТНО-РЕЗОНАНСНЫХ ПРИМЕНЕНИЙ

P. K. Yadaw [1], J. Mitrić [2], N. Romčević [2], V. Dubey[3*], N. K. Swamy [1], M. C. Rao [4*], R. Koutavarapu [5*]

УДК 535.37;543.422.25

[1] Школа инженерии и технологий, Университет ISBM, Гариябанд, Индия
[2] Институт физики Белграда, Белград, Сербия
[3] Университет Северо-Восточного Хилла (NEHU), Шиллонг, Мегхалая, Индия; e-mail: jsvikasdubey@gmail.com
[4] Колледж Андхра Лойола, Виджаявада, Индия; e-mail: raomc72@gmail.com
[5] Колледж машиностроения и информационных технологий, Университет Юннам, Республика Корея; e-mail: ravindra_physicist@ynu.ac.kr

(Поступила 29 апреля 2023)

Оксид гадолиния, легированный эрбием или иттербием ($Gd_2O_3:Er^{3+}/Yb^{3+}$), использован для доставки лекарств и магнитно-резонансных (МР) применений. Образцы синтезированы традиционным золь-гель-методом. Полученный образец является однофазным и кристаллизуется в кубической

[**] Полный текст публикуется в JAS V. 91, No. 3 (http://springer.com/journal/10812) и в электронной версии ЖПС Т. 91, № 3 (http://www.elibrary.ru/title_about.asp?id=7318; sales@elibrary.ru).

структуре. Измерения с помощью ИК-Фурье-спектроскопии подтвердили создание люминофора $Gd_2O_3:Er^{3+}/Yb^{3+}$. СЭМ-изображения показали, что частицы однородной формы, наностержни с размером частиц от 55 до 5 нм. Согласно ПЭМ-изображениям, наночастицы Gd_2O_3, совместно легированные Er^{3+} и Yb^{3+}, представляют собой совокупность наностержней толщиной 2–4 нм и длиной 18–20 нм. Представлен анализ фотолюминесценции образцов люминофоров для переменных концентраций легирующих ионов. При легировании Er^{3+}/Yb^{3+} наностержень Gd_2O_3 излучает интенсивное зеленое излучение и несколько пиков красного излучения под действием излучения лазера ближнего ИК-диапазона с длиной волны 980 нм. Приготовленные образцы могут быть полезны для систем оптической визуализации, сформированные наностержни могут использоваться в качестве основного носителя для доставки лекарств.

Ключевые слова: *активированные редкоземельными элементами люминофоры, рентгеновская дифракция, ИК-Фурье-спектроскопия, сканирующая электронная микроскопия, фотолюминесценция, магнитный резонанс.*

Introduction. Up-conversion (UC) luminescence materials are widely used in many fields, such as biomedical imaging, solid-state lighting, security encoding and temperature sensors [1, 2]. Some rare earth ions, containing Er^{3+}, Ho^{3+}, Tm^{3+}, and Eu^{3+}, have been widely used in UC phenomenon research [3–5]. The Er^{3+} ion is one of the most commonly used ions for UC luminescence; owing to its energy levels, $^4I_{9/2}$ and $^4I_{11/2}$ can be easily populated by near-infrared laser diodes. During recent years, plenty of results have reported the UC luminescence of the Er^{3+}/Yb^{3+} co-doped phosphors. For a 980-nm laser, Yb^{3+} ion has high absorption efficiency and the luminescence efficiency of the Er^{3+} ion can be increased through the energy transfer from Yb^{3+} to Er^{3+}. However, doping with the Yb^{3+} ion is not enough to enhance the luminescence efficiency of the Er^{3+} ion. Some research groups reported that adding an appropriate Li^+ ion to the rare earth ion-doped system can enhance UC luminescence efficiency [6, 7]. For the UC phenomenon, host materials with lower phonon energy contribute to enhancing the emission efficiency of the activation ion. The lower phonon energy helps to reduce nonradiative losses, thereby increasing luminescence efficiency [8]. As an excellent matrix, Gd_2O_3 has low phonon frequency (phonon cut off ~600 cm^{-1}), and great chemical and thermal stability [7]. Gd_2O_3 materials can be synthesized with different rare earth ions for UC emission [8]. Rare earth-doped materials based on Gd_2O_3 can be used as fluorescence and magnetic resonance imaging (MRI) labels.

The nanotechnology may be capable of increasing the percentage of the early diagnosis of cancer, through enhanced imaging [9, 10]. Nanotechnology has great potential in increasing the potency and selectivity of chemical, biological and physical approaches aimed at eliciting cancer cell deaths, although minimizing the collateral toxicity to the nonmalignant cells [11]. For a variety of diseases including cancer, Wang et al. [12] discussed photodynamic therapy (PDT) as a major non-invasive treatment modality. PDT is based on up-conversion of the nanoparticles (UCNPs) and has received ample attention in recent years. Below near-infrared (NIR) light excitation, UCNPs are capable of emitting higher energy visible light, which can then easily activate the surrounding photo-sensitizer molecules aiming to produce singlet oxygen. This singlet oxygen then ultimately kills cancer cells.

Until prepared materials were discovered recently, europium-based yttrium oxide ($Y_2O_3:Eu^{3+}$), a red phosphor, was broadly used in numerous optical display-related applications. At the present time, it has evolved to become a prime focus of research amongst numerous groups owing to its exceptional optical damage threshold, low toxicity, vacuum-ultraviolet transparency, strong luminescence intensity, high chemical stability and high quantum yield [13–15]. Numerous techniques have been tested and conveyed for the synthesis of $Y_2O_3:Eu^{3+}$ phosphor, which includes chemical vapour deposition [16], solid-state reactions and techniques [17], sol–gel routes [18], microwave heating [19], auto-combustion [20] and hydrothermal techniques [21]. Yet, only a small number of reports exist to date about the synthesis techniques of the size-controlled, $Y_2O_3:Eu^{3+}$ nanophosphor, less than ~10 nm in size [18, 22]. This is a well-known fact that the morphology and size of the host particles affect the characteristics of the as-prepared phosphors very intensively and plays a vital role in biological applications such as bio-labelling [23]. The size of the biological labelling materials that exceeds 10 nm has a significant impact on carriage over the vascular-endothelium or nuclear-envelope, flow by means of urine and intracellular tracking [24, 25]. According to Feng et al., UC of nanophosphors can create visibly or near-infrared emissions under continuous wave NIR stimulation [26]. In this present study, we proposed the up-conversion of the luminescent behaviour of Er^{3+}/Yb^{3+} activated Gd_2O_3 phosphor for biomedical applications.

Experimental. Gd_2O_3 phosphors doped with different concentrations of Er^{3+}/Yb^{3+} ions (0.1–2.5 mol. %) were prepared by using the sol–gel synthesis route. Highly purified citric acid, [Yb $(NO_3)_3 \cdot 5H_2O$], $[Er(NO_3)_3 \cdot 5H_2O]$ and $[Gd(NO_3)_3 \cdot 6H_2O]$, were primarily taken without further purification as starting materials. At first, all the initial materials were primarily weighed using a 150-mL glass beaker and dissolved in 10 mL of deionized water. Then, the as-prepared metal citrate complex was carefully stirred together using a magnetic stirrer. After 1 h of stirring at 500 rpm, the basic translucent aqueous solutions were achieved. Then, these translucent solutions were again dried in an oven at 110°C until uniformly dried gels were created. The brown flakes were treated by heating these dry gels at 400°C for about 120 min. To get the final product, the brown flakes were again calcined in a muffle furnace at a temperature of about 1000°C for 180 min in an air atmosphere.

The X-ray diffraction (XRD) patterns of the samples were captured using a RIGAKUM-MiniFlex-II diffractometer functioning with Bragg–Brentano focusing geometry. CuK_α radiation (λ = 1.54060 Å) had been used as an X-ray source. These instruments were generally operated at a high voltage of 40 kV and a low operating current of 30 mA. The XRD patterns were noted with a scan rate of about 5°/min within a range of 10–70°. Perkin Elmer-Spectrum 100 Fourier Transform Infrared (FTIR) Spectrometer was used to measure different bands within the produced phosphor and analyse functional groups, if any, as well as the bending and stretching of bonds in the fingerprint region. A scanning electron microscope (S-3400, Hitachi, Japan), was used to examine the morphology of these samples. The TEM instrument used in this research work was the JEOL/JEM 2100 Model. The spectro-fluorophotometer instruments (RF-5301PC-SHIMADZU) were used to record the excitation spectrum and photoluminescence (PL) emission of the samples under a 980-nm laser excitation wavelength.

Results and discussion. *XRD studies.* The X-ray diffraction patterns of Er^{3+}/Yb^{3+}-activated Gd_2O_3 phosphors are presented in Fig. 1, for an optimized concentration (2.0 mol.%) of Er^{3+}/Yb^{3+}. The sample is monophased and crystallizes in a cubic structure in the 199th space group, I 21 3. All peaks are assigned according to the literature with no further evidence of any impurities. Figure 2 represents the crystal structure of $Gd_2O_3:Er^{3+}/Yb^{3+}$ phosphor. Debye–Scherrer's formula was used to determine crystallite size [27, 28]:

$$D = 0.9\lambda / \beta \cos\theta, \quad (1)$$

where D is particle size, the symbol β is the full width of the peak at half maximum, the λ is the wavelength of the X-ray diffraction source, and θ is the angle of the diffraction.

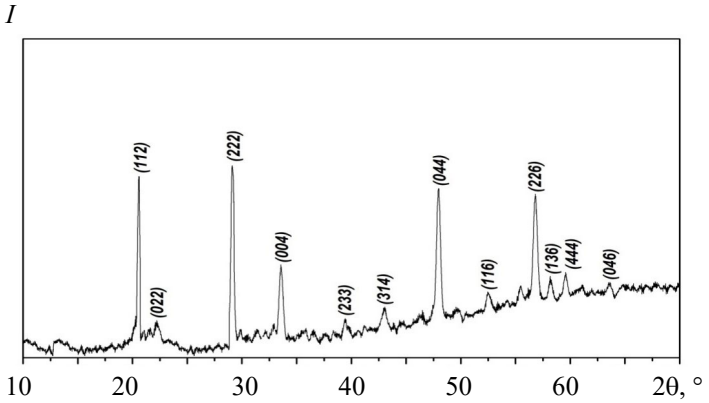

Fig. 1. XRD patterns of $Gd_2O_3:Er^{3+}/Yb^{3+}$ (2.0 mol.%) phosphor.

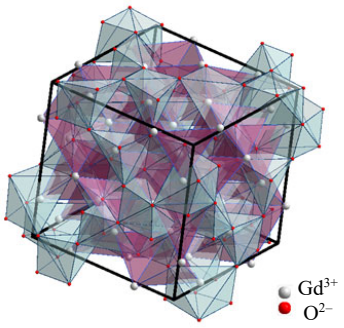

Fig. 2. Crystal structure of $Gd_2O_3:Er^{3+}/Yb^{3+}$ phosphor.

FTIR studies. The FTIR spectrum of the $Gd_2O_3:Er^{3+}/Yb^{3+}$ (2.0 mol.%) sample is presented in Fig. 3. This transmittance spectrum exhibits very strong peaks at 552 and 457 cm^{-1}. These are characteristic modes of gadolinium and oxide (Gd-O) vibrations. The various peaks at 801 and 1381 cm^{-1} arise because of doping ions, and its vibrations with oxygen ions. The peak at 801 cm^{-1} corresponds to the Er-O vibration, whereas the peak at 1381 cm^{-1} describes the ytterbium and oxide (Yb-O) vibration. Altogether, these observed peaks confirm the formation of $Gd_2O_3:Er^{3+}/Yb^{3+}$ phosphor and are presented in Table 1. Also, the peak at ~3434 cm^{-1} is allotted to the intermolecular H-bonding of H_2O. These prepared specimens may have absorbed some of the moisture from the laboratory or atmosphere.

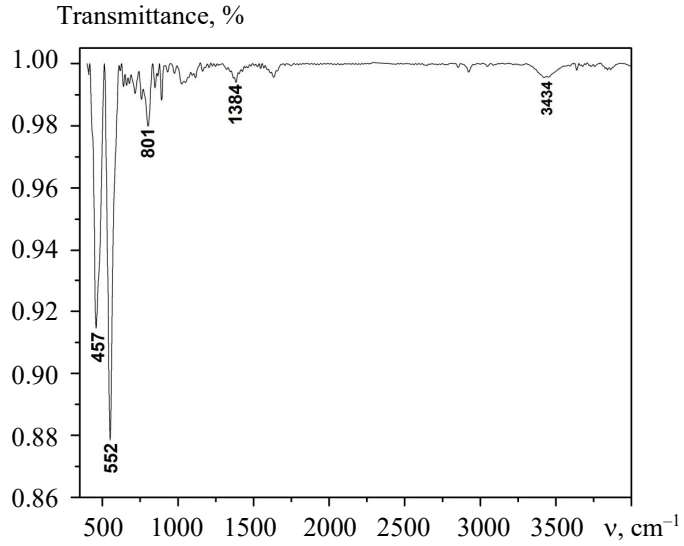

Fig. 3. FTIR spectrum of $Gd_2O_3:Er^{3+}/Yb^{3+}$ (2.0 mol.%) phosphor.

TABLE 1. Assigned IR Modes of $Gd_2O_3:Er^{3+}/Yb^{3+}$ (2.0 mol.%) Phosphor

Experimentally obtained IR mode, cm^{-1}	Assignation
457	Gd–O vibration
552	Gd–O vibration
801	Er–O vibration
1384	Yb–O vibration
3434	intermolecular H-bonding in H_2O

SEM and TEM analysis. The scanning electron microscopy (SEM) micrographs of $Gd_2O_3:Er^{3+}/Yb^{3+}$ (2.0 mol.%) sample are presented in Fig. 4 with different magnifications (50, 5, and 1 μm). Micrographs clearly indicate that the particles are crystallized in uniform shape, showing nano-rod formation, with the particle size ranging from 55 to 5 nm. This gradient in particle size is expected as these samples are known for their agglomeration [29]. Figure 5 represents the transmission electron microscopy (TEM) images of $Gd_2O_3:Er^{3+}/Yb^{3+}$ (2.0 mol.%) phosphor with different sizes. The formation of nano-rods is also confirmed by high-resolution TEM images presented in Figs. 5a,b. The TEM images revealed that Er^{3+} and Yb^{3+} co-doped Gd_2O_3 nanoparticles are the collection of nanorods 2–4 nm thick and 18–20 nm long. The synthesized samples show nano-rod shapes, along with no other critical differences in the morphology. This pattern is fairly comparable with the results obtained by SEM analysis.

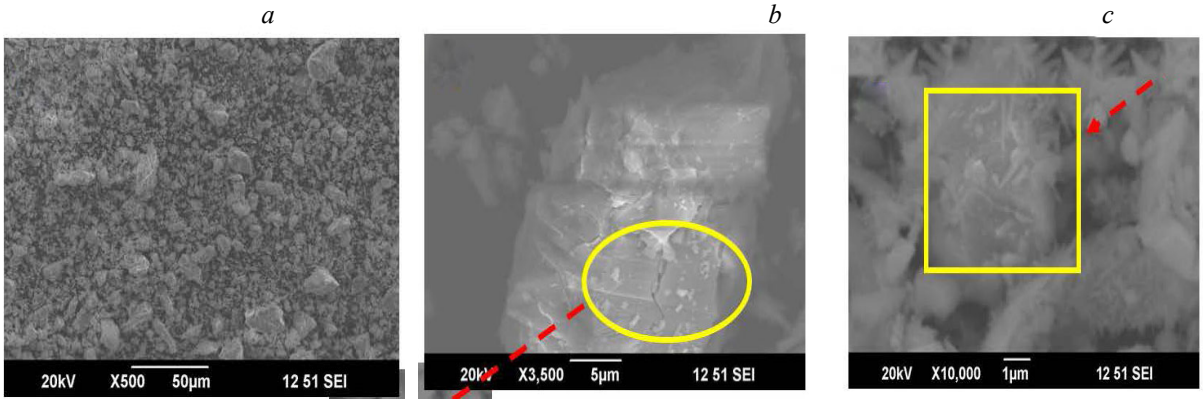

Fig. 4. SEM micrographs of $Gd_2O_3:Er^{3+}/Yb^{3+}$ (2.0 mol.%) phosphor with different magnifications (a) 50 μm, (b) 5 μm, and (c) 1 μm.

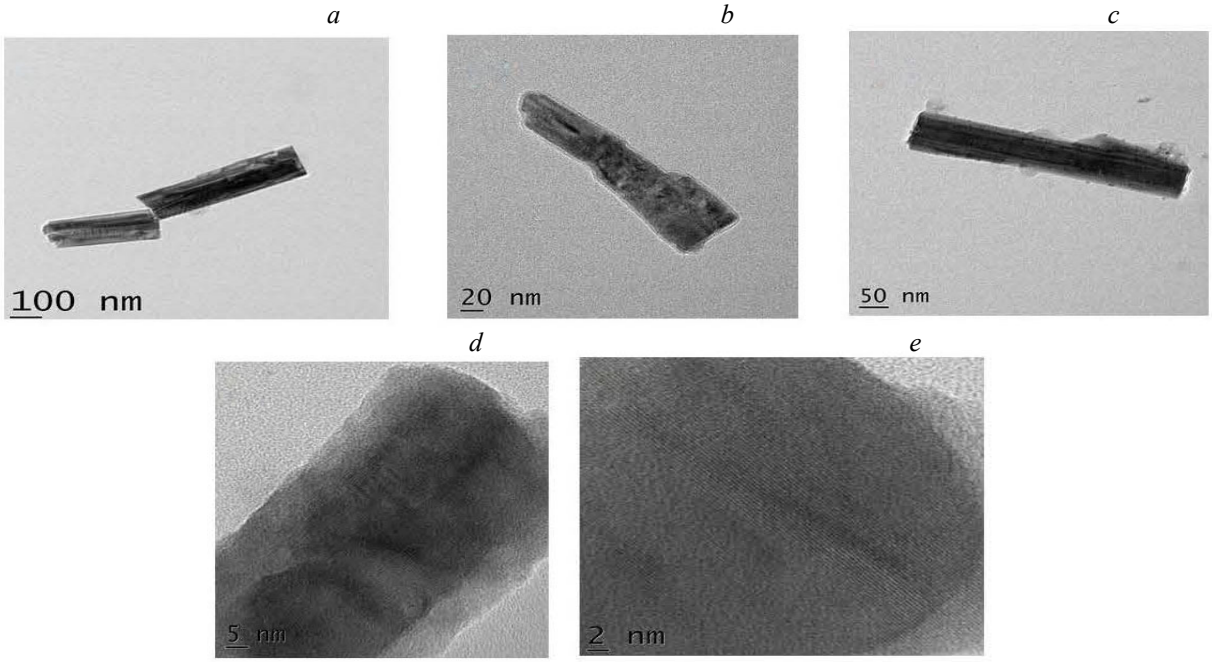

Fig. 5. TEM images of $Gd_2O_3:Er^{3+}/Yb^{3+}$ (2.0 mol.%) phosphor: a–e??.

Photoluminescence spectroscopy. The photoluminescence excitation spectrum of $Gd_2O_3:Er^{3+}/Yb^{3+}$ (2.0 mol.%) phosphor is presented in Fig. 6a with a 980-nm excitation laser line and corresponding up-conversion emission spectra at room temperature shown in Fig. 6b. All spectra display characteristic emission peaks from erbium (Er^{3+}) in the host cubic Gd_2O_3. Herein, Er^{3+} behaves as an activator, whereas Yb^{3+} behaves as a sensitizer. Conferring to the energy levels of erbium (Er^{3+}) ions, the detected peaks, 555 and 523 nm are in the green region and are allocated to their transitions $^4S_{3/2}\rightarrow{}^4I_{15/2}$ and $^2H_{11/2}\rightarrow{}^4I_{15/2}$ of Er^{3+} correspondingly. With the intention to understand the UC emission band's UC mechanisms, the up-conversion intensity (I) of the various transitions is studied as a function of the pump power. In the case of the Er^{3+}/Yb^{3+}-doped phosphor, the phenomenon deals with UC luminescence behaviour. Photon UC is a process in which the sequential absorption of two or more photons leads to the emission of light at a shorter wavelength than the excitation wavelength. It is an anti-Stokes-type emission. An example is the conversion of infrared light to visible light. UC can take place in both organic and inorganic materials, through a number of different mechanisms. There are three basic mechanisms for photon UC in inorganic materials and at least two distinct mechanisms in organic materials. In inorganic materials photon up-conversion occurs through energy transfer UC (ETU), excited-state absorption (ESA), and photon avalanche (PA). Such processes can be observed in materials with very different sizes and structures, including optical fibres, bulk crystals or nanoparticles, as long as they contain any of the active ions mentioned above. Organic molecules can up-convert photons through sensitized triplet–triplet annihilation and energy pooling [30–34].

In the UC process, the UC intensity is directly proportional to n^{th} power of the entire pump power, where symbol n is the number of pumped photons absorbed per the up-converted photons produced. The plot of UC intensity against pump photons shows a straight line, which is displayed in Fig. 6c, with a slope n. Below 980-nm excitation, the slope values attained are 1.29/0.02 and 1.37/0.03 for 555 nm ($^4S_{11/2}\rightarrow{}^4I_{15/2}$) emission correspondingly. These outcomes show that a two-photon process is accountable for the green UC. The activator concentration is increased more as the emission intensity begins to drop (Fig. 6d). The extensive increase in ion-to-ion interactions causes the shortest distance amongst interacting activators as the rise in concentration causes concentration quenching. The spectral profile of the fluorescent light as a major function of different activator concentrations is observed. The outcomes clearly show the CIE chromaticity coordinates of complete emission of transformed light, resulting in various colours in the complete emission of light.

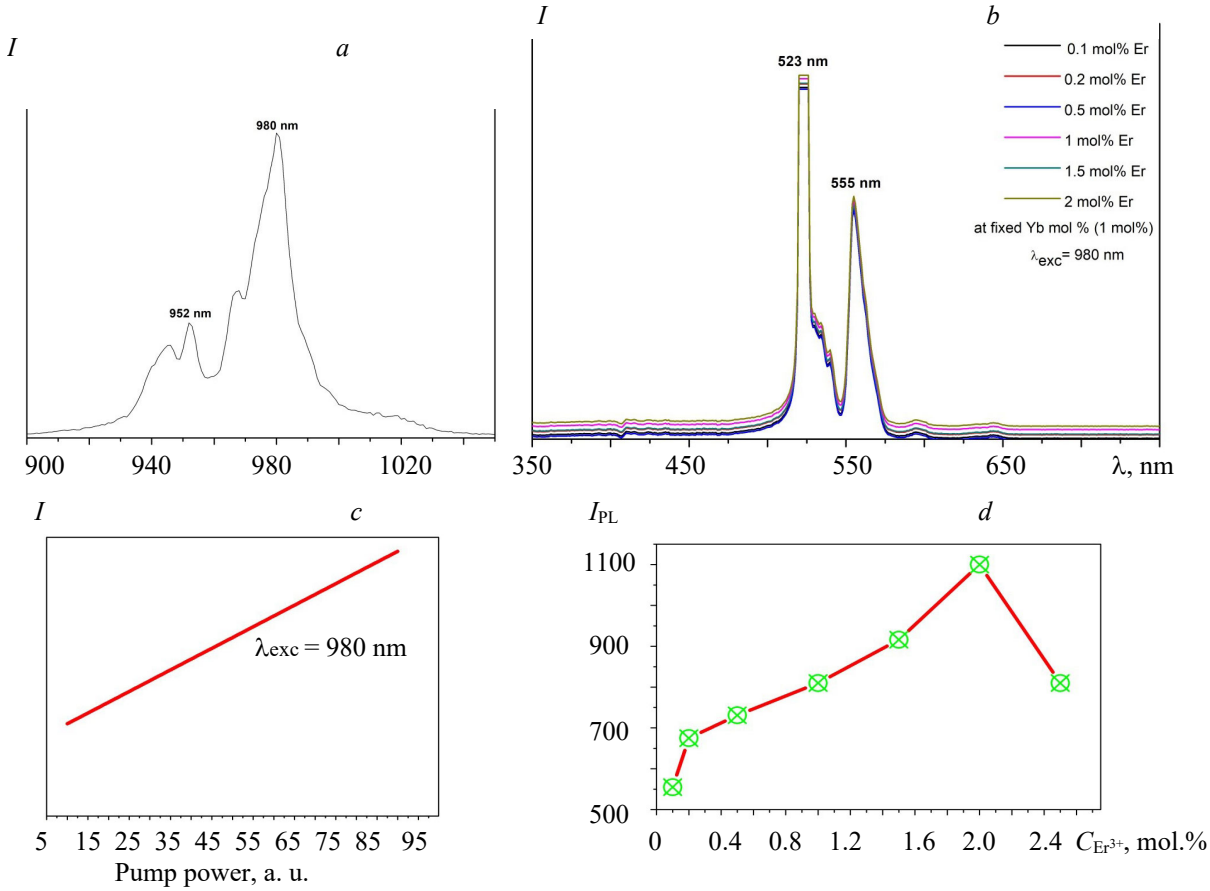

Fig. 6. (a) PL excitation spectrum of $Gd_2O_3:Er^{3+}/Yb^{3+}$ (2.0 mol.%) phosphor below 980 nm laser excitation wavelength. (b) PL emission spectra of $Gd_2O_3:Er^{3+}/Yb^{3+}$ phosphor below 980 nm laser excitation. (c) The up-conversion emission intensities depend on the excitation power of Er^{3+}/Yb^{3+}-doped Gd_2O_3 phosphor. (d) Concentration quenching (cross-relaxation phenomenon) of $Gd_2O_3:Er^{3+}/Yb^{3+}$ phosphor below 980-nm laser excitation.

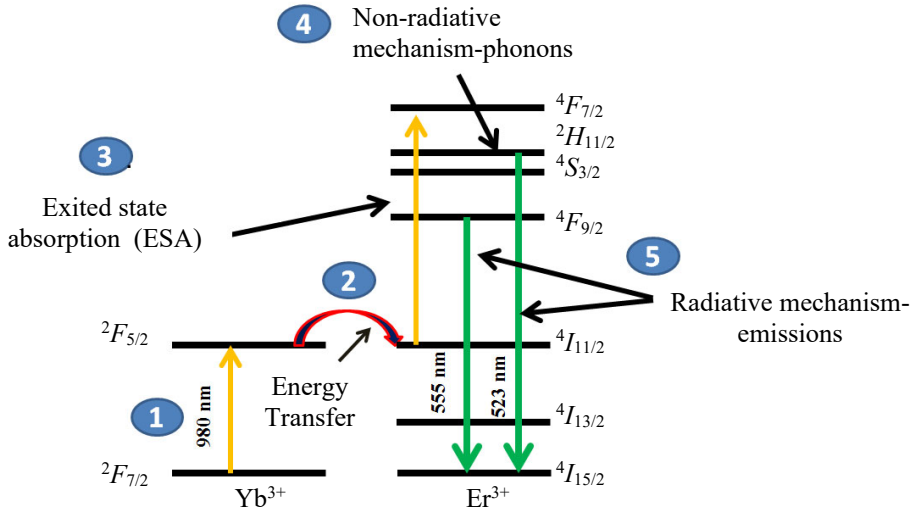

Fig. 7. Energy transfer mechanism for up-conversion behaviour of $Gd_2O_3:Er^{3+}/Yb^{3+}$ phosphor.

Several well-known mechanisms can be used to populate the excited states for UC: 980 nm laser excitation, energy transfer (ET) excited state absorption, non-radiative mechanism (phonon) and radiative mechanism emission [35–37]. The photon avalanches are judged to be a probable mechanism of UC for the reason that no inflection points are detected in the power study (Fig. 7). Figure 7 presents an energy level diagram of erbium and ytterbium (Er^{3+}/Yb^{3+}) ions in addition to the possible UC mechanisms corresponding to the related green emissions for 980-nm excitation. Again, using the spectral energy distribution of the $Gd_2O_3:Er^{3+}/Yb^{3+}$ samples, the CIE co-ordinates are determined using the spectrophotometric technique (Fig. 8) and $x = 0.28$ and $y = 0.48$ are the CIE colour coordinates for the Er^{3+}/Yb^{3+} (2.0 mol. %)-doped sample (these coordinates are quite near to the green light emission). As a result, this phosphor has good colour tenability, when exposed to green light. The produced phosphor could be useful in the application of green light-emitting diodes.

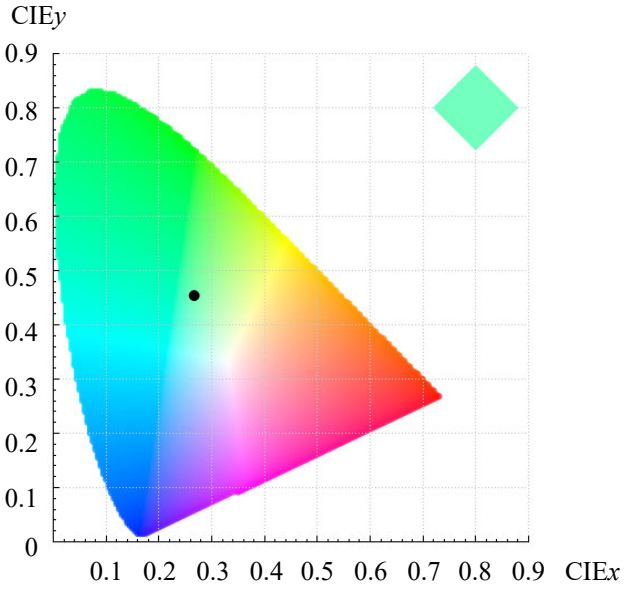

Fig. 8. CIE coordinates 1931 for $Gd_2O_3:Er^{3+}/Yb^{3+}$ (2.0 mol.%) phosphor.

Conclusions. $Gd_2O_3:Er^{3+}/Yb^{3+}$ phosphors were prepared, along with various concentrations of the dopant ions. These samples were mainly characterized using different techniques, for instance, XRD, FTIR, SEM, TEM, and PL. XRD patterns showed that $Gd_2O_3:Er^{3+}/Yb^{3+}$ phosphors crystallize in cubic structure. FTIR measurements confirmed the creation of the $Gd_2O_3:Er^{3+}/Yb^{3+}$ phosphor. SEM and TEM measurements showed the formation of nano-rods. PL measurements showed excitation and emission characteristics of as-prepared phosphor for possible magnetic resonance and drug delivery applications. The CIE colour coordinates ($x = 0.28$ and $y = 0.48$) for the Er^{3+}/Yb^{3+} (2.0 mol. %) doped sample were quite near to the green light emission. As a result, this phosphor had good colour tenability, when exposed to green light. The produced phosphor could be useful in the application of green light-emitting diodes. The up-conversion behaviour of phosphor showed drug delivery abilities and hence could be suitable and potentially used for MRI and other supplementary uses such as fluorescent imaging.

REFERENCES

1. H. Liu, X. He, H. Jia, Y. Zheng, R. Bai, Y. Zhang, *Optik*, **228**, 166155 (2021).
2. A. Urbina-Frías, T. López-Luke, J. Oliva, P. Salas, A. Torres-Castro, E. De la Rosa, *J. Lumin.*, **172**, 154–160 (2016).
3. J. Tang, Y. Huang, M. Sun, J. Gou, Y. Zhang, G. Li, Z. Xiao, *J. Lumin.*, **197**, 153–158 (2018).
4. P. Singh, P. K. Shahi, A. Rai, A. Bahadur, S. B. Rai, *Opt. Mater.*, **58**, 432–438 (2016).
5. A. Brenier, *Chem. Phys. Lett.*, **290**, No. 4-6, 329–334 (1998).
6. E. Kolobkova, A. Alkhlef, L.Y. Mironov, O. Bogdanov, *Ceram. Int.*, **46**, No. 16, 26396–26402 (2020).

7. G. Chen, R. Lei, H. Wang, F. Huang, S. Zhao, S. Xu, *Opt. Mater*., **77**, 233–239 (2018).
8. J. Zhang, Z. Zhai, G. Chen, *J. Alloys Compd*., **610**, 409–415 (2014).
9. L. Nystrom, L. E. Rutqvist, S. Wall et al., *Lancet*, **341**, 973–978 (1993).
10. S. Winawer, R. Fletcher, D. Rex et al., *Gastroenterol*., **124**, 544–560 (2003).
11. W.H. Gmeiner, S. Ghosh, *Nanotechnol. Rev*., **3**, No. 2, 111–122 (2015).
12. C. Wang, L. Cheng, Z. Liu, *Theranostics*, **3**, No. 5, 317–330 (2013).
13. F. Wang, W. B. Tan, Y. Zhang, X. Fan, M. Wang, *Nanotechnol*., **17**, R1–R13 (2006).
14. E. Wakefield, P. Holland, J. Dobson, J. L. Hutchison, *Adv. Mater*., **13**, 1557–1560 (2001).
15. Y. C. Kang, H. S. Roh, S. B. Park, *Adv. Mater*., **12**, 451–477 (2000).
16. J. McKittrick, C. F. Bacalski, G. A. Hirata, K. M. Hubbard, S. G. Pattillo, K. V. Salazar, M. Trkula, *J. Am. Ceram. Soc*., **83**, 1241–1250 (2000).
17. P. Maestro, D. Huguenin, A. Seigneurin, F. Deneuve, P. L. Lann, J. F. Berar, *J. Electrochem. Soc*., **139**, 1472–1479 (1992).
18. B. K. Gupta, D. Haranath, S. Saini, V. N. Singh, V. Shanker, *Nanotechnol*., **21**, 055607 (2010).
19. S. Dutta, Q. Mohammad, S. S. Manoharan, *J. Mater. Sci. Lett*., **21**, 1077–1085 (2002).
20. T. Ye, Z. Guiwen, Z. Weiping, X. Shangda, *Mater. Res. Bull*., **32**, 501–511 (1997).
21. X. Li, Q. Li, Z. Xia, L. Wang, W. Yan, J. Wang, R. I. Boughton, *Cryst. Growth Des*., **6**, 2193–2194 (2006).
22. A. P. Jadhav, A. Pawar, C. W. Kim, H. G. Cha, U. Pal, Y. S. Kang, *J. Phys. Chem. C*, **113**, 16652 (2009).
23. Y. C. Kang, I. W. Lenggoro, S. B. Park, K. Okuyama, *J. Solid State Chem*., **146**, 168–175 (1999).
24. A. M. Smith, X. Gao, S. Nie, *Photochem. Photobiol*., **80**, 377–385 (2004).
25. T. Kushida, M. Tanaka, *Phys. Rev. B*, **65**, 195118 (2002).
26. W. Feng, C. Han, F. Li, *Adv. Mater*., **25**, 5287–5303 (2013).
27. K. Ravindranadh, B. Babu, C. V. Reddy, J. Shim, M. C. Rao, R. V. S. S. N. Ravikumar, *Appl. Mag. Res*., **46**, No. 1, 1–15 (2015).
28. Sk. Muntaz Begum, G. Nirmala, K. Ravindranadh, T. Aswani, M. C. Rao, *J. Mol. Struct*., **1006**, No. 1, 344–347 (2011).
29. V. Dubey, R. Tiwari, Raunak Kumar Tamrakar, Jagjeet Kaur, S. Dutta, Subrata Das, H. G. Visser, S. Som, *J. Lumin*., **180**, 169–176 (2016).
30. T. N. Singh-Rachford, F. N. Castellano, *Coord. Chem. Rev*., **254**, No. 21-22, 2560–2573 (2010).
31. D. H. Weingarten, *Nat. Commun*., **8**, 1480 (2017).
32. G. Bilir, O. Erguzel, *Mater. Res. Express*, **3**, No. 10, 106201 (2016).
33. Y. Zhang, H. Jia, X. He, Y. Zheng, R. Bai, H. Liu, *J. Lumin*., **236**, 118111 (2021).
34. E. Hemmer, T. Yamano, H. Kishimoto, N. Venkatachalam, H. Hyodo, K. Soga, *Acta Biomater*., **9**, No. 1, 4734–4743 (2013).
35. D. M. Bubb, D. Cohen, S. B. Qadri, *Appl. Phys. Lett*., **87**, No. 13, 131909 (2005).
36. L. S. Wang, Y. H. Zhou, Z. W. Quan, J. Lin, *Mater. Lett*., **59**, No. 10, 1130–1133 (2005).
37. H. Guo, N. Dong, M. Yin, W. Zhang, L. Lou, S. Xia, *J. Phys. Chem. B*, **108**, No. 50, 19205–19209 (2004).